

UNIVERSITY OF OKLAHOMA

GRADUATE COLLEGE

ENSEMBLE KALMAN FILTER ASSIMILATION OF DOPPLER RADAR DATA
FOR THE INITIALIZATION AND PREDICTION OF CONVECTIVE STORMS

A DISSERTATION

SUBMITTED TO THE GRADUATE FACULTY

in partial fulfillment of the requirement for the

degree of

Doctor of Philosophy

By

MINGJING TONG
Norman, Oklahoma
2006

ENSEMBLE KALMAN FILTER ASSIMILATION OF DOPPLER RADAR DATA
FOR THE INITIALIZATION AND PREDICTION OF CONVECTIVE STORMS

A DISSERTATION APPROVED FOR THE
SCHOOL OF METEOROLOGY

BY

Ming Xue, Committee Chair

Kelvin Droegemeier

Lance Leslie

Alan Shapiro

Sivaramakrishnan Lakshmivarahan

Acknowledgements

I would like to express my sincere gratitude to my advisor, Dr. Ming Xue, for his guidance and mentoring, and for his encouragement and support at all levels. He provided me with many good and important suggestions, when I was developing the EnKF system. I thoroughly enjoyed and was inspired by countless discussions between us on my research, including those at our regularly weekly meetings.

Besides my advisor, I would like to thank all other members of the dissertation committee: Dr. Kelvin Droegemeier, Dr. Lance Leslie, Dr. Alan Shapiro, and Dr. Sivaramakrishnan Lakshmivarahan for reading this dissertation and offering comments on my research.

I am very grateful to my colleagues at CAPS. Dr. William Martin contributed to the initial development of the EnKF analysis code. I thank Dr. Keith Brewster for helping me with the radar emulator. I am grateful to Dr. Ming Hu for providing radar data used in Chapter 6. My research is also benefited from discussions with all members of the research group led by Dr. Xue.

I especially thank Dr. Frederick Carr for his invaluable comments on my research and suggestions on my doctoral study. Thanks also extend to staffs at school of meteorology and CAPS, particularly, Celia Jones, Marcia Pallutto, Eileen Hasselwander and Scott Hill for their kind help. I also thank my officemates, Haixia and Elaine, for their friendships, discussions on research and careers.

My deepest thanks go to my family for their unconditional love and support. I thank my husband, Ying, for sharing my frustrations and joys throughout my dissertation work, and for his always willing to offer help when I encountered problems with code debugging. I especially own much to my parents Guangsheng Tong and Shufen Zhou, and parents in law Shirong Xiao and Keqiong Pan for taking care of my son for three years. Without their constant support and encouragement, the research would not have been possible.

This work was primarily supported by NSF grants ATM-0129892 and ATM-0530814. Some support was also provided by an FAA grant via DOC-NOAA NA17RJ1227. The computations were performed at the Pittsburgh Supercomputing Center supported by NSF and on IBM Regatta operated by OSCER of University of Oklahoma.

Table of Contents

Acknowledgements	IV
Table of Contents.....	VI
List of Tables	X
List of figures.....	XI
Abstract	XIX
Chapter 1 Introduction and Overview	1
1.1 Background and Motivation	1
1.2 Dissertation Outline	4
Chapter 2 The Ensemble Kalman Filter	8
2.1 Theoretical background of EnKF	9
2.1.1 Error evolution	9
2.1.1.1 Theory of stochastic dynamic prediction.....	9
2.1.1.2 The Monte Carlo method	12
2.1.2 Filter theory and Kalman filter	12
2.1.2.1 Filter theory.....	12
2.1.2.2 The Kalman filter	14
2.2 The ensemble Kalman filter and its variations	16
2.2.1 Stochastic update method (EnKF)	18
2.2.2 Deterministic update method (EnSRF)	20
2.2.3 Issues associated with the implementation of ensemble-based Kalman filters	22
2.2.3.1 Evaluation of the covariance matrices	22
2.2.3.2 Covariance localization.....	24
2.2.3.3 Sequential assimilation of observations.....	25
2.2.3.4 Filter divergence	26
2.2.3.5 Model error	27

Chapter 3 Ensemble Kalman Filter Assimilation of Doppler Radar Data with a Compressible Nonhydrostatic Model: OSS Experiments	30
3.1 Introduction.....	31
3.2 Assimilation system and experimental design.....	33
3.2.1. The prediction model and truth simulation.....	33
3.2.2. Simulation of radar observations	35
3.2.3. The EnKF data assimilation procedure.....	38
3.3 The Assimilation Experiments.....	41
3.3.1. Assimilations using radial velocity data only	41
3.3.2. Impact of assimilating reflectivity data.....	49
3.3.3. Assimilation of both radial velocity and reflectivity	53
3.3.4. Retrieval of microphysical fields	59
3.4 Forecasts from ensemble-mean analyses.....	62
3.5 Summary and discussion	67
Chapter 4 Simultaneous Estimation of Microphysical Parameters and Atmospheric State with Radar Data and Ensemble Square-root Kalman Filter: Sensitivity Analysis and Parameter Identifiability	70
4.1 Introduction.....	70
4.2 Microphysics description.....	74
4.2.1 Microphysics scheme.....	74
4.2.2 Uncertainties in the microphysical parameters	77
4.3 Model and experimental settings	80
4.3.1 The prediction model and truth simulation.....	80
4.3.2 Experimental design for sensitivity analysis.....	81
4.4 Results of Sensitivity Analysis	84
4.4.1 Sensitivity of pure forecast to microphysical parameters	84
4.4.2 Sensitivity of the distribution of hydrometeors to the microphysical parameters.....	87
4.4.3 Sensitivity of the EnSRF analyses to microphysical parameters.....	94
4.5 Parameter identifiability	102
4.5.1 Parameter identifiability as revealed by the response function.....	102

4.5.2	Parameter identifiability as revealed by the correlation between model outputs of observations and parameters.....	104
4.6	Summary and conclusions	111
Chapter 5 Simultaneous Estimation of Microphysical Parameters and Atmospheric State with Radar Data and Ensemble Square-root Kalman Filter: Parameter Estimation Experiments.....		115
5.1	Introduction.....	115
5.2	Data Assimilation Procedure	119
5.2.1	The EnSRF data assimilation configurations.....	119
5.2.2	Observation operators for radar data.....	122
5.3	The design of parameter estimation experiments	125
5.4	Results.....	131
5.4.1	Results of Experiments Estimating Single Parameters	131
5.4.2	Results of Multiple Parameter Estimation	137
5.4.2.1	Simultaneous estimation of two parameters	138
5.4.2.2	Simultaneous estimation of three parameters	143
5.4.2.3	Simultaneous estimation of four parameters.....	147
5.4.2.4	Simultaneous estimation of five parameters.....	151
5.5	Discussions	153
5.6	Summary and conclusions	159
Chapter 6 Assimilation of Real Radar Data for the May 29, 2004 Central Oklahoma Tornadoic Thunderstorm Case		163
6.1	Introduction.....	163
6.2	The 29-30 May 2004 case, data and observation operators.....	165
6.2.1	Case description	165
6.2.2	Radar data and forward observation operators	168
6.3	Assimilation experiments using homogeneous environmental conditions provided by single sounding.....	170
6.3.1	The EnSRF assimilation system and experiments	170
6.3.1.1	Model configurations	170
6.3.1.2	The EnSRF assimilation experiments.....	171
6.3.1.3	Verification of EnSRF analysis	176

6.3.2 Results	178
6.3.2.1 Dual-radar analysis	178
6.3.2.2 Single-radar analyses	184
6.3.2.3 Forecast starting from single-radar analysis	196
6.4 Assimilation experiments using inhomogeneous environmental conditions provided by 3DVAR analysis.....	200
6.4.1 Experimental design.....	201
6.4.2 Results of analysis.....	202
6.4.3 Results of forecast.....	211
6.5 Summary and discussions.....	214
Chapter 7 Summary and Future work.....	218
7.1 Summary.....	218
7.2 Future work.....	223
References	226
Nomenclature	235

List of Tables

Table 3.1 List of Data Assimilation Experiments.....	42
Table 4.1 A summary of the uncertainty ranges, defined by the lower bound \underline{p}_i and upper bound \bar{p}_i , and the true (control) values for intercept parameters n_{0h} , n_{0s} , n_{0r} , and hail and snow densities ρ_h and ρ_s used in this study.	79
Table 4.2. List of the parameters values, p_i , and the logarithmical deviations of these parameters from their control values, $\Delta 10 \log_{10}(p_i)$, in the simulation and assimilation sensitivity experiments. The parameter that is changed from its control value is listed for the corresponding sensitivity experiment while other parameters used the control values.	88
Table 4.3. List of the time scales of the system response to the change in one of the microphysical parameters in terms of analysis reflectivity for assimilation sensitivity experiments N0h45, N0s37, N0r87, ρ_h 400 and ρ_s 400.	102
Table 4.4. Temporally averaged root-mean-square of correlations between forecast Z or V_r and one of the microphysical parameters as estimated from single-parameter and multiple-parameter forecast ensembles. Temporal averaging was performed upon data outputs at 5-min intervals from $t = 25$ to 100 min.	110
Table 5.1. List of the true value of each microphysical parameter and the true value P_i^t , the upper bound \bar{P}_i and lower bound \underline{P}_i of each logarithmically transformed microphysical parameter $P_i = 10 \log_{10}(p_i)$. σ_{P_i} stands for the standard deviation of the initial parameter perturbations for P_i , and $\underline{\sigma}_{P_i}$ is minimum ensemble spread of P_i used in ensemble inflation.....	128
Table 5.2. The three initial guesses for each parameter in its original form p_{i0}^m and the logarithmical form P_{i0}^m ($m=1,2,3$), which are used in single-parameter estimation experiments.	132
Table 5.3. Two initial guesses of each parameter in the original form p_0^m and the logarithmical form P_0^m ($m=1,2$) used in multiple-parameter estimation experiments.	139

List of figures

- Fig. 2.1. Schematic plot of the EnKF. The dot without ‘×’ donates the model state of an ensemble member in phase space, with green indicating forecast (or background) state and red indicating analysis state. The dot with ‘×’ donates the ensemble mean. The circle indicates the spread of the forecast ensemble. 18
- Fig. 3.1. Vertical velocity [contours and shading at intervals of 4 m s^{-1} ; solid (dash) contours represent positive (negative) values] and horizontal wind (vectors, plotted every other grid point; m s^{-1}), at level $z = 6 \text{ km}$: (a)-(d) truth simulation; analyses from VrP (e)-(h), ZP (i)-(l); VrZPc (m)-(p); VrPZF (q)-(t), at $t = 40, 60, 80$ and 100 min during the assimilation period..... 43
- Fig. 3.2. Horizontal wind (vectors; m s^{-1}), perturbation potential temperature (thick black lines for 0 K and thin dashed contours at 0.5 K intervals) and computed reflectivity (thin solid contours and shading at intervals of 5 dBZ , starting from 15 dBZ) at $z = 250 \text{ m}$: truth (a)-(d), EnKF analyses from VrP (e)-(h), VrZPc (i)-(l) and VrPZF (m)-(p). 44
- Fig. 3.3. The retrieved (a) perturbation q_v (solid (dash) contours represent positive (negative) values) (b) q_c , (c) q_r , (d) q_i , (e) q_s and (f) q_h . (contours and shading at intervals of 0.5 g kg^{-1} for q_v perturbation, q_c , q_i and q_s , and of 1.0 g kg^{-1} for q_r and q_h .) in the x-z plane at $y = 29 \text{ km}$ that pass through the maximum updraft at $t = 60 \text{ min}$: (a1)-(f1) truth simulation, (a2)-(f2) VrP, (a3)-(f3) VrPnoIce, (a4)-(f4) ZP and (a5)-(f5) VrPZF. 46
- Fig. 3.4. The rms errors of ensemble-mean forecast and analysis, averaged over points at which the reflectivity is greater than 10dBZ for: a) u , b) v , c) w and d) perturbation potential temperature θ' , e) perturbation pressure p' , f) q_c , g) q_r , h) q_v (the curves with larger values), q_i (the curves with lower values), i) q_s and j) q_h , for experiment VrP (black), experiment ZP (gray) and experiment VrF (black dotted lines). Units are shown in the plots. The drop of the error curves at specific times corresponds to the reduction of error by analysis. 47
- Fig. 3.5. Forecast error correlations estimated from an ensemble at $t = 80 \text{ min}$ for experiment ZP in the x-z plane at $y=29 \text{ km}$, which passes through the maximum updraft. The error correlation [thick solid (dash) contours represent positive (negative) correlations at intervals of 0.2] between forecast reflectivity Z at $x=32 \text{ km}$ and $z=6 \text{ km}$ (indicated by a black dot) and (a) u , (b) w , (c) θ' , (d) p' , (e) q_c , (f) q_r , (g) q_i , and (h) q_h . The shading and thin solid (thin dashed) contours in (a)-(d) indicate positive (negative) values of model fields from the truth simulation with increment of 4 ms^{-1} for u and w ; 2 K for θ' and 40Pa for p' . The shading and thin contours in (e)-(h) indicate the values of mixing ratio of water and ice fields from the truth simulation with increment of 0.5 g kg^{-1} for q_c , and q_i and 1 g kg^{-1} for q_r and q_h 52

- Fig. 3.6. As in Fig. 3.4, but for experiment VrZPa (black) and experiment VrP (gray). 54
- Fig. 3.7. As in Fig. 3.4, but for experiment VrZPb (black) and experiment VrP (gray). 55
- Fig. 3.8. As in Fig. 3.4, but for experiment VrZPc (black) and experiment VrP (gray). 58
- Fig. 3.9. As in Fig. 3.4, but for experiment VrPZF (thin black curves) and experiment VrP (thin gray curves). The additional thick black curves are for the analysis and forecast ensemble spread of VrPZF, and the spread is calculated only at the points where reflectivity is greater than 10 dBZ, as the errors are. 58
- Fig. 3.10. RMS error of (a) q_i , (b) q_s , (c) q_h for VrP (gray) and VrPnoIce (black). 62
- Fig. 3.11. Vertical velocity (contours and shading at intervals of 4 ms^{-1}) and horizontal wind (vectors; m s^{-1}) at 6 km level for (a)-(e) truth simulation and the forecast beginning from the ensemble-mean analysis at $t = 80 \text{ min}$: (f)-(j) forecast from ensemble-mean analysis of VrPZF, and (k)-(o) forecast from ensemble-mean analysis of VrP. Note the difference in the plotting domains before and after 150 min. 64
- Fig. 3.12. The rms errors of forecasts averaged over the entire domain for: (a) w (m s^{-1}), (b) θ' (K) and (c) qr (g kg^{-1}). The forecasts begin from ensemble-mean analysis at $t = 60 \text{ min}$ (dot), $t = 80 \text{ min}$ (dash) and $t = 100 \text{ min}$ (solid) of experiment VrP (gray thin curves), VrPZF (black thick curves). 65
- Fig. 4.1. (a) Number concentration per mm diameter size and (b) mass-weighted mean terminal velocity of rain (for N0r87: $n_{0r} = 8 \times 10^7 \text{ m}^{-4}$, N0r86: $n_{0r} = 8 \times 10^6 \text{ m}^{-4}$ and N0r36: $n_{0r} = 3 \times 10^6 \text{ m}^{-4}$), snow (for N0s37: $n_{0s} = 3 \times 10^7 \text{ m}^{-4}$, N0s36: $n_{0s} = 3 \times 10^6 \text{ m}^{-4}$, N0s16: $n_{0s} = 1.19 \times 10^6 \text{ m}^{-4}$ and $\rho_s = 400 \text{ kg m}^{-3}$) and hail/graupel (for N0h45: $n_{0h} = 4.0 \times 10^5 \text{ m}^{-4}$, N0h14: $n_{0h} = 1.59 \times 10^4 \text{ m}^{-4}$, N0h44: $n_{0h} = 4 \times 10^4 \text{ m}^{-4}$ and $\rho_h = 400 \text{ kg m}^{-3}$). The terminal velocities are calculated for an air density of 1.0 kg m^{-3} . The default values of the microphysical parameters are $n_{0r} = 8 \times 10^6 \text{ m}^{-4}$, $n_{0s} = 3 \times 10^6 \text{ m}^{-4}$, $n_{0h} = 4 \times 10^4 \text{ m}^{-4}$, $\rho_h = 913 \text{ kg m}^{-3}$ and $\rho_s = 100 \text{ kg m}^{-3}$ unless otherwise indicated by the curve legends. 76
- Fig. 4.2. The variations of the response function J for radial velocity (left panels) and reflectivity (right panels), plotted against the logarithmic-form deviations of the parameters from their true values for the simulation sensitivity experiments. The response functions are calculated using 'error-free' observations. 85
- Fig. 4.3. Temporally and spatially averaged mixing ratios (g kg^{-1}) as a function of height for control simulation (thin black curves) and for simulations N0h45 (thick black) and N0h14 (thick gray) (a and f); N0s37 (thick black) and N0s16 (thick gray) (b and g); N0r87 (thick black) and N0r36 (thick gray) (c and h); ρ_h400 (thick black) and ρ_h576 (thick gray) (d and i); and ρ_s400 (thick black) and ρ_s63 (thick gray) (e and j). Temporal averaging was performed upon data output at 5-min intervals from $t = 25$ to 100 min. Spatial averaging was performed horizontally over all grid points in the $64 \text{ km} \times 64 \text{ km}$ horizontal domain. 89

- Fig. 4.4. Vertical cross sections of mixing ratios (g kg^{-1}) of hydrometeors and radar reflectivity (dBZ) through the maximum updraft at $t = 70$ min for control simulation (a-c) ; N0h45 (d-f); N0s37 (g-i); N0r87 (j-l); ρ_h 400 (m-o) and ρ_s 400 (p-r). 90
- Fig. 4.5. The response functions ΔJ_{V_r} (a and c) and ΔJ_Z (b and d) of the assimilation sensitivity experiments against the logarithmic-form deviation of the parameters from their true values. 96
- Fig. 4.6. The same as Fig. 4.3, but for EnSRF data assimilation sensitivity experiments N0h45 (thick black) and N0h14 (thick gray) (a and f); N0s37 (thick black) and N0s16 (thick gray) (b and g); N0r87 (thick black) and N0r36 (thick gray) (c and h); ρ_h 400 (thick black) and ρ_h 576 (thick gray) (d and i); and ρ_s 400 (thick black) and ρ_s 63 (thick gray) (e and j). 98
- Fig. 4.7. Vertical cross sections of the ensemble mean of radar reflectivity (dBZ) through the maximum updraft at $t = 70$ min for control data assimilation experiment (a), assimilation sensitivity experiments N0h45 (b), N0s37 (c), N0r87 (d), ρ_h 400 (e) and ρ_s 400 (f). 99
- Fig. 4.8. Time evolution of (a) ΔJ_{V_r} and (b) ΔJ_Z from assimilation sensitivity experiments N0h45, N0s37, N0r87, ρ_h 400 and ρ_s 400 (c.f., Table 4.2). 100
- Fig. 4.9. Correlation coefficients calculated from the ensemble members of single-parameter ensemble forecasts at $t = 70$ min. The correlation [thick solid (dash) contours represent positive (negative) values at intervals of 0.2] between forecast Z and (a) n_{oh} at 1.5° , (b) n_{os} at 1.5° , (c) n_{or} at 0.5° (d) ρ_h at 1.5° (e) ρ_s at 0.5° , (f) n_{oh} at 5.3° , (b) n_{os} at 5.3° , (c) n_{or} at 4.3° (d) ρ_h at 5.3° (e) ρ_s at 6.2° elevation levels. The shading and thin solid contours represent Z from simulations N0h45 (a and f); N0s37 (b and g); N0r87 (c and h); ρ_h 400 (d and i); and ρ_s 400 (e and j). 106
- Fig. 4.10. As in Fig. 4.9, but the correlation coefficients are estimated from the members of 5-parameter forecast ensemble at $t = 70$ min. The shading and thin solid contours represent Z from control simulation. 106
- Fig. 5.1. The evolution of the parameter distribution from single-parameter estimation experiments through the assimilation cycles for n_{oh} (a)-(c), n_{os} (d)-(f), n_{or} (g)-(i), ρ_s (j)-(l), and ρ_h (m)-(n). The three columns are for different initial guesses of the parameters which are given in Table 5.2. The straight horizontal lines indicate the true values of the parameters, the solid stair-like curves indicate the ensemble mean of the estimated parameter and the dashed lines curves indicate the $1 \sigma_{P_i}$ ensemble width. 133
- Fig. 5.2. The evolution of the ensemble means of (a) the intercept parameter of hail/graupel n_{oh} (a), and the density of snow ρ_s (b). The five line types represent

five estimation experiments with different realizations of the initial parameter ensemble. 136

Fig. 5.3. The rms errors of the ensemble-mean forecast and analysis, averaged over points at which the reflectivity is greater than 10 dBZ for q_c (the 1st column), q_r (the 2nd column), q_i (the 3rd column), q_s (the 4th column), q_h (the 5th column), for the CNTL data assimilation experiment (black), parameter estimation experiments (dashed) and data assimilation experiment with imperfect parameter kept throughout the assimilation cycles (gray). The experiments shown have (wrong) initial guesses of $\rho_h = 400 \text{ kg m}^{-3}$ (a-e), $n_{0r} = 8 \times 10^7 \text{ m}^{-4}$ (f-j), and $\rho_s = 400 \text{ kg m}^{-3}$ (k-o), which correspond to the experiments in Fig. 5.1m, Fig. 5.1i and Fig. 5.1l. 137

Fig. 5.4. The evolution of the parameter distribution (solid curves: ensemble mean, dashed curves: $1 \sigma_{p_i}$ ensemble width) vs. true parameter values (straight lines) for experiments simultaneously estimating n_{0h} (the upper row) and ρ_h (the lower row). The four columns are the results of four experiments with different combination of the initial guesses of the two parameters. 140

Fig. 5.5. The evolutions of the ensemble means together with the true values (straight line) of n_{0h} (a)-(b), and ρ_h (c)-(d), from experiments estimating (n_{0h}, ρ_h) starting from $(4 \times 10^5 \text{ m}^{-4}, 400 \text{ kg m}^{-3})$. The different line types in each column represent different experiments. The left column shows the results of experiments using different realizations of the initial ensemble and data with different errors. The experiments in the right column use the same data as that indicated by the gray curves in the left column but with different initial ensemble realizations. 141

Fig. 5.6. The same as Fig. 5.3, but for the two-parameter set (n_{0h}, ρ_h) . The experiments shown have initial guess or imperfect value of $(n_{0h}, \rho_h) = (4 \times 10^6 \text{ m}^{-4}, 400 \text{ kg m}^{-3})$ (a-e), and $(n_{0h}, \rho_h) = (4 \times 10^6 \text{ m}^{-4}, 400 \text{ kg m}^{-3})$ (f-j), which correspond to the experiments in the 1st and the 4th column of Fig. 5.4, respectively. 142

Fig. 5.7. The evolutions of the ensemble means together with the true values (straight lines) of n_{0s} (upper panel) and ρ_s (lower panel) from experiments simultaneously estimating (n_{0s}, ρ_s) starting from four different initial guesses (one column for each). The gray and black curves are from the experiments using 40 and 100 ensemble members, respectively. 143

Fig. 5.8. The left and central columns show the ensemble means of n_{0r} (a)-(b), n_{0s} (d)-(e), and n_{0h} (g)-(h) of the experiments estimating three intercept parameters simultaneously. In the right column are the average ensemble-mean absolute errors of the experiments in the left column (black solid) and experiments in the central column (gray dash) of $10 \log_{10}(n_{0r})$ (c), $10 \log_{10}(n_{0s})$ (f), and $10 \log_{10}(n_{0h})$ (i). The 8 different line types represent the experiments starting from 8 different initial guesses of the intercept parameters, which are combinations of the values listed in Table 5.3. The experiments shown in the left column assimilated ‘error-free’ data while those in the central column used ‘error-containing’ data. 145

- Fig. 5.9. The same as Fig. 5.3, but for the three-parameter set (n_{0r}, n_{0s}, n_{0h}) . The experiments shown have initial guesses or imperfect values of $(n_{0r}, n_{0s}, n_{0h}) = (0.03 \text{ m}^{-4}, 0.007 \text{ m}^{-4}, 0.00004 \text{ m}^{-4})$ (a-e), and $(n_{0r}, n_{0s}, n_{0h}) = (0.03 \text{ m}^{-4}, 0.007 \text{ m}^{-4}, 0.00004 \text{ m}^{-4})$ (f-j), which correspond to the thin black curves and the thick black curves in the 2nd column of Fig. 5.8, respectively..... 147
- Fig. 5.10. The same as Fig. 5.4, but for experiments estimating n_{0r} (a-c), n_{0s} (d-f), n_{0h} (g-i), and ρ_h (j-l), simultaneously. The results of 6 (2 in each column) of totally 16 experiments with different initial guesses of $(n_{0r}, n_{0s}, n_{0h}, \rho_h)$ are presented, with each experiment presented by the same type of curves in each column..... 149
- Fig. 5.11. The evolution of the average ensemble-mean absolute error of $10\log_{10}(n_{0r})$ (a), $10\log_{10}(n_{0s})$ (b), $10\log_{10}(n_{0h})$ (c), and $10\log_{10}(\rho_h)$ (d), calculated from the 16 experiments simultaneously estimating $(n_{0r}, n_{0s}, n_{0h}, \rho_h)$ using error-containing data (gray) and error-free data (black)..... 151
- Fig. 5.12. The same as Fig. 5.3, but for the four-parameter set $(n_{0r}, n_{0s}, n_{0h}, \rho_h)$. The experiments shown have initial guesses of $(n_{0r}, n_{0s}, n_{0h}, \rho_h) = (0.2 \text{ m}^{-4}, 0.3 \text{ m}^{-4}, 0.004 \text{ m}^{-4}, 700 \text{ kg m}^{-3})$ (a-e), $(n_{0r}, n_{0s}, n_{0h}, \rho_h) = (0.03 \text{ m}^{-4}, 0.007 \text{ m}^{-4}, 0.04 \text{ m}^{-4}, 400 \text{ kg m}^{-3})$ (f-j), and $(n_{0r}, n_{0s}, n_{0h}, \rho_h) = (0.03 \text{ m}^{-4}, 0.3 \text{ m}^{-4}, 0.04 \text{ m}^{-4}, 700 \text{ kg m}^{-3})$ (k-o), which correspond to the black curves in the 1st, 2nd and 3rd column of Fig. 5.10, respectively. To be consistent, 100 ensemble members are used in the control experiment shown here. 152
- Fig. 5.13. Same as Fig. 5.4, but for n_{0r} (a)-(c), n_{0s} (d)-(f), n_{0h} (g)-(i), ρ_s (j)-(l), and ρ_h (m)-(o) from experiments simultaneously estimating the four parameters. The results of 6 of a total of 16 experiments with different initial guesses of $(n_{0r}, n_{0s}, n_{0h}, \rho_h)$ are presented, with each experiment represented by the same type of curves in each column..... 154
- Fig. 5.14. Correlation coefficients calculated from the forecast ensemble at $t = 70$ min from single-parameter estimation experiments. The correlation coefficients [thick solid (dashed) contours represent positive (negative) values at intervals of 0.2] between Z at 1.5° elevation and n_{0h} (a), n_{0s} (b), n_{0r} (c), ρ_h (d), and ρ_s (e); and the correlation coefficients between Z at 5.3° elevation and n_{0h} (f), n_{0s} (g), n_{0r} (h), ρ_h (i), and ρ_s (j). The shading and thin solid contours represent Z from the truth simulation. 157
- Fig. 5.15. As in Fig. 5.14, but for correlation coefficients between n_{0h} and ρ_h from two experiments estimating (n_{0h}, ρ_h) . (a)-(d) are for the experiment corresponding to the thick black curves in Fig. 5.5b, d that yields a good estimation, and (e)-(h) are for the experiment corresponding to the thick gray curves in Fig. 5.5a, c that has a poor estimation. 159
- Fig. 6.1. Storm positions indicated by the area greater than 40 dBZ at the first elevation of the KTLX radar with a time interval of 1 hour. The locations of the KTLX and KVNK radar are marked by \times . The x and y distances are relative to the KTLX radar. The location of the maximum reflectivity is marked by $+$. The bold

rectangular box indicates the analysis and prediction domain. The star indicates Oklahoma City. Several counties are also labeled.....	166
Fig. 6.2. Surface wind (vectors), mean sea level pressure (black contours, at intervals of 2.5 hPa) and surface specific humidity (gray contours at intervals of 2 g kg ⁻¹) from NCEP Eta model analyses at (a) 1800 May 29, and (b) 0000 May 30, 2004.....	167
Fig. 6.3. (a) The observed Norman, OK (OUN) sounding at 0000 UTC, May 30, and (b) the modified sounding used in data assimilation experiments.....	169
Fig. 6.4. (a) Dual-radar analyzed radial velocity as viewed from KTLX radar at the 1.25° elevation and (b) the corresponding observation; (c) analyzed radial velocity as viewed from KVNIX radar and (d) the corresponding; (e) ensemble mean analysis of reflectivity in the 1.25° elevation plane of KTLX radar and (f) the corresponding observation, valid at 0100 UTC, May 30. The analysis shown is the ensemble mean.	180
Fig. 6.5. Diagnostics and scores for the dual-radar analysis. (a) radial velocity rms differences with respect to the KTLX observations for ensemble mean analysis (solid black), ensemble mean forecast (dashed black), horizontally uniform wind from the sounding (dotted gray) and the ensemble spread (standard deviation) of the prior (forecast) radial velocity (solid gray). (b) The same as (a) but with respect to the KVNIX radial velocity. (c) The same as (a) but with respect to the KTLX reflectivity. (d) The same as (c), but with respect to the KVNIX reflectivity.....	181
Fig. 6.6. Ratio $(\sigma_o^2 + \sigma_f^2) / \sigma_v^2$ from dual-radar analysis corresponding to (a) KTLX radar and (b) KVNIX radar; and from single-radar analysis corresponding to (c) KTLX radar and (d) KVNIX radar for radial velocity (black) and reflectivity data (gray).....	183
Fig. 6.7. The same as Fig. 6.5, but for the single-radar analysis that assimilates KTLX radar data only.....	185
Fig. 6.8. The same as Fig. 6.4, but for the single-radar control experiment that assimilates KTLX radar data only.	186
Fig. 6.9. Horizontal velocity vectors (m s ⁻¹) and reflectivity contours (at intervals of 10 dBZ starting from 10dBZ, with the 40 dBZ contours highlighted) of ensemble mean analyses at 0030 UTC (a - d) and 0100 UTC (e - h) from dual-radar analysis experiment (a, b, e and f) and the single-radar analysis experiment (c, d, g and h). The left and right columns are for the 1.5 km and 4 km height levels, respectively. 'C' in the figure marks the circulation centers and 'A' marks the anticyclonic circulation center.	189
Fig. 6.10. Storm-relative horizontal wind vectors and reflectivity contours (at 10 dBZ intervals starting from 10 dBZ) for dual-radar (upper panel) and single-radar (lower panel) analyses at z = 4km (left panel) and z=8km (right panel), at 0100 UTC, 30 May 2004.	190

- Fig. 6.11. Same as Fig. 6.9, but for vertical velocity (color shading at intervals of 2.5 m s⁻¹) and reflectivity (contours at intervals of 10 dBZ starting from 10dBZ).... 191
- Fig. 6.12. The same as Fig. 6.9, but for vertical vorticity (thick contours at intervals of 0.003 s⁻¹) and reflectivity (thin contours at intervals of 10 dBZ starting from 10dBZ) at the surface (left column) and at the 1.5 km height level (right column). 193
- Fig. 6.13. Surface horizontal velocity vectors (m s⁻¹), perturbation (from sounding-defined base state) potential temperature (shaded dashed contours at 2 K intervals) and reflectivity (only 10dBZ contour is plotted and highlighted) from ensemble mean analysis of single-radar analysis experiment at (a) 0030 UTC and (b) 0100 UTC; of dual-radar analysis experiment at (c) 0030 UTC and (d) 0100 UTC..... 195
- Fig. 6.14. Reflectivity as viewed from KTLX radar at the 1.25° elevation of the predicted storm initialized from single-radar ensemble mean analysis at 0100 UTC at (a) 0115 UTC, (b) 0130 UTC, (c) 0145 UTC, (d) 0200 UTC, (e) 0230 UTC and (f) 0300 UTC of 30 May 2004. 197
- Fig. 6.15 The radar reflectivity observed by KTLX radar on the 1.25° elevation level at (a) 0115 UTC, (b) 0130 UTC, (c) 0145 UTC, (d) 0200 UTC, (e) 0230 UTC and (f) 0300 UTC of 30 May 2004..... 198
- Fig. 6.16. Horizontal velocity vectors (m s⁻¹), vertical velocity (color shading) and reflective (contours at intervals of 10 dBZ starting from 10dBZ) at z=1.5 km from ensemble mean forecast initialized from single-radar ensemble mean analysis using KTLX data at 0100 UTC at (a) 0110 UTC, (b) 0120 UTC, (c) 0130 UTC, (d) 0140 UTC, (e) 0150 UTC and (f) 0200 UTC of 30 May 2004.199
- Fig. 6.17. Diagnostics and scores for the dual-radar analysis. (a) radial velocity rms differences with respect to the KTLX observations for ensemble mean analysis (solid black), ensemble mean forecast (dashed black), Environmental state obtained from the forecast initialized from 3DVAR analysis (dashed gray). (b) The same as (a) but with respect to the KVNx radial velocity. (c) The same as (a) but with respect to the KTLX reflectivity. (d) The same as (c), but with respect to the KVNx reflectivity. 203
- Fig. 6.18. The same as Fig. 6.17, but for single-radar case. 204
- Fig. 6.19. Innovation statistics for the dual-radar analysis. (a) Observed innovation std dev σ_v (thick solid black), rms observation error σ_o (solid gray), rms ensemble spread σ_f (dashed black), and predicted innovation std dev $\sqrt{\sigma_o^2 + \sigma_f^2}$ (thin solid black) corresponding to KTLX radar for radial velocity. (b) The same as (a) but corresponding to KVNx radar for radial velocity. (c) The same as (a) but for reflectivity. (d) the same as (b) but for reflectivity. 205
- Fig. 6.20. The same as Fig. 6.19, but for single-radar analysis. 206

Fig. 6.21. Vertical velocity [contours and shading, solid (dash) contours represent positive (negative) w] and horizontal storm-relative winds (vectors, plotted every other grid point) and reflectivity (contours at intervals of 10 dBZ starting from 10dBZ, with the 40 dBZ contours highlighted) at 4 km MSL from dual-radar analysis experiment. (a) ensemble mean analysis at 0055 UTC (b) ensemble mean forecast of dual-radar analysis at 0010 UTC (c) ensemble mean analysis at 0100 UTC.....	207
Fig. 6.22. The same as Fig. 6.21, but for the ensemble mean analyses and forecast at 1.5 km MSL.	208
Fig. 6.23. The same as Fig. 6.21, but for single-radar ensemble mean analysis at (a) 4km and (b) 1.5 km.	209
Fig. 6.24. Surface horizontal storm-relative velocity vectors ($m s^{-1}$), perturbation potential temperature (shaded dashed contours at 2 K intervals) and reflectivity (only 10dBZ contour is plotted and highlighted) from (a) dual-radar ensemble mean analysis and (b) single-radar ensemble mean analysis at 0100 UTC.....	210
Fig. 6.25. Reflectivity as viewed from KTLX radar at the 1.25° elevation of the predicted storm initialized from the dual-radar ensemble mean analysis at 0100 UTC at (a) 0115 UTC, (b) 0130 UTC, (c) 0145 UTC, (d) 0200 UTC, (e) 0230 UTC and (f) 0300 UTC.....	212
Fig. 6.26. The same as Fig. 6.25, but the forecast is initialized for single-radar analysis.	213

Abstract

Operational Doppler weather radar networks, such as the WSR-88D radar network of the United States, provide the key sources of data for initializing storm-scale numerical weather prediction (NWP) models. Because Doppler radars only observe a very limited set of parameters and the spatial coverage of radar data is often incomplete, advanced data assimilation methods are necessary to fully determine the state of the atmosphere. In this dissertation, the ensemble Kalman filter (EnKF) algorithm is employed to assimilate radar data for the prediction of convective storms.

An EnKF data assimilation system is first developed based on the general purpose compressible nonhydrostatic ARPS (Advanced Regional Prediction System) model including multi-class ice microphysics. Simulated radar radial velocity and reflectivity data from a single radar are first assimilated and their relative impacts on the analysis and forecast are evaluated. The EnKF works almost perfectly in such perfect-model OSS (Observing System Simulation) experiments, in which wind, thermodynamic and microphysical fields of a supercell thunderstorm are retrieved very accurately. The ensuing forecasts remain very good for at least 2 hours. Physically consistent background error covariances are obtained which play a crucial role in successful estimation of the model state.

The presence of model error poses a major challenge for real data applications. For convective-scale prediction, microphysics parameterization is a major source of model error and uncertainty. Parameter estimation via state augmentation using the EnKF method is applied to the correction of errors in fundamental parameters common

in single-moment ice microphysics schemes, after parameter sensitivity and identifiability are examined. OSSEs are performed in which individual parameters are estimated separately or in different combinations. The estimation of individual parameters is shown to be successful while the level of difficulty increases as more parameters are estimated simultaneously. Explanations are given as to why under certain circumstances the filter fails to estimate the correct values of parameters. Still, the state estimation is generally improved even when estimated parameters are inaccurate.

Finally, our EnKF system is applied to a real case of tornadic thunderstorm. The initial storm environment is either horizontally homogeneous as defined by a single sounding or three dimensional as obtained from a 3DVAR analysis of all available conventional observations. A full suite of model physics is employed in the latter case. Radial velocity and reflectivity from either one or two WSR-88D radars are assimilated. Analyzed radial velocity and reflectivity fields match the observations well. The flow fields show dynamically consistent patterns typical of supercell storms, including strong mid-level rotation and updraft, and low-level hook echo. The subsequent hour-long prediction maintains the supercell characteristics and propagates in the right direction, but the detailed structure and propagation speed of the predicted storm differ from the observed ones towards the later part of the prediction. Model errors, in particular those related to microphysics and resolution, are suggested as the major source of forecast errors, while the lack of low-level radar data coverage may have also contributed to the inaccuracy of analysis or model initial condition.

Chapter 1

Introduction and Overview

1.1 Background and Motivation

Numerical weather prediction (NWP) is an initial-boundary value problem: given an estimate of the current state of the atmosphere, the model predicts its future state. To produce an accurate numerical weather forecast, it is very important to have a precise representation of current atmospheric state. This is achieved through data assimilation. Data assimilation is the process of finding the model representation of the atmospheric state that is most consistent with the current and past observations (Lorenc 1995). Usually, observations are sparse in space and time and contain errors. They are insufficient to completely determine the state of the atmosphere. Additional information, in particular, the evolution with time of the atmosphere, can be obtained by using a numerical model, which is based on the knowledge of the behavior and structure of the atmosphere. The simplest use of the model is to carry information forward in time from a past analysis, to provide the background state for a new analysis (Lorenc 1995). Therefore, the goal of data assimilation is to find the optimal combination of the model forecast background and observations with weights determined by their error characteristics.

Research on numerical weather prediction at the scale of convective storms was motivated by the installation of the WSR-88D Doppler radar network and the

continuous increase in computing power, which facilitate the use of high-resolution nonhydrostatic numerical models (Lilly 1990; Droegemeier 1990; Xue et al. 1996; Droegemeier 1997; Xue et al. 2003). Doppler radars provide high-resolution measurements of radial velocity, reflectivity and velocity spectrum, with complete volume scans every 5 to 10 minutes. They are the only existing instruments that are capable of providing routine observations with spatial and temporal resolutions sufficient for resolving convective storms. Therefore, to produce accurate storm-scale numerical weather forecast, it is necessary to incorporate the radar data into the NWP model. The major challenge of initializing storm-scale NWP through radar data assimilation is that only radial velocity and reflectivity (velocity spectrum width is also available but is not as useful) are measured and they are not the model state variables. The assimilation problem now involves the retrieval of unobserved variables. Hence, advanced data assimilation methods are needed to successfully analyze the unobserved wind, thermodynamic and microphysical fields from Doppler radar observations.

In recent years, various techniques have been developed for analyzing and retrieving atmospheric state at the convective scale from Doppler radar data. These methods range from purely kinematic to sophisticated 4D variational method (4DVAR) that employs a nonhydrostatic prediction model and its adjoint (e.g., Gal-Chen 1978; Sun et al. 1991; Qiu and Xu 1992; Shapiro et al. 1995; Sun and Crook 1997; Gao et al. 1999; Wu et al. 2000; Weygandt et al. 2002a; Hu et al. 2006a; Hu et al. 2006b). Most of the work deals with retrieval and assimilation of radial velocity and/or reflectivity data from single Doppler radar because dual or multiple-Doppler coverage is not generally available. For the purpose of initializing NWP models, the 4DVAR method (e.g., Sun

and Crook 1997; Gao et al. 1998) promises to provide an initial condition that is consistent with the prediction model and is able to effectively use multiple volume scans from radar. However, the high cost of developing and maintaining an adjoint code, especially one that can run efficiently on distributed-memory parallel computer systems and the need to include in the adjoint of detailed physical processes, which are more important at the convective scale, have limited 4DVAR assimilations of Doppler radar and other high-resolution data to relatively simple applications and model settings.

Ensemble Kalman filter (EnKF) has been introduced as a data assimilation method for about a decade. No until recently, it has been applied in storm-scale data assimilation with considerable success. Because of the need to run an ensemble of forecast and analysis of nontrivial sizes (usually a few tens to a few hundreds), the overall computational cost of ensemble-based assimilation methods is also significant. Fortunately, a significant portion of the assimilation procedure, including the forecast component, is easily parallelizable. There is no need in general for the adjoint of the forward observation operators. Therefore, indirect observations with complex observation operators, at least those that involve primarily local influences, can be easily included. Furthermore, the analysis code is more or less independent of the prediction model, just the opposite of 4DVAR method. In addition, the system provides valuable uncertainty information on both analysis and forecast, and when combined with an existing ensemble prediction system, the incremental cost can be small.

The EnKF method is, however, not as mature as 4DVAR. The testing of the EnKF with real data, especially at the thunderstorm scale, remains very limited. EnKF also shares some of the common problems with 4DVAR, including issues with model

errors, linear assumption associated with the optimality of solution, and Gaussian error assumption. For systems that involve error growth at very different temporal and spatial scales, more difficulties may arise. For these reasons, much research is still needed before reliable operational implementations of ensemble-based assimilation methods can be achieved.

1.2 Dissertation Outline

The goal of this research is to develop an EnKF data assimilation system and to investigate its ability in radar data assimilation and parameter estimation for storm-scale numerical weather prediction. In Chapter 2, the theoretical background of the EnKF is presented. The framework of the EnKF and its variations are introduced and some issues associated with this method are discussed.

Chapter 3 describes the EnKF system for Doppler radar data assimilation that we developed. It is tested with simulated radial velocity and/or reflectivity data from a single Doppler radar for a supercell storm. The simulated radar data used in this chapter are assumed to be located on model grid points. Different from earlier radar data assimilation work with EnKF, our data assimilation system is based on a general purpose compressible nonhydrostatic model with a complex multi-class microphysics scheme. The relative impact of radial velocity and reflectivity data on the analysis and subsequent forecast are investigated.

A variant of the EnKF, the ensemble square-root Kalman filter (Whitaker and Hamill 2002) is then implemented and applied to studies from Chapter 4. The system now couples with realistic radar emulators or forward observation operators, with radar

geometry and earth curvature effects taken into account. Simulated radar data can be sampled on radar elevation levels. More realistic emulation of radar antenna pattern based on a Gaussian power-gain function is included. The system is flexible and permits a variety of OSS (Observing System Simulation) experiments examining various issues related to optimal radar configurations and scan strategies. The first work related to this has been published, in which the impact of data from a standard WSR-88D network radar and those from a network of closely-spaced, low-cost short-range radars planned for the Oklahoma test bed of CASA (Center for Adaptive Sensing of the Atmosphere, a new NSF Engineering Research Center), are examined, for the analysis and forecast of a supercell storm system (Xue et al. 2006). The results are not described in this dissertation.

The model state estimation with the EnKF is very encouraging with mostly Observing System Simulation Experiment (OSSE) studies. However, the forecast errors due to model deficiencies are neglected in most of these studies. There are two types of model error: random errors due to the cumulative effect of unresolved processes on the resolved flow, and systematic errors due either to parameters not being adequately constrained by available observations or to the structure of the model being incapable of representing the phenomena of interest (Allen *et al.* 2003). In Chapter 4 and Chapter 5, systematic error resulting from uncertain parameters used in the prediction model is considered.

Since microphysical parameterization is an important source of uncertainty or error for convective-scale data assimilation and prediction, we focus on five fundamental microphysical parameters that are closely involved in the definition of

drop/particle size distributions of microphysical species in a commonly used single-moment microphysics scheme. The feasibility of using the EnKF method and radar data to correct errors in these parameters through simultaneous state and parameter estimation is investigated in Chapter 4 and Chapter 5.

In Chapter 4, sensitivity experiments are conducted to examine the sensitivity of pure model forecast as well as model state estimation to the microphysical parameters to be estimated. The time scales of forecast response to errors in individual parameters are also investigated. The solution uniqueness of the estimation problem that is intimately related to parameter identifiability is examined for individual parameters. Parameter identifiability is also addressed by estimating the correlations between the parameters and the observed variables.

In Chapter 5, the ensemble square-root Kalman filter is employed for the state variable and parameter estimation. The five microphysical parameters are estimated individually or in different combinations starting from different initial guesses. The identifiability of parameter combinations is further discussed.

Encouraged by the OSSE results, we move to using real radar data in Chapter 6. In the chapter, the ensemble square-root filter is applied to the central Oklahoma tornadic thunderstorm case of 29-30 May 2004. This long-lasting tornadic thunderstorm swept through central Oklahoma and produced 16 tornadoes. The evolution of the main storm was recorded by the Oklahoma City WSR-88D radar (KTLX) and the WSR-88D radar to its north at Enid, Oklahoma (KVNK). The data from the two radars are assimilated alone or together. The single-radar and dual-radar wind analyses are compared with each other. The initial storm environment is either horizontally

homogeneous as defined by a single sounding or three dimensional as obtained from a 3DVAR analysis of all available conventional observations. A full suite of model physics is employed in the latter case. The ability of the EnSRF system in producing good state estimation for real cases in the presence of various potential sources of errors is discussed. Short range forecasts are produced starting from the analyzed states and verified against radar observations.

Chapter 7 summarizes the results of this research and discusses additional issues and topics that can be examined in the future.

Chapter 2

The Ensemble Kalman Filter

The ensemble Kalman filter was first introduced by Evensen (1994). The search for this new data assimilation scheme was motivated by two major problems in applying the extended Kalman filter for data assimilation in a nonlinear quasi-geostrophic model and the extreme computational cost of standard Kalman filter. The first problem encountered was the unbounded error variance growth caused by the closure scheme used by the extended Kalman filter, where third- and higher-order statistical moments in the error covariance evolution equation are neglected (Evensen 1992). The second problem occurred when including open boundaries with the extended Kalman filter, which significantly complicates the treatment of the error evolution equation. Approximate methods therefore must be used, but they also have potential problems (Evensen 1993).

The theory of stochastic dynamic prediction that describes the evolution of error statistics is the basis for both ensemble Kalman filter (EnKF hereafter) and extended Kalman filter (EKF hereafter). The only difference is the approximation method used by these two methods. The EnKF is based on the Monte Carlo method and the EKF is based on an approximate stochastic dynamic prediction equation. In the following sections, the background of the theory of stochastic dynamic prediction and the estimation theory, on which the Kalman filter is based, will be described. The equations

of the EnKF will then be presented and issues associated with applying this data assimilation scheme in meteorology will be discussed.

2.1 Theoretical background of EnKF

The material in this section mainly follows Evensen (1994), Evensen and van Leeuwe (1996), Evensen (2003), Jazwinski (1970), Houtekamer and Mitchell (1998), Houtekamer and Mitchell (2001), Whitaker and Hamill (2002) and Hamill (2004).

2.1.1 Error evolution

2.1.1.1 Theory of stochastic dynamic prediction

The theory of stochastic dynamic prediction was first introduced by Epstein (1969). Here, we explain the basic idea of this theory in terms of the state of the atmosphere. The true state of the atmosphere cannot be known precisely, because of the sparseness of the measurements, errors in the measurements and uncertainties in the interpolation or analysis scheme. Therefore, there is no way to determine for sure whether an initial state estimate and its subsequent forecast are right or wrong. Any initial state estimate only represents an individual member of an infinite ensemble of possible states that are consistent with the data. The state of the atmosphere and its time evolution can, therefore, be represented in terms of a probability distribution and its evolution.

The state of a dynamic system, e.g., the atmospheric system, at a particular time t is represented by a vector of state variables $\mathbf{x}_t \in \mathcal{R}^n$. The state vector can be represented by a single point in an n -dimensional phase space ϕ . The uncertainty in the state vector can be represented by a large ensemble of possible states, with each

assigned an individual probability. The time evolution of the state vector can be described by continuous motion of the point along a trajectory in phase space governed by dynamic laws. The ensemble of possible states moves through the phase space governed by the same dynamic laws. The density of the ensemble has an associated probability, so that the dynamic equations can not only be used to generate predictions of the physical state itself, but also the predictions of the probability density, which is important for the state estimate, because the probability density contains all the statistical information (Evensen 1994).

The evolution of the state of a continuous dynamical system with a finite-dimensional state, which is subject to random disturbances, can be represented by a stochastic differential equation. Assume we have a nonlinear forecast model M , which contains additive white Gaussian errors, the time evolution of the state can be written as

$$d\mathbf{x}_t = M(\mathbf{x}_t, t)dt + G(\mathbf{x}_t, t)d\mathbf{q}_t \quad (t \geq t_0), \quad (2.1)$$

where \mathbf{q}_t is a Brownian motion process with covariance $E[d\mathbf{q}_t d\mathbf{q}_t^T] = \mathbf{Q}(t)dt$ and $G(\mathbf{x}_t, t)$ is the model-error forcing. Here and hereafter, the boldface characters donate vectors or matrices and the use of the italicized font donates a scalar. Our notation generally follows that of Ide et al. (1997). Eq. (2.1) is a Itô stochastic differential equation, which describes a Markov process^{1*}. This equation states that an increment in time will cause an increment of model states, which in addition, is influenced by the stochastic forcing term representing the model error (Evensen 2003).

¹ Markov process is a random process whose future probabilities are determined by its most recent values. See Jazwinski, A. H., 1970: *Stochastic Processes and Filtering Theory*. Academic Press, 376 pp. page 95 for the proof.

The evolution of the probability density function (pdf) of this process can be described by the forward Kolmogorov's equation or the Fokker-Planck equation:

$$\frac{\partial p(\mathbf{x}_t, t)}{\partial t} + \sum_i^n \frac{\partial (p(\mathbf{x}_t, t) M_i)}{\partial x_i} = \frac{1}{2} \sum_{i,j=1}^n \frac{\partial^2 [p(\mathbf{x}_t, t) (G\mathbf{Q}G^T)_{ij}]}{\partial x_i \partial x_j}. \quad (2.2)$$

The derivation can be found in section 4.9 of Jazwinski (1970). The right hand side of Eq. (2.2) includes the effects of model error, including flattening the pdf due to model uncertainty as well as noise-included drift. If the pdf could be solved from this equation, it would be possible to calculate statistic moments (e.g. the mean and the error covariances) at different time levels. However, for a model with dimension of more than $O(10^6)$, as is typical of atmospheric models, it is not practical to solve this equation.

For a linear system, if the pdf of the initial condition is Gaussian, where the pdf is completely characterized by its mean and covariance matrix, the pdf will remain Gaussian all the time (see proof on page 111 of Jazwinski 1970). The exact equations for the evolution of the mean and the covariance matrix can be derived without solving the Kolmogorov's equation.

For a nonlinear system, the mean and covariance will not generally characterize the pdf. The evolution equations for different statistical moments are coupled (e.g Eq. 29-30 in Evensen 1994). Even if the pdf of the initial state is Gaussian, it will not remain so. However, the mean does determine the mean path and the covariance represents the magnitude of the errors in the prediction. In the EKF, the evolution equations of mean and covariance are derived based on the linearization of the forecast model and all moments with order higher than the covariance are neglected.

2.1.1.2 The Monte Carlo method

Another way to approximate the evolution of error statistics is to use Monte Carlo method, which is the basis of the ensemble-based Kalman filters. A large cloud of states, that is, points in phase space, can be used to represent a specific pdf. By integrating such an ensemble of the states forward in time, it is easy to calculate approximate estimates for moments of the pdf at different time levels. When the ensemble size, N , increases, the errors in the solution for the pdf approach zero at a rate proportional to $1/\sqrt{N}$. For ensemble size of $O(100)$, the errors will be dominated by statistical or sampling errors, rather than by dynamical errors (Evensen 1994).

2.1.2 Filter theory and Kalman filter

2.1.2.1 Filter theory

The estimation problem is to obtain a best estimate of the true state of a system, given observations that contain errors. Suppose \mathbf{x}_t ($n \times 1$) donates the true state of a stochastic dynamic system at time t , the evolution of the state can be described by the stochastic differential equation [e.g., the Itô stochastic differential equation (2.1) for a continuous stochastic dynamic system]. Let $\mathbf{Y}_\tau = [\mathbf{y}_1, \dots, \mathbf{y}_\tau]$ donates the observations at and before τ . The problem of estimating \mathbf{x}_t , given \mathbf{Y}_τ becomes a filtering problem if $t = \tau$. Obviously, the conditional probability density function of \mathbf{x}_t given \mathbf{Y}_t , $p(\mathbf{x}_t | \mathbf{Y}_t)$, is the complete solution of the filtering problem, because $p(\mathbf{x}_t | \mathbf{Y}_t)$ embodies all the

statistical information about \mathbf{x}_t , which is contained in the available observations and in the initial condition $p(\mathbf{x}_0)$ (Jazwinski 1970).

With the $p(\mathbf{x}_t | \mathbf{Y}_t)$, the estimate of the state $\hat{\mathbf{x}}_t$ at time t could be obtained through several approaches. One approach is to define a loss function $L(\tilde{\mathbf{x}}_t)$, where $\tilde{\mathbf{x}}_t \equiv \mathbf{x}_t - \hat{\mathbf{x}}_t$ represents the error in the estimate, and seek the estimate $\hat{\mathbf{x}}_t$ of \mathbf{x}_t which minimizes the average or expected loss $E[L(\tilde{\mathbf{x}}_t)]$. A particular loss function is

$$L(\xi) = \xi^T \mathbf{S} \xi, \quad (2.3)$$

where ξ is an n -vector and \mathbf{S} is a $n \times n$ positive semi-definite weighting matrix. If \mathbf{S} is the identity matrix, $L(\tilde{\mathbf{x}}_t)$ reduces to the sum of the squared error. The estimate that minimizes the expectation of the loss function (2.3) is called the *minimum variance estimate*, which turns out to be the conditional mean $E[\mathbf{x}_t | \mathbf{Y}_t]$.

Another approach is by using the Bayes' rule,

$$p(\mathbf{x}_t | \mathbf{Y}_t) = \frac{p(\mathbf{Y}_t | \mathbf{x}_t) p(\mathbf{x}_t)}{p(\mathbf{Y}_t)}, \quad (2.4)$$

Estimation based on the maximization of the joint conditional posterior probability density function is called *joint maximum likelihood (Bayesian) estimation*. The estimate is the mode of the joint conditional density (2.4). If the density is Gaussian or just symmetric and unimodal, then the mode coincide with the mean. In that case the *maximum likelihood estimate* is the same as the *minimum variance estimate*. As noted by Jazwinski (1970), the maximum likelihood estimation is of questionable value unless the pdf is unimodal and concentrated near the mode.

2.1.2.2 The Kalman filter

The goal of the filter problem, in the context of minimum variance estimation, is to seek equations of evolution of the conditional pdf, $p(\mathbf{x}_t | \mathbf{Y}_t)$, and the conditional mean $\hat{\mathbf{x}}_t = E[\mathbf{x}_t | \mathbf{Y}_t]$. Under the assumption of linear dynamics with state-independent Gaussian model and observation errors, the result of seeking these evolution equations is the Kalman filter (See Jazwinski 1970 section 7.2, 7.3 for the derivation), which is an optimal filter consists of equations of evolution for the conditional mean $\hat{\mathbf{x}}_t$ and covariance matrix \mathbf{P}_t .

An extension of the Kalman filter to nonlinear problem is the extended Kalman filter (EKF, see Jazwinski 1970 section 7.2, 7.3 for the derivation). For a nonlinear system described by the statistical differential equation (2.1) and nonlinear observations

$$\mathbf{y}_t = H(\mathbf{x}_t) + \boldsymbol{\varepsilon}_t, \quad (2.5)$$

where $\boldsymbol{\varepsilon}_t \sim N(0, \mathbf{R}_t)$, $\hat{\mathbf{x}}_0 = \mathbf{x}_0 + \mathbf{e}_0$ and $\mathbf{e}_0 \sim N(0, \mathbf{P}_0)$, the extended Kalman filter consists of forecast via

$$\mathbf{x}_{t+1}^f = M(\mathbf{x}_t^a), \quad (2.6)$$

$$\mathbf{P}_{t+1}^f = M\mathbf{P}_t^a M + \mathbf{Q}_{t+1}, \quad (2.7)$$

and analysis

$$\mathbf{x}_t^a = \mathbf{x}_t^f + \mathbf{K}[\mathbf{y}_t - H(\mathbf{x}_t^f)], \quad (2.8)$$

$$\mathbf{P}_t^a = (\mathbf{I} - \mathbf{K}\mathbf{H})\mathbf{P}_t^f. \quad (2.9)$$

with the Kalman gain

$$\mathbf{K} = \mathbf{P}_t^f \mathbf{H}^T (\mathbf{H} \mathbf{P}_t^f \mathbf{H}^T + \mathbf{R}_t)^{-1}, \quad (2.10)$$

where superscripts a and f denote analysis and forecast, respectively. We have omitted ‘ $\hat{\cdot}$ ’ of state vector, which means the estimate of the state, in equation (2.6)-(2.9) for convenience and will continue to do so. $\mathbf{M} = \frac{\partial M}{\partial \mathbf{x}}$ is the Jacobian matrix of M and

$\mathbf{H} = \frac{\partial H}{\partial \mathbf{x}}$ is the Jacobian matrix of H . The model state evolves with full nonlinear model

in Eq. (2.6), while in Eq. (2.7), the error covariance evolves through linearizing the model about the nonlinear trajectory, with higher-order moments neglected. The analysis, \mathbf{x}_t^a , is estimated then by correcting the forecast (background or prior estimate), \mathbf{x}_t^f , using the observation increment, $\mathbf{y}_t - H(\mathbf{x}_t^f)$, weighted by the Kalman gain. Eq. (2.9) shows the updating of the forecast error covariance to reflect the reduction in uncertainty from assimilating the observations.

An attractive feature of the Kalman filter relative to analysis scheme like statistical interpolation and 3DVAR is that the Kalman filter gives a systematical way to calculate the time evolution of the forecast error covariance matrix according to the model dynamics, so that the adjustment of the background to the analysis is flow-dependent. However, the calculation of the error covariance evolution of the Kalman filter is hard to implement in realistic system because of the extreme computational cost. To integrate the error covariance matrix in Eq. (2.7) for a system with dimension of n is equivalent to performing $O(n)$ tangent-linear model integration, which is not acceptable with NWP models with dimension of more than $O(10^6)$.

2.2 The ensemble Kalman filter and its variations

Evensen (1994) proposed the ensemble Kalman filter algorithm for solving the two problems of EKF with nonlinear dynamics, i.e., the closure scheme associated with linearization, where third- and higher-moments in the error covariance equation are discarded, and the huge computational cost associated with the storage and forward integration of the error covariance matrix.

The ensemble Kalman filter begins with a best guess initial condition based on information from observations and statistics. An ensemble of initial states is generated in which the mean equals the best guess initial condition and the variance is specified based on the uncertainty in the first-guess initial state. Evensen (1994) suggested that the covariance of the ensemble should reflect the true scales of the system.

The ensemble Kalman filter integrates the ensemble of model states until observations are available:

$$\mathbf{x}_{t+1,i}^f = M(\mathbf{x}_{t,i}^a) + \mathbf{q}_{t,i} \quad (i=1, \dots, N), \quad (2.11)$$

where i represents the i th member of the ensemble, N is the number of ensemble members and $\mathbf{q}_{t,i}$ is the stochastic forcing accounting for errors in the model. Here, the model errors are assumed to be unbiased $E(\mathbf{q}_t) = 0$ with error covariance $E(\mathbf{q}_t \mathbf{q}_t^T) = \mathbf{Q}_t$. $\mathbf{x}_{t,i}^a$ at $t=0$ is the ensemble member of the initial guess states. Each ensemble member is updated using the prediction equation, but the forecast error covariances are calculated from the ensemble forecast

$$\mathbf{P}^f \cong \mathbf{P}_e^f = \overline{(\mathbf{x}^f - \bar{\mathbf{x}}^f)(\mathbf{x}^f - \bar{\mathbf{x}}^f)^T}, \quad (2.12)$$

and the analysis error covariances are calculated from the ensemble of updated model states

$$\mathbf{P}^a \cong \mathbf{P}_e^a = \overline{(\mathbf{x}^a - \bar{\mathbf{x}}^a)(\mathbf{x}^a - \bar{\mathbf{x}}^a)^T}, \quad (2.13)$$

where the overbars denote the expected values. The forecast and analysis error covariances are given by matrix P. This is equivalent to a Monte Carlo method for integrating the Kolmogorov's equation, which is the fundamental equation for evolution of error statistics. The improvement of the ensemble Kalman filter over the EKF is that no closure approximations or linearizations have been applied and the error covariance calculations are practical for modest-sized ensembles. The updated ensemble is integrated forward until new observations are available again and the sequential data assimilation cycle is repeated (Fig. 2.1).

At the analysis step, the model state update equation can be formed either stochastically or deterministically. The most well-known *ensemble Kalman filter* or “EnKF” belongs to the stochastic method, because of the use of the ‘perturbed observations’ in the analysis update equation. This ‘perturbed observations’ scheme is first implemented by Houtekamer and Mitchell (1998) and later clarified by Burgers *et al.* (1998). Determinist methods, such as *ensemble square root filter* (EnSRF) (Whitaker and Hamill 2002), *ensemble adjustment Kalman filter* (EAKF) (Anderson 2001) and *ensemble transform Kalman filter* (ETKF) (Bishop *et al.* 2001), were proposed to address the adaptive observational network design problem and to avoid sampling error issues associated with the perturbed-observation method, which as demonstrated by Tippett *et al.* (2003) to belong to a broad class of square root filters.

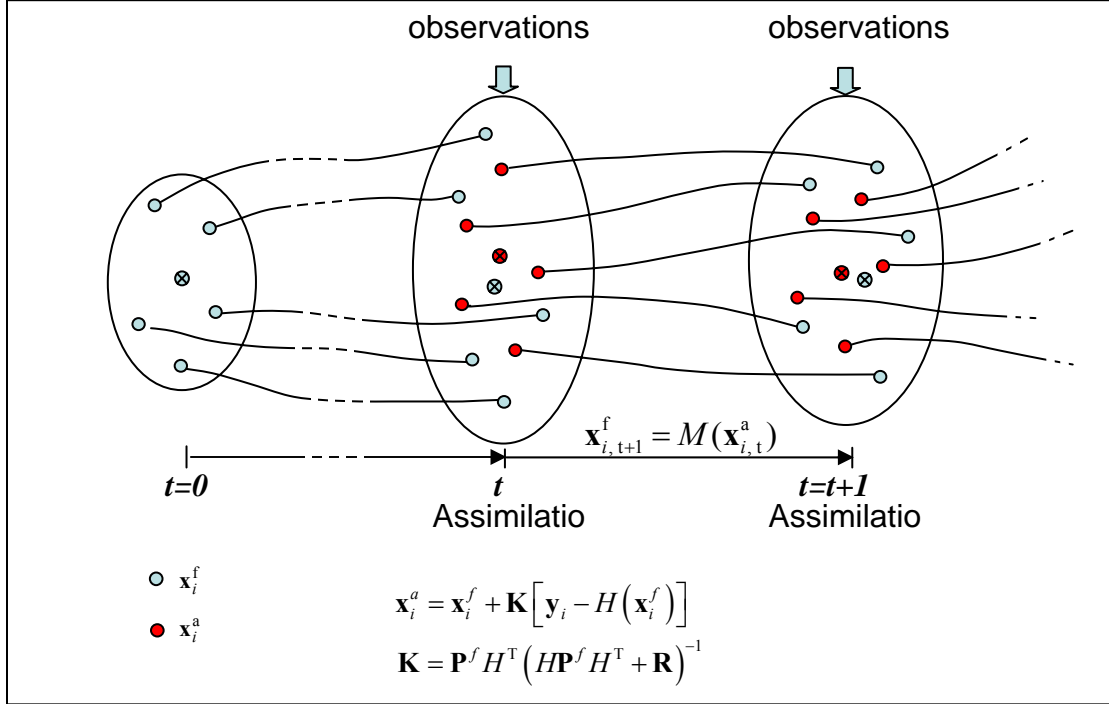


Fig. 2.1. Schematic plot of the EnKF. The dot without ‘×’ donates the model state of an ensemble member in phase space, with green indicating forecast (or background) state and red indicating analysis state. The dot with ‘×’ donates the ensemble mean. The circle indicates the spread of the forecast ensemble.

In the following, we only give the update equations of the EnKF with the ‘perturbed-observation’ method and the update equations of the EnSRF (Whitaker and Hamill 2002), because they are the schemes that are used in our study.

2.2.1 Stochastic update method (EnKF)

In the stochastic method, observations are treated as random variables having a distribution with the mean equaling to the first guess observations, \mathbf{y}_i , and error covariances given by matrix \mathbf{R} . Thus an ensemble of observations are obtained by

$$\mathbf{y}_i = \mathbf{y} + \boldsymbol{\varepsilon}_i \quad (i = 1, \dots, N), \quad (2.14)$$

and the observation error covariance matrix \mathbf{R} , is calculated from the random errors added to the observations, as given in Eq. (2.14):

$$\mathbf{R} = \mathbf{R}_e = \overline{\boldsymbol{\varepsilon}\boldsymbol{\varepsilon}^T}, \quad (2.15)$$

where $\boldsymbol{\varepsilon}$ is the observation error vector. Evensen (2003) justified the treatment of the observations as random variables in two aspects. First, the actual observation error covariance matrix is poorly known and the errors introduced by the ensemble representation can be less than the initial uncertainty in \mathbf{R} if the ensemble size is large enough. Second, the errors introduced by ensemble representation of \mathbf{R} has less impact than the use of the ensemble representation of \mathbf{P} , because \mathbf{R} only affects the amount of adjustment by the background error covariances, $\mathbf{P}^f\mathbf{H}^T$, and has no impact on the structure of $\mathbf{P}^f\mathbf{H}^T$ as \mathbf{P} does.

At the analysis step, each ensemble member is updated by equation

$$\mathbf{x}_i^a = \mathbf{x}_i^f + \mathbf{K}(\mathbf{y}_i - \mathbf{H}\mathbf{x}_i^f), \quad (2.16)$$

$$\mathbf{K} = \mathbf{P}^f\mathbf{H}^T(\mathbf{H}\mathbf{P}^f\mathbf{H}^T + \mathbf{R})^{-1}, \quad (2.17)$$

where \mathbf{y}_i are ‘perturbed observations’, defined by Eq. (2.14). \mathbf{H} in its standard notion is the linearized version of H in a matrix form. H is the observation operator, which converts the model states to the observed parameters. It will be shown later that the EnKF permits the use of nonlinear H . Expressing the variables as an ensemble mean (denoted by an overbar) and a deviation from the mean (denoted by a prime), update equation (2.16) can be written in the form of two equations:

$$\bar{\mathbf{x}}^a = \bar{\mathbf{x}}^f + \mathbf{K}(\bar{\mathbf{y}} - \mathbf{H}\bar{\mathbf{x}}^f), \quad (2.18)$$

$$\mathbf{x}_i^a = \mathbf{x}_i^f + \mathbf{K}(\mathbf{y}_i' - \mathbf{H}\mathbf{x}_i^f). \quad (2.19)$$

It was shown by Burgers *et al.* (1998) that by treating the observations as random variables, such that $\overline{\mathbf{y}'\mathbf{y}'^T} = \mathbf{R}$, the analysis error covariance matrix estimated is

$$\begin{aligned} \mathbf{P}_e^a &= \overline{(\mathbf{x}^a - \bar{\mathbf{x}}^a)(\mathbf{x}^a - \bar{\mathbf{x}}^a)^T} \\ &= \overline{(\mathbf{x}^f - \bar{\mathbf{x}}^f - \mathbf{K}_e\mathbf{H}(\mathbf{x}^f - \bar{\mathbf{x}}^f) + \mathbf{K}_e(\mathbf{y} - \bar{\mathbf{y}}))(\mathbf{x}^f - \bar{\mathbf{x}}^f - \mathbf{K}_e\mathbf{H}(\mathbf{x}^f - \bar{\mathbf{x}}^f) + \mathbf{K}_e(\mathbf{y} - \bar{\mathbf{y}}))^T} \\ &= (\mathbf{I} - \mathbf{K}_e\mathbf{H})\mathbf{P}_e^f(\mathbf{I} - \mathbf{K}_e\mathbf{H})^T + \mathbf{K}_e\mathbf{R}\mathbf{K}_e^T + (\mathbf{I} - \mathbf{K}_e\mathbf{H})\mathbf{D}_e + \mathbf{D}_e^T(\mathbf{I} - \mathbf{K}_e\mathbf{H})^T, \end{aligned} \quad (2.20)$$

where \mathbf{D}_e is the forecast-observation error covariance matrix defined by $\mathbf{D}_e = \overline{\mathbf{x}^f\mathbf{y}'^T}\mathbf{K}_e^T$.

When the ensemble size approaches infinite, the gain estimated from the ensemble, \mathbf{K}_e , approaches the true gain, \mathbf{K} , and the forecast-observation covariance will become negligible, then \mathbf{P}_e^a will converge to the analysis error covariance matrix of the EKF,

$$\mathbf{P}_e^a = (\mathbf{I} - \mathbf{K}\mathbf{H})\mathbf{P}^f(\mathbf{I} - \mathbf{K}\mathbf{H})^T + \mathbf{K}\mathbf{R}\mathbf{K}^T = (\mathbf{I} - \mathbf{K}\mathbf{H})\mathbf{P}^f. \quad (2.21)$$

If unperturbed observations are assimilated in Eq. (2.16), there will be no $\mathbf{K}\mathbf{R}\mathbf{K}^T$ term, so that analysis error covariance will be underestimated and observations will not be properly weighted in subsequent assimilation cycles.

2.2.2 Deterministic update method (EnSRF)

Whitaker and Hamill (2002) demonstrated that in the stochastic method, when the ensemble sizes are finite, the noise added to the observations produces spurious forecast-observation error covariances associated with sampling error in the estimation of the observation-error covariances, i.e., forecast-observation covariance term, \mathbf{D}_e , in

Eq. (2.20) is not negligible. The methods that correct the background ensemble without adding random noise to observations, so that the analysis error covariance matrix estimated from the ensemble converges to that of the EKF, are called deterministic methods (Tippett et al. 2003; Hamill 2004). One of such methods is the ensemble square root filter algorithm (EnSRF) proposed by Whitaker and Hamill (2002), and it has been applied in recent convective-scale data assimilation studies with radar data (Snyder and Zhang 2003; Zhang et al. 2004; Dowell et al. 2004; Xue et al. 2006). This method will be used in our study from Chapter 4.

Data assimilation cycles are performed in the EnSRF similarly to that in the EnKF. The only difference is that the ensemble mean and the deviations of ensemble members from the mean are updated separately using different equations. The ensemble mean is updated using Eq. (2.18) with the traditional Kalman gain. The deviation of the ensemble member from the mean is updated by using a modified Kalman gain, $\tilde{\mathbf{K}}$, that is reduced in magnitude relative to the traditional Kalman gain \mathbf{K} :

$$\mathbf{x}_i^{t_a} = \mathbf{x}_i^{t_f} - \tilde{\mathbf{K}}\mathbf{H}\mathbf{x}_i^{t_f}. \quad (2.22)$$

When observations are assimilated serially, one at a time, $\mathbf{H}\mathbf{P}^f\mathbf{H}^T$ and \mathbf{R} are scalars, $\tilde{\mathbf{K}} = \alpha\mathbf{K}$ with

$$\alpha = \left(1 + \sqrt{\frac{\mathbf{R}}{\mathbf{H}\mathbf{P}^f\mathbf{H}^T + \mathbf{R}}} \right)^{-1}. \quad (2.23)$$

Here α is a constant with a value between 0 and 1, which is obtained by requiring that the analysis error covariance matches what would be predicted by the EKF. Multiplying \mathbf{K} by α reduces the excess variance reduction by using \mathbf{K} to update deviations from the

mean. In the stochastic EnKF, the excess variance reduction is compensated for by the introduction of noise to observations. The computational cost of the EnSRF is no more than that of the EnKF, when observations are processed one at a time. Whitaker and Hamill (2002) demonstrated by comparing the EnKF and the EnSRF in a hierarchy of models that the EnSRF produces analysis ensemble whose ensemble mean error is lower than the EnKF for the same ensemble size.

2.2.3 Issues associated with the implementation of ensemble-based Kalman filters

2.2.3.1 Evaluation of the covariance matrices

In practice, there is no need to calculate and store the full matrix \mathbf{P}^f , instead $\mathbf{P}^f \mathbf{H}^T$ and $\mathbf{H} \mathbf{P}^f \mathbf{H}^T$ are estimated directly using the ensemble (Evensen 1994; Evensen and van Leeuwen 1996; Houtekamer and Mitchell 1998):

$$\mathbf{P}^f \mathbf{H}^T \cong \frac{1}{N-1} \sum_{i=1}^N \left(\mathbf{x}_i^f - \bar{\mathbf{x}}^f \right) \left(H(\mathbf{x}_i^f) - \overline{H(\mathbf{x}^f)} \right)^T, \quad (2.24)$$

and

$$\mathbf{H} \mathbf{P}^f \mathbf{H}^T \cong \frac{1}{N-1} \sum_{i=1}^N \left(H(\mathbf{x}_i^f) - \overline{H(\mathbf{x}^f)} \right) \left(H(\mathbf{x}_i^f) - \overline{H(\mathbf{x}^f)} \right)^T. \quad (2.25)$$

Equation (2.24) evaluates the covariances between forecasted values at analysis points and observation points, while (2.25) evaluates the covariances between forecasted values at observation points. It can be seen from Eqs. (2.24) and (2.25) that the nonlinear observation operator can be used in the evaluation of covariances, which is an

advantage of the EnKF compared to the traditional extended Kalman filter for nonlinear problems (Evensen 2003).

Another problem associated with the evaluation of the Kalman gain is the rank deficiency problem. The rank of the error covariance matrix \mathbf{P}^f is less than or equal to the number of members in the ensemble. The rank of $\mathbf{HP}^f\mathbf{H}^T$ will be the least of the rank of \mathbf{P}^f and the rank of \mathbf{H} . If the number of data is greater than the ensemble size, $\mathbf{HP}^f\mathbf{H}^T$ will be singular. Adding the measurement error covariance matrix \mathbf{R} increases the rank of matrix $\mathbf{HP}^f\mathbf{H}^T + \mathbf{R}$, but there is still no guarantee that the system becomes well conditioned. The conditioning of matrix $\mathbf{HP}^f\mathbf{H}^T + \mathbf{R}$ can also be poor due to the correlation between neighboring data points (Evensen and van Leeuwen 1996).

Evensen and van Leeuwen (1996) proposed a way for solving the conditioning problem caused by dependent data through data reduction and eigenvalue selection. The analysis equation (2.16) can be rewritten as

$$\mathbf{x}_i^a = \mathbf{x}_i^f + \mathbf{B}^T \mathbf{b}_i, \quad (2.26)$$

where $\mathbf{B} = \mathbf{HP}^f$. Vector \mathbf{b}_i can be obtained by solving

$$\left(\mathbf{HP}^f\mathbf{H}^T + \mathbf{R} \right) \mathbf{b}_i = \mathbf{y}_i - \mathbf{H}\mathbf{x}_i^f. \quad (2.27)$$

By using eigenvalue decomposition when solving (2.27) and discarding the contribution to \mathbf{b}_i from noisy eigenvectors corresponding to the least significant eigenvalues, the noise resulting from the poor conditioning can be eliminated. However, the data reduction in Evensen and van Leeuwen (1996) is actually data thinning, which may be only suitable for some large scale problems, because additional information about

small-scale structure is discarded. In next section, another data selection method will be introduced, which can also help deal with the rank deficiency problem.

2.2.3.2 Covariance localization

It was found in Houtekamer and Mitchell (1998) that with limited ensemble size, the estimated background error correlations between analysis point and observations at large distance is noisy and not reliable. To eliminate those noisy background error correlations, only data within a given cutoff radius are used for each analysis point. This method for improving covariance estimate from the ensemble is often called ‘covariance localization’. A better way to filter the small background-error correlations associated with remote observations is by using a Schur product of the background error covariances calculated from the ensemble and a correlation function with local support (Houtekamer and Mitchell 2001). The Schur product of a correlation matrix \mathbf{A} with a covariance matrix \mathbf{B} is a matrix \mathbf{C} having the same dimension. By using Schur product, the Kalman gain can be rewritten as

$$\mathbf{K} = \left[\rho \circ (\mathbf{P}^f \mathbf{H}^T) \right] \left[\rho \circ (\mathbf{H} \mathbf{P}^f \mathbf{H}^T) + \mathbf{R} \right]^{-1}, \quad (2.28)$$

where operation $\rho \circ$ donates a Schur product (an element-by-element multiplication) of a correlation matrix \mathbf{A} with the covariance matrix \mathbf{B} . Element $A_{i,j}$ is obtained as a correlation function $\rho(r,L)$ with local support applied to the 3D distance between points r_i and r_j . The correlation function generally decreases monotonically with distance and become zero beyond a pre-specified critical distance L .

Covariance localization can greatly improve the conditioning of matrix $\mathbf{H} \mathbf{P}^f \mathbf{H}^T$. As soon as the number of ensemble member N exceeds the number of selected local

observations, $\mathbf{HP}^f\mathbf{H}^T$ (and $\mathbf{P}^f\mathbf{H}^T$) have full rank (Houtekamer and Mitchell 1998). The Schur product tends to reduce and smooth the effect of observations at intermediate distances, which results in smooth analysis increment. However, covariance localization is a heuristic attempt to modify the model of background error covariances so that a limited-size ensemble will not represent distant, distinct features as dynamically interrelated, while it only appears to be due to limited ensemble size (Hamill 2004). The optimal length scale of the correlation function needs to be determined by numerical experiments and generally increases with the ensemble size.

2.2.3.3 Sequential assimilation of observations

To avoid the need to store and invert very large matrices when solving the Kalman filter equations, the observations are organized into batches and are assimilated sequentially (Houtekamer and Mitchell 2001). The sequential processing of the observations is valid when errors of the observations are independent and uncorrelated with the background errors. The analysis obtained by assimilating one batch of observations will be used as the background for the assimilation of the next batch of observations. The application of the EnSRF algorithm requires that the observations are assimilated serially, one at a time (Whitaker and Hamill 2002). When observations are assimilated one at a time, $\mathbf{HP}^f\mathbf{H}^T$ and \mathbf{R} become scalar and the inverse of $\mathbf{HP}^f\mathbf{H}^T + \mathbf{R}$ is trivial to compute. The sequential assimilation of observations combined with covariance localization makes the EnKF algorithm feasible for large systems.

2.2.3.4 Filter divergence

The EnKF tends to have systematically underestimated error covariances due to the sampling errors in the estimation of \mathbf{P}^f for small ensemble sizes. This was first pointed out by Houtekamer and Mitchell (1998) as an inbreeding problem: the ensemble is updated with a gain calculated from that same ensemble. This problem was further analyzed by van Leeuwen (1999). He found that the negative bias in the estimate of \mathbf{P}^a due to the sampling error in the estimate of \mathbf{P}^f is also associated with the nonlinear dependency of \mathbf{K} on \mathbf{P}^f , which can compensate for the effect suggested by Houtekamer and Mitchell (1998). With the negative bias, the ensemble analysis error variance will systematically underestimate ensemble mean analysis error. The buildup of the sampling error effect during the assimilation cycles will cause the computed background error covariance to be too small. The result is that the EnKF progressively ignores new observations in successive cycles, leading to a useless ensemble.

To deal with the ‘inbreeding’ problem, Houtekamer and Mitchell (1998) proposed a double EnKF scheme (DEnKF), in which the covariances estimated from one ensemble are used by the other ensemble to obtain the analysis. However, van Leeuwen (1999) suggested that the DEnKF will result in an overestimation of the error variance. This was found to be true by Whitaker and Hamill (2002).

Anderson (2001) proposed a simple method called ‘covariance inflation’ to compensate for the negative variance bias, in which the forecast error covariances are multiplied by a constant factor slightly larger than one. This is equivalent to increasing

the deviation of each ensemble member about the ensemble mean before the first observation is assimilated:

$$\mathbf{x}_i^f \leftarrow r(\mathbf{x}_i^f - \bar{\mathbf{x}}^f) + \bar{\mathbf{x}}^f . \quad (2.29)$$

Selection of the inflation factor also needs numerical experimentation; large inflation factor may cause balance problems. Filter divergence can also be caused by neglecting model error term, which will be discussed in the next section.

2.2.3.5 Model error

When the Monte Carlo method was first proposed by Evensen (1994) for error covariance evolution and estimation, he suggested that the effect of external error growth associated with the imperfection of the numerical model must be included to give reliable estimates for the evolution of errors. Without taking model error into account, the forecast error covariance estimated from the ensemble will miss the model-error covariance term \mathbf{Q} as was shown in Hamill (2004), which also leads to too small ensemble spread that can cause filter divergence. However, most early EnKF applications did not explicitly include model errors, but simply applied covariance inflation to compensate for the small ensemble spread. The problem is that covariance inflation can only increase the ensemble spread, it can not change the subspace spanned by the ensemble. Without accounting for the external error growth, the ensemble may deviates from the subspace that contains the truth, in which situation covariance inflation may not be effective.

When taking into account the model error, the ensemble of model states should be integrated forward in time according to the stochastic equation (2.1). In practice, this

involves integrating the standard numerical model but with stochastic noise included in the prognostic equations. The EnKF allows a wide range of noise models and the stochastic term can also be added to poorly known model parameters (Evensen 2003). In Evensen and van Leeuwen (1996), pseudo random fields drawn from a distribution having the prescribed error statistics are added to each ensemble member every a few time steps. In doing so a component of random walk in phase space is included, which increases the variance of the ensemble. Evensen (2003) proposed a way to simulate the time evolution of model errors:

$$\mathbf{q}_k = \beta \mathbf{q}_{k-1} + \sqrt{1 - \beta^2} \mathbf{w}_{k-1}, \quad (2.30)$$

where \mathbf{w}_{k-1} is a sequence of white noise drawn from a distribution of smooth pseudo-random fields with mean equal to 0 and variance equal to 1. The coefficient $\beta \in [0,1)$ determines the time decorrelation of the stochastic forcing.

Rather than including stochastic noise into the forecast model, Mitchell and Houtekamer (2000) added random perturbations to the background fields of each ensemble member prior to the assimilation of observations. The perturbations they generated have a balanced relationship between different variables, so that the model error is similar in structure to the background error of their 3DVAR algorithm. Houtekamer *et al.* (2005) later applied this method in their real data study.

Use of multiple forecast models is another way to account for model error. This method has been reviewed by Hamill (2004) and will not be discussed here. Finally, systematic model error caused by uncertain model parameters can be corrected through parameter estimation. Anderson (2001) first suggested estimation of poorly known

parameters in the model through state augmentation with ensemble-based data assimilation algorithm. We explore the possibility of estimating some microphysical parameters using the EnSRF and radar data in Chapter 4 and Chapter 5.

Chapter 3

Ensemble Kalman Filter Assimilation of Doppler Radar Data with a Compressible Nonhydrostatic Model: OSS Experiments²

This chapter reports on the development of a Doppler radar data assimilation system based on the ensemble Kalman filter (EnKF) method. This system is tested with simulated radar data from a model generated supercell thunderstorm. As a first implementation, we assume that the forward models are perfect and radar data are sampled at the analysis grid points. A general purpose compressible nonhydrostatic atmosphere prediction model is used with the inclusion of a multi-class ice microphysics scheme. New aspects compared to previous studies include the demonstration of the ability of the EnKF method in retrieving multiple microphysical species associated with a multi-class ice microphysics scheme, and in accurately retrieving the wind and thermodynamic variables. Also new are the inclusion of reflectivity observations and the determination of the relative role of radial velocity and reflectivity data as well as their spatial coverage in recovering the full flow and cloud fields. In general, the system is able to reestablish the model storm extremely well after

² This chapter is an extended version of our published paper: Tong, M. and M. Xue, 2005: Ensemble Kalman filter assimilation of Doppler radar data with a compressible nonhydrostatic model: OSS Experiments. *Mon. Wea. Rev.*, **133**, 1789-1807.

a number of assimilation cycles, and best results are obtained when both radial velocity and reflectivity data, including reflectivity information outside precipitation regions, are used. Significant positive impact of the reflectivity assimilation is found even though the observation operator involved is nonlinear. The results also show that a compressible model that contains acoustic modes hence the associated error growth performs at least as well as an anelastic model used in previous EnKF studies at the cloud scale.

3.1 Introduction

Since its first introduction by Evensen (1994), the ensemble Kalman filter (EnKF) technique for data assimilation has received much attention. A rapidly increasing number of studies are appearing that examine its performance for various applications. In the field of meteorology, EnKF was first applied to large-scale data assimilation problems and observations are treated as random variables that are subject to perturbations (Burgers et al. 1998; Houtekamer and Mitchell 1998; Evensen 2003). Deterministic methods were developed more recently to avoid sampling errors associated with the use of perturbed observations or to address the adaptive observational network design problem; these methods include the ensemble square-root filter (EnSRF, Whitaker and Hamill 2002; Tippett et al. 2003), ensemble adjustment filter (Anderson 2001) and ensemble transform Kalman filter (Bishop et al. 2001), all of the three belong to the broader class of square-root filters (Tippett et al. 2003).

In general, the EnKF and related methods are designed to simplify or make possible the computation of flow-dependent error statistics. Rather than solving the

equation for the time evolution of the probability density function of model state, the EnKF methods apply the Monte Carlo method to estimate the forecast error statistics. A large ensemble of model states are integrated forward in time using the dynamic equations; the moments of the probability density function are then calculated from this ensemble for different times (Evensen 2003).

Very recently, the EnKF was applied to the assimilation of simulated Doppler radar data for a modeled convective storm (Snyder and Zhang 2003; Zhang et al. 2004) and of real radar data by Dowell et al. (2004). Very encouraging results are obtained in these studies in retrieving wind, temperature and moisture field for convective storms. The first two studies assimilated only radial velocity data, while in Dowell *et al.* (2004), the use of reflectivity data is limited to the update of rainwater mixing ratio only. Neither of these studies included ice microphysics processes, and the assimilation system was based on an anelastic cloud model. Warm-rain microphysics scheme is also used in all afore-quoted 4DVAR studies except for Wu et al (2000) in which a simplified ice microphysics scheme was used. Dual-polarization radar data were assimilated by Wu et al (2000) by first deriving hydrometeor mixing ratios from regular and differential reflectivities.

In this chapter, we report on the development of an EnKF system based on a general-purpose compressible nonhydrostatic model, and on the application of the system to the assimilation of simulated radial velocity and/or reflectivity data from a single Doppler radar. The forecast model employs a complex multi-class ice microphysics scheme. The performance of the EnKF scheme in 'recovering' the complete state of the model thunderstorms, including wind, temperature, pressure and

all water and ice fields are examined. The relative impact of radial velocity and reflectivity data as well as their spatial coverage on the analysis are also investigated. The use of a compressible model, the inclusion of three-category ice microphysics in addition to the liquid water species, and the retrieval of multiple microphysics species with and without reflectivity data are aspects that are new compared to previous studies.

Even though we also performed experiments using ensemble square-root filter, we report here only results using the perturbed observation method. The rest of this chapter is outlined as follows. In Section 3.2, we describe our EnKF assimilation procedure and the design of OSS (Observing System Simulation) experiments. In Section 3.3 we present the experiment results. The impact of various analyses on the forecast is discussed in Section 3.4. A summary and conclusion section is given in Section 3.5.

3.2 Assimilation system and experimental design

3.2.1. The prediction model and truth simulation

In this chapter, we test our EnKF assimilation system using simulated data from a classic May 20, 1977 Del City, Oklahoma supercell storm case (Ray et al. 1981). Such simulation experiments are commonly referred to as Observing System Simulation Experiments (OSSE, see, e.g., Lord et al. 1997). The forecast model used is the Advanced Regional Prediction System (Xue et al. 2000; 2001; 2003). In this study, the ARPS is used in a 3D cloud model mode and the prognostic variables include three velocity components u , v , w , potential temperature θ , pressure p , and six categories of

water substances, *i.e.*, water vapor specific humidity q_v , and mixing ratios for cloud water q_c , rainwater q_r , cloud ice q_i , snow q_s and hail q_h . In addition, turbulence kinetic energy is also predicted which is used to determine turbulent mixing coefficients based on a 1.5-order turbulence closure scheme. The microphysical processes are parameterized using the three-category ice scheme of Lin *et al.* (1983) and its implementation follows Tao and Simpson (1993). More details on the model can be found in (Xue *et al.* 2000; 2001).

For all experiments, the physical domain is $64 \times 64 \times 16 \text{ km}^3$. The model grid comprises of $35 \times 35 \times 35$ grid points (including points that facilitate the specification of boundary conditions), with grid intervals of 2 km in the horizontal directions and 0.5 km in the vertical. The truth simulation or nature run is initialized from a modified real sounding as used in Xue *et al.* (Xue *et al.* 2001). The CAPE of the sounding is about 3300 J kg^{-1} . A 4 K ellipsoidal thermal bubble centered at $x = 48$, $y = 16$ and $z = 1.5$ km, with radii of 10 km in x and y and 1.5 km in z direction is used to initiate the storm. Open conditions are used at the lateral boundaries. A wave radiation condition is also applied at the top boundary. Free-slip conditions are applied to the bottom boundary. The length of simulation is up to three hours. A constant wind of $u = 3 \text{ m s}^{-1}$ and $v = 14 \text{ m s}^{-1}$ is subtracted from the observed sounding to keep the primary storm cell near the center of model grid. Despite the differences in resolutions, the evolution of the simulated storms is very similar to those documented in Xue *et al.* (2001).

During the truth simulation, the initial convective cell strengthens over the first 20 minutes. The strength of the cell then decreases over the next 30 minutes or so, which is associated with the splitting of the cell into two at around 55 minutes (Fig.

3.1). The right moving (relative to the storm motion vector which is towards north-northeast) cell tends to dominate the system; the updraft reaches a peak value of 44 ms^{-1} at 90 minutes. The left moving cell starts to split again at 95 minutes. The initial cloud started to form at about 10 minutes, and rainwater formed at about 15 minutes. Ice phase fields appeared at about 20 minutes.

3.2.2. Simulation of radar observations

As a first implementation, we assume that the simulated observations are available on the scalar grid points. Future work will assume the availability of data in radar coordinate. The simulated radial velocity, V_r , is calculated from

$$V_r = u \cos \phi \sin \varphi + v \cos \phi \cos \varphi + (w - w_t) \sin \phi + \text{a random error}, \quad (3.1)$$

where ϕ is the elevation angle and φ the azimuth angle of radar beams, and u , v and w are the model-simulated velocities interpolated to the scalar points of staggered model grid. The random error is drawn from a normal distribution with zero mean and standard deviation of 1 m s^{-1} . Since V_r is sampled directly from velocity fields, the effect of hydrometeor sedimentation does not come into play.

The simulated logarithmic reflectivity factor (referred to simply as reflectivity), in dBZ, is estimated from equations as follows:

$$Z = 10 \log_{10} \left(\frac{Z_e}{1 \text{ mm}^6 \text{ m}^{-3}} \right) + \text{a random error}. \quad (3.2)$$

The equivalent reflectivity factor, Z_e , is made up of three components,

$$Z_e = Z_{er} + Z_{es} + Z_{eh}, \quad (3.3)$$

where Z_{er} , Z_{es} and Z_{eh} are contributions from rain water, snow and hail. The random error is drawn from a normal distribution with zero mean and standard deviation of 5 dB. Reflectivity relations corresponding to the 10 cm wavelength of WSR-88D radars are given below and used in our experiments.

The rain component of the reflectivity is calculated, based on Smith *et al* (1975), from

$$Z_{er} = \frac{10^{18} \times 720 (\rho q_r)^{1.75}}{\pi^{1.75} n_{0r}^{0.75} \rho_r^{1.75}}, \quad (3.4)$$

where $\rho_r = 1000 \text{ kg m}^{-3}$ is the density of rainwater, ρ in kg m^{-3} the density of air. $n_{0r} = 8 \times 10^6 \text{ m}^{-4}$ is the intercept parameter in the assumed Marshall-Palmer exponential rain drop size distribution.

If the temperature is less than 0 C° , then the component of reflectivity is, for dry snow,

$$Z_{es} = \frac{10^{18} \times 720 K_i^2 \rho_s^{0.25} (\rho q_s)^{1.75}}{\pi^{1.75} K_r^2 n_{0s}^{0.75} \rho_i^{2.0}}. \quad (3.5)$$

Here $\rho_s = 100 \text{ kg m}^{-3}$ is the density of snow and $\rho_i = 917 \text{ kg m}^{-3}$ the density of ice. $n_{0s} = 3 \times 10^6 \text{ m}^{-4}$ is the intercept parameter for snow. $K_i^2 = 0.176$ is the dielectric factor for ice and $K_r^2 = 0.93$ the same for water. Wet snow, which occurs at temperature higher than 0 C° , is treated in a similar way as rain water, and the equivalent reflectivity factor-mixing ratio relation is

$$Z_{es} = \frac{10^{18} \times 720 (\rho q_s)^{1.75}}{\pi^{1.75} n_{0s}^{0.75} \rho_s^{1.75}}. \quad (3.6)$$

For hail, the wet hail formulation of Smith *et al* (1975) is used, i.e.,

$$Z_{eh} = \left(\frac{10^{18} \times 720}{\pi^{1.75} n_{0h}^{0.75} \rho_h^{1.75}} \right)^{0.95} (\rho q_h)^{1.6625}, \quad (3.7)$$

where $\rho_h = 913 \text{ kg m}^{-3}$ is the density of hail. Hail intercept parameter of $n_{0h} = 4 \times 10^4 \text{ m}^{-4}$ is used, which is slightly larger than that used in Smith *et al* (1975), implying more hails of smaller sizes. The same value is used in the ARPS implementation of Lin *et al.* (1983) microphysics scheme. SI units are used in all equations above. Relations similar to the above are used in, e.g., Ferrier (1994). The above equations define the observation operator denoted as H in the following section. When creating simulated observations for our OSS experiments, we impose a lower limit of $1 \text{ mm}^6 \text{ m}^{-3}$ on the equivalent reflectivity factor to yield a lower limit of 0 dBZ for the logarithmic reflectivity factor.

The ground-based radar is located at the southwest corner of the computational domain, i.e., at the origin of x - y coordinate (c.f., Fig. 3.1). For data sampling and assimilation, we assume that the observation operators, given by the above equations, are perfect. As with most atmospheric data assimilation systems, the prediction model is also assumed to be perfect, i.e., no model error is explicitly taken into account. It is worth noting here that observation operators for reflectivity factors are nonlinear and because of that the error distribution of reflectivity data is likely non-Gaussian. Discussions on the non-Gaussian nature of error distributions associated with nonlinear observation operators can be found in, e.g., Lorenc (2003). One of the goals of this study is to assess the effectiveness of such data given these characteristics that violate the basic assumptions used in deriving the optimal EnKF solution.

3.2.3. The EnKF data assimilation procedure

In this chapter, our EnKF implementation is primarily based on the algorithm described by Evensen (1994), Houtekamer and Mitchell (1998) and Burgers *et al.* (1998), which uses the perturbed-observation method. In this algorithm, the ensemble mean is supposed to be the best estimate of the true state and the spread of the ensemble around the mean is a good estimate of the error in the ensemble mean (Evensen 2003).

As discussed in Section 2.2.3.1, the nonlinear observation operator H is directly used in Eqs. (2.24-2.25), \mathbf{H} and its transpose are not evaluated directly (the transpose of \mathbf{H} or the adjoint of the observation operator is needed by variational assimilation methods). The underlying assumption of standard extended Kalman filter theory (which is the basis of EnKF) is that the forecast model and the observation operator are linear. The nonlinearity in the forecast model and the observation operator (such as that of reflectivity data) can make the algorithm suboptimal. Strong nonlinearity would also render initially Gaussian error distributions non-Gaussian. In this study, the performance of the EnKF in such a situation will be examined.

We start the initial ensemble forecast at the 20 minutes of model time when the storm cell developing out of an initial bubble reaches peak intensity. To initialize the ensemble members, random noises are added to the initially horizontally homogeneous background that is based on the environmental sounding. The random noises are sampled from Gaussian distributions with zero mean and standard deviation of 3 m s^{-1} for u , v , and w , and 3 K for potential temperature. The pressure, moisture, and microphysical variables are not perturbed. The technique of adding initial perturbation has been discussed by former studies of Snyder and Zhang (2003) and Dowell et al

(2004). They found that adding initial perturbations to the entire computational domain would introduce spurious cells in individual members. Limiting the perturbation region around the observed storm area helps improve the assimilation result. However, for general applications of the EnKF, the ensemble forecast should cover all scales of motion. We chose to apply the initial perturbations to the entire domain except for the grid points at the lateral boundary to keep the system more general. The open lateral boundary condition is sensitive to boundary errors and initial perturbations introduced at the boundary were found to trigger spurious storm development within some ensemble members. Assimilating reflectivity in clear area region is found to help suppress spurious cells in the interior domain, hence allowing a more general application of initial perturbations.

The observations are assimilated every 5 minutes. The first analysis is performed at 25 minutes and one hundred ensemble members are used. As mentioned earlier, observations are perturbed by adding Gaussian noises, with a standard deviation of 1 m s^{-1} for radial velocity and 5 dBZ for reflectivity. The observation errors are assumed to be uncorrelated; therefore, observations can be and are analyzed sequentially one at a time, following Houtekamer and Mitchell (2001). When using a small (relative to the degrees of freedom of the analysis system) ensemble to estimate the background error covariances, the estimated values between distant grid points are not reliable. Therefore covariance localization is necessary (Houtekamer and Mitchell 1998, 2001; Hamill et al. 2001; Anderson 2001).

In our earlier study (Tong and Xue 2004), we limited the influence region of each observation to a rectangular region with half width of two grid intervals in both

horizontal and vertical directions, equivalent to 4 and 1 km in the horizontal and vertical, respectively. Some useful information beyond that region of influence was not utilized (though the computation was faster). To spatially smooth the analysis increments as well as to localize covariances, Houtekamer and Mitchell (2001) proposed a method that applies Schur (elementwise) product of the background error covariance calculated from the ensemble and a correlation function with local support. This method was also used by Dowell et al. (2004). In the same way, we multiply each element of the background error matrix $\mathbf{P}\mathbf{H}^T$ with a weight computed from correlation function given by Eq. (4.10) of Gaspari and Cohn (1999). The weight decreases gradually from 1 at the observation point to zero at an effective cutoff radius and remains zero beyond. Through assimilation experiments with cutoff radii ranging from 4 to 10 km, we found that 8 km worked the best with 100 ensemble members. This value is therefore used in all experiments presented in this chapter. The use of a smooth filter function is found to produce significantly better analysis than the sharp cutoff function used earlier in Tong and Xue (2004).

The EnKF algorithm tends to underestimate the analysis uncertainty owing to the use of limited ensemble size. To solve this problem, we tested the double ensemble method (Houtekamer and Mitchell 1998), in which the statistics estimated from one ensemble is used to update the other. However, this approach overestimated the analysis uncertainty in our case and did not help improve our analysis. We also tested the covariance inflation approach of Anderson (2001), which did not work well at first. As found in Snyder and Zhang (2003), it enhances the spurious cell in ensemble members. A modification is then made by applying covariance inflation to the grid points that will

be influenced directly during the analysis update by the observations found within the precipitation (where observed $Z > 10$ dBZ) regions. To do this, we check for each grid point to see if within 8 km radius (the same radius used by the covariance localization) there is at least one reflectivity data greater than 10 dBZ. If it is true, then covariance inflation is applied to this grid point. This is found to improve our analysis. The inflation factor we used is 1.07 or 7 percent when radial velocity or/and reflectivity data in the precipitation region are assimilated. When reflectivity data of complete coverage are used, the inflation factor is increased to 1.1 (10 percent). Zhang et al (2004) proposed another alternative to the traditional covariance inflation that is to avoid enhancing spurious cells but Caya et al (2005) found that the use of the method degrades the quality of analysis.

3.3 The Assimilation Experiments

Table 3.1 lists eight experiments to be discussed in this chapter. The assimilation scheme is first tested by assimilating radial velocity or reflectivity data alone or by assimilating both. Further, data coverage tests are performed in which each data type is available either in the entire domain or only in regions where reflectivity exceeds 10 dBZ (referred to as precipitation region). Additional variations have to do with the ways analysis variables are updated during the assimilation cycles. The results are discussed in the following sections.

3.3.1. Assimilations using radial velocity data only

In experiment VrP (see Table 3.1), we assume that the radial velocity data are available

Experiment	Observation: Radial velocity (V_r) and/or Reflectivity (Z)	Update q_r, q_s, q_h	Update u, v, w, q_v, q_c, q_i when assimilating reflectivity
VrP	V_r ($Z > 10$ dBZ)	yes	
VrF	V_r	yes	
ZP	Z ($Z > 10$ dBZ)	yes	yes
VrZPa	V_r & Z ($Z > 10$ dBZ)	yes	yes
VrZPb	V_r & Z ($Z > 10$ dBZ)	yes	no
VrZPc	V_r & Z ($Z > 10$ dBZ)	yes	yes, start from 4 th cycle
VrPZF	V_r ($Z > 10$ dBZ) & Z	yes	yes, start from 4 th cycle
VrPnoIce	V_r ($Z > 10$ dBZ)	no	

Table 3.1 List of Data Assimilation Experiments

in precipitation regions where reflectivity is greater than 10 dBZ. After only one analysis cycle (at $t = 25$ min), the basic patterns of middle-level horizontal winds around the storm appear reasonable (not shown). After three more analysis cycles, *i.e.*, by 40 min., the basic structures of updraft and horizontal flow (Fig. 3.1e) as well as perturbation temperature (not shown) above the low-level cold pool are reasonably well retrieved. The low-level cold pool and the associated divergence are too weak at this time (Fig. 3.2e). Some hydrometeors can be retrieved at this time, but their amount and locations are not yet accurate. Two more assimilation cycles later, at 50 min., the strength of the updraft and the magnitude of the temperature perturbation (except that in the low-level cold pool) become reasonably good.

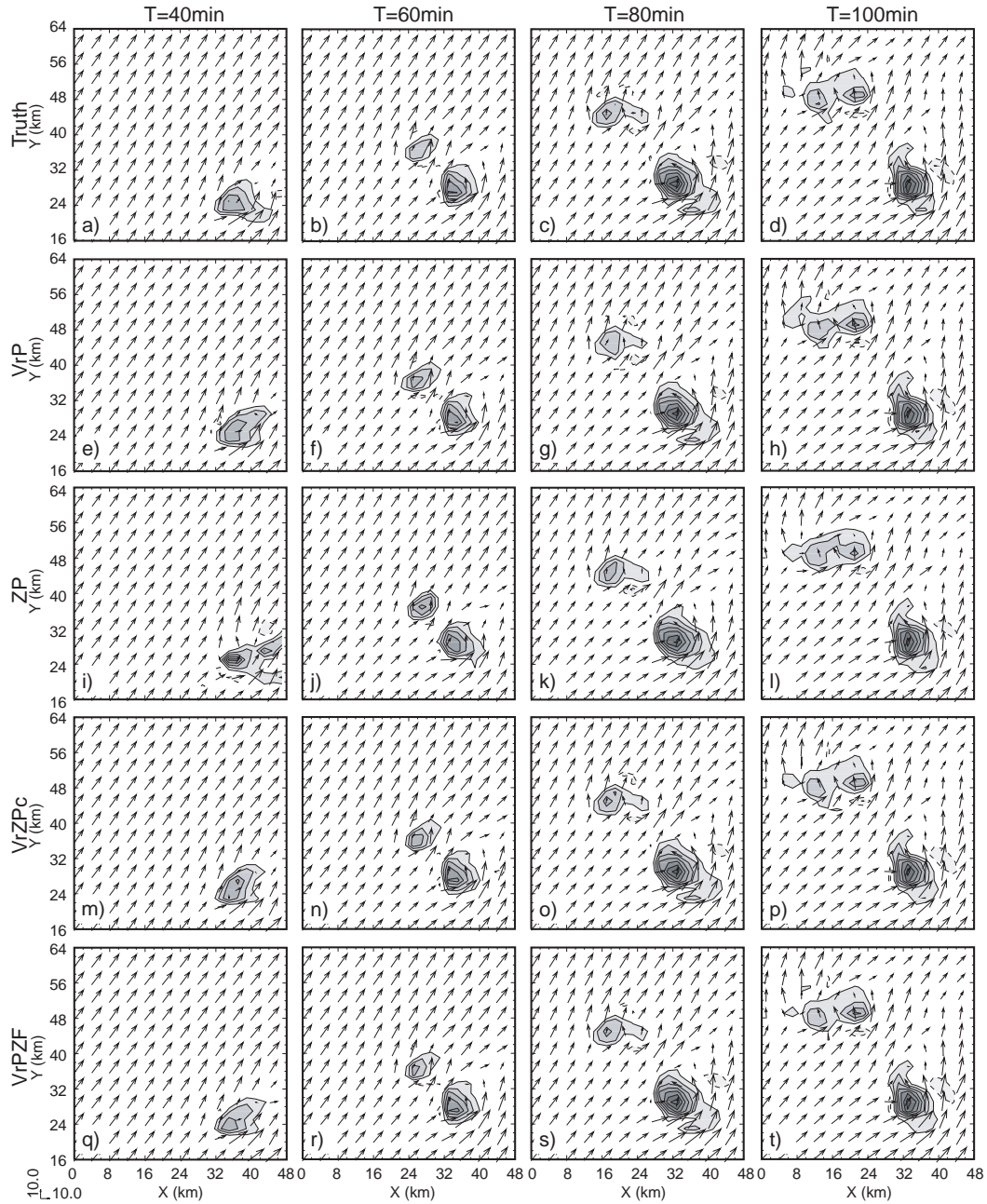


Fig. 3.1. Vertical velocity [contours and shading at intervals of 4 m s^{-1} ; solid (dash) contours represent positive (negative) values] and horizontal wind (vectors, plotted every other grid point; m s^{-1}), at level $z = 6 \text{ km}$: (a)-(d) truth simulation; analyses from VrP (e)-(h), ZP (i)-(l); VrZPc (m)-(p); VrPZF (q)-(t), at $t = 40, 60, 80$ and 100 min during the assimilation period.

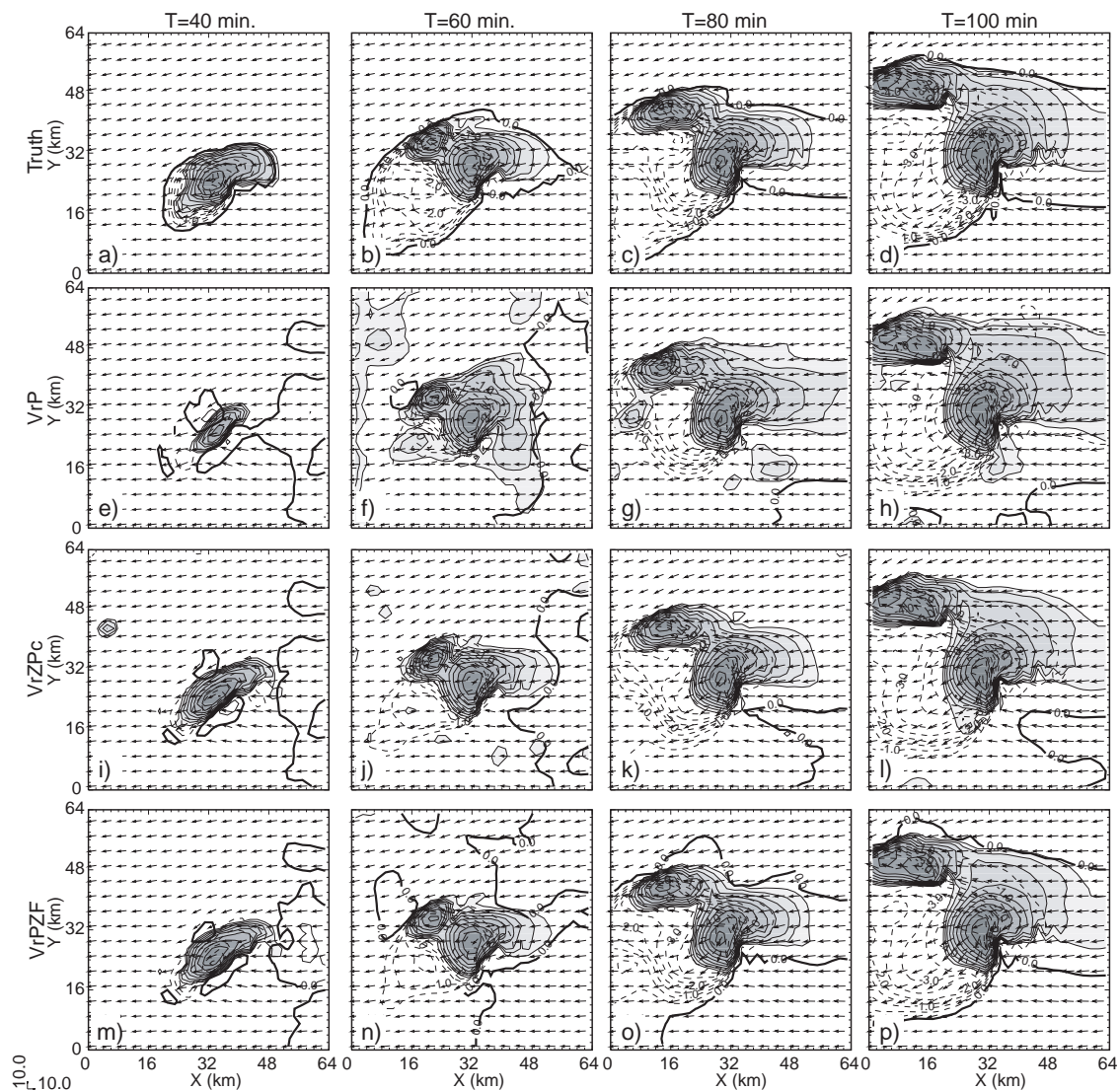


Fig. 3.2. Horizontal wind (vectors; m s^{-1}), perturbation potential temperature (thick black lines for 0 K and thin dashed contours at 0.5 K intervals) and computed reflectivity (thin solid contours and shading at intervals of 5 dBZ, starting from 15 dBZ) at $z = 250$ m: truth (a)-(d), EnKF analyses from VrP (e)-(h), VrZPc (i)-(l) and VrPZF (m)-(p).

At 60 min., the retrieved microphysical fields also become rather close to the truth as seen from the vertical cross-sections (Fig. 3.3 (a2)-(f2)), so do most other fields (Fig. 3.1f and Fig. 3.2f). The largest differences at this time are found at the low levels (Fig. 3.2f) where precipitation and cooling in the otherwise unperturbed low-level

inflow region exist, and near the western boundary. Evaporative cooling due to spurious precipitation in some ensemble members was the cause. Much of the error is corrected by subsequent analyses and by 100 min. (Fig. 3.2h); the precipitation in the inflow region is generally gone except for a small area ahead of the rear-flank gust front. The low-level flow and reflectivity patterns as well as the shape of the cold pool now agree quite well with the truth (Fig. 3.2h and d); although small differences are still found with the exact location of the boundary of rain-cooled regions (as indicated by the zero degree θ' contours) and in the areal coverage of leading precipitation region on the east-northeast side. The agreement at the 6 km level is even better (Fig. 3.1h and d). These results indicate that even with radial velocity data in precipitation region only, the EnKF system is able to rebuild the model storm remarkably well after a sufficient number of assimilation cycles. Analysis of such quality can only be expected of methods that make use of multiple radar volume scans effectively and in a way that is compatible with the hopefully correct model physics.

We use the root-mean-square (*rms*) error of ensemble mean analysis to judge quantitatively the quality of the analysis. The *rms* errors are averaged over the grid points where the reflectivity is greater than 10 dBZ. The *rms* errors of velocities, temperature, cloud and hydrometeor variables in experiment VrP are seen to decrease rapidly during the first four assimilation cycles (over 20 minutes) and the analysis tends to converge at about 70 minutes (Fig. 3.4, black curves). When the analysis converges, the *rms* analysis error for horizontal wind components is generally less than 1 m s^{-1} and about 0.5 m s^{-1} for vertical velocity. For perturbation potential temperature θ' , the analysis error decreases to less than 0.5 K at 60 minutes. Such velocity errors are

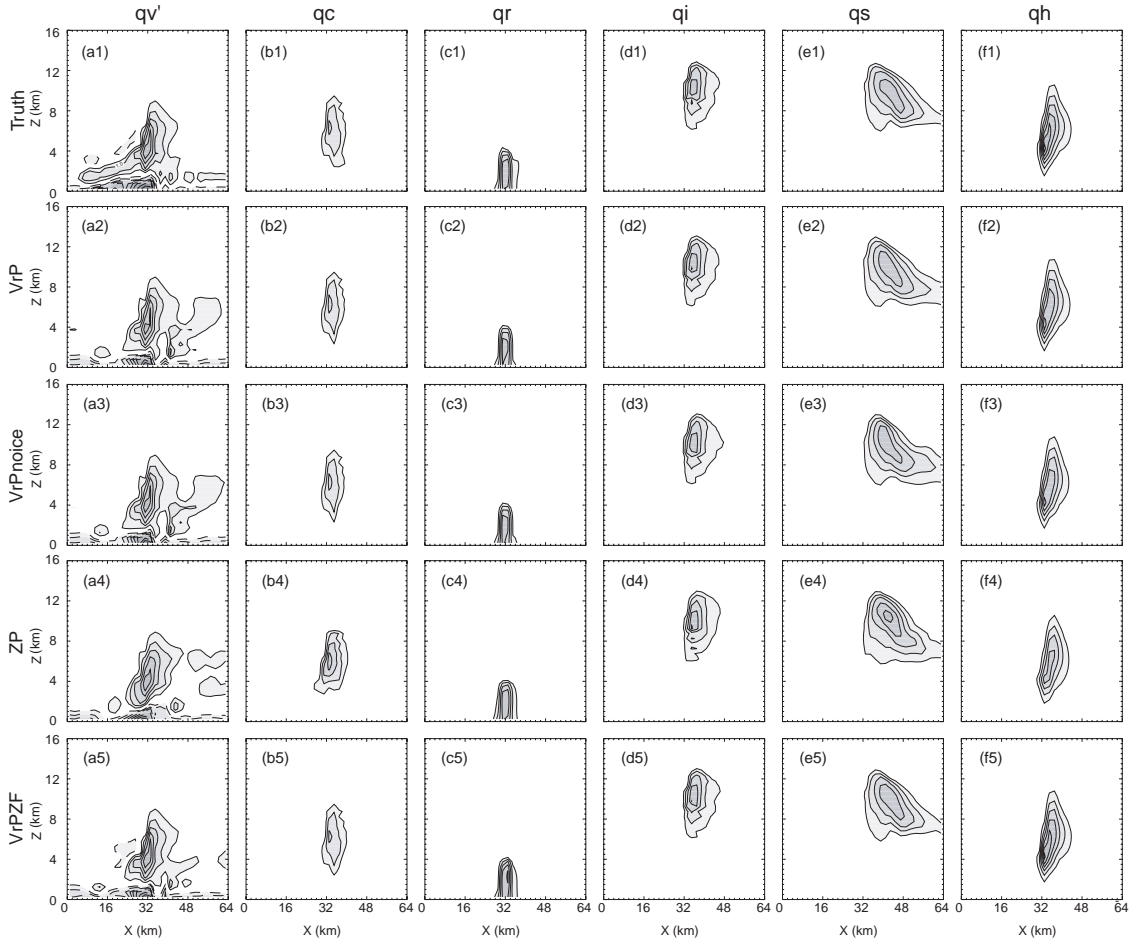


Fig. 3.3. The retrieved (a) perturbation q_v (solid (dash) contours represent positive (negative) values) (b) q_c , (c) q_r , (d) q_i , (e) q_s and (f) q_h . (contours and shading at intervals of 0.5 g kg^{-1} for q_v perturbation, q_c , q_i and q_s , and of 1.0 g kg^{-1} for q_r and q_h .) in the x-z plane at $y = 29 \text{ km}$ that pass through the maximum updraft at $t = 60 \text{ min}$: (a1)-(f1) truth simulation, (a2)-(f2) VrP, (a3)-(f3) VrPnoIce, (a4)-(f4) ZP and (a5)-(f5) VrPZF.

similar to or less than the observational errors added to the radial velocity. It means that after eight to ten assimilation cycles, the EnKF system is producing a very good estimate of the state of the simulated storm.

In experiment VrF, in which V_r data cover the entire domain, the analysis converges more quickly and the analysis errors are smaller (black dotted lines in Fig. 3.4). The retrieved winds, potential temperature, pressure and water vapor content are

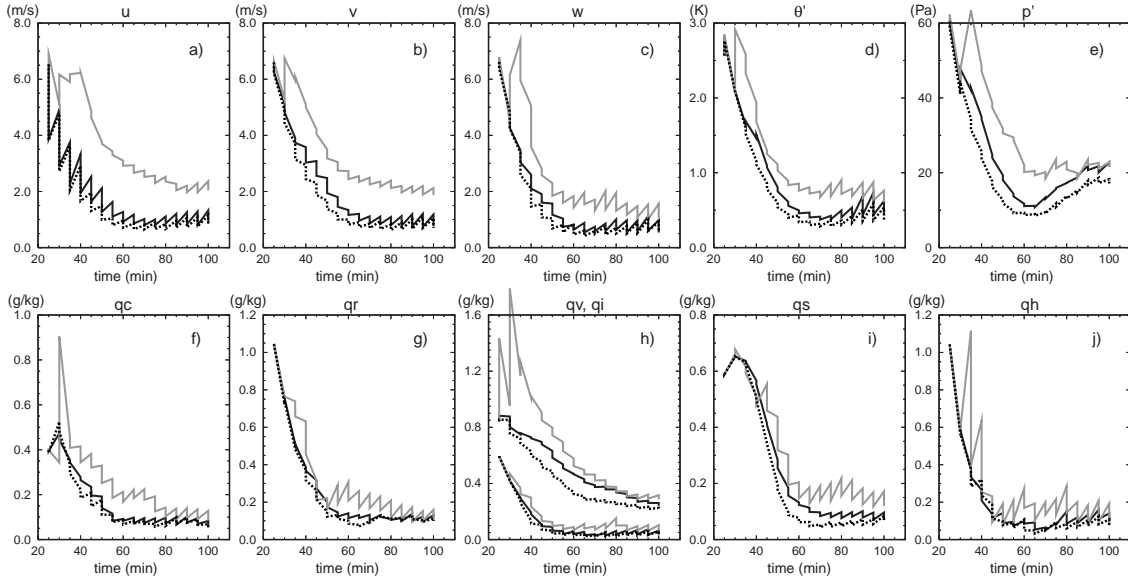


Fig. 3.4. The rms errors of ensemble-mean forecast and analysis, averaged over points at which the reflectivity is greater than 10dBZ for: a) u , b) v , c) w and d) perturbation potential temperature θ' , e) perturbation pressure p' , f) qc , g) qr , h) qv (the curves with larger values), qi (the curves with lower values), i) qs and j) qh , for experiment VrP (black), experiment ZP (gray) and experiment VrF (black dotted lines). Units are shown in the plots. The drop of the error curves at specific times corresponds to the reduction of error by analysis.

significantly better than those of VrP case. The retrieved microphysical fields are also improved, but not as much as when full coverage reflectivity data are used (results to be presented later). For radial velocity data to be available outside the precipitation region, the radar has to be operating in high sensitivity mode, which is generally not the case with the WSR-88D network when precipitation is present. However, when such data are available, our experiment shows clear positive impact of the data.

In our earlier study (Tong and Xue 2004), we found that when pressure field is analyzed (updated by the analysis procedure), the pressure error increases instead of decreases after each analysis cycle. A careful examination of the results reveals that the main problem was associated with a domain-wide pressure drift in the forecast that

often occurs in simulations using a small computational domain and an open boundary condition. The background error covariance between pressure and observations in the presence of pressure drift was apparently not correct, causing negative analysis impact on pressure field. In all experiments presented here, the pressure detrending option of ARPS model is turned on, which forces the domain-mean perturbation Exner function to zero after each forecast time step. The model solution, at least in the dry case, should be independent of the perturbation Exner function to an arbitrary constant.

After applying pressure detrending, pressure drift is much controlled and the update of pressure by analysis does reduce its error in general, though not as much as for other fields (cf. e.g., black curves in Fig. 3.4e and Fig. 3.4c). At 40 min. in the current experiment (VrP), the basic pattern of perturbation pressure can be reasonably reconstructed (not shown). Noticeable noises associated with acoustic oscillations remain at low levels at this time which are reduced by additional assimilation cycles. However, it can be seen in Fig. 3.4e (black curve), the forecast error of the pressure perturbation starts to increase again at 65 min., and the error is not effectively reduced by further analysis. It is found that in this case some positive pressure drift still occurs in the ensemble-mean forecast and analysis below 4 km. The positive pressure perturbation associated with the cold pool is about 20 Pa higher than in the truth. The low pressure below the updraft is not as low as it should be. Such pressure biases appear to be preventing the EnKF scheme to work effectively in reducing the pressure errors, which is only indirectly related to V_r . It will be shown later that when reflectivity data are assimilated, the pressure drift problem is alleviated and the analysis of pressure is improved.

3.3.2. Impact of assimilating reflectivity data

Reflectivity is a measurement that is provided by all types of weather radar. In this section, we examine if reflectivity data alone is sufficient for the model to reproduce the true storm; we also study its value when used in combination with radial velocity data. We note that the observation operator for reflectivity is nonlinear and there exist more uncertainties with reflectivity operator (because of uncertainties with cloud microphysics, effects of attenuation, among others) than with radial velocity. In our model, the rainwater, snow and hail mixing ratios, q_r , q_s , and q_h , are directly related to observed reflectivity through Eqs. (3.4)-(3.7). Therefore, the experiments further test the performance of the EnKF scheme for nonlinear observations.

In experiment ZP (see Table 3.1), reflectivity (Z) data greater than 10 dBZ are assimilated but not radial velocity. Generally, the analysis obtained by assimilating reflectivity data only is not as good as the analysis assimilating radial velocity data alone. As can be seen in Fig. 3.4 (gray curves), the analysis acts to reduce the *rms* errors in q_r , q_h , q_s , q_c , q_i , w and θ' from the third cycle with the reduction of error in q_h being much larger. Significant reduction in errors of horizontal wind components and in q_v did not start until after four to five cycles. In fact, during the first two cycles, the update of most variables increases rather than decreases the error (see, *e.g.*, the gray curves in Fig. 3.4d for θ' and Fig. 3.4h for q_v). Significant reduction in errors of horizontal wind components and in q_v did not start until after four to five cycles.

The delay in the reduction of or even increase in the *rms* errors in variables not directly related to Z is related to our initial perturbation method. When the ensemble

members are initialized, cloud and hydrometeor fields are not perturbed. This is reasonable because the location of precipitation region is unknown before observational data are introduced. Adding hydrometeor perturbations everywhere in the model is undesirable because non-zero values in certain variables like cloud ice should only exist under certain conditions. If the initial background contains some information about the cloud, then random perturbations can be added to the related fields in a way similar to that for the other fields. Without direct adding initial perturbations to them, it takes the model a couple of assimilation cycles to develop cloud and hydrometeors and to establish coherent covariance structures for a reliable estimation of error covariances. For these reasons, updating indirectly related variables in the first few cycles increases their errors. Enough ensemble spread is established starting from the third assimilation cycle; from then on, the analysis is able to correct forecast errors in fields including w , θ' , q_c , q_r , q_i , q_s and q_h (Fig. 3.4). Reliable covariances between reflectivity and p , q_v and horizontal wind components are slower to establish and the analysis correction starts a couple of cycles later.

Because of the lack of reliable covariances, the retrieved model fields in ZP are not good at 40 min. (Fig. 3.1i). By 45 min., the storm updraft and temperature perturbation pattern become reasonable. The locations of the hydrometeors are now close to the truth. However, horizontal wind patterns are still not very good at this time. From 60 minutes on, the basic structure and the evolution of the storm including the split storm cells become rather accurate. The errors in all fields are further reduced in the subsequent assimilation cycles (Fig. 3.4), but remain higher than the VrP case by the end of the assimilation period (100 min.).

Retrieving the model state from the observed variables in the EnKF system relies heavily on a good estimate of the flow-dependent multivariate background error covariances. Fig. 3.5 shows, for experiment ZP, the forecast background error correlations between reflectivity at point $x = 32$ km, $z = 6$ km and model variables at each grid point in an x - z vertical cross section through the maximum updraft ($y = 29$ km) at 80 min. (the correlation patterns for other experiments at this time are similar). As can be seen, for the water and ice fields, significant correlations are mostly confined to the regions where their non-zero values are found. For w and θ' , the correlation patterns also match those of w and θ' themselves in general, and significant correlations extend through much of the troposphere depth, which is consistent with the nature of deep convection. The maximum correlations for w and θ' exceed 0.8, indicating that they are highly correlated with reflectivity. Generally, positive correlations are associated with updraft and high buoyancy; negative correlations are found in the recirculation regions. The correlation for θ' spreads above the tropopause in a wavy pattern to both upstream and downstream, which should be related to the gravity wave propagation in the stable stratification there.

Even for pressure, coherent structures of significant correlation exist. Maximum negative correlation is found at the mid levels where perturbation pressure has a minimum; maximum positive correlation exists near the cloud top. This correlation pattern can be explained by the rotating supercell storm dynamics. Stronger updraft rotation produces lower mid-level pressure which promotes stronger updraft therefore produces more reflectivity. Stronger updraft, accompanied by larger reflectivity, will produce larger positive pressure perturbations at the cloud top due to both hydrostatic

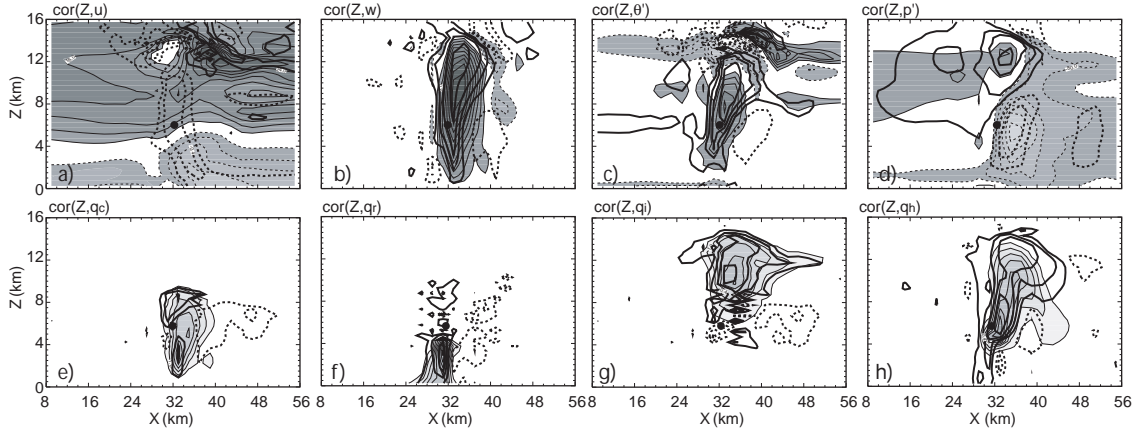


Fig. 3.5. Forecast error correlations estimated from an ensemble at $t = 80$ min for experiment ZP in the x - z plane at $y=29$ km, which passes through the maximum updraft. The error correlation [thick solid (dash) contours represent positive (negative) correlations at intervals of 0.2] between forecast reflectivity Z at $x=32$ km and $z=6$ km (indicated by a black dot) and (a) u , (b) w , (c) θ' , (d) p' , (e) q_c , (f) q_r , (g) q_i , and (h) q_h . The shading and thin solid (thin dashed) contours in (a)-(d) indicate positive (negative) values of model fields from the truth simulation with increment of 4 ms^{-1} for u and w ; 2 K for θ' and 40 Pa for p' . The shading and thin contours in (e)-(h) indicate the values of mixing ratio of water and ice fields from the truth simulation with increment of 0.5 g kg^{-1} for q_c , and q_i and 1 g kg^{-1} for q_r and q_h .

and Bernoulli effects. These suggest that the error correlations estimated from the forecast ensemble are dynamically consistent. It is these valuable correlations that act to spread the information from the observation points to the finite domain surrounding them and that retrieve the unobserved variables from the observed ones. The results also justify our choice of the influence region in covariance localization. Most significant correlations within 4 km from the center of the influence region are kept and smaller weights are given to the correlations extending up to 8 km.

3.3.3. Assimilation of both radial velocity and reflectivity

In the next set of experiments (VrZPa-c, VrPZF, see Table 3.1), we combine the radial velocity and reflectivity data into the assimilation process. Experiment VrZPa is a combination of VrP and ZP, in which both the radial velocity and reflectivity in precipitation regions ($Z > 10$ dBZ) are assimilated, using the same procedure as in VrP and ZP. Compared to VrP (Fig. 3.6), when additional reflectivity data are introduced, the analyses of q_r , q_s and q_h are generally improved, especially for q_r and q_h , as indicated by lower errors after each analysis. The forecast error growth in this experiment is faster, however, even for those three variables directly related to Z .

The analysis errors of q_v and p' remain higher than those in VrP until 60 and 80 min., respectively, but become noticeably smaller afterwards. For most part of the assimilation period, the wind components are not as accurate as those retrieved by assimilating only V_r , but can reach the same accuracy in the last a few cycles. For θ' , q_c and q_i , the analysis errors from VrZPa are larger in the first 2-3 cycles, smaller in the next few then remain similar to those in VrP case.

The lack of significant positive impact by the inclusion of reflectivity data, especially during the first few assimilation cycles, is due to the reasons discussed earlier for ZP. In the first two to four cycles, background error covariances between reflectivity and the model variables that are not directly related to Z are not reliable. Updating these variables based on reflectivity data and the unreliable covariances hurts the analysis, as indicated by the increase of errors in w , θ' , q_c and q_v by, e.g., the second analysis cycle (the error increase is actually rather bad for q_c and q_v , see Fig. 3.6). The increased

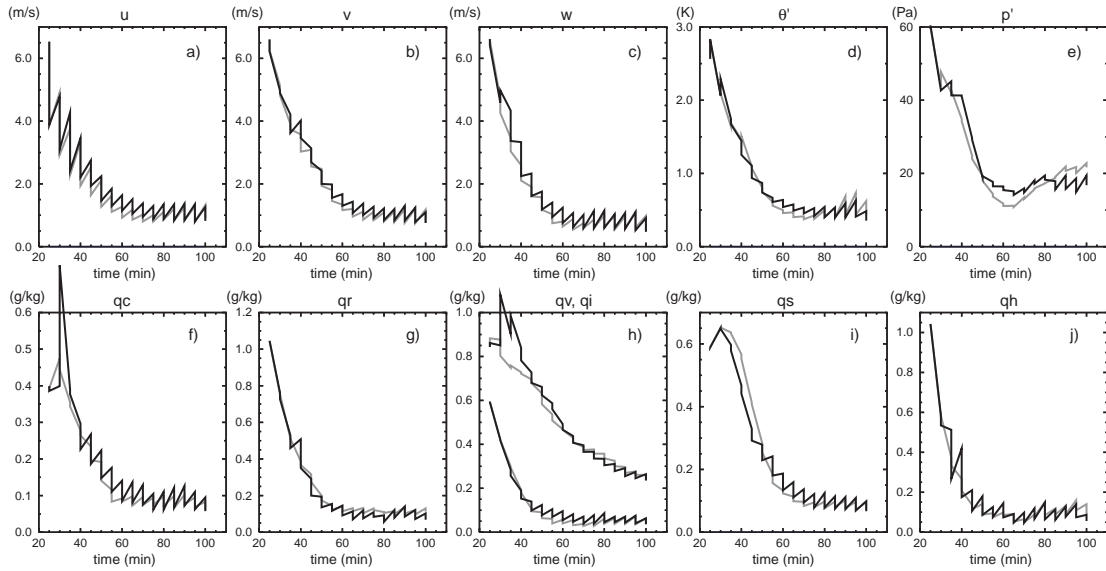


Fig. 3.6. As in Fig. 3.4, but for experiment VrZPa (black) and experiment VrP (gray).

analysis errors lead to less accurate forecast and faster error growth. Despite all this, the analyses towards the end of the assimilation period is similar or better for most fields in VrZPa than in VrP, indicating significant positive impact of Z when good error estimation becomes available. Interestingly, the degradation of the analysis in the early cycles by the assimilation of rainwater content is also noted by Caya et al. (2005), which includes warm rain microphysics.

We note that in Dowell et al. (2004) which employs warm rain microphysics, it is found that updating q_r only when assimilating reflectivity observations help maintain a realistic structure of the precipitation core and improve velocity verification score. We performed a corresponding experiment, VrZPb (black curves in Fig. 3.7), in which only q_r , q_s , and q_h are updated when assimilating reflectivity. As was found in VrZPa, the analyses of q_r , q_s and q_h are improved over those of VrP. The analysis of q_v is also better. For most of the other variables, the improvement over VrP is generally small, if

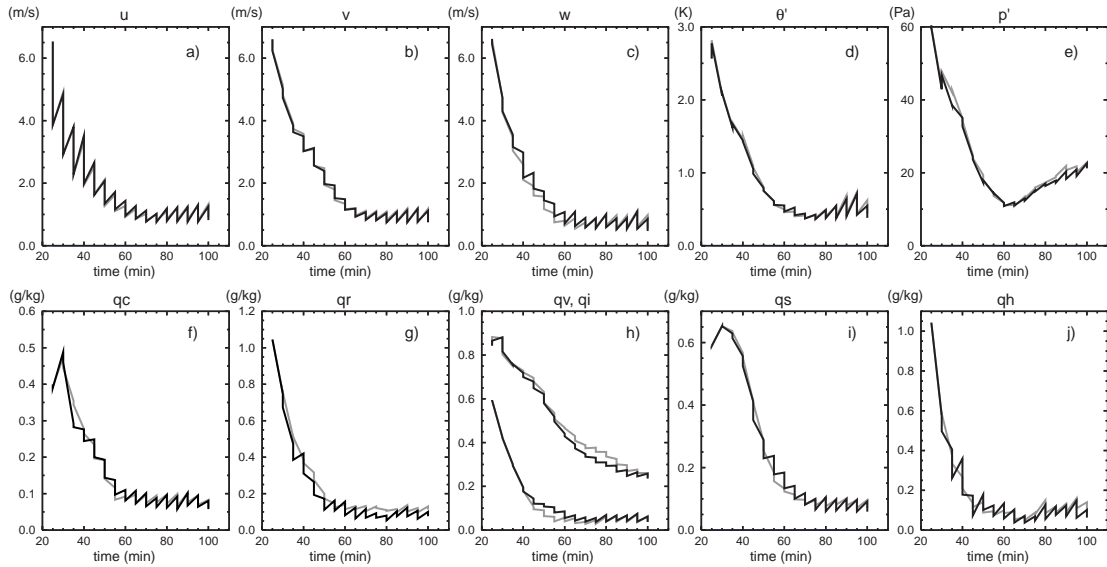


Fig. 3.7. As in Fig. 3.4, but for experiment VrZPb (black) and experiment VrP (gray).

any (Fig. 3.7). There are also a few cycles in which the retrieved w and q_i are not as good as those of VrP. Since it was shown earlier that reflectivity does have significant correlations with indirectly related variables (Fig. 3.5), we do not believe it appropriate to completely exclude those variables from the analysis update when assimilating reflectivity data. A better solution needs to be found.

From previous experiments, it can be seen that the negative impact of using reflectivity to update variables rather than q_r , q_s , and q_h is mainly caused by the incorrect background covariances in the first two to three cycles. After that, the reflectivity becomes beneficial in retrieving those model fields. To see if we can further improve the analysis, in experiment VrZPc (Table 3.1), we apply the update due to reflectivity only to q_r , q_s , and q_h before the fourth cycle. Starting from the fourth cycle, all models variables are updated. It is shown in Fig. 3.8 that doing so improves the analysis overall. The retrieved q_v , potential temperature and pressure are improved over

VrP more than those in experiment VrZPb. Significant improvement could also be found in q_c and q_s . For velocity components, the improvements are also slightly larger, especially in the later cycles.

The retrieved updraft and horizontal wind field in the middle level are shown in Fig. 3.1 in panels m through p. The detailed structures of the updraft of the split cells starting from 60 min (panels n through p) are retrieved better than those in either VrP (plots f through h) or ZP (plots j through l). At 80 and 100 min., the pattern and strength of the left mover, a less organized therefore more difficult one analyze, are clearly better retrieved by experiment VrZPc. Fig. 3.2 shows the retrieved low-level cold pool, gust front and precipitation pattern by different experiments, in terms of the low-level θ' , wind vectors and model computed reflectivity. The benefit of using reflectivity data can be better seen from this figure. Without reflectivity data (VrP), the retrieved precipitation is much less, especially during the early cycles. Spurious echoes are found in the clear air region in both cases but much less so in VrZPc (Fig. 3.2). They are related to spurious cells in individual ensemble members. The assimilation of reflectivity data reduced the spurious echoes.

In the previous experiments, only reflectivity larger than 10 dBZ is assimilated. In reality, reflectivity outside the precipitation regions also contains valid information. At least it indicates the absence of precipitating particles there. One can therefore assume that the reflectivity data cover the entire region within the radar range, which in our current case means the entire computational domain. In our next OSS experiment, named VrPZF (Table 3.1), reflectivity information is available everywhere while radial velocity data remain available in precipitation ($Z > 10$ dBZ) regions only. As in VrZPc,

u , v , w , θ' , q_v , q_c , and q_i are updated starting from the fourth cycle when assimilating reflectivity while q_r , q_s and q_h are updated from beginning.

The complete coverage of reflectivity data can remove spurious cells that would otherwise develop in the data void regions. The *rms* analysis errors in VrPZF (Fig. 3.9, thin black curves) are decreased more over those in VrP or VrZPc (Fig. 3.8). The retrieved horizontal wind fields, the strength of the updraft (Fig. 3.1), the low-level perturbation potential temperature (Fig. 3.2) and the microphysical fields (Fig. 3.3) are more accurate than those retrieved by any of the previous experiments. The reflectivity computed from the analysis (Fig. 3.2m-p) very closely resembles that in the truth simulation with no spurious echoes found in the clear air region. Towards the later period of assimilation, the strength of the low-level cold pool can be retrieved very well by all of the three experiments (Fig. 3.2). However, only when complete reflectivity data coverage is used, as in the case of VrPZF, can the extent of the low-level rain-cooled air, as indicated by the 0 K contour of perturbation potential temperature, be accurately determined. This is actually very important for the subsequent forecast as spurious cooling in the inflow region is found in some cases to reduce the CAPE in the inflow and adversely affects the evolution of ensuing forecast. VrPZF produces the best forecast (more later) among all assimilation experiments, for this and other reasons.

Finally, we briefly discuss the ensemble spread which is defined as the square root of the ensemble variance and plotted in Fig. 3.9 for experiment VrPZF. Since EnKF estimates the forecast error using the ensemble spread, in ideal situation, the ratio of the spread of the ensemble to the error of the ensemble mean forecast is equal to $\sqrt{N/(N+1)}$ (Murphy 1988). As we can see from Fig. 3.9, the ensemble spread

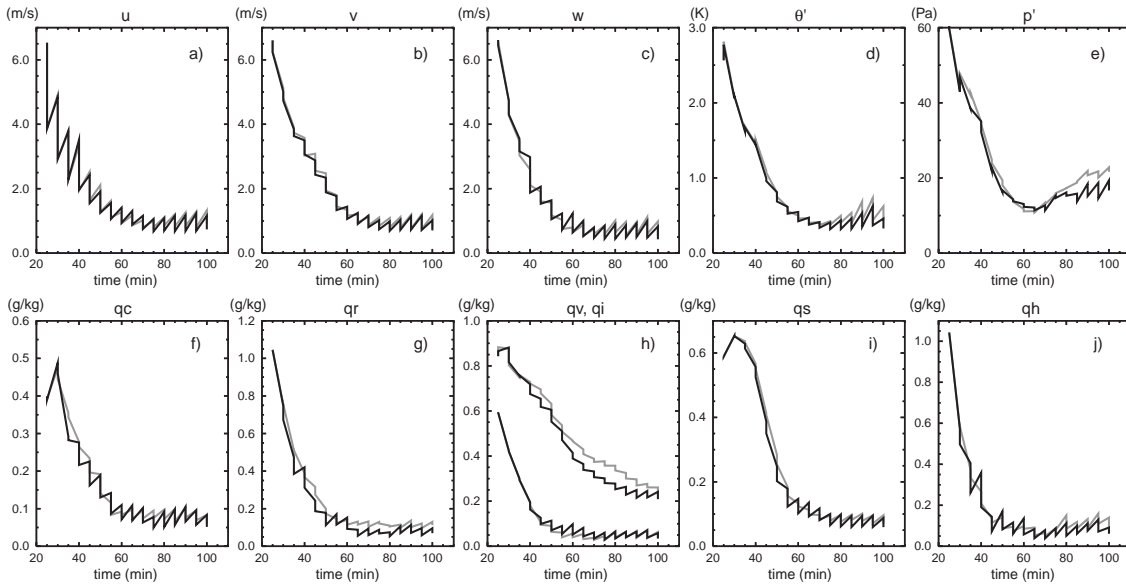


Fig. 3.8. As in Fig. 3.4, but for experiment VrZPc (black) and experiment VrP (gray).

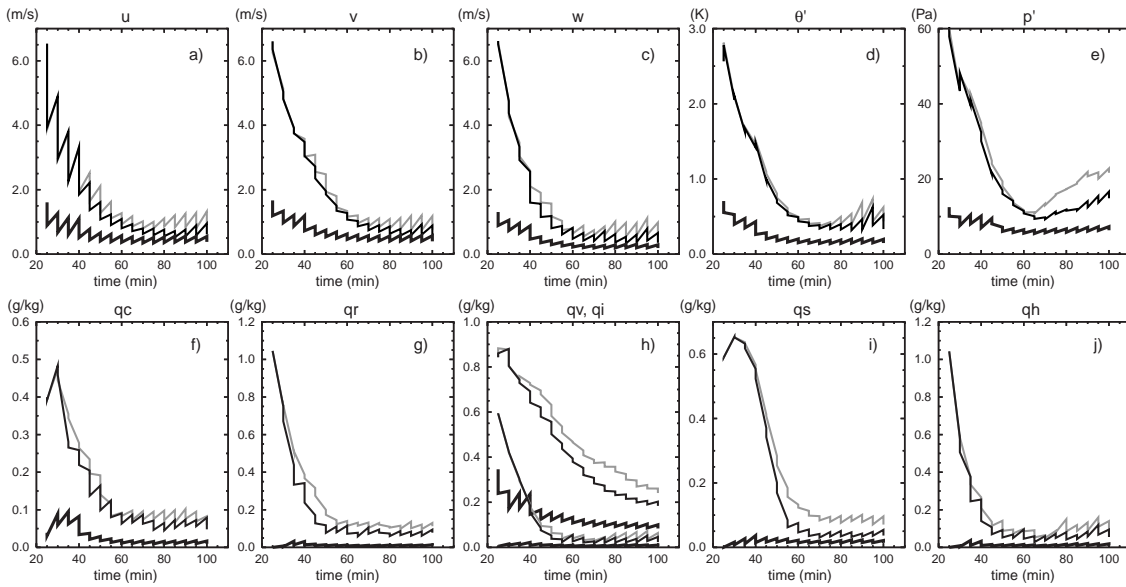


Fig. 3.9. As in Fig. 3.4, but for experiment VrPZF (thin black curves) and experiment VrP (thin gray curves). The additional thick black curves are for the analysis and forecast ensemble spread of VrPZF, and the spread is calculated only at the points where reflectivity is greater than 10 dBZ, as the errors are.

gradually approaches the ensemble mean forecast error for most variables, a favorable sign. During the early cycles, the ensemble spread is much smaller than the rms error and therefore provides a poor representation of forecast error, a behavior also observed by Snyder and Zhang (2003). The ratio increases rapidly during the first 6 to 8 cycles for most variables (mainly because of the rapid decrease in forecast errors) then becomes more stable. In the last four or so cycles, this ratio starts to decrease again, especially for u , v , w , θ' and p' . Such a decrease is typically observed as EnKF goes through successive assimilation cycles (e.g., Houtekamer and Mitchell 1998) owing to a systematic underestimation of the analysis variance. In our case, this decrease in the later cycles is mainly due to the faster error growth in the forecast rather than to change in the ensemble spread; in fact, the ensemble spread remains essentially constant in the later cycles. The faster forecast error growth is, we believe, due to the more transient nature of the flow after the storm went through more than two splits. Snyder and Zhang (2003) noted, however, a continued increase in the spread-to-error ratio, and attributed the increase to the presence of spurious cells in individual members. A similar behavior is also observed in our experiment, VrP, in which spurious cells are not effectively suppressed as they are in VrPZF. We further note that in the last few cycles of VrPZF, despite the increased forecast errors (Fig. 3.9), the analysis errors do not increase or increase very little, indicating that the filter is well behaved.

3.3.4. Retrieval of microphysical fields

The microphysics retrieval is an important aspect of convective-scale data assimilation. Relatively few previous data assimilation studies have focused on this

problem. Most of these studies used only a simple microphysical parameterization and the ice phase is usually excluded. The more recent attempt of Wu et al (2000) uses a 4DVAR system to assimilate dual-polarization radar data into a cloud model. Generally, a good bulk ice microphysics parameterization includes ice categories for cloud ice (individual crystals), snow (aggregates), and graupel and/or hail. As pointed out by Wu et al (2000), such a model will have a complex adjoint model involving many nonlinearities, and the 4DVAR system based on such adjoint tends to have poor convergence properties. For these reasons, Wu et al (2000) made simplifications by using a scheme without the snow category and by merging cloud water and cloud ice categories. Such simplifications reduce the degrees of freedom (or the number of control or analysis variables), and also reduce the number of, usually highly nonlinear, microphysical processes. In addition, in Wu et al (2000), the reflectivity and differential reflectivity data are converted first to rain and hail mixing ratios before assimilation, rather than being assimilated directly. The differential reflectivity data are necessary for such a conversion.

In our study, the original detailed ice microphysics parameterization of Lin et al (1983) is used and only standard reflectivity is assumed available. As a result, our problem is more difficult because more water and ice species have to be determined and no dual polarization information is available. Yet, the EnKF scheme does not seem to have any serious difficulty. Fig. 3.3 shows the distribution of the perturbation water vapor and five categories of water substances for the truth run and for selected assimilation experiments. It can be seen that the EnKF data assimilation system is able to establish detailed microphysical structures that have very high fidelity. The quality of

actual analysis does depend on the usage and availability of data, as indicated quantitatively by the error plots discussed earlier.

To better understand the way the EnKF scheme works and the role of updating microphysical fields, we performed another experiment, named VrPnoIce, in which ice variables q_i , q_s , and q_h are not updated by the analysis and only radial velocity in precipitation regions are assimilated. The differences in error between VrPnoIce and VrP start to show from the third cycle and increase with successive cycles (Fig. 3.10). It can be seen that without the analysis update to these three variables, the *rms* error of q_s *analysis* is greater than even that of the ensemble-mean *forecast* of experiment VrP. The q_s field at 60 min (Fig. 3.3 (e3)) exhibits larger spatial coverage in VrPnoIce and is less accurate than that of VrP (Fig. 3.3 (e2)). The smaller difference in the earlier period reflects relatively weak link (through background error covariance) between V_r and these three variables. The link apparently becomes stronger and more effective in correcting errors in these fields at the later stage (as in the case of VrP). On the other hand, despite the lack of direct correction in VrPnoIce to q_i , q_s , and q_h , the errors in these fields are still reduced with time in general. Such reductions are achieved through model dynamics; when other model fields are improved, fields that are not directly updated have to adjust and become consistent with these fields. This points to the power of model-based dynamic data assimilation methods.

Further comparison of VrP and ZP helps us understand the interactions between the analyses of different variables. We see from Fig. 3.4, that the errors in the wind, temperature and pressure fields remain much higher in ZP case than in VrP for almost the entire assimilation period, with the differences being largest during the earlier

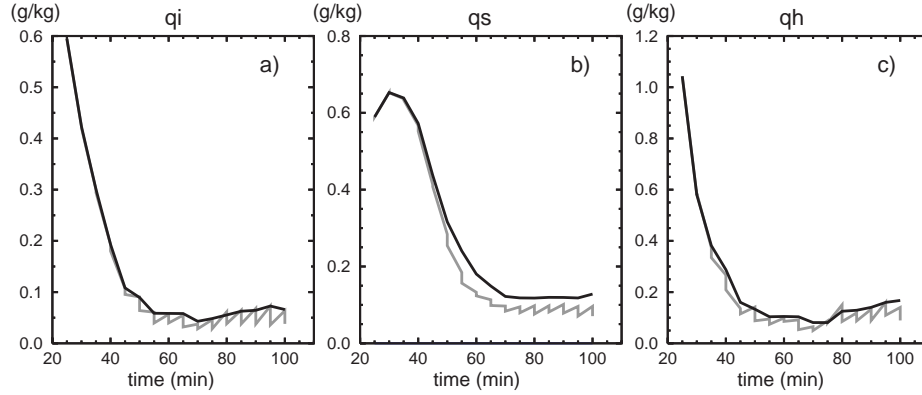


Fig. 3.10. RMS error of (a) q_i , (b) q_s , (c) q_h for VrP (gray) and VrPnoIce (black).

cycles. During this early period, the assimilation of reflectivity data in ZP is very effectively in reducing errors in q_h , q_s as well as in q_r while the generally poor analysis of the other fields is causing rapid increases in the forecast error. We note here that the fact that q_r , q_s and q_h are directly related to Z does not guarantee a good retrieval of them because without the help of error covariances offered by the EnKF scheme, the problem is underdetermined. When reflectivity data are combined with radial velocity data, very accurate microphysical fields can be retrieved (Fig. 3.2 and Fig. 3.3). With V_r data only (the case of VrP), the maximum value of q_h in Fig. 3.3(f2) is 5.73 g kg^{-1} at 60 min while the true value is 6.63 g kg^{-1} . If the ice hydrometeors are not updated when assimilating V_r (experiment VrPnoIce), the maximum is larger than 1 g kg^{-1} smaller than the truth. The addition of full-coverage reflectivity data (Fig. 3.3 (f5)) yields a maximum value of 6.37 g kg^{-1} that is closer to the truth.

3.4 Forecasts from ensemble-mean analyses

Since the goal of data assimilation is to provide a good initial condition for numerical weather prediction, in this section, we look at the quality of forecasts

produced from the analyses. Fig. 3.11 shows the truth and two forecasts over a 130 minute period that are initialized from the ensemble-mean analyses from experiments VrP and VrPZF at 80 min. Within the first 20 minutes (from 80 to 100 min), the forecast of VrPZF maintains most details of the storm very well, including the strength, structure and location of the updraft and the further splitting of the left mover. Within the first hour of forecast, the position of the right mover is forecast very accurately by experiment VrPZF. After that, the center of the right moving cell is displaced about 4 to 8 km eastward during its southeastward propagation. The forecast beginning from VrP roughly captures the evolution of the storm but not as accurately as in VrPZF. The right mover propagates southeastwards even faster than in VrPZF and reaches the southern boundary earlier; at 210 min., the structure of forecast storm is rather different from that of true one.

Fig. 3.12 shows the *rms* errors (averaged over the entire domain) of forecasts beginning from the ensemble-mean analyses of different times from experiments VrP and VrPZF. Generally, more accurate estimate of the initial condition yields better forecast. It can be seen that for all these forecasts, within the first 80 minutes, both the forecast error and the forecast error growth rate of VrPZF (black thick curves) is smaller than those of VrP (gray thin curves). For the forecasts starting from 80 min., a large difference is seen in rainwater at around 120 min between the forecast errors of these two experiments (Fig. 3.12c). Within the first 40 minutes of forecast, the q_r forecast error in VrP grows much faster than in VrPZF. The low-level rainwater was over-forecast by experiment VrP. For example, at 105 min, the maximum value of the forecast rainwater at 250 m AGL is 8.54 g kg^{-1} for experiment VrP, while that of the

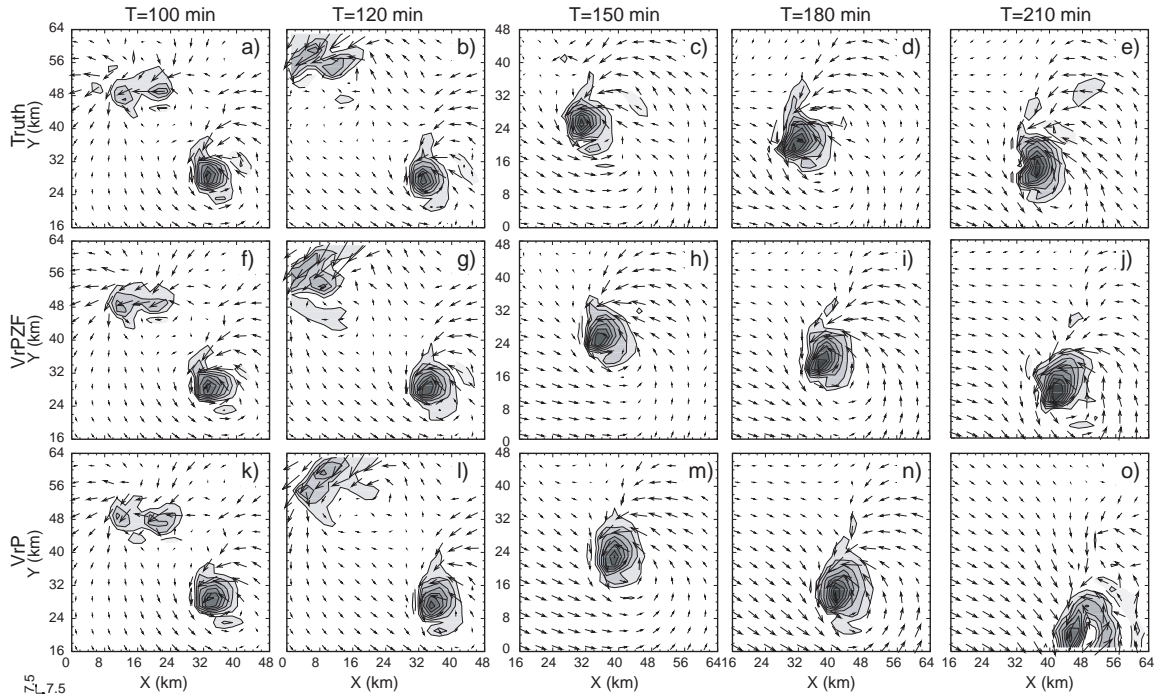


Fig. 3.11. Vertical velocity (contours and shading at intervals of 4 ms^{-1}) and horizontal wind (vectors; m s^{-1}) at 6 km level for (a)-(e) truth simulation and the forecast beginning from the ensemble-mean analysis at $t = 80 \text{ min}$: (f)-(j) forecast from ensemble-mean analysis of VrPZF, and (k)-(o) forecast from ensemble-mean analysis of VrP. Note the difference in the plotting domains before and after 150 min.

truth is only 5.91 g kg^{-1} (not shown). The low-level rainwater was also over-forecast by experiment VrPZF, but not as much. The forecast distribution of the rainwater in VrPZF is always closer to the truth than in VrP. The comparison of the forecast errors of these two experiments further verifies the benefit of assimilating reflectivity data in both precipitation and clear air regions. For forecasts starting from the ensemble-mean analysis of VrF (not shown here), the errors are smaller than those of VrP, but generally bigger than those of VrPZF within the 80 minutes of forecast.

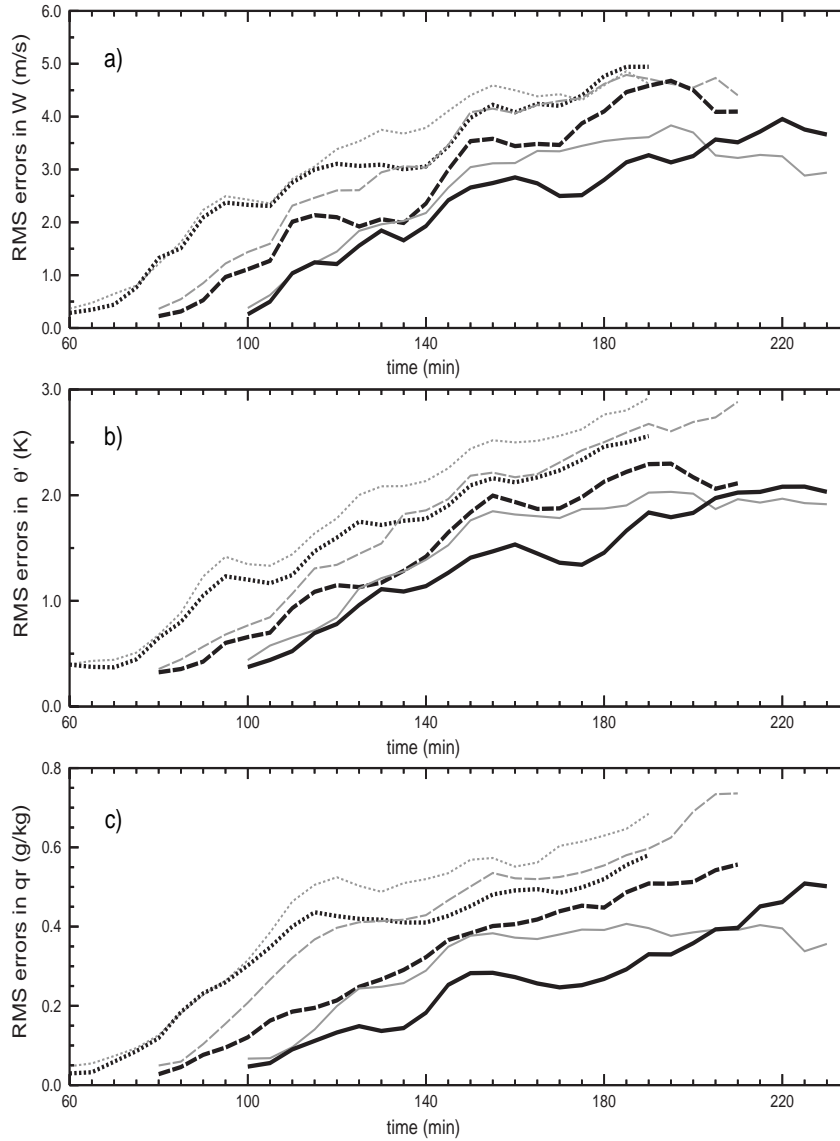


Fig. 3.12. The rms errors of forecasts averaged over the entire domain for: (a) w (m s^{-1}), (b) θ' (K) and (c) qr (g kg^{-1}). The forecasts begin from ensemble-mean analysis at $t = 60$ min (dot), $t = 80$ min (dash) and $t = 100$ min (solid) of experiment VrP (gray thin curves), VrPZF (black thick curves).

We note that for the forecasts starting from 100 min, the errors of VrPZF grow faster after 175 min and eventually become larger than those of VrP. This is found to be mainly associated with the slower southeastward propagation of the forecast storm in VrPZF than the true storm. Usually, phase error increases with the length of forecast. In

this case, the center of the updraft forecast by experiment VrPZF is located 2 to 8 km, or 1 to 4 grid intervals, north of the true storm during the last 50 minutes. The center of the updraft in VrP is closer to the true storm during the later forecast period. However, within the last 20 minutes phase error also occurs within VrP. The forecast storm moves faster than the true storm and the center of the updraft becomes displaced by 2 to 4 km to the south of the true storm. Still, the storm structure in VrPZF is better than that in VrP at this stage.

The success of the forecast depends not only on the accuracy of the analysis of storm, but also on the analysis of the storm environment. In our initial tests, in which the boundary zone is perturbed at the initial time of ensemble forecast, we obtained similarly good analyses. However, the forecasts from some of these analyses deteriorated quickly with time. In a forecast starting from analysis at 100 min, the right mover quickly decays and moves northeastward. We found in that case the low-level air was drier and the CAPE was reduced in the storm inflow region. Spurious cells triggered near the boundary in individual ensemble members contributed to this. Not perturbing the boundary at the initial time and the use of zero reflectivity information outside the precipitation regions helped alleviate the problem. For general applications, other means and data should be employed to ensure a good analysis of the storm environment, which for prediction purpose appears to be at least as important as the analysis of the storms themselves.

3.5 Summary and discussion

In this study we applied the ensemble Kalman filter technique to the assimilation of simulated radar radial velocity and reflectivity data, using a compressible model with a complex multi-class ice microphysics scheme. The inclusion of a complex multi-class ice microphysics has not been done before in either EnKF or 4DVAR assimilation of radar data. Doing so introduces additional model state (ice microphysics) variables that impose additional challenges to the retrieval problem. Previously published EnKF research did not carefully examine the impact of assimilating reflectivity data either, nor has attention been paid to the analysis quality of microphysical variables. Our work also represents the first time that a compressible model is used in the context of EnKF assimilation at the cloud scale.

The EnKF method is shown to have great potentials for the assimilation of such data and for thunderstorm prediction. Although the observation operator for the reflectivity data is nonlinear, which may lead to non-Gaussian error distribution and violate the basic assumptions of the Kalman filter algorithm, direct assimilation of reflectivity data is shown to provide positive impact overall on the analysis and subsequent forecast.

Flow-dependent forecast error covariances estimated from the ensemble states play a critical role in the assimilation process. Through them not only can the wind and thermodynamic fields be retrieved accurately, all five categories of cloud and hydrometeor variables can also be retrieved successfully. Compared to 4DVAR, the EnKF is a much easier yet effective method to obtain microphysical fields that are compatible with the model dynamics, thermodynamics and microphysics. Compared to

early efforts that insert radar observations directly into numerical models without the use of covariance information (e.g., Liou et al. 1991), the EnKF method enjoys a much greater success. The importance of spatial covariance information is further supported by that fact that worse analysis is obtained when the effective radius of covariance localization is too small (results not shown).

Reliable and dynamically consistent multivariate covariances between the observed quantities and the state variables not directly related to them can be obtained after a few assimilation cycles, even when the ensemble is started from initial guesses made of an environmental sounding plus random perturbations. Spatial covariance structures are shown to be dynamically consistent. After the initial two to three cycles, useful observational information can be spread in space and to indirectly related variables. Delaying the update of indirectly related variables until after first few cycles when assimilating reflectivity data produces the best analysis. Using reflectivity information in clear air regions is very beneficial in suppressing spurious storms (assuming that the radar network provides a complete spatial coverage). The forecast initiated from the ensemble-mean analysis using V_r and full coverage reflectivity data is shown to be the best within about 80 minutes of all three forecasts presented. We should point out here if the EnKF assimilation system is run in a continuously-cycled mode, as an operational system should be, or if the ensemble is initialized in a more physical way, such as using the breeding method (Toth and Kalnay 1997), then the delay in updating indirectly related variables may not be necessary.

The EnKF data assimilation results reported here used 100 ensemble members. We found that 40 ensemble members are enough to produce good analysis result, except

that the filter convergence rate is a little slower. With 40 members, the radius of the data influence region needs to be smaller. A radius of 6 km is found to produce the best result in this case.

Snyder and Zhang (2003) noted that the results of their EnKF experiments were subject to some random variability associated with the specific realizations of the initial ensemble and observation errors. In this study, we have repeated some of the experiments with different realizations and we did not notice any significant deviation from the results reported here in terms of the error characteristics. The larger ensemble size used here may account for some of the reduced variability.

For larger applications, the analysis algorithm needs to be parallelized for distributed-memory parallel platforms. For our current application, we used shared-memory parallelization via OpenMP for the computation of the background error covariance $\mathbf{P}^f \mathbf{H}^T$, which is the most expensive part of the algorithm. Four processors of IBM Regatta (model p-690) give a speedup of 3.5 for the analysis. The ensemble forecasts were distributed among a number of processors.

Finally, we note that caution should be used when interpreting OSSE results. Both forecast model and forward observation operators are assumed perfect in the current work. The effects of model error need to be studied in the future. Much work is still needed in moving us in the direction of real case and real data. We also mention that similar set of assimilations using square-root EnKF, which does not perturb the observations (as used in, e.g., Snyder and Zhang 2003), has also been conducted with generally similar conclusions.

Chapter 4

Simultaneous Estimation of Microphysical Parameters and Atmospheric State with Radar Data and Ensemble Square-root Kalman Filter: Sensitivity Analysis and Parameter Identifiability

4.1 Introduction

The accuracy of numerical weather prediction (NWP) depends very much on the accuracy of the initial state estimation and the accuracy of the prediction model. Various advanced data assimilation techniques have been developed in the recent decades that improve the estimation of model initial conditions. Among these methods are the four-dimensional variational assimilation (4DVAR) (Le Dimet and Talagrand 1986; Courtier and Talagrand 1987) and the ensemble-based assimilation methods (Evensen 1994; Evensen and van Leeuwen 1996; Burgers et al. 1998; Houtekamer and Mitchell 1998; Bishop et al. 2001; Anderson 2001; Whitaker and Hamill 2002; Evensen 2003; Tippett et al. 2003), which have the advantage of closely involving a numerical model in the data assimilation process. However, errors in the model can directly affect the effectiveness of these data assimilation methods.

For convective-scale NWP, explicit microphysics schemes are used to predict the evolution of clouds and precipitation. Most microphysics schemes use the 'bulk' approach of parameterization, in which the particle or drop size distributions (DSDs) are parameterized in functional forms. Often, significant uncertainties exist with the treatment of the microphysical processes and the microphysical parameters. McCumber *et al.* (1991) tested the sensitivity of tropical convective system simulations to the changes in size distribution parameters. Ferrier *et al.* (1995) also performed a microphysical parameter sensitivity study when simulating squall systems in the mid-latitude and tropical environments. More recently, Gilmore *et al.* (2004) examined the precipitation uncertainty of simulated midlatitude multicell and supercell storms due to uncertainties inherent in the parameters defining the hail/graupel distribution. The sensitivity of simulated supercell storms to hail size distributions was also investigated by van den Heever and Cotton (2004) by systematically varying the mean hail diameter. All these studies demonstrate that the structure and evolution of simulated convective systems are very sensitive to microphysical parameterizations. Variations in microphysical parameters, such as collection efficiencies, DSD parameters and particle densities, have profound effects upon the characteristics of precipitation systems and their associated dynamical processes.

Because of many assumptions involved, the microphysical parameterization can be an important source of model error for convective-scale data assimilation and prediction. Parameter estimation is a common approach to dealing with model error associated with uncertain parameters. The inverse problem of parameter estimation concerns with the optimal determination of the parameter by observing the dependent

variable(s) collected in the spatial and time domains (Yeh 1986). Various methods have been used for parameter estimation, among which variational parameter estimation with an adjoint model is popular in the literature of meteorology and oceanography (Navon 1997). The ensemble Kalman filter method has recently been tested successfully for the atmospheric state estimation or data assimilation at the convective scale with simulated radar data (Snyder and Zhang 2003; Zhang et al. 2004; Tong and Xue 2005a; Xue et al. 2006) and real radar data (Dowell et al. 2004). The results with simulated data, under the perfect model assumption, have been excellent, while the quality of state estimation with real data, when model error inevitably exists, is generally not as good (Dowell et al. 2004). More recently, Aksoy *et al.* (2006) used EnKF for the simultaneous estimation of state variables and model parameters in a relatively simple two-dimensional sea-breeze model with encouraging success.

In this study, we set out to investigate the ability of the EnKF in correcting the errors in some of the fundamental parameters in model microphysics, where complex process interactions and high nonlinearities usually exist. In the framework of EnKF, parameter estimation is realized by treating the uncertain parameters as independent model variables and using the covariance information sampled from the ensemble to estimate the parameters given available observations (Anderson 2001). Such a technique is often referred to as state vector augmentation. Parameter estimation through state vector or control variable augmentation can also be performed using variational methods, as discussed earlier. Recently, Crook and Sun (2004) applied the 4D variational method to the retrievals of a multiplier in the rain terminal velocity and the rain water evaporation rate.

The well-posedness as well as parameter identifiability are the main issues that are directly related to the possibility of successful parameter estimation, no matter what technique is used. The inverse problem for parameter estimation is often ill-posed (Chavent 1974; Yakowitz and Duckstein 1980). As was reviewed by Yeh (1986), the ill-posedness is generally characterized by the nonuniqueness and instability of the identified parameters. In the case of nonuniqueness, the identified parameters will differ according to the initial estimate of the parameters, and there is no guarantee that the estimated parameter will be close to its “true” value. The instability of the inversion solution stems from the fact that small errors in the observations will cause serious errors in the identified parameters. Yakowitz and Duckstein (1980) demonstrated that a small sensitivity of the model output in terms of observations to the change of unknown parameters (parameters to be estimated) implies identification instability. The problem is that a larger difference in the parameter may be manifested by only very small changes in the model output of observations, which may be smaller than anticipated measurement error.

As the first part of this parameter estimation study, we investigate the possibility of retrieving some microphysical parameters with the EnKF method through a detailed sensitivity analysis. The issue of parameter identifiability will be addressed. The results will guide us to best design the parameter estimation experiments and will also help us validate our parameter retrieval results. The microphysical parameters chosen for this study are the intercept parameters of rain, snow, and hail/graupel size distributions, and the bulk densities of hail/graupel and snow. These parameters have been shown by the sensitivity studies referenced earlier to have significant effect on the precipitation

processes and dynamics of convective storms. Other model parameters are assumed to be correct.

This chapter is organized as follows. In Section 4.2, we briefly describe the microphysics scheme and its limitations, which partly motivate this study. The uncertainties of the chosen microphysical parameters based on previous observational studies will also be discussed. Section 4.3 briefly describes the numerical model, the simulation configuration for a supercell thunderstorm and the experimental setup for sensitivity analysis. Section 4.4 discusses the results of sensitivity analysis. The parameter identifiability issue is addressed in section 4.5. Summary and conclusions are given in Section 4.6. Results of the parameter estimation experiments will be presented in Chapter 5.

4.2 Microphysics description

4.2.1 Microphysics scheme

The ice microphysics scheme in the ARPS (Xue et al. 2000; Xue et al. 2001; Xue et al. 2003) model used by this study is a 5-class (cloud water, rain, cloud ice, snow and hail/graupel) single-moment bulk scheme after Lin et al. (1983, hereafter LFO83). The scheme assumes that the drop size distributions (DSD) of rain, snow and hail/graupel have an exponential form:

$$n_x(D) = n_{0,x} \exp(-\lambda_x D_x), \quad (4.1)$$

where x represents r (rain), s (snow) or h (hail), for particular hydrometeor species. The same form of exponential DSD is also assumed for non-precipitating cloud water and

cloud ice. $n_x(D)\delta D$ in Eq. (4.1) is the number of drops per unit volume between diameters D and $D+\delta D$ and n_{0x} is the so-called intercept parameter, which is the value of n_x for $D = 0$. The slope parameter, which equals to the inverse of the mean size diameter of each distribution, is diagnosed as:

$$\lambda_x = \left(\frac{\pi \rho_x n_{0x}}{\rho q_x} \right)^{0.25}, \quad (4.2)$$

where ρ_x is the constant particle bulk density, ρ is the air density and q_x is the hydrometeor mixing ratio.

With single-moment bulk microphysics schemes, only one moment of the DSD functions is predicted. In the LFO83 scheme, as well as almost all single-moment schemes, the mixing ratio of each hydrometeor, which is proportional to the third moment of the DSD function, is predicted and the intercept parameter n_{0x} is a prescribed constant. It can be seen from Eqs. (4.1) and (4.2) that the DSD is a function of two adjustable parameters n_{0x} and ρ_x . For a given mixing ratio q_x , the larger is the intercept parameter or the density, the more the hydrometeor spectrum is weighted towards smaller drops (Fig. 4.1). For model simulations, adjusting these parameters can directly impact the bulk terminal velocity and the number concentration of species, which can result in the change of the trajectories of the hydrometeors within the cloud and the particle growth rates. These changes in the microphysical processes will affect the water budgets within the cloud and hence the latent heating and hydrometeor loading, which in turn lead to the changes of the buoyancy and subsequent updraft and downdraft patterns.

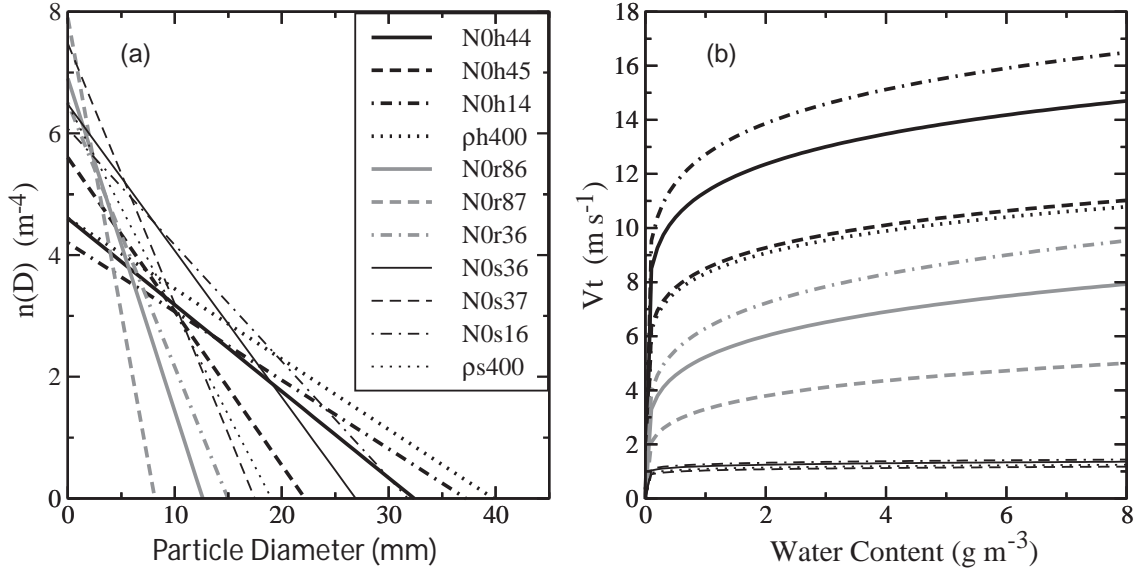


Fig. 4.1. (a) Number concentration per mm diameter size and (b) mass-weighted mean terminal velocity of rain (for N0r87: $n_{0r} = 8 \times 10^7 \text{ m}^{-4}$, N0r86: $n_{0r} = 8 \times 10^6 \text{ m}^{-4}$ and N0r36: $n_{0r} = 3 \times 10^6 \text{ m}^{-4}$), snow (for N0s37: $n_{0s} = 3 \times 10^7 \text{ m}^{-4}$, N0s36: $n_{0s} = 3 \times 10^6 \text{ m}^{-4}$, N0s16: $n_{0s} = 1.19 \times 10^6 \text{ m}^{-4}$ and ρ_s400 : $\rho_s = 400 \text{ kg m}^{-3}$) and hail/graupel (for N0h45: $n_{0h} = 4.0 \times 10^5 \text{ m}^{-4}$, N0h14: $n_{0h} = 1.59 \times 10^4 \text{ m}^{-4}$, N0h44: $n_{0h} = 4 \times 10^4 \text{ m}^{-4}$ and ρ_h400 : $\rho_h = 400 \text{ kg m}^{-3}$). The terminal velocities are calculated for an air density of 1.0 kg m^{-3} . The default values of the microphysical parameters are $n_{0r} = 8 \times 10^6 \text{ m}^{-4}$, $n_{0s} = 3 \times 10^6 \text{ m}^{-4}$, $n_{0h} = 4 \times 10^4 \text{ m}^{-4}$, $\rho_h = 913 \text{ kg m}^{-3}$ and $\rho_s = 100 \text{ kg m}^{-3}$ unless otherwise indicated by the curve legends.

With the use of prescribed parameters, typical single-moment microphysics schemes generally cannot adequately represent convective clouds within various types of precipitation systems. For example, the parameterization of the LFO83 scheme is formulated for the intense continental storms with the presence of high-density hails, while the somewhat similar scheme of Rutledge and Hobbs (Rutledge and Hobbs 1984) is more suitable for oceanic systems. The differences come from either the treatment of the microphysical processes and/or the use of different parameters, such as those of hydrometeor density and DSD intercept.

More sophisticated bulk microphysics schemes try to overcome the above limitations by predicting more than one moment of the distribution function and/or dividing the hydrometeors into more categories. By predicting two moments (Ziegler 1985; Murakami 1990; Ferrier 1994; Meyers et al. 1997; Cohard and Printy 2000) or three moments (Milbrandt and Yau 2005a, b) of the distribution function, the DSD parameters are effectively treated as prognostic variables rather than being prescribed as constants. More recently, Straka and Mansell (2005) developed a single-moment bulk microphysics scheme with ten ice categories, which allows for a range of particle densities and fall velocities for simulating a variety of convective storms with less need for parameter tuning.

Although sophisticated microphysical schemes are attractive and represent the future direction of convective-scale modeling and NWP, they are expensive and much research is still needed before they can be widely used. The increased number of prognostic variables in the model also poses a larger problem for state estimation or model initialization. The single-moment bulk schemes are widely used in current research and operational models; the ultimate goal of our current line of study is therefore to overcome, to the extent possible, the shortcomings of such single-moment schemes by constraining uncertain microphysical parameters using data, i.e., by estimating the parameters as well as the model state variables using radar observations.

4.2.2 Uncertainties in the microphysical parameters

The parameters selected for this study are the intercept parameters of rain, snow and hail/graupel DSDs, and the densities of snow and hail. Observational and sensitivity

studies indicate that the coefficients associated with the formula for hydrometeor fall speeds and the collection efficiency parameters are also uncertain and can affect the microphysical processes significantly. In this study, we focus on the density and intercept parameters, because they are more fundamental and directly affect a large number of processes in the microphysics parameterization.

As pointed out earlier, with the LFO83 single-moment bulk microphysics scheme, the intercept parameters and the bulk densities of snow and hail are assumed to be constant in space and time. The default values of the intercept parameters for rain, snow and hail size distributions in the ARPS model are $8 \times 10^6 \text{ m}^{-4}$, $3 \times 10^6 \text{ m}^{-4}$ and $4 \times 10^4 \text{ m}^{-4}$, respectively, following LFO83. The densities of rainwater, snow and hail are specified to be 1000 kg m^{-3} , 100 kg m^{-3} and 913 kg m^{-3} , respectively (see Table 4.1).

A number of observational studies indicate that the intercept parameters of hydrometeor distributions can vary widely among precipitation systems occurring in different large-scale environments. The observed hail/graupel intercept parameter, n_{0h} , as reviewed by Gilmore *et al.* (2004), ranges from 10^2 m^{-4} to greater than 10^8 m^{-4} . Observed snow intercept parameter, n_{0s} , varies from 10^5 m^{-4} to 10^8 m^{-4} (Gunn and Marshall 1958; Passarelli 1978; Houze *et al.* 1979; Lo and Jr. 1982; Mitchell 1988; Braham 1990). Joss and Waldvogel (1969) found that n_{0r} varies between 10^6 m^{-4} and 10^8 m^{-4} . A number of studies have shown a systematic decrease in n_{0r} as precipitation changed from convective to stratiform (Waldvogel 1974; Tokay *et al.* 1995; Tokay and Short 1996; Cifelli *et al.* 2000).

Parameter p_i	\underline{p}_i	\bar{p}_i	True (control) values of parameters, p_i^t
Hail/graupel intercept n_{0h} (m^{-4})	4×10^3	4×10^6	4×10^4
Snow intercept n_{0s} (m^{-4})	5×10^5	1×10^8	3×10^6
Rain intercept n_{0r} (m^{-4})	3×10^6	8×10^7	8×10^6
Density of hail/graupel ρ_h (kg m^{-3})	400	913	913
Density of snow ρ_s (kg m^{-3})	20	400	100

Table 4.1 A summary of the uncertainty ranges, defined by the lower bound \underline{p}_i and upper bound \bar{p}_i , and the true (control) values for intercept parameters n_{0h} , n_{0s} , n_{0r} , and hail and snow densities ρ_h and ρ_s used in this study.

In the LFO83 scheme, the term hail is used loosely to represent high-density graupel, ice pellets, frozen rain and hailstones. According to Pruppacher and Klett (1978), the bulk density of hail has been found to vary between 700 kg m^{-3} and 900 kg m^{-3} and the observed density of graupel ranges from 50 kg m^{-3} to 890 kg m^{-3} . The term snow in the LFO83 scheme is used to represent snow crystals, snowflakes and low-density graupel particles. Graupel is a densely rimed snow crystal or aggregate and falls about 2 times faster than dry snow (Judson and Doesken 2000). Snow density varies greatly from one snow event to the next. The density of freshly fallen snow observed in literature varies from 10 kg m^{-3} to approximately 350 kg m^{-3} (Judson and Doesken 2000).

All these indicate that there exist great uncertainties with the values of the intercept and density parameters, and assuming same values for all precipitation events can lead to significant errors in the prediction model. Estimating their values for specific events using data is likely to significantly reduce such errors or uncertainties.

4.3 Model and experimental settings

4.3.1 The prediction model and truth simulation

The forecast model used in this study and the truth simulation are inherited from Chapter 3. Briefly, the ARPS (Xue et al. 2000), a fully compressible and nonhydrostatic atmospheric prediction system is used, and the model contains 12 prognostic state variables, including three velocity components u , v , w , potential temperature θ , pressure p , the mixing ratios for water vapor q_v , cloud water q_c , rainwater q_r , cloud ice q_i , snow q_s and hail q_h , plus the turbulence kinetic energy used by the 1.5-order subgrid-scale turbulence closure scheme.

The truth simulation is for the May 20, 1977 Del City, Oklahoma supercell storm case (Ray et al. 1981; Xue et al. 2001). The physical model domain is $64 \times 64 \times 16$ km³. The grid spacing is 2 km in the horizontal directions and 0.5 km in the vertical. A sounding of 3300 J kg⁻¹ CAPE is used to define the environmental condition and a 4 K ellipsoidal thermal bubble is used to initiate the storm. Open conditions are used at the lateral boundaries. Free-slip conditions are applied to the top and the bottom boundaries. A constant wind of $u = 3$ m s⁻¹ and $v = 14$ m s⁻¹ is subtracted from the observed sounding to keep the primary storm cell near the center of model grid. More detailed information about the natural run or truth simulation can be found in Chapter 3. The actual sounding used by the truth simulation can be found in Xue et al. (2001) and the general evolution of the storm is similar to that documented there. The default values of the microphysical parameters in the model are predetermined to be the true values and are used in the truth simulation (Table 4.1).

4.3.2 Experimental design for sensitivity analysis

In this study, the forward method is used for sensitivity analysis (Crook 1996). For each parameter, we perform a set of sensitivity experiments, within which only the parameter considered is varied within its range of uncertainty while all other model parameters are set to be their true values. The true values of the microphysical parameters are used in the control experiment (CNTL). We first examine the influence of each of the five parameters on the model simulation. Then we estimate the influence of the parameter values on the model state estimation via the ensemble square-root filter (EnSRF, Whitaker and Hamill 2002) algorithm and deduce the limits within which the model parameters may be estimated. The EnSRF is a variation of the standard EnKF, which does not require perturbing the observations. The particular configurations of radar data assimilation using the EnSRF algorithm are described in Chapter 5.

Suppose $\mathbf{p} = (p_1, p_2, \dots, p_5)^T = (n_{0r}, n_{0s}, n_{0h}, \rho_s, \rho_h)^T$ is the vector of the uncertain microphysical parameters. An admissible set P_{ad} of \mathbf{p} based on the parameter range can be defined as

$$P_{ad} = \{p \mid \underline{p}_i \leq p_i \leq \bar{p}_i, i = 1, 2, \dots, 5\}, \quad (4.3)$$

where \underline{p}_i and \bar{p}_i are the lower and upper bounds of the i th parameter. The values of \underline{p}_i and \bar{p}_i applied in this study can be found in Table 4.1. The admissible set P_{ad} of \mathbf{p} given in Table 4.1 may not span all observed parameter values that might have appeared in the literature. For example, for the q_h category, we do not chose any value for intercept parameter n_{0h} that is larger than $4 \times 10^6 \text{ m}^{-4}$ (corresponding to small graupel

cases). For the q_s category, we do not allow it to represent high-density snow or graupel so that the density of snow, ρ_s , is no larger than 400 kg m^{-3} . Part of the reason is that we are not adjusting other related microphysical parameters accordingly, such as the coefficients in the terminal velocity equations for the precipitating hydrometeors, and we want to keep the parameter values physically reasonable. For the purpose of this study, limiting the admissible ranges of some of the parameters, when they are changed alone, makes sense.

The parameter estimation problem consists of finding an estimated value $\hat{\mathbf{p}}$ of \mathbf{p} from information taken from the observations, the parameter-to-observation mapping, and the prior information about the parameters. The problem can often be constructed as finding $\hat{\mathbf{p}} \in P_{ad}$, such that $J(\hat{\mathbf{p}}) \leq J(\mathbf{p}) \quad \forall \mathbf{p} \in P_{ad}$. $J(\hat{\mathbf{p}})$ here is the output criterion, which is generally the minimization of a “norm” of the difference between the observations and the model output of observations. Therefore, in this study, we are especially interested in the sensitivity of the model output, in the forms of observations, to the microphysical parameters. The response function for the sensitivity analysis is therefore defined as

$$J_\eta(\mathbf{p}) = \frac{1}{\sigma_\eta^2} \sum_{i=1}^M (\eta_i(\mathbf{p}) - \eta_i^*)^2, \quad (4.4)$$

where $\eta_i(\mathbf{p})$ and η_i^* are, respectively, the model solution in the form of observation and the corresponding observation. The observations in the current case contain the simulated observations of radial velocity V_r and/or reflectivity Z . The forward observation operators that project the model state to the observations will be described

in Chapter 5. The observation errors are included by adding random errors to the ‘error-free’ observations to give

$$\mathbf{V}_r^* = \mathbf{V}_r(\mathbf{x}^t, \mathbf{p}^t) + \sigma_{V_r} \mathbf{v}, \quad (4.5)$$

$$\mathbf{Z}^* = \mathbf{Z}(\mathbf{x}^t, \mathbf{p}^t) + \sigma_Z \mathbf{v}, \quad (4.6)$$

where \mathbf{v} represents the Gaussian random variable vector with zero mean and unit standard deviation and σ_{V_r} and σ_Z are the standard deviations of the observation errors added to V_r and Z , respectively. In this study, the relative sensitivity of the model output of V_r and Z with respect to the five parameters will be compared, which will help us decide the right data to use for parameter estimation. To facilitate the comparison, the difference between the model output of V_r or Z and the simulated observation is normalized by the estimated observation *rms* error σ_{V_r} or σ_Z . The summation in Eq. (4.4) is over the data points where reflectivity is greater than 0 dBZ.

The response function defined in Eq. (4.4) is calculated for each sensitivity experiment and for the control experiment. For data assimilation sensitivity experiments, the ensemble mean of the analyzed model state at each analysis time is used to calculate $\eta_i(\mathbf{p})$. To reveal the relative effect of model error associated with uncertain microphysical parameters on the analysis, the actual response function presented for analysis is

$$\Delta J_\eta(\mathbf{p}) = J_\eta(\mathbf{p}) - J_{\eta,c}(\mathbf{p}^t), \quad (4.7)$$

where $J_{\eta,c}(\mathbf{p}^t)$ is the response function calculated from the control data assimilation experiment.

4.4 Results of Sensitivity Analysis

In this section, we examine the sensitivity of the pure model prediction and of the EnSRF state estimation to the microphysical parameters that we intend to estimate. As discussed earlier, a sufficient level of sensitivity is necessary for successful parameter estimation.

4.4.1 Sensitivity of pure forecast to microphysical parameters

Fig. 4.1 shows the variations of J_{V_r} and J_Z against the deviation of the parameters from their true values. The response functions are calculated from the output of pure model forecast (without data assimilation) every 5 minutes and averaged over the expected data assimilation window, i.e. from 25 min to 100 min. These forecasts start from true atmospheric state at 20 minutes with parameter errors introduced at the same time. The observational data used in calculating the response functions are extracted from the truth simulation and are ‘error-free’, i.e., they are $\mathbf{V}_r(\mathbf{x}^t, \mathbf{p}^t)$ and $\mathbf{Z}(\mathbf{x}^t, \mathbf{p}^t)$ defined in Section 4.3.2. The microphysical parameters are expressed in logarithmic form since most of them can vary by more than an order of magnitude. The symbols on each curve represent parameter values sampled from P_{ad} . It is stated that V_r or Z is more sensitivity to one parameter than the other if the same amount of change in the parameter value causes more change in the response function from that of the truth simulation.

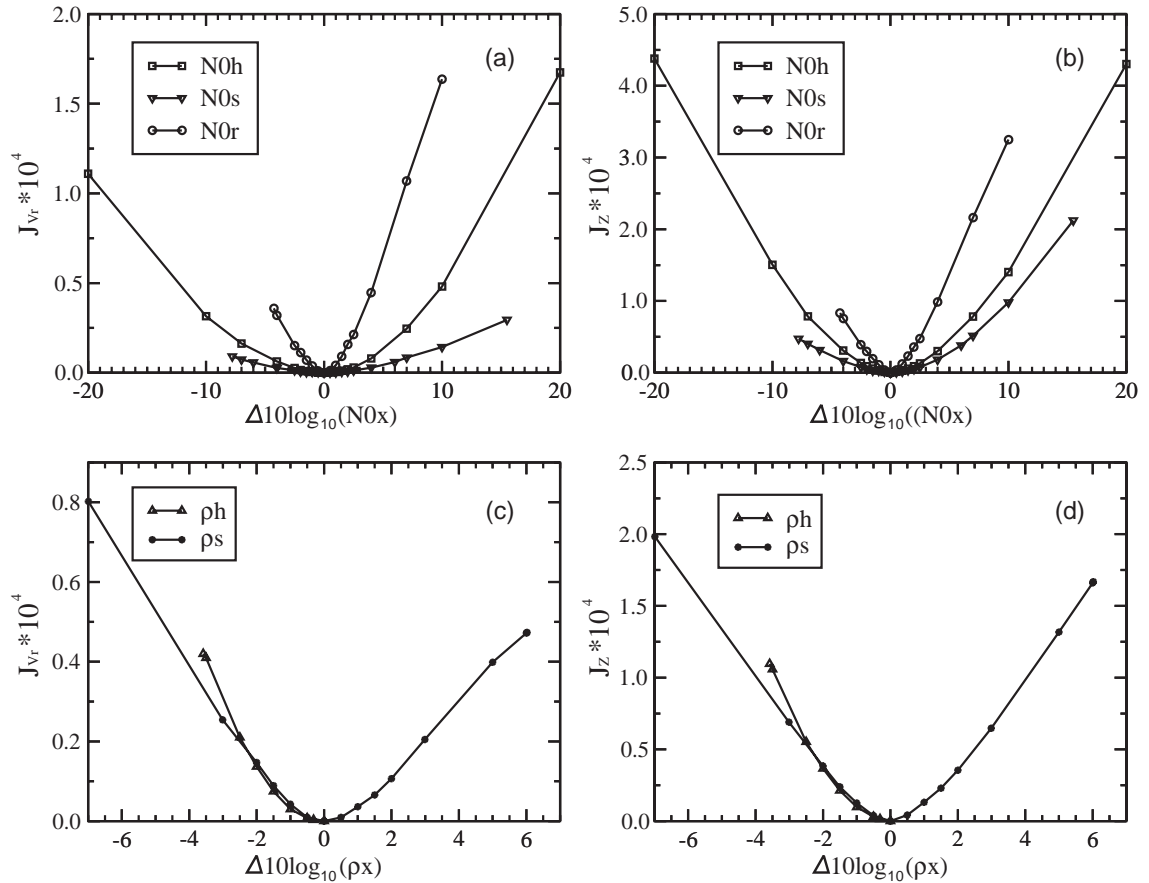


Fig. 4.2. The variations of the response function J for radial velocity (left panels) and reflectivity (right panels), plotted against the logarithmic-form deviations of the parameters from their true values for the simulation sensitivity experiments. The response functions are calculated using ‘error-free’ observations.

As can be seen from Fig. 4.2, model reflectivity shows a much stronger sensitivity to all five parameters than model radial velocity. We note here that in this study, the reflectivity formulation is assumed to be perfect, i.e., the correct values of the intercept parameters and densities from the control simulation are used in simulating the reflectivity data and during the data assimilation. The reflectivity formulation used is similar to that used in Tong and Xue (2005) and will be further described in Chapter 5.

For the three intercept parameters, at $\Delta 10 \log(n_{0x}) = 10$, or when the intercept parameters are an order of magnitude larger than their control values, J_Z is larger than J_{V_r} by a factor of 2.1 for n_{0r} , a factor of 3.5 for n_{0h} and a factor of 7.7 for n_{0s} (Fig. 4.2a, b). For the densities of hail and snow, at $\Delta 10 \log(\rho_x) = -2$, J_Z is larger than J_{V_r} by a factor of 3. This is not surprising because the microphysical fields are more directly affected by microphysical parameterization than the velocity field. The larger sensitivity of Z to the microphysical parameters suggests that Z data should be more useful for microphysical parameter estimation.

With respect to the three intercept parameters, both radial velocity and reflectivity show the largest sensitivity to the intercept of rain and the smallest sensitivity to the intercept of snow. With a change of +5 in the three logarithmic-form intercept parameters, which corresponds to $n_{0r} = 2.53 \times 10^7 \text{ m}^{-4}$, $n_{0s} = 9.49 \times 10^6 \text{ m}^{-4}$ and $n_{0h} = 1.26 \times 10^5 \text{ m}^{-4}$, the variation of J_Z due to the change in n_{0r} is more than twice as large as that due to the change in n_{0h} (Fig. 4.2b) and the corresponding variation of J_{V_r} due to the change in n_{0r} is more than 3 times larger than that due to the change in n_{0h} (Fig. 4.2a). Both radial velocity and reflectivity show comparable sensitivity to ρ_s and ρ_h , when $-2.5 \leq \Delta 10 \log(\rho_x) \leq 0$, and larger sensitivity to ρ_h when $\Delta 10 \log(\rho_x) < -2.5$ (Fig. 4.2c and d).

4.4.2 Sensitivity of the distribution of hydrometeors to the microphysical parameters

To better understand how the model simulated supercell storm is influenced by varying the microphysical parameters and how such changes affect reflectivity, which is observed, we now examine the variation of the microphysical fields due to the change of the parameters. In addition to the control simulation, two sensitivity experiments will be presented for each of the five parameters. For each of three intercept parameters, the two values are chosen such that $\Delta 10 \log(n_{0x}) = 10$ and $= -4$, respectively. For the densities of hail and snow, one sensitivity experiment has $\Delta 10 \log(\rho_x) = -2$, and the other has the lower bound value of ρ_h and the upper bound value of ρ_s , respectively (Table 4.2). Fig. 4.3 shows the vertical profiles of the time-averaged hydrometeor mixing ratios for the ten forecast sensitivity experiments plus those of the control simulation.

As the hail intercept n_{0h} increases (decreases) or the hail density ρ_h decreases (increases), the hydrometeor species have a similar trend of variations (Fig. 4.3a, f, d and i). The variation in the hydrometeors due to the increase by one order of magnitude in n_{0h} is generally larger than that caused by the decrease of ρ_h from its upper bound to the lower bound. Among the five hydrometeor species, q_s and q_h have the largest sensitivity to hail parameters n_{0h} and ρ_h .

Larger hail intercept or smaller hail density results in more q_h aloft and less q_s in the anvil of the storm (Fig. 4.3a, d and Fig. 4.4e, n). Also, in both cases, more q_r and q_i

Parameter	Larger deviation			Smaller deviation		
	Expt.	p_i	$\Delta 10 \log_{10}(p_i)$	Expt.	p_i	$\Delta 10 \log_{10}(p_i)$
n_{0h} (m ⁻⁴)	N0h45	4×10^5	10	N0h14	1.59×10^4	-4
n_{0s} (m ⁻⁴)	N0s37	3×10^7	10	N0s16	1.19×10^6	-4
n_{0r} (m ⁻⁴)	N0r87	8×10^7	10	N0r36	3.18×10^6	-4
ρ_h (kg m ⁻³)	$\rho_h 400$	400	-3.58	$\rho_h 576$	576	-2
ρ_s (kg m ⁻³)	$\rho_s 400$	400	6	$\rho_s 63$	63	-2

Table 4.2. List of the parameters values, p_i , and the logarithmical deviations of these parameters from their control values, $\Delta 10 \log_{10}(p_i)$, in the simulation and assimilation sensitivity experiments. The parameter that is changed from its control value is listed for the corresponding sensitivity experiment while other parameters used the control values.

can be found in the storm. It can be seen from Fig. 4.1 that increasing n_{0h} or decreasing ρ_h results in higher number concentrations and smaller terminal fall speed of hail. Reduced terminal velocity results in more q_h being suspended aloft. Comparing Fig. 4.4b with Fig. 4.4e and Fig. 4.4n, we can see that more q_h is present at higher altitudes. In both experiments N0h45 and $\rho_h 400$, one more maximum q_h center appears at around 7 km in addition to the maximum center at about 5 km AGL. We can also see that out of the updraft core, more q_h are horizontally advected into the anvil region. The longer residence time of q_h aloft results in more collection of snow in the updraft region and lower amounts of snow being transported to the anvil region. Because of the slower fall speed, less q_h and q_r within the convective core reach the ground after the storm becomes mature. The increase in q_r at the low levels (Fig. 4.3a, d) is mainly due to the

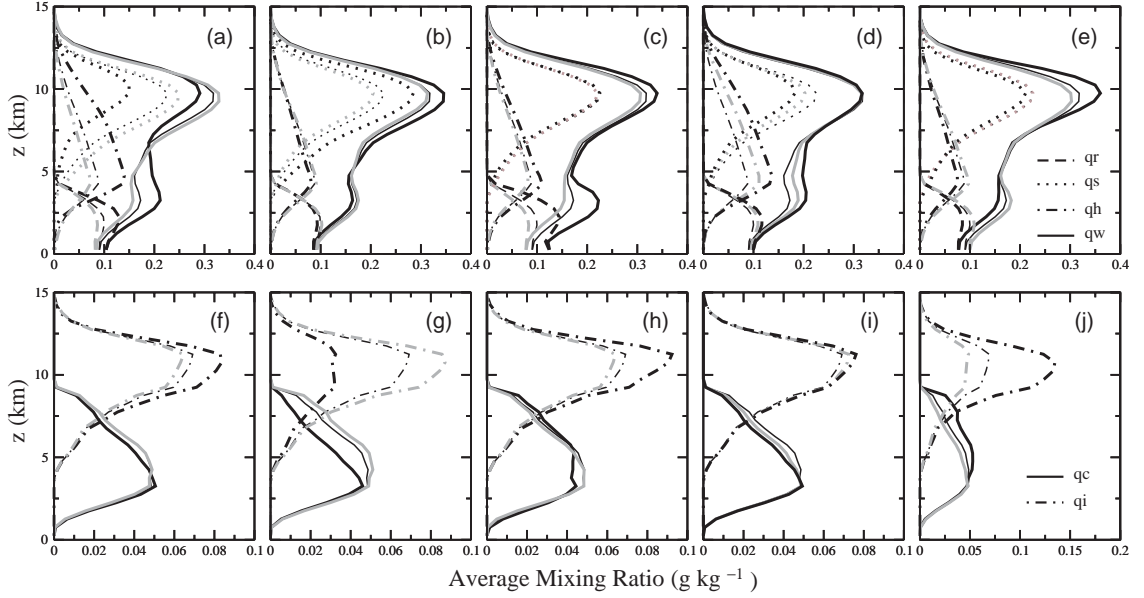


Fig. 4.3. Temporally and spatially averaged mixing ratios (g kg^{-1}) as a function of height for control simulation (thin black curves) and for simulations N0h45 (thick black) and N0h14 (thick gray) (a and f); N0s37 (thick black) and N0s16 (thick gray) (b and g); N0r87 (thick black) and N0r36 (thick gray) (c and h); ρ_h400 (thick black) and ρ_h576 (thick gray) (d and i); and ρ_s400 (thick black) and ρ_s63 (thick gray) (e and j). Temporal averaging was performed upon data output at 5-min intervals from $t = 25$ to 100 min. Spatial averaging was performed horizontally over all grid points in the $64 \text{ km} \times 64 \text{ km}$ horizontal domain.

increased q_h in the anvil region and more hails/graupels are converted to raindrops after they fall below melting level from the anvil. Therefore, larger hail intercept or smaller hail density results in stronger reflectivity within the anvil precipitation region (Fig. 4.4c, f, o). The increase of q_i at high levels especially for the larger hail intercept case, N0h45 (Fig. 4.3f), is probably caused by the depletion of snow by hail/graupel and the fact that less cloud ice is accreted by snow. Finally, q_w increases (decreases) between 2.5 km and 7 km, when n_{0h} increases (decreases) or ρ_h decreases (increases), which is mainly due to the increase (decreases) in q_h at the middle level. Above 7 km, the amount of q_w is less sensitive to ρ_h than to n_{0h} , mainly because the amount of change in

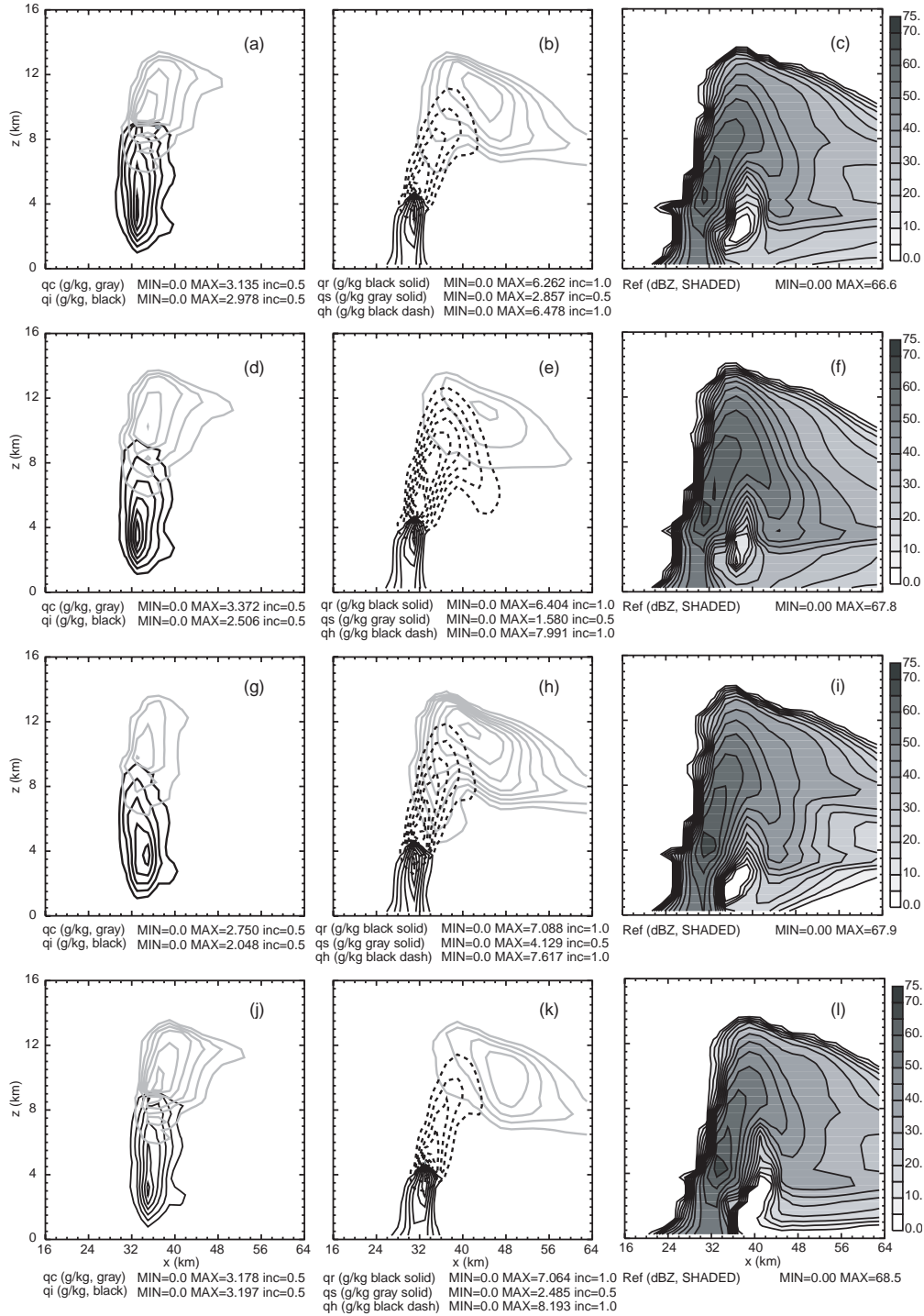


Fig. 4.4. Vertical cross sections of mixing ratios (g kg⁻¹) of hydrometeors and radar reflectivity (dBZ) through the maximum updraft at $t = 70$ min for control simulation (a-c); N0h45 (d-f); N0s37 (g-i); N0r87 (j-l); ρ_h 400 (m-o) and ρ_s 400 (p-r).

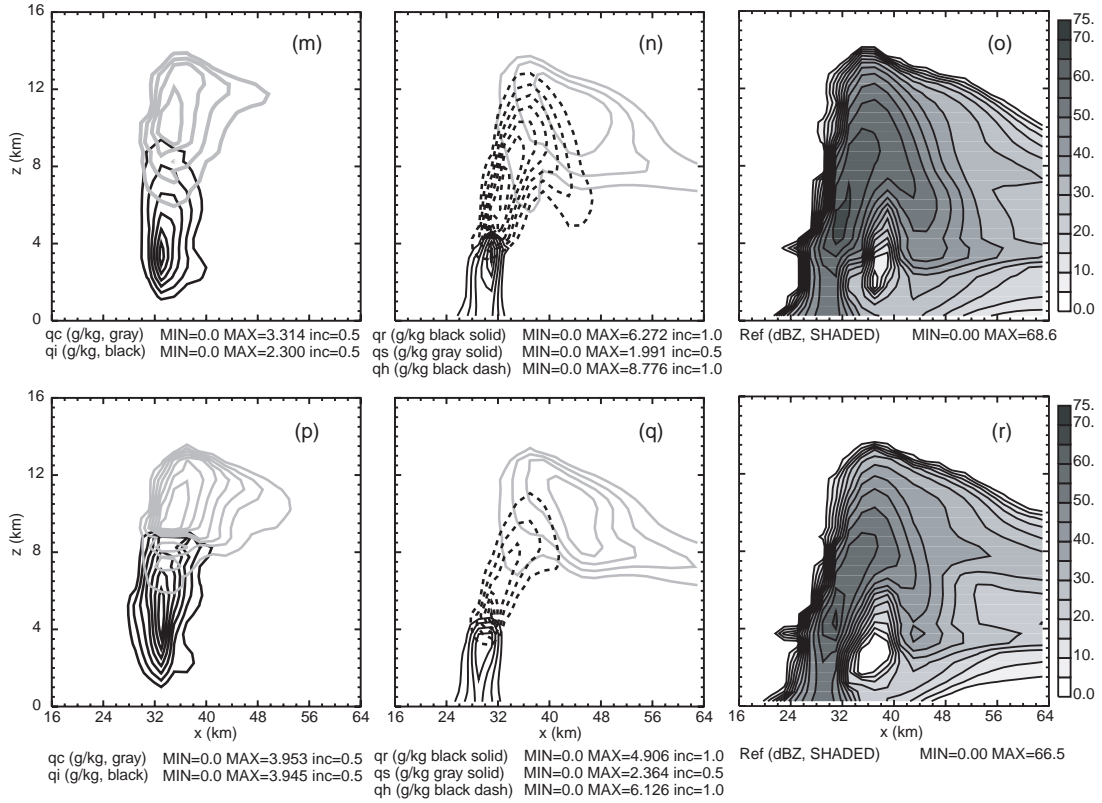


Fig. 4.4. Continued.

q_s due to the change in ρ_h is less than that due to the change in n_{0h} .

Now, we look at the variation of the microphysical fields due to the change in snow intercept n_{0s} or snow density ρ_s . It can be seen from Fig. 4.1a that as n_{0s} or ρ_s increases (decreases), the snow size distribution is more heavily weighted toward smaller (larger) particles. However, the trend of variation in the total number concentration of snow is different for the trend of variation in n_{0s} or ρ_s . For a given q_s , a larger snow intercept results in a larger number concentration, while a larger snow density results in a smaller number concentration of snow. The terminal fall speed of snow is not very sensitive to the change in snow intercept or snow density (Fig. 4.1b).

The species most sensitive to the change in snow parameters are q_i and q_c (Fig. 4.3g, j, note the different x-axis scale of Fig. 4.3j from those of Fig. 4.3f, g, h and i). The sensitivity of q_s to the increase in ρ_s up to its upper bound is not as large as that to the increase by an order of magnitude in n_{0s} , because the amount of change in number concentration in the latter case is much larger than that in the former case (Fig. 4.1a). For the same trend of variation in the snow intercept parameter and the snow density, the three species q_i , q_c and q_s have inverse trends of variation, while the total amounts of q_r , q_h and q_w have the same trend. The amount of q_r , q_h or q_w is less sensitive to n_{0s} than to ρ_s (Fig. 4.3b and e).

Three production terms of snow in the LFO83 scheme, namely, the accretion of cloud water by snow, accretion of cloud ice by snow and deposition growth of snow, are proportional to the snow intercept parameter and inversely proportional to the snow density. When the number concentration of snow increases due to the increase in n_{0s} or decrease in ρ_s , more cloud water and cloud ice are depleted by the accretion and deposition growth of snow and less q_i is advected to the anvil region (c.f., Fig. 4.4a,b with Fig. 4.4g,h).

Fig. 4.4c, Fig. 4.4i and Fig. 4.4r show that the most sensitive region of reflectivity to the snow parameters is the anvil precipitation region. Note that the reflectivity formulation used here is a function of only q_r , q_s and q_h . Even though q_i and q_c are very sensitive to the changes in n_{0s} and ρ_s , they do not contribute to the reflectivity change. When n_{0s} or ρ_s increases, in the anvil precipitation region close to the eastern boundary of the domain, the reflectivity below 6 km becomes weaker. This

is mainly caused by the decrease in the amount of q_h between 3 km and 6 km and the decrease in q_r below 3 km in that region, which can be seen more clearly by using smaller contour intervals (not shown). The interaction between snow and hail/graupel at middle levels probably explains the change in q_h in that region. For example, the accretion of snow by hail/graupel is inversely proportional to both n_{0s} and ρ_s in the LFO83 scheme; therefore, as n_{0s} or ρ_s increases, less q_h is produced by accreting snow. Less q_h at the middle levels results in less q_h melting to become q_r as hail falls below the freezing level. Also note that the reflectivity in the anvil region above 7 km becomes stronger as n_{0s} increases, which is primarily due to the increase in q_s there. The reflectivity in the upper level anvil is less sensitive to the change in snow density because q_s is less sensitive to ρ_s than to n_{0s} .

Finally, we examine the sensitivity of the microphysical fields to the intercept parameter of rain. Fig. 4.3c and Fig. 4.3h show that q_r and q_i are the most sensitive species to the change in n_{0r} while q_s is not very sensitive to n_{0r} . Larger (smaller) n_{0r} results in more (less) q_r , q_i , q_h and q_w . For the reflectivity field, one sensitive region is located within and below the updraft core (Fig. 4.4l). Comparing Fig. 4.4l with Fig. 4.4c, we can see that larger n_{0r} results in higher reflectivity in that region, because q_r and q_h are enhanced there (Fig. 4.4b and Fig. 4.4k). Also, the reflectivity in the anvil precipitation region does not reach the ground when n_{0r} increases. This is because less q_r is found below 2 km in that region (not shown).

It can be seen from Fig. 4.1a that larger (smaller) n_{0r} results in higher (lower) number concentration of rain and the distribution is more heavily weighted toward drizzle (larger raindrops). More small raindrops will enhance the accretion of rain by

graupel/hail, which is proportional to n_{0r} in the LFO83 scheme. Therefore, q_h also increases as n_{0r} increases. The riming growth of hail/graupel results in less hail/graupel being transported to higher levels (Fig. 4.4b, k). Thus, the interaction between hail/graupel and cloud ice are reduced and more q_i is suspended aloft (Fig. 4.4a, j). Fig. 4.4b shows that the terminal fall speed of raindrops decreases (increases) as n_{0r} increases (decreases). As n_{0r} increases, both the increase in the number of small raindrops and the decrease in the terminal fall speed enhance the evaporation rate for raindrops at the low levels, which leads to less rain reaching the ground below the anvil and a stronger cold pool. Among all the five DSD parameters, the minimum temperature below 2 km is most sensitive to the intercept parameter of rain (not shown).

4.4.3 Sensitivity of the EnSRF analyses to microphysical parameters

The sensitivity analyses based on the pure-forecast experiments reveal how much the numerical prediction of storms could be affected by the errors in the microphysical parameters. Our main goal here is to apply the EnSRF method to simultaneously estimate the microphysical parameters and the model state variables. Since the numerical model is closely involved in the EnSRF data assimilation process, it is important to know how much the model state estimation will be affected by the errors in the microphysical parameters. The possibility of estimating these parameters through data assimilation depends on how sensitive the *analyses* of the model state variables are to these parameters although the sensitivity to the model simulation is a prerequisite.

The details of data assimilation and parameter estimation procedure are described in Chapter 5. The initial forecast ensemble is initialized at 20 min, with smoothed random perturbations added to a horizontally homogeneous ensemble mean defined by the environmental sounding. The data are assimilated every 5 min starting at 25 min and the assimilation window ends at 100 min. Fig. 4.5 shows the time-averaged response function ΔJ_η of each assimilation sensitivity experiment, plotted against the deviations of the five parameters from their true values. For the control assimilation experiment, ΔJ_η equal to 0 according to Eq. (4.7). The response functions shown in Fig. 4.5 are calculated using observations that are assimilated into the model. The standard deviations of observation errors for V_r and Z are assumed to be 1 m s^{-1} and 3 dBZ , respectively.

Similar to what was found in the forecast sensitivity experiments, the analyzed radial velocity is less sensitive than the analyzed reflectivity to each of the five microphysical parameters. This indicates again that the reflectivity data is more useful for estimating the microphysical parameters. Also, the same trends of change in the hydrometeor species and in the reflectivity fields due to the changes in the parameter values (Fig. 4.3 and Fig. 4.4) are found in the analyzed model fields from the assimilation sensitivity experiments (Fig. 4.6 and Fig. 4.7).

The relative sensitivity of the analyzed V_r or Z to different parameters appears to be different from that in the simulation experiments. First, the relative sensitivities of the analysis to the three intercept parameters are less symmetric than that of the pure forecast. For example, the sensitivities of the analyzed Z to the three intercept

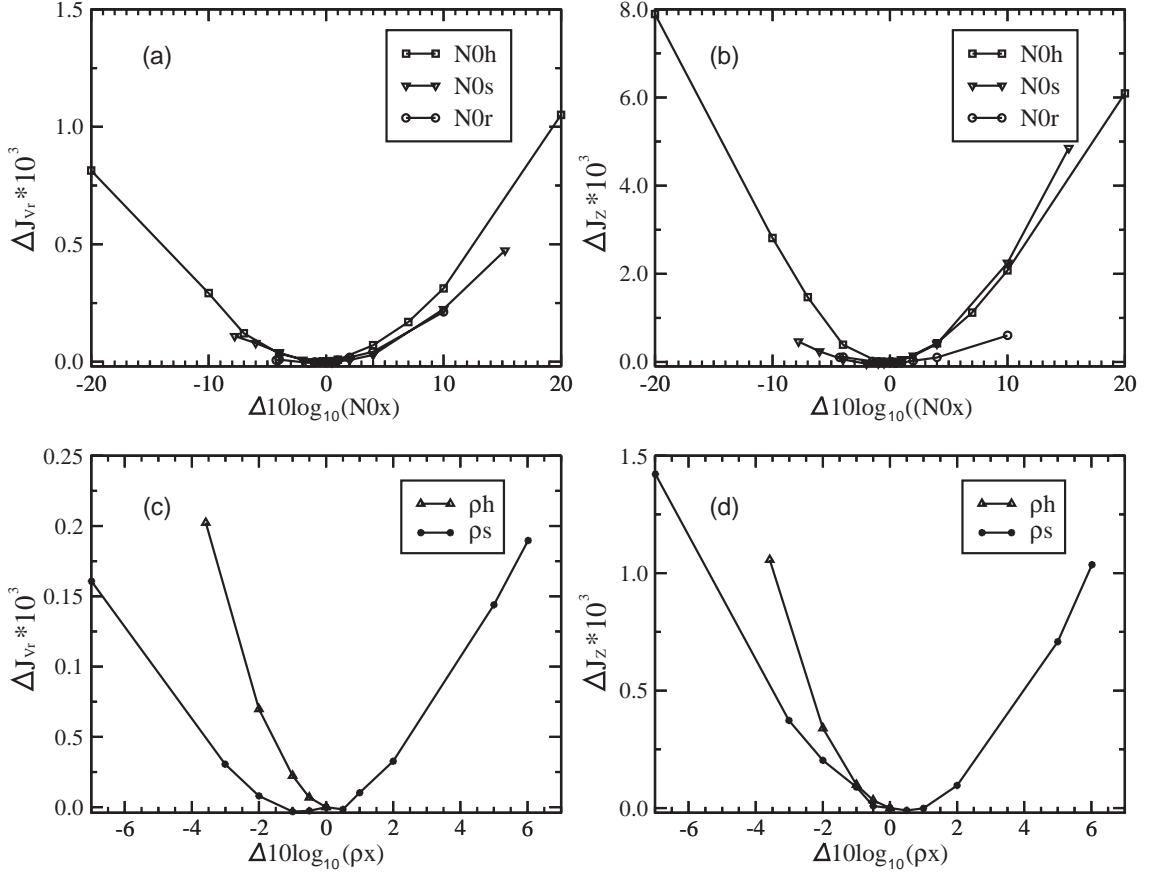


Fig. 4.5. The response functions ΔJ_{V_r} (a and c) and ΔJ_Z (b and d) of the assimilation sensitivity experiments against the logarithmic-form deviation of the parameters from their true values.

parameters can be listed at an increasing order as $\Delta J_Z(n_{0r}) < \Delta J_Z(n_{0h}) < \Delta J_Z(n_{0s})$ and $\Delta J_Z(n_{0s}) \approx \Delta J_Z(n_{0r}) < \Delta J_Z(n_{0h})$, when the intercept parameters have positive and negative deviations, respectively (Fig. 4.5b). Second, the relative sensitivities of radial velocity with respect to different intercept parameters are not always consistent with those of reflectivity. For example, Fig. 4.5a shows that the analyzed V_r is more sensitive to n_{0h} than to n_{0s} as the two parameters positively deviate from their true values, while with the same kind of deviation in the two parameters, the analyzed Z is somewhat more

sensitive to n_{0s} than to n_{0h} . Different from what was found in the simulation sensitivity experiments, the analysis generally has the smallest sensitivity to the intercept parameter of rain (Fig. 4.5a and b). In addition, the analysis is apparently less sensitive to ρ_s than to ρ_h (Fig. 4.5c and d) when ρ_s and ρ_h have negative deviations.

Fig. 4.7 shows the analyzed reflectivity from the assimilation sensitivity experiments, which have the same changes in the microphysical parameters as the forecast experiments shown in Fig. 4.4. Without any error in the parameters, the analyzed Z from the control assimilation experiment matches that of the truth simulation very well (Fig. 4.4c and Fig. 4.7a). The differences in Z at low level anvil precipitation region (below 3km) between the control experiment (Fig. 4.7a) and sensitivity experiments (Fig. 4.7b, c, d, e and f) are smaller than those in Fig. 4.4. It can be seen from Fig. 4.6 and Fig. 4.3 that the estimated q_r , q_h , and therefore q_w below 4 km in almost all cases are less sensitive to the changes in the parameters than the corresponding species in the forecast experiments (dash and dash-dot curves in Fig. 4.6a-e and Fig. 4.3a-e). That is why we see smaller sensitivity of analyzed Z at the low levels. Among the five assimilation sensitivity experiments, the analyzed Z from experiment N0r87 (Fig. 4.7d) looks most like that of the CNTL. Fig. 4.4l shows that in the absence of data assimilation, the error in n_{0r} result in much weaker reflectivity and even no reflectivity at the low-level anvil precipitation region. Probably because of the more effective correction to q_r and q_h during the data assimilation process, the analyzed Z shows the smallest sensitivity to n_{0r} .

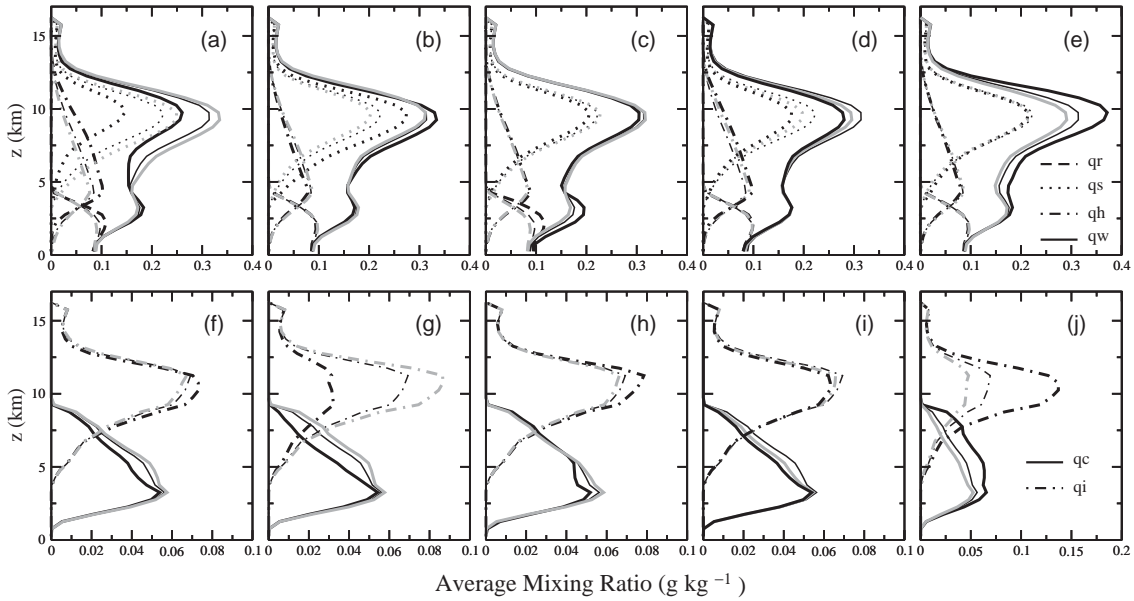


Fig. 4.6. The same as Fig. 4.3, but for EnSRF data assimilation sensitivity experiments N0h45 (thick black) and N0h14 (thick gray) (a and f); N0s37 (thick black) and N0s16 (thick gray) (b and g); N0r87 (thick black) and N0r36 (thick gray) (c and h); ρ_h400 (thick black) and ρ_h576 (thick gray) (d and i); and ρ_s400 (thick black) and ρ_s63 (thick gray) (e and j).

Fig. 4.5 shows only the temporally averaged sensitivity of the EnSRF analysis in terms of the observed quantities, Z and V_r , to the five parameters. In fact, the time scale of the system's response in terms of measured quantity to the parameters, i.e., how fast the model responds to the changes in the parameters, is an important factor that will affect the parameter estimation. For sequential data assimilation methods, if the response is slow, then it will take a long time and many analysis cycles to correct the parameters. For methods with assimilation windows of a limited length, such as the four-dimensional variational data assimilation method, the parameter estimation may fail completely if the response is weak within the given assimilation window.

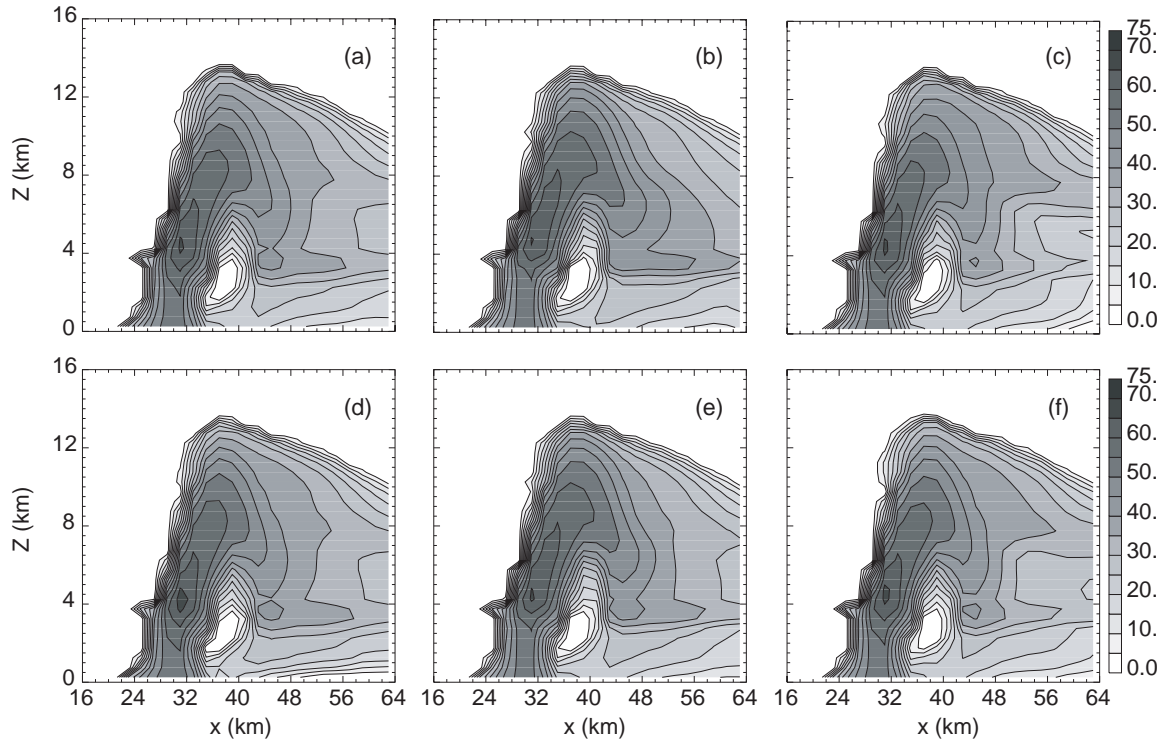


Fig. 4.7. Vertical cross sections of the ensemble mean of radar reflectivity (dBZ) through the maximum updraft at $t = 70$ min for control data assimilation experiment (a), assimilation sensitivity experiments N0h45 (b), N0s37 (c), N0r87 (d), ρ_h400 (e) and ρ_s400 (f).

The time scale of the system's response to individual parameters is examined through assimilation sensitivity experiments, with one parameter perturbed in each of them. To facilitate the comparison among different parameters, the intercept parameters are chosen to be an order of magnitude larger than their true values. The hail and snow densities are chosen to have their lower and upper bounds, respectively. The five experiments are N0h45, N0s37, N0s87, ρ_h400 and ρ_s400 (Table 4.2).

Fig. 4.8 shows the time series of the response functions, ΔJ_{V_r} and ΔJ_Z , at each analysis time from the five experiments. Since the analyzed Z is much more sensitive to

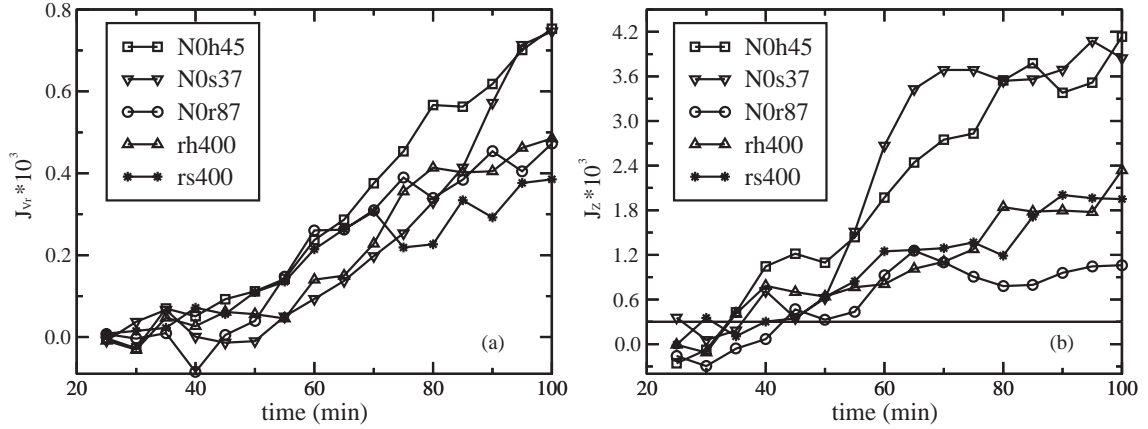


Fig. 4.8. Time evolution of (a) ΔJ_{V_r} and (b) ΔJ_Z from assimilation sensitivity experiments N0h45, N0s37, N0r87, ρ_h 400 and ρ_s 400 (c.f., Table 4.2).

the changes in the parameters than the analyzed V_r , we are more interested in the system response time in terms of Z . As can be seen from Fig. 4.8b, in most cases, either the response functions ΔJ_Z are close to or below 0 in the first two assimilation cycles, or ΔJ_Z decreases to be close to or below 0 from the first to the second cycle. Significant and continuous increase in ΔJ_Z usually occurs after the first two assimilation cycles. The negative values are also found when the response functions are calculated using error-free observation data (not shown). Reasonable system response to the errors in the parameters should result in positive response functions. The negative values during the initial cycles are probably a reflection that the model state estimation is poor at this stage therefore the system response is not reliable.

It is not easy to tell exactly how large the system response in terms of ΔJ_Z needs to be to allow successful parameter identification from the observations. The straight line in Fig. 4.8b is our estimation of the minimum threshold for reliable system response. This minimum threshold is chosen such that the unreliable responses as

indicated by the negative values of ΔJ_z in the first two assimilation cycles are no larger than this threshold. Based on the minimum threshold of reliable response given in Fig. 4.8, the system response time scale can be defined as the time for ΔJ_z to increase over and remain above the minimum threshold.

Fig. 4.8 lists our estimation of the system response time scales for the five assimilation sensitivity experiments. Among the five assimilation sensitivity experiments examined, the shortest response time is 15 min or 3 assimilation cycles, and the longest time is 25 min or 5 assimilation cycles. The time scales of the model response to the same amount of change in the intercept parameters can be listed in an increasing order as $T_{n_{0h}} \leq T_{n_{0s}} \leq T_{n_{0r}}$. The system also responds more quickly to the change in ρ_h as it decreases from its upper bound to its lower bound values than to the change in ρ_s as it increases from the control value to its upper bound, although the time averaged response function ΔJ_z of ρ_s400 has almost the same value as that of ρ_h400 (Fig. 4.5d).

It can be seen from Fig. 4.8b that the times that ΔJ_z curves cross the minimum threshold are also the times at which ΔJ_z has a large growth rate from the earlier analysis time for all experiments except ρ_s400 . The significant increase in ΔJ_z in ρ_s400 occurs between 45 and 50 min, 5 minutes longer than the time scale listed in Table 4.3. After the first significant increase, the response function grows more moderately in N0r87, ρ_h400 and ρ_s400 . A large growth in the response function occurs again during the later assimilation cycles of N0h45 and N0s37.

Experiment	time	Number of cycles
N0h45	15 min	3
N0s37	20 min	4
N0r87	25 min	5
ρ_h400	15 min	3
ρ_s400	25 min	5

Table 4.3. List of the time scales of the system response to the change in one of the microphysical parameters in terms of analysis reflectivity for assimilation sensitivity experiments N0h45, N0s37, N0r87, ρ_h400 and ρ_s400 .

4.5 Parameter identifiability

4.5.1 Parameter identifiability as revealed by the response function

An important issue associated with parameter estimation is the parameter identifiability. The concept of identifiability addresses the question of whether it is at all possible to obtain unique solutions of the inverse problem for unknown parameters of interest in a model from data collected in the spatial and time domains (Navon 1997). Various definitions of parameter identifiability can be found in the literature (Kitamura and Nakagiri 1977; Chavent 1979; Sun and Yeh 1990). A definition suitable for the estimation process using the output least square error criterion was given by Chavent

(1979). A parameter is said to be least-square identifiable if the least squares performance function for identifying the parameter has a unique minimum in a given region and if the minimization is continuously dependent on the measurement errors.

The response function defined by Eq. (4.4) is actually the performance function that is to be minimized if the inverse problem is solved by using the output least square error criterion. As shown in Fig. 4.2, the response functions of both V_r and Z against the variations of all five parameters in the simulation sensitivity experiments all have a concave shape, and there is a unique minimum for each case. This is an indication of a unique mapping between the parameters and the model solution in terms of radar observations, even though the microphysical process and the observation operators are highly nonlinear.

The response functions ΔJ_z from the assimilation sensitivity experiments also show concave shapes (Fig. 4.5), but the curves have more gentle slopes and flatter bottoms than the corresponding functions of simulation sensitivity experiments (c.f., Fig. 4.2). The minimum of the response functions is not always located exactly at the zero deviation point as was found in the simulation sensitivity case, but is always very close to that of the control experiment and the minimum is very close to 0. The smaller gradient of the analysis response function indicates that the signal of model error is weaker when data are used to constraint the model state evolution. The concave shape of the response functions and their single minimum indicate a high probability of finding the true minimum. These results suggest that the five parameters considered can be identified, at least individually, from radar data with a certain degree of accuracy, even when they are estimated simultaneously with the model state variables.

From the flatness of the response functions near the bottom of their curves (Fig. 4.5), we can estimate the limit of the accuracy that the parameters can be estimated. Fig. 4.5a and Fig. 4.5b show that if the three intercept parameters vary within the range of $\Delta 10 \log(n_{0x}) = \pm 1$, the analysis will not sense the errors in the intercept parameters much in terms of V_r and Z . In another word, if the error of the estimated intercept parameters is within $\Delta 10 \log(n_{0x}) = \pm 1$, then the parameter estimation is considered by the estimation system as successful already. The range of the error allowed by 'successful parameter estimation' in terms of V_r and Z is $\Delta 10 \log(\rho_x) = \pm 0.5$ for the snow and hail/graupel densities according to Fig. 4.5c and Fig. 4.5d.

4.5.2 Parameter identifiability as revealed by the correlation between model outputs of observations and parameters

The uniqueness of the inverse problem for single-parameter estimation can be easily revealed by the shape of the response or performance/cost function. However, as the number of the estimated parameters increases, it is no longer straightforward to present the response function as function of parameter deviations. Another way to examine whether it is possible to identify the parameters from the observation information, especially when the parameters vary simultaneously, is to calculate the correlation coefficients between the parameters and the model output of the observed quantities, i.e., $\text{cov}(\eta, p_i)$, from the members of the forecast ensemble. This is especially helpful in understanding the ensemble-based parameter estimation, because with such a method

the estimated parameter is adjusted according to the covariances calculated from the ensemble.

Several ensemble forecast experiments were performed. For each of the ensemble forecasts, the microphysical parameters were perturbed about their means individually for single-parameter experiments or simultaneously for multiple-parameter experiments. Their control values are chosen to be their ensemble means, except for ρ_h whose mean is set to be 700 kg m^{-4} to allow for both positive and negative perturbations. The standard deviations of the parameter perturbations are roughly half of their largest deviations from their control values, i.e., $\frac{1}{2} \max(|\underline{p}_i - p_i^t|, |\bar{p}_i - p_i^t|)$. The initial state uncertainty was taken into account by randomly perturbing model state variables about their means, which are from the true simulation at 20 min. The standard deviation of the perturbations added to each model variable equals to 10 percent of the ensemble mean analysis *rms* error of the control assimilation experiment at the end of the data assimilation cycles. The correlation coefficients are calculated at points where the reflectivity of the truth simulation is greater than 0 dBZ.

Fig. 4.9 shows the spatial structures of the correlation coefficients, at selected radar elevation levels, between each of the five microphysical parameters and the 70 min forecast reflectivity fields from the five single-parameter ensemble forecast experiments. The reflectivity fields shown in Fig. 4.9 are from simulation experiments N0h45, N0s37, N0r87, ρ_h 400 and ρ_s 400 (Table 4.2). Fig. 4.10 shows the spatial structure of the correlation coefficients calculated from a 5-parameter ensemble forecast

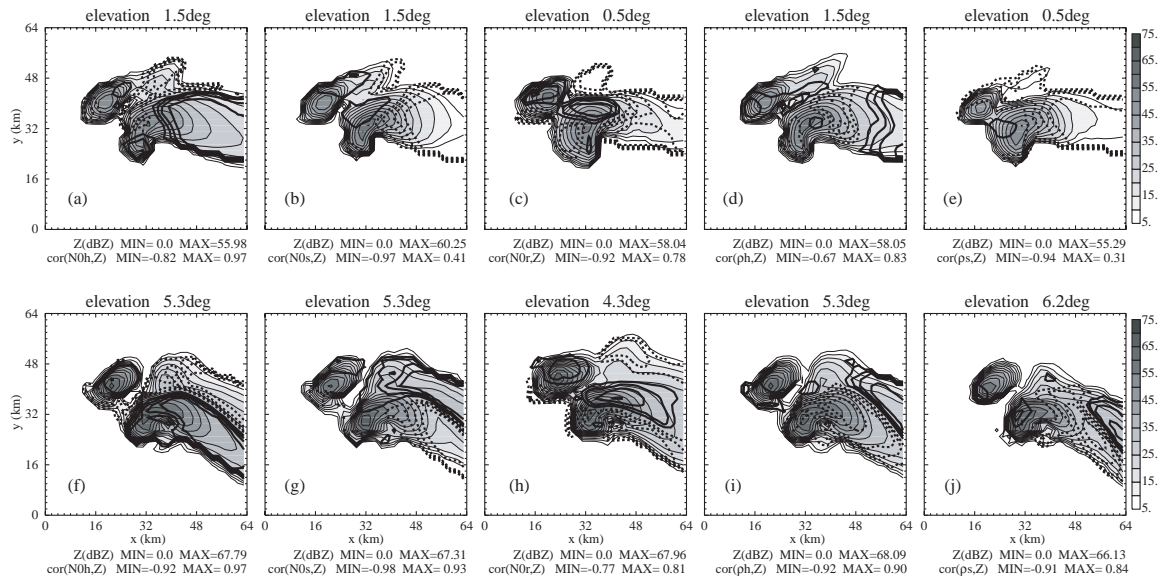


Fig. 4.9. Correlation coefficients calculated from the ensemble members of single-parameter ensemble forecasts at $t = 70$ min. The correlation [thick solid (dash) contours represent positive (negative) values at intervals of 0.2] between forecast Z and (a) n_{0h} at 1.5° , (b) n_{0s} at 1.5° , (c) n_{0r} at 0.5° (d) ρ_h at 1.5° (e) ρ_s at 0.5° , (f) n_{0h} at 5.3° , (b) n_{0s} at 5.3° , (c) n_{0r} at 4.3° (d) ρ_h at 5.3° (e) ρ_s at 6.2° elevation levels. The shading and thin solid contours represent Z from simulations N0h45 (a and f); N0s37 (b and g); N0r87 (c and h); ρ_h 400 (d and i); and ρ_s 400 (e and j).

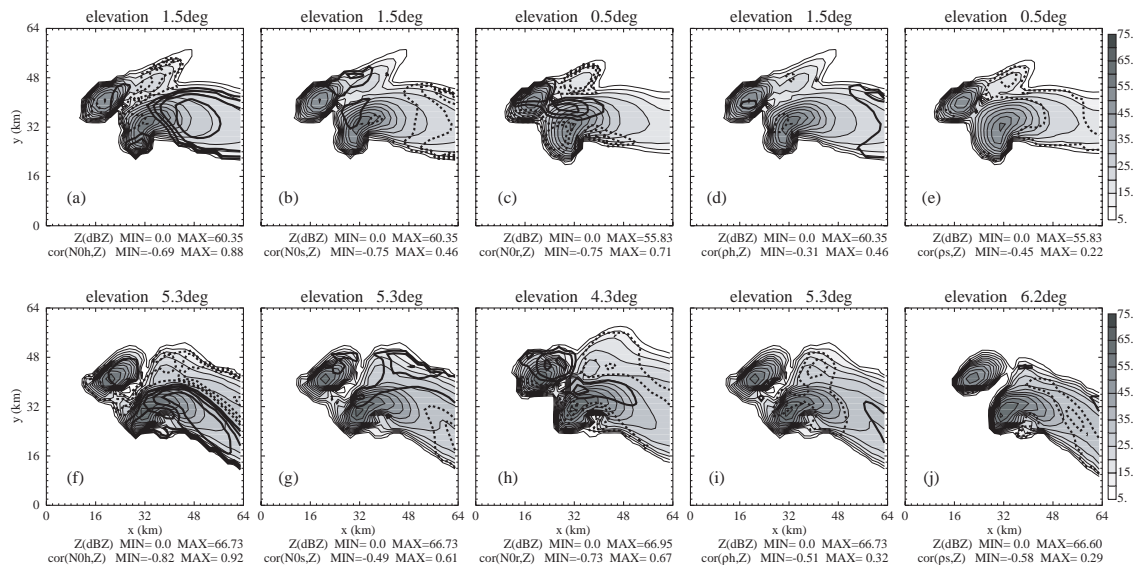


Fig. 4.10. As in Fig. 4.9, but the correlation coefficients are estimated from the members of 5-parameter forecast ensemble at $t = 70$ min. The shading and thin solid contours represent Z from control simulation.

experiment, in which all five parameters are perturbed. The reflectivity field shown in the figure is from the truth simulation.

It can be seen from Fig. 4.9 that in certain regions of the storm, the microphysical parameters are highly correlated with reflectivity. The maximum values of $|cor(Z, p_i)|$ for the five single-parameter cases are all greater than 0.9. A large part of the storm is dominated by regions where $|cor(Z, p_i)| \geq 0.6$. This confirms again that these five individual parameters can be identified from the reflectivity data.

Comparing the reflectivity fields from simulation sensitivity experiments in Fig. 4.9 with that of control simulation in Fig. 4.10, we can see that the locations of the positive and negative correlation regions are consistent with the variation in reflectivity due to the change in parameter value. For example, as n_{0h} increases (experiment N0h45), stronger reflectivity is found in the anvil precipitation region (gray shades in Fig. 4.9a, Fig. 4.10a), therefore n_{0h} is positively correlated with Z in that region, as indicated by positive thick contours in Fig. 4.9a. The reflectivity in Fig. 4.9f and Fig. 4.9i represents precipitation between 3 km and 7 km, given that the radar is located at the southwest corner of the domain. The further the reflectivity echo is away from the radar, the higher is the displayed hydrometeors located. As n_{0h} increases (as in N0h45) or ρ_h decreases (as in ρ_h400), more q_h is transported aloft and less q_s exists in the anvil, resulting in larger reflectivity at middle levels and smaller reflectivity at higher levels. This is why the reflectivity closer to the radar is positively (negatively) correlated with n_{0h} (ρ_h) and the reflectivity further away from the radar is negatively (positively) correlated with n_{0h} (ρ_h) in Fig. 4.9f and Fig. 4.9i. Another example is that as n_{0r}

increases (as in N0r87), less q_r falls to the ground from the anvil. Therefore, the reflectivity echo in the low level anvil precipitation region close to the east boundary becomes weaker (Fig. 4.9c and Fig. 4.10c) and the reflectivity there is negatively correlated with n_{0r} .

Fig. 4.10 shows that as the number of adjustable parameters increases to five, the maximum value of $|cor(Z, p_i)|$ decreases for all parameters and the area with significant correlation also decreases. This indicates that as the number of uncertain parameter increases, the identifiability of each parameter decreases. From Fig. 4.10 we can see some common correlation regions for different parameters, e.g., the negative correlation region at lower level anvil precipitation region for n_{0s} , n_{0r} and ρ_s (Fig. 4.9b, c and e), and the positive-negative correlation pattern at higher level anvil region for n_{0s} , ρ_h and ρ_s (Fig. 4.9g, i and j). When all the parameters vary simultaneously, the correlations in those common regions become very weak (Fig. 4.10b, c, e, g, i and j), which implies that the contribution of a particular parameter to the change of reflectivity is hard identify if its contribution is similar to those of other parameters. However, parameters, such as n_{0h} , whose contribution is different from other parameters, are easier to identify. It can be seen from Fig. 4.10a and Fig. 4.10f that as the number of uncertain parameter increases, large correlation coefficients still cover a larger part of the storm for n_{0h} .

Comparing the spatial correlation patterns in Fig. 4.9 with those in Fig. 4.10, we can see that the positive and negative correlation coefficients estimated from the 5-parameter experiment are at similar locations as those estimated from single-parameter

experiments, even though in certain regions of the storm, significant values of correlation coefficient are missing in the 5-parameter case. This suggests that it may still be possible to estimate five parameters simultaneously, because the information contained in the correlation coefficients remains correct. However, because the correlations for some parameters become weaker, whether errors in the observations will cause instability in parameter estimation is uncertain.

To evaluate the relative identifiability of different parameters, we calculate the root-mean-square of the correlation between observations and each parameter as

$$R(\text{cov}(\eta, p_i)) = \left\{ \frac{1}{M} \sum_{m=1}^M [\text{cov}(\eta, p_i)]^2 \right\}^{1/2}, \quad (4.8)$$

where M is the number of data points where reflectivity is greater than 10 dBZ. Table 4.4 shows the temporally averaged $R(\text{cov}(\eta, p_i))$ calculated from single-parameter and multiple-parameter forecast ensembles. The time averaged root-mean-square correlation coefficients between radial velocity and each of the five parameters, $R(\text{cor}(V_r, p_i))$, are always smaller than the corresponding ones for reflectivity, $R(\text{cor}(Z, p_i))$. The correlations generally decrease as the number of uncertain parameter increases. Among the single-parameter experiments, n_{0h} has the highest correlation with either V_r or Z . When both n_{0h} and ρ_h are uncertain, n_{0h} has a higher correlation with both V_r and Z , and the *rms* correlation for ρ_h decreases much more than that for n_{0h} . When the snow intercept parameter n_{0s} and snow density ρ_s are treated as uncertain, the *rms* correlations between Z and the two parameters have a larger decrease than the corresponding correlations for V_r . For the three-intercept parameter case, both V_r and Z

have the highest correlation with n_{0h} and the lowest correlation with n_{0s} . As the number of uncertain parameters increases from 3 to 5, there is no significant change in the correlation level for the common parameters. The additional parameters ρ_h and ρ_s have relatively low correlations with radar observations compared with the intercept parameters. For the 5-parameter case, n_{0h} and n_{0r} have relatively high correlations with radar observations. The correlation analysis presented in this section helps us further understand the parameter identifiability, especially in the multi-parameter cases.

Exp.	n_{0h}		n_{0s}		n_{0r}		ρ_h		ρ_s	
	V_r	Z								
1-para	0.44	0.61	0.24	0.46	0.35	0.41	0.24	0.43	0.27	0.44
2-para (n_{0h}, ρ_h)	0.42	0.58					0.16	0.19		
2-para (n_{0s}, ρ_s)			0.23	0.39					0.27	0.37
3-para	0.42	0.57	0.17	0.24	0.34	0.35				
4-para	0.41	0.54	0.17	0.23	0.33	0.33	0.15	0.19		
5-para	0.40	0.54	0.16	0.22	0.33	0.33	0.16	0.2	0.19	0.2

Table 4.4. Temporally averaged root-mean-square of correlations between forecast Z or V_r and one of the microphysical parameters as estimated from single-parameter and multiple-parameter forecast ensembles. Temporal averaging was performed upon data outputs at 5-min intervals from $t = 25$ to 100 min.

4.6 Summary and conclusions

The possibility of estimating five fundamental microphysical parameters from radar observations is investigated by addressing issues associated with parameter sensitivity and identifiability. These five parameters are the intercept parameters for rain, snow and hail/graupel, and the bulk densities of hail/graupel and snow, which are usually pre-specified constants in single-moment bulk microphysics schemes and are involved in the definition of drop/particle size distributions. The identifiability of individual parameters is examined from two aspects: the sensitivity of the model forecast or model state estimation in terms of the observed quantities to the changes in the parameter values and the uniqueness of the inverse problem solution for parameter estimation.

Sensitivity analyses were carried out based on pure-forecast and data assimilation sensitivity experiments for a supercell thunderstorm case. Within these experiments, the microphysical parameters are varied within their observed ranges of uncertainty individually. A response function, which measures the difference between the observations and the corresponding model state subjecting the parameter perturbations, was calculated for each of the sensitivity experiments.

Both forecast and assimilation sensitivity experiments show that the errors in the microphysical parameters have larger impact on model microphysical fields than on wind fields. The model radar reflectivity is more sensitive to the microphysical parameters than the model radial velocity is. Generally, the larger the sensitivity is, the higher is the likelihood of correct parameter identification. Therefore, radar reflectivity is preferred over radial velocity for microphysical parameter estimation. Among the

three intercept parameters, the pure forecast, in term of V_r or Z , is most sensitive to n_{0r} and least sensitive to n_{0s} . It has a similar sensitivity to ρ_h and ρ_s within their common ranges of deviation from their true values. The relative sensitivities of the estimated or analyzed model state in terms of V_r and Z to different parameters are somewhat different from the case of forecast sensitivity. Among the three intercept parameters, the analyzed V_r and Z are generally most sensitive to n_{0h} and least sensitive to n_{0r} . The analyzed V_r and Z were found to be more sensitive to ρ_h than to ρ_s within their common ranges of deviation. The possible reasons of the difference in the responses between the two cases require further investigation. It will require an understanding of the nonlinear dynamics of the data assimilation process and its interaction with the parameter errors.

Another factor that affects parameter estimation is the time scale of the system response to the parameter changes. The shorter the response time, the faster the parameters can be corrected through data assimilation cycles. The time series of the response functions were presented for five sensitivity experiments, which include an increase in the three intercept parameters individually by an order of magnitude and the use of the upper and lower bound values for the snow and hail/graupel densities, respectively. According to these experiments, the five parameters can be listed in an increasing order of the response time as $T_{n_{0h}} = T_{\rho_h} < T_{n_{0s}} < T_{n_{0r}} \leq T_{\rho_s}$. The response times are found to be between 15 to 25 minutes or 3 to 5 assimilation cycles. For this particular radar data assimilation problem, when the model is perfect, at least 8 assimilation cycles (40 minutes) are needed to arrive at a good state estimation. Within

such a time window, successful estimation of these parameters can therefore be expected, although in practice, too small initial parameter errors can slow down the estimation process.

The response functions calculated for the forecast sensitivity experiments for all five individual parameters show concave shapes and have unique minima equaling those of the truth simulation. The response functions obtained from assimilation sensitivity experiments also show concave shapes, but the gradients of the response functions with respect to the parameters become smaller, especially, when the parameters are very close to their true values. It is most likely that each of the five microphysical parameters can be estimated individually from radar reflectivity data. From the assimilation sensitivity experiments, we can also estimate the likely accuracy of the estimated parameters, which is limited by the flatness of the response functions near their minimum. The likely accuracy limit in the logarithmic unit is about 1 for intercept parameters or about 0.5 for particle densities. The errors in the parameters smaller than the limits should have negligible impact on the model state estimation.

The identifiability of the microphysical parameters, especially when they vary simultaneously, was also evaluated from their correlations with the model output of radar observations based on ensemble forecasts. For single-parameter cases, all five parameters are highly correlated with radar reflectivity, in terms of the maximum values and area coverage of the significant correlations. The correlations with radial velocity are lower. The physical meanings of the correlations between the microphysical parameters and radar reflectivity can be explained by the hydrometeor changes caused by the changes in the parameters. As the number of uncertain parameters increases, both

the level and the area coverage of significant correlations decrease, which implies that the degree of difficulties will be higher with multiple-parameter estimation.

In Chapter 5, the details of the simultaneous estimation of the microphysical parameters and model state variables using the EnSRF algorithm from radar data will be presented. The sensitivity analysis and parameter identifiability discussed here will guide us with the experiment design and help us understand the results of estimation. The parameter identifiability issue will be further discussed based on the estimation results.

Chapter 5

Simultaneous Estimation of Microphysical Parameters and Atmospheric State with Radar Data and Ensemble Square-root Kalman Filter: Parameter Estimation Experiments

5.1 Introduction

Various studies over the recent years have demonstrated that the ensemble Kalman filter (EnKF) method (Evensen 1994; Burgers et al. 1998; Houtekamer and Mitchell 1998; Evensen 2003) and its variations (Bishop et al. 2001; Anderson 2001; Whitaker and Hamill 2002) form a viable approach to atmospheric data assimilation, for both large-scale (e.g., Houtekamer and Mitchell 2001; Houtekamer et al. 2005) and small-scale (e.g. Snyder and Zhang 2003; Zhang et al. 2004; Dowell et al. 2004; Tong and Xue 2005a; Xue et al. 2006) applications. For the convective-scale radar data assimilation, the flow-dependent multivariate background error covariances provided by the ensemble-based assimilation method play an essential role, because most state variables are not directly observed at the convective scale. It has been shown that dynamically consistent wind, thermodynamic and microphysical fields can be retrieved accurately using EnKF methods from simulated radar radial velocity and reflectivity observations (Snyder and Zhang 2003; Zhang et al. 2004; Tong and Xue 2005a; Xue et al. 2006).

Encouraged by these Observing System Simulation Experiment (OSSE) results, researchers have been moving towards using real data (e.g., Dowell et al. 2004; Houtekamer et al. 2005) and exploring the possibility of operational implementation of ensemble-based data assimilation methods (e.g., Houtekamer et al. 2005).

In most OSSE studies, only forecast errors due to uncertain initial conditions are taken into account, while forecast errors due to model deficiencies are neglected. However, in real-world applications, significant challenge can be encountered due to the presence of model error. With EnKF, the flow-dependent multivariate covariances are estimated and evolved through the model evolution of each ensemble member. Whether they can be determined correctly depends on whether the model evolutions are correct and systematic model errors can cause the ensemble member not being drawn from the distribution that produces truth because the model attractor and the system attractor differ (Hansen 2002).

Systematic errors can result from uncertain parameters used in the prediction model. One way to account for the model error of this type is through parameter estimation, so that the parameters can be more adequately constrained by available observations. Different techniques, such as the maximum likelihood method (Dee 1995), extended Kalman filter (Hao and Ghil 1995) and variational method (Yu and O'Brien 1991; Zou et al. 1992), have been applied to the parameter estimation problem in meteorology and oceanography. Navon (1997) reviewed the variational approach via an adjoint model for parameter estimation and discussed the issue of parameter identifiability. Recently, Crook et al. (2004) applied the 4DVAR method to estimate a coefficient in a hydrometeor terminal velocity formulation of their cloud model.

Anderson (2001) first suggested that the EnKF can be used for parameter estimation by including the model parameters as part of the model state and estimating them simultaneously with the model state. Annan et al. (2005a) successfully applied the EnKF method to simultaneously estimate 12 parameters in a low-resolution coupled atmosphere-ocean model with steady-state dynamics. Annan and Hargreavers (2004) also successfully applied this method to perform multivariate parameter estimation in the presence of chaotic dynamics with the Lorenz model. More recently, they extended their results to a realistic intermediate complexity atmospheric GCM with both identical twin experiments and reanalysis data (Annan et al. 2005b). However, in contrast to weather prediction, the climate forecasts depend strongly on parameterizations rather than initial conditions (Annan et al. 2005a). Kivman (2003) found that the EnKF performed poorly when applied to simultaneous state and parameter estimation in the Lorenz model. He attributed this to utilizing only two statistical moments in the analysis step by all Kalman filter-based methods, which are unable to deal with highly non-Gaussian probability distributions in the parameter space. Experiments assimilating simulated surface observations into a parameterized 1D PBL model as well as estimating the parameter of soil moisture availability by Hacker and Snyder (2005) suggested that the EnKF may help mitigate model error via parameter estimation. Aksoy *et al.* (Aksoy et al. 2006) applied the EnKF method to simultaneous estimation of up to 6 parameters and the model state with a two-dimensional, hydrostatic, non-rotating, and incompressible sea-breeze model. They found that the estimation of single imperfect parameters with the EnKF is successful, while the quality of estimation deteriorates when the number of estimated parameters increases.

Numerical modeling studies for convective systems have demonstrated large sensitivity in terms of cloud characteristics, surface rainfall, radar reflectivity structures, and downdraft intensity to microphysical parameterization (McCumber et al. 1991; Ferrier et al. 1995; Gilmore et al. 2004; van den Heever and Cotton 2004). Errors in microphysical parameterization therefore have direct impact on simulation and data assimilation for convective systems. The basic assumption for the bulk microphysical scheme is that the particle or drop size distributions (DSDs) can be represented in functional forms. For single-moment bulk microphysics scheme, a large part of the error lies with the uncertain parameters that are used to define the drop size distributions, which are usually predetermined constants. In reality, those parameters can vary with space and time and among systems in different larger environment. The purpose of this two-part study is to examine the impact of the errors in these microphysical parameters on the retrieved model state and to correct these errors, when possible, using the EnKF method through parameter estimation. To our knowledge, this is the first attempt as such.

The microphysics scheme used in the ARPS model (Xue et al. 2000; Xue et al. 2001; Xue and Min 2003), on which our EnKF data assimilation system is based, is the 5-class (cloud water, rain, cloud ice, snow and hail/graupel) single-moment bulk scheme after Lin et al. (1983, LFO83 hereafter). Additional information of the microphysics scheme can be found in Chapter 4. The microphysical parameters to be estimated include the intercept parameters of hail, snow and rain drop size distributions, the densities of hail and snow. The sensitivity of the model forecast and estimated state of a supercell thunderstorm to these parameters are analyzed in detail in Chapter 4,

together with discussions on issues associated with parameter identifiability. In this second part, we focus on estimating those microphysical parameters using the EnKF method and radar data.

The remainder of this chapter is organized as follows. Section 5.2 outlines our ensemble square root filter (EnSRF) data assimilation system and its configurations. The EnSRF can be considered a variation of the EnKF method, which does not require perturbing the observations. In section 5.3, we describe our parameter estimation procedures. The results of parameter estimation experiments, based on simulated data for a supercell storm, are discussed in section 5.4. Parameter identifiability is further discussed in section 5.5. Summary and conclusions are given in section 5.6.

5.2 Data Assimilation Procedure

As the first attempt trying to estimate uncertain microphysical parameters, OSSEs are conducted. The information of the prediction model and the truth simulation for a supercell thunderstorm can be found in Chapter 4. The details of the EnSRF data assimilation configurations as well as the observation operators are described below.

5.2.1 The EnSRF data assimilation configurations

For the control data assimilation experiment (CNTL) using EnSRF, the model is assumed to be perfect, i.e., the true values of microphysical parameters are used. In this case, only the model state variables are estimated via the EnSRF. The procedure of initializing the ensemble is different from our earlier work in Tong and Xue (2005a, hereafter TX05) or Xue et al. (2006, hereafter XTD06). Instead of using random

perturbations, spatially smoothed perturbations are added to the first guess of the initial condition that is horizontally homogeneous as defined by the May 20, 1977 Del City, Oklahoma supercell sounding. This way of the initial perturbation construction is similar to that of Caya et al. (2005). For each model variable at grid point (l, m, n) , the spatially smoothed perturbation is calculated as

$$\varepsilon(l, m, n) = E \sum_{(i, j, k) \in S} r(i, j, k) W(i, j, k), \quad (5.1)$$

where $r(i, j, k)$ is a random number sampled independently from a normal distribution with zero mean and unit deviation. $W(i, j, k)$ is a 3D distance-dependent weighting function and E is a scaling parameter for obtaining the right variance of the perturbation field. The fifth-order correlation function (Eq. 4.10) of Gaspari and Cohn (1999) is used here for W . It is chosen for its closeness to the Gaussian function as well as the much lower computational cost in its numerical evaluation. The summation is over all the grid points that are located within a 3D radius, which is set to 6 km in this study. This radius is chosen based on the typical decorrelation length scale of background errors of the current type of assimilation problems and is actually the same cut off radius used by the covariance localization (more later).

After the smoothed initial perturbations are obtained, they are rescaled, by determining E in Eq. (5.1) so that the standard deviation of each perturbation field is equal to a desired value. The standard deviations are, respectively, 2 m s^{-1} for velocity components, 2 K for perturbation potential temperature, and 0.6 g kg^{-1} for q_v , q_c , q_r , q_i , q_s and q_h . For the mixing ratios of hydrometeors, the perturbations are only added in regions within 6 km horizontal distance from the observed precipitation. They are

further limited to the heights where the particular hydrometeor species are expected. Negative values of perturbed mixing ratios are set to zero. The perturbations for the velocity components, potential temperature and specific humidity are added to the entire domain except at the lateral boundaries. Our previous studies (TX05 and XTD06) show that spurious cells that may be triggered by added perturbations in non-precipitation regions can be suppressed by assimilating reflectivity data everywhere.

It is found that by using the spatially smoothed initial perturbations, the ensemble spread of most model variables can grow quickly within the first 5 minutes of forecast while the grid-point-based random perturbations used in TX05 would initially decay significantly in the model, decreasing the spread. Perturbing microphysical fields, which was not done in TX05 or XTD06, also contributes to larger ensemble spread in microphysical variables. Larger initial ensemble spread results in smaller ensemble mean root-mean-square (*rms*) errors in early assimilation cycles. It is also found that with this new method of initial perturbations, updating model variables that are indirectly related, via observation operator, to reflectivity no longer, as it did in TX05, hurts the analysis during the earlier assimilation cycles. Therefore, in our current configuration, we do not withhold the updating of those indirectly-related variables when assimilating reflectivity data.

The same background error covariance localization procedure as used in TX05 and XTD06 is applied here to avoid the influence of unreliable covariances at large distances from the observations. No covariance inflation is applied here, because we found that the difference of the analysis *rms* errors caused by covariance inflation is smaller than that caused by different realizations of the initial ensemble members. We

do find some sensitivity of the analysis to the realization of the initial ensemble, mostly in the first few cycles, but the sensitivity is not as large as that found in Snyder and Zhang (2003). The sensitivity of the analysis to the realization of the initial perturbations is not as large when the initial ensemble members are created by adding grid-point-based random noise.

Forty or one hundred ensemble members are used in the experiments to be reported in this chapter. The first ensemble forecast cycle starts at 20 minutes of the simulated supercell storm. Forecast ensemble members are integrated for 5 minutes before the first analysis, at 25 minutes. Both radial velocity and reflectivity, including reflectivity in non-precipitation regions, are assimilated in all experiments while only reflectivity data are used for microphysical parameter estimation. Other settings are very similar to those of XTD06.

5.2.2 Observation operators for radar data

For OSSEs, simulated observations are collected from a truth simulation or nature run (see, e.g., Lord et al. 2001). As in XTD06, the radar radial velocity and reflectivity data are sampled from the atmosphere of the truth simulation by using a radar emulator, which is also the observation operator used to assimilate the data. The radial velocity and reflectivity data are assumed to be available from a WSR-88D radar located at the south-west corner of the $64 \text{ km} \times 64 \text{ km}$ model domain and the radar operates in the standard precipitation mode, having 14 elevations with the lowest elevation at 0.5° and the highest at 19.5° . The maximum range is 230 km. The effects of the curvature of the earth and the beam bending due to vertical change of refractivity are taken into account

by using the simple 4/3 effective earth radius model discussed in Doviak and Zrnic (1993).

Following XTD06, the simulated observations are assumed to be available on the original radar elevation levels. On each elevation level, it is assumed that the observations are already interpolated from the radar polar coordinates to the Cartesian coordinates. The radar emulator does power-gain-based sampling in the vertical direction to project the data from the model levels to the radar elevation levels:

$$\eta_e = \frac{\sum G \eta_g \Delta z}{\sum G \Delta z}, \quad (5.2)$$

where η_e and η_g are respectively the elevation level and grid point values of either radial velocity (V_r) or reflectivity factor (Z in $\text{mm}^6 \text{m}^{-3}$). Δz is the depth of the model grid layer in which grid point value η_g is found. The two-way power weighting function is assumed to be of Gaussian form,

$$G = \exp \left[-4 \ln 4 \left(\frac{\phi_g - \phi_0}{\phi_w} \right)^2 \right], \quad (5.3)$$

following Wood and Brown (1997), where ϕ_w is the one degree beam width. ϕ_g is the elevation angle for the grid point value and ϕ_0 the elevation at the beam center.

The grid point values of radial velocity involved in the numerator of Eq. (5.2) are calculated from

$$V_{rg} = u \cos \phi_g \sin \varphi_\beta + v \cos \phi_g \cos \varphi_g + (w - w_t) \sin \phi_g, \quad (5.4)$$

where ϕ_g is the *local* elevation angle (as defined earlier) and φ_g the azimuth angle of the radar beam that goes through the given grid point. u , v and w are the model air velocity components interpolated to the scalar point of a staggered model grid and w_t is the bulk terminal fall velocity calculated at scalar points. The fall velocity is calculated from

$$w_t = \frac{w_{tr}Z_{er} + w_{ts}Z_{es} + w_{th}Z_{eh}}{Z_{er} + Z_{es} + Z_{eh}}, \quad (5.5)$$

where Z_{er} , Z_{es} and Z_{eh} are the equivalent reflectivity factors (in $\text{mm}^6 \text{m}^{-3}$) of rain, snow and hail respectively. w_{tr} , w_{ts} and w_{th} are the mass-weighted mean terminal velocities of rain, snow and hail. We employ Eqs. (11), (12) and (13) of LFO83 to calculate these terminal velocities, which are consistent with those in our assimilation model. In XTD06, it was assumed that the terminal velocity effect had already been removed from the radial velocity data. Including the terminal velocity effect explicitly adds an additional degree of sophistication, and the proper estimation of the terminal velocity in the data assimilation process does rely on a reasonable estimate of the hydrometeor state variables.

When Eq. (5.2) is applied to reflectivity, the grid point values of equivalent reflectivity, Z_e , in $\text{mm}^6 \text{m}^{-3}$, is calculated from the mixing ratios of rainwater, snow and hail, using the formulae found in TX05, except that the reflectivity equation for dry hail is now included, following Smith et al. (1975). A transition zone from dry to wet hail is defined to be between -2.5°C and 2.5°C . After the values of equivalent reflectivity on elevation levels are obtained, they are transformed into the commonly used reflectivity,

Z , in dBZ ($Z = 10 \log_{10}(Z_e)$). In our data assimilation system, reflectivity Z , in dBZ, is directly assimilated.

The five microphysical parameters to be estimated are also involved in the calculation of radar reflectivity and terminal velocity. However, in this study, only the errors in the prediction model are considered. The observation operators are therefore assumed to be perfect (imperfect observation operators will be considered in a future study), i.e. the true values of these parameters, denoted by vector \mathbf{p}^t , are used in the observation operators for all experiments. The default values of microphysical parameters in the LFO83 scheme are assumed to be the true values (Table 5.1). The ‘error-free’ observation data, denoted by vectors $\mathbf{V}_r(\mathbf{x}^t, \mathbf{p}^t)$ and $\mathbf{Z}(\mathbf{x}^t, \mathbf{p}^t)$, can be obtained by applying the radar emulator to the truth simulation. The observation errors are included by adding random errors to the ‘error-free’ observations to give

$$\mathbf{V}_r^* = \mathbf{V}_r(\mathbf{x}^t, \mathbf{p}^t) + \sigma_{V_r} \mathbf{v}, \quad (5.6)$$

$$\mathbf{Z}^* = \mathbf{Z}(\mathbf{x}^t, \mathbf{p}^t) + \sigma_Z \mathbf{v}, \quad (5.7)$$

where \mathbf{v} represents the Gaussian random variable vector with zero mean and unit standard deviation and σ_{V_r} and σ_Z are the standard deviations of the observation errors added to V_r and Z , respectively. Here we assume that $\sigma_{V_r} = 1 \text{ m s}^{-1}$ and $\sigma_Z = 3 \text{ dBZ}$.

5.3 The design of parameter estimation experiments

As mentioned earlier, the parameter estimation with the EnSRF is realized by considering the parameters as part of the model state, an approach that is often referred to as the state vector augmentation. In the single-moment bulk microphysics scheme of

LFO83 used by ARPS, the DSD parameters are spatially and temporally invariant constants. The default values of the DSD parameters used by the LFO83 scheme are assumed to be their true values. We will first estimate the five DSD parameters individually, and then increase the number of estimated parameters gradually from two to five. The parameters that are not estimated assume their true values.

Suppose vector $\mathbf{p} = (p_1, \dots, p_L)^T$ is the L -dimensional vector of the unknown DSD parameters that are to be estimated, where L varies from 1 to 5 in our study. The prior information on the unknown DSD parameters is their range of variations. The admissible set of \mathbf{p} based on parameter range ($P_{ad} = \{\mathbf{p} \mid \underline{p}_i \leq p_i \leq \bar{p}_i, i = 1, 2, \dots, L\}^T$) has been discussed and given in Chapter 4. To investigate the uniqueness of the inverse problem that is intimately related to parameter identifiability, our parameter estimation experiments start from different initial guesses of \mathbf{p} , which are chosen from P_{ad} . An initial parameter ensemble is constructed by randomly sampling the parameters from their prior distributions, which are assumed to be Gaussian with the means equal to the initial guesses of the parameters. The uncertainty associated with the intercept parameters can be more than an order of magnitude (see Chapter 4). Initial sampling of the parameter ensemble from a broad prior distribution can easily result in unphysical negative values. Problems in the analysis can also result in negative intercept parameter and density. Therefore, the five microphysical parameters are logarithmically transformed and multiplied by 10 before the analysis, and then transformed back in the forecast step. The use of the logarithmic form may also improve the Gaussian assumption on the parameter error distribution. Table 5.1 lists the true values of the

logarithmically transformed parameters and their upper and lower bounds. Working with the new parameter vector $\mathbf{P} = 10 \log_{10}(\mathbf{p}) = (P_1, \dots, P_L)^T$, the initial ensemble of P_i is drawn from $N(P_{i0}, \sigma_{P_i}^2)$, where P_{i0} is an initial guess of P_i . Ideally, the initial ensemble spread of parameter P_i , i.e., the standard deviation, σ_{P_i} , of the prior distribution of the parameter, should represent the error in the first guess, P_{i0} . However, the initial error is usually unknown in reality. In this study, the ensemble spread of each DSD parameter is initialized to be roughly half of its largest deviation from its default values in the model, i.e., $\sigma_{P_i} = \frac{1}{2} \max(|\underline{P}_i - P_i^t|, |\bar{P}_i - P_i^t|)$ (see Table 5.1), for all parameter estimation experiments.

Parameter estimation was found to be sensitive to the realization of the initial ensemble in our initial study (Tong and Xue 2005b). To take into account the effect of randomness in the realization of the initial ensemble for parameters as well as model state variables, different realizations of the initial ensemble are applied to each parameter estimation experiment. Another source of randomness comes from the random errors added to the simulated observation data, i.e. the vector \mathbf{v} in Eqs. (5.6) and (5.7). In this study, a total of 32 sets of radar observation data are generated with different realizations of \mathbf{v} , so that different observations are used for different experiments estimating the same parameter vector \mathbf{P} . The first requirement of identifiability is that all estimations must converge to the same point \mathbf{P}' regardless of the starting point \mathbf{P}_0 (Sun et al. 2001). However, numerical experiments can only be conducted with limited number of starting points \mathbf{P}_0 . The conclusions taken from the

Parameter p_i/P_i	p_i^t	P_i^t	\underline{P}_i	\overline{P}_i	σ_{P_i}	$\underline{\sigma}_{P_i}$
$n_{0h} (\text{m}^{-4})/10\log_{10}(n_{0h})$	4×10^4	46.02	26.02	66.02	10	1.0
$n_{0s} (\text{m}^{-4})/10\log_{10}(n_{0s})$	3×10^6	64.77	56.9897	80	7	1.0
$n_{0r} (\text{m}^{-4})/10\log_{10}(n_{0r})$	8×10^6	69.03	64.77	79.03	5	1.0
$\rho_h (\text{kg m}^{-3})/10\log_{10}(\rho_h)$	913	29.6	26.02	29.6	2	0.5
$\rho_s (\text{kg m}^{-3})/10\log_{10}(\rho_s)$	100	29.6	13.01	26.02	3.5	0.5

Table 5.1. List of the true value of each microphysical parameter and the true value P_i^t , the upper bound \overline{P}_i and lower bound \underline{P}_i of each logarithmically transformed microphysical parameter $P_i = 10 \log_{10}(p_i)$. σ_{P_i} stands for the standard deviation of the initial parameter perturbations for P_i , and $\underline{\sigma}_{P_i}$ is minimum ensemble spread of P_i used in ensemble inflation.

limited number of numerical trials should be more robust, if the randomness in the filter configuration is taken into account.

At each analysis step, the covariances between the parameters and the observations are calculated and used in the update equation of the EnSRF. From the sensitivity analysis in Chapter 4 we found that the forecasted as well as the analyzed radar reflectivity is more sensitive to the microphysical parameters than radial velocity. It was also found that radar reflectivity has a higher correlation with each of the microphysical parameters than radial velocity. The microphysical parameters are more likely to be estimated from reflectivity data than from radial velocity data. Our initial test using radial velocity data alone for parameter estimation was not very successful. As a result, only reflectivity data greater than 10 dBZ will be considered for parameter estimation.

A critical problem we were confronted with during the parameter estimation is ‘filter divergence’. The tendency of filter divergence is much more pronounced with the estimation of global parameters than with model state because of two reasons. First, at each analysis step, about 400 (in the first cycle) to more than 4000 (in the last cycle) reflectivity data are available for updating the few global parameters, while the data used to update model variables at certain grid point are limited through spatial covariance localization. The parameter ensemble spread narrows quickly by the repeated application of the data. Another reason for such continuous narrowing is that these parameters are not dynamic; their errors do not grow during the forecast as those of state variables do. In our case, without a special treatment that prevents ‘filter divergence’, the parameter ensemble becomes useless after only two or three assimilation cycles and the parameters can no longer be influenced by observations before they converge to their true values.

To compensate for the infinitely diminishing of the parameter ensemble, a similar ensemble inflation procedure as used in Aksoy *et al.* (Aksoy et al. 2006) is employed. A minimum standard deviation $\underline{\sigma}_{P_i}$ is pre-specified, so that when the posterior standard deviation becomes smaller than $\underline{\sigma}_{P_i}$, the parameter ensemble spread is adjusted back to $\underline{\sigma}_{P_i}$. For successful parameter estimation, the error in the ensemble-mean should have negligible impact on the state estimation. Based on the sensitivity analysis in Chapter 4, the upper bound of the parameter error ($|P_i - P_i^f|$) allowed by 'successful parameter estimation' in terms of V_r and Z is 1 for the three intercept

parameters and is 0.5 for the snow and hail/graupel densities. These values will be used as the minimum ensemble spreads $\underline{\sigma}_{P_i}$ for parameter ensemble inflation.

However, our early single-parameter estimation experiments show that if all reflectivity data larger than 10 dBZ are used, the minimum ensemble spread $\underline{\sigma}_{P_i}$ has to be much smaller than that given in Table 5.1, otherwise, the estimated parameter is over adjusted, which is manifested as large oscillations in the estimated parameter time series around the true value (Tong and Xue 2005b). The over-adjustment to the estimated parameter is mainly caused by the large number of data used for parameter estimation. The correlation information determines the direction to which the parameter should be adjusted, while the variance determines the amount of adjustment. As shown in Chapter 4, the reflectivity in a large part of the storm is highly correlated with the individual parameters, which implies that a major portion of the data could provide the right direction of adjustment, but constantly inflating the variance can cause over-adjustment.

In Chapter 4, we also found that the correlations between the DSD parameters and the reflectivity decrease as the number of adjustable parameter increases. In certain regions of the storm, the correlations become very weak ($|r| < 0.2$) for some parameters. This may explain why the results of our early multiple-parameter estimation experiments, in which all reflectivity data are used to correct the values of the parameters, are poor, because the data in weak correlation regions can not provide reliable direction information. Since not all reflectivity data within the storm are effective in correcting the errors in the parameters, in this study we introduce a data selection procedure based on prior correlation information. At each analysis time, we first calculate the correlation between each estimated parameter and the reflectivity at

all data points from ensemble members. We then sort the correlations and pick the data points with larger correlations for the corresponding parameter. We fix the minimum ensemble spread $\underline{\sigma}_p$ to be the upper bound of the ensemble mean error of the estimated parameter, which has negligible impact on the state estimation (Table 5.1). The number of data to be used for parameter estimation is adjustable. We tested the number of data from 20 to 60 based on single-parameter experiments, and finally decided to use 30. A smaller number of data leads to a slower convergence rate, while a number of more than 50 results in over-adjustment to the parameters. There is no significant difference between experiments using 30 and 40 data.

5.4 Results

5.4.1 Results of Experiments Estimating Single Parameters

All single-parameter estimation experiments reported here use 40 ensemble members. The results of estimating the five microphysical parameters individually (with the other four having their true value) are presented in Fig. 5.1. The initial guesses of the parameters are listed in Table 5.2. Fig. 5.1 shows the evolutions of the mean and spread of the parameters during the 80 min assimilation period. In each plot, the thick solid step-like curves represent the ensemble mean while the thin dashed lines indicate one standard deviation ($1\sigma_p$) ensemble width. The constant values between 20 min and 25 min indicate the initial distributions. The true values of the parameters are shown by the straight horizontal lines. As mentioned earlier, the experiments shown in Fig. 5.1 have

Parameter p_i	p_{i0}^1	P_{i0}^1	p_{i0}^2	P_{i0}^2	p_{i0}^3	P_{i0}^3
n_{0h} (m ⁻⁴)	4×10^3	36.02	4×10^5	56.02	4×10^6	66.02
n_{0s} (m ⁻⁴)	7×10^5	58.45	3×10^7	74.77	1×10^8	80
n_{0r} (m ⁻⁴)	3×10^6	64.77	2×10^7	73.01	8×10^7	79.03
ρ_h (kg m ⁻³)	400	26.02	700	28.45	750	28.75
ρ_s (kg m ⁻³)	50	16.99	300	24.77	400	26.02

Table 5.2. The three initial guesses for each parameter in its original form p_{i0}^m and the logarithmical form P_{i0}^m ($m=1,2,3$), which are used in single-parameter estimation experiments.

different random realizations of the initial ensemble and observation errors.

It can be seen from Fig. 5.1 that within a few (usually 4 to 5) assimilation cycles, the posterior ensemble spread of the estimated parameter decreases to the pre-specified minimum ensemble spread $\underline{\sigma}_{p_i}$. The scenario of very successful parameter estimation should be that the true value of the estimated parameter is located within the $1 \underline{\sigma}_{p_i}$ ensemble width, because $\underline{\sigma}_{p_i}$ is assigned to be the upper bound of the error that has negligible effect on the model state estimation. Generally, all five parameters can converge to their true values in these single-parameter experiments, albeit at different rates. The estimations of ρ_h appear most successful (Fig. 5.1m, n, o); the estimated ρ_h converges to the true value after only 5 assimilation cycles. After that, its error remains true value, the estimated n_{0h} remains very close to the true value most of the time (Fig. 5.1a, b, c). One type of behavior is that the estimated parameter closely oscillates around the true value (e.g. Fig. 5.1f). In other cases, e.g., for n_{0r} and ρ_s , even after the parameter has approached the true value, deviations from the true value by more than

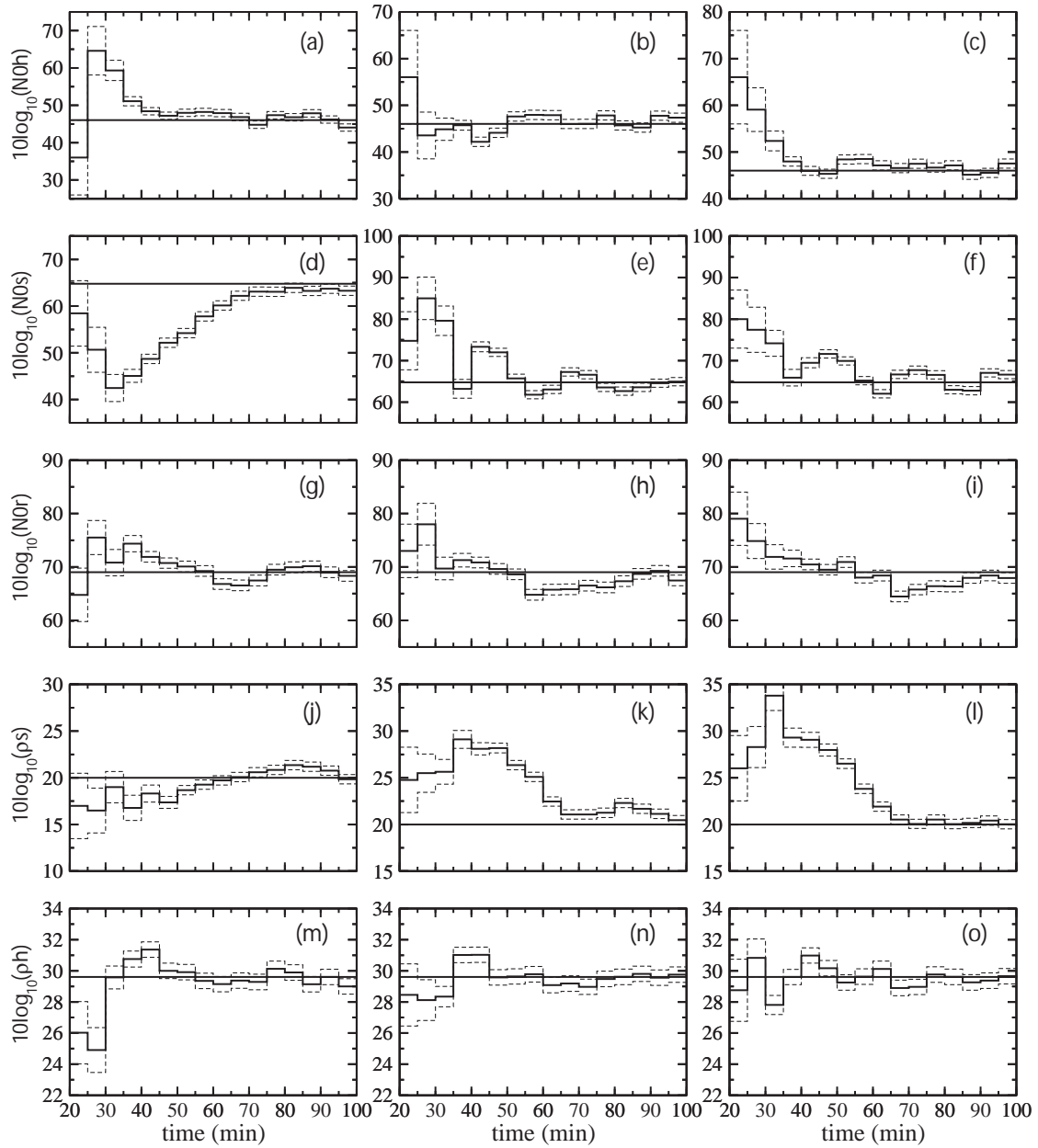


Fig. 5.1. The evolution of the parameter distribution from single-parameter estimation experiments through the assimilation cycles for n_{Oh} (a)-(c), n_{Os} (d)-(f), n_{Or} (g)-(i), ρ_s (j)-(l), and ρ_h (m)-(o). The three columns are for different initial guesses of the parameters which are given in Table 5.2. The straight horizontal lines indicate the true values of the parameters, the solid stair-like curves indicate the ensemble mean of the estimated parameter and the dashed lines curves indicate the $1 \sigma_p$ ensemble width.

$2\sigma_p$ may still occur, although eventually the error becomes no larger than σ_p (e.g. Fig. 5.1h, i, k).

The experiments in Fig. 5.1 show that the estimated parameter does not always consistently approach the truth from the beginning. In the first 1 or 2 assimilation cycles, the parameter can deviate further away from the truth. This has happened to all five parameters (e.g. Fig. 5.1a, e, h, l, m). The initially large inaccuracy can generally be corrected within the next 1 to 2 cycles (e.g. Fig. 5.1a, m). However, in some cases, this initial inaccuracy can significantly affect the convergence rate of parameter estimation. For example, the ensemble means of n_{os} in Fig. 5.1d and ρ_s in Fig. 5.1l reach beyond their admissible values within the first 2 assimilation cycles. It takes several assimilation cycles to draw them back to their reasonable and eventually true values.

At least two factors can affect the convergence rate of the estimated parameter. One is the time scale of the model response to the error in the parameter during the data assimilation process. The results of the sensitivity experiments in Chapter 4 indicate that with the current data assimilation configuration, the model responses to the parameter errors are not reliable within the first two assimilation cycles. This probably explains why inaccurate estimates of the parameter often occur in the first two cycles.

Another factor is associated with the random sampling of the initial parameter perturbations. Fig. 5.2 shows the effect of the randomness in drawing the initial parameter ensemble from a specific distribution function on the results of parameter estimation. The estimation of n_{oh} and ρ_s with first guesses of $4 \times 10^5 \text{ m}^{-3}$ and 400 kg m^{-3} , respectively, are presented. For each parameter, five estimation experiments were performed, with the only difference being with the realization of the initial parameter

ensemble. It can be seen that different realizations result in different convergence rate of the estimated parameter. Even though sensitivity experiments N0h45 and ρ_s400 in Chapter 4 show that the system responses quicker to the corresponding change in n_{0h} than that in ρ_s , the quality of initial sampling can still cause slow convergence for n_{0h} as shown by the thick gray curve in Fig. 5.2a. On the other hand, the estimated ρ_s can approach to the truth within 3 assimilation cycles for some cases as shown by the thick black curve in Fig. 5.2b. Obviously, the realization of the initial parameter ensemble has significant impact on the convergence rate.

The impact of parameter estimation on the model state is shown in Fig. 5.3. The results of experiments ρ_h400 , N0r87, ρ_s400 (dashed curves), for which the initial guesses of ρ_h , n_{0r} and ρ_s are 400 kg m^{-3} , $8 \times 10^7 \text{ m}^{-4}$ and 400 kg m^{-3} , respectively, are presented. The corresponding parameter evolutions can be found in Fig. 5.1m, Fig. 5.1i and Fig. 5.1l. The results of another set of experiments ($\rho_h400\text{NE}$, N0r87NE and $\rho_s400\text{NE}$), in which the wrong initial guess of the parameter is kept without parameter estimation, as well as the results of CNTL (the perfect-parameter case) are also shown in the figure for comparison purposes. The rms errors are shown for the microphysical species only because they are more sensitive to microphysical parameter errors.

For very successful parameter estimations like experiment ρ_h400 in Fig. 5.1m, the errors in the estimated model variables are indistinguishable from those of the perfect-parameter (CNTL) case (Fig. 5.3a-e). In the experiment estimating n_{0r} (N0r87), parameter estimation definitely improves the model state estimation over the case without parameter estimation (N0r87NE, Fig. 5.3f-j). The errors of the state variables

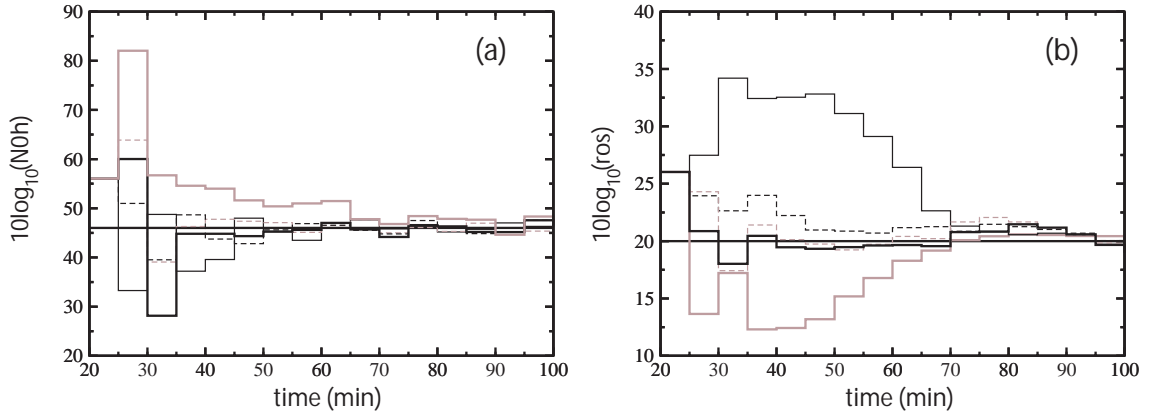


Fig. 5.2. The evolution of the ensemble means of (a) the intercept parameter of hail/graupel n_{oh} (a), and the density of snow ρ_s (b). The five line types represent five estimation experiments with different realizations of the initial parameter ensemble.

are very close to those of CNTL most of the time, except for the larger errors in q_r between 65 and 85 min, which is consistent with the larger error in the estimated n_{or} during that time (Fig. 5.1i).

The third row of Fig. 5.3 shows the results of a relatively poor case of ρ_s estimation. With the parameter estimation, the errors in the model state variables are even larger than the case of no parameter estimation (ρ_s400NE) before 60 min. This is mainly due to the incorrect estimation of ρ_s within the first few assimilation cycles; the error in the estimated ρ_s is larger than its initial error before 50 min (Fig. 5.11). However, as the estimated ρ_s converges to the true value, the errors in the state variables eventually become comparable to those of CNTL in the last 3 to 4 cycles.

Although a limited number of trials are presented here for single-parameter estimation, we are confident that each of the microphysical parameter can converge to the true value, no matter where they are started from. This is supported by the findings

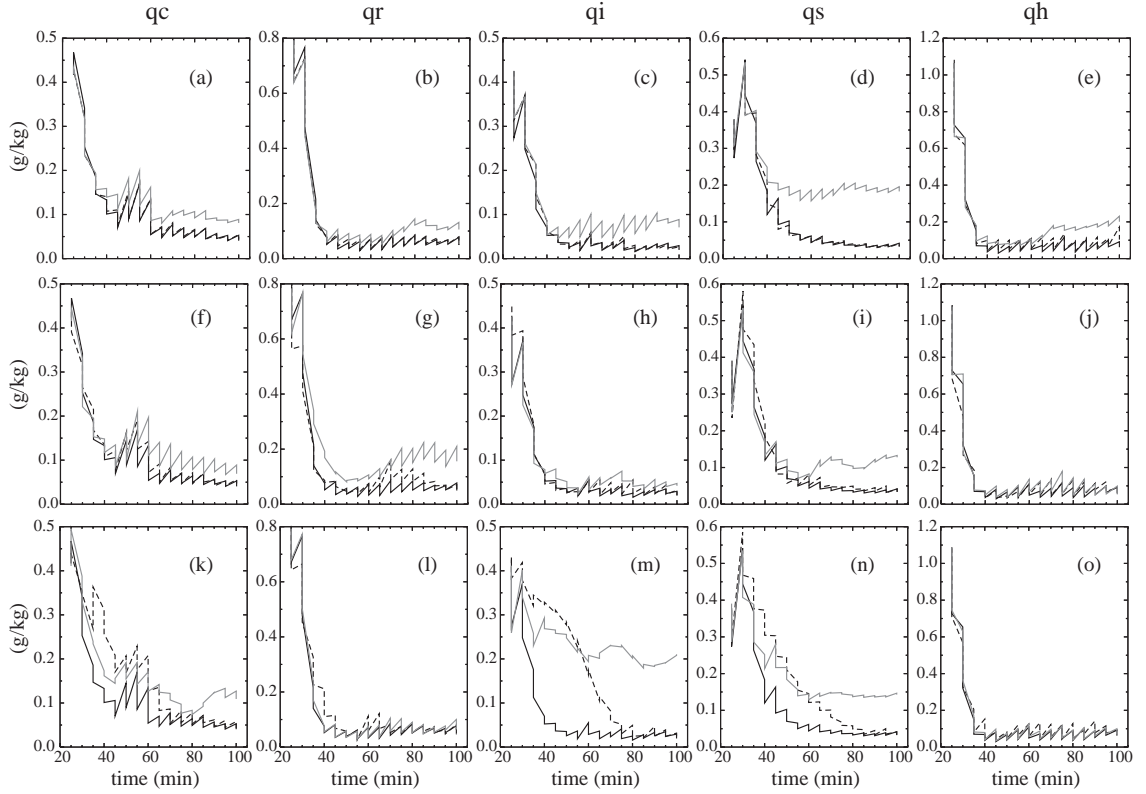


Fig. 5.3. The rms errors of the ensemble-mean forecast and analysis, averaged over points at which the reflectivity is greater than 10 dBZ for q_c (the 1st column), q_r (the 2nd column), q_i (the 3rd column), q_s (the 4th column), q_h (the 5th column), for the CNTL data assimilation experiment (black), parameter estimation experiments (dashed) and data assimilation experiment with imperfect parameter kept throughout the assimilation cycles (gray). The experiments shown have (wrong) initial guesses of $\rho_h = 400 \text{ kg m}^{-3}$ (a-e), $n_{or} = 8 \times 10^7 \text{ m}^{-4}$ (f-j), and $\rho_s = 400 \text{ kg m}^{-3}$ (k-o), which correspond to the experiments in Fig. 5.1m, Fig. 5.1i and Fig. 5.1l.

in Chapter 4 that the response function for each of the microphysical parameter has a unique global minimum.

5.4.2 Results of Multiple Parameter Estimation

In this subsection, we present the results of the experiments, in which multiple microphysical parameters are estimated in different combinations. The parameters not estimated are assumed perfect. Firstly, 2-parameter combinations of (n_{oh}, ρ_h) or (n_{os}, ρ_s)

that controls the hail/graupel or snow DSD are estimated simultaneously. In other experiments, three intercept parameters (n_{0h} , n_{0s} , n_{0r}) are estimated simultaneously. In the 4-parameter case, the intercept parameters and the hail density are estimated together. Finally, all five parameters start with wrong initial guesses are estimated simultaneously.

To investigate the uniqueness of the inverse solution for multiple-parameter estimation and to reduce the chance for the results to be fortuitous in some way, two values are picked from the admissible set P_{ad} for each parameter and the combinations of the chosen values are used as the initial guesses of the parameter vectors. The chosen initial values for each microphysical parameter are listed in Table 5.3. The experiments are also repeated by using ‘error-free’ observations for some combinations.

5.4.2.1 Simultaneous estimation of two parameters

Fig. 5.4 shows the results of the experiments estimating (n_{0h} , ρ_h) using imperfect data. Four combinations of the initial guesses of these two parameters, namely, ($4 \times 10^5 \text{ m}^{-4}$, 400 kg m^{-3}), ($4 \times 10^5 \text{ m}^{-4}$, 700 kg m^{-3}), ($4 \times 10^6 \text{ m}^{-4}$, 400 kg m^{-3}) and ($4 \times 10^6 \text{ m}^{-4}$, 700 kg m^{-3}), are tested (Table 5.3). The four initial guesses represent four q_h distributions with the mass more heavily weighted toward small graupels than that represented by the true values of the two parameters ($4 \times 10^4 \text{ m}^{-4}$, 913 kg m^{-3}). It can be seen from Fig. 5.4 that the two parameters converge to their truth values in all four cases. After converging to the true values, the errors in the parameters are less than or very close to σ_{P_i} .

To further investigate the identifiability of this two-parameter set, we also tested another initial guess of ($n_{0h} = 4 \times 10^3 \text{ m}^{-4}$, $\rho_h = 400 \text{ kg m}^{-3}$). This combination may be

Parameter p_i	p_0^1	P_0^1	p_0^2	P_0^2
$n_{0h} (\text{m}^{-4})$	4×10^5	56.02	4×10^6	66.02
$n_{0s} (\text{m}^{-4})$	7×10^5	58.45	3×10^7	74.77
$n_{0r} (\text{m}^{-4})$	3×10^6	64.77	2×10^7	73.01
$\rho_h (\text{kg m}^{-3})$	400	26.02	700	28.45
$\rho_s (\text{kg m}^{-3})$	50	16.99	300	24.77

Table 5.3. Two initial guesses of each parameter in the original form p_0^m and the logarithmical form P_0^m ($m = 1, 2$) used in multiple-parameter estimation experiments.

unphysical because the small intercept parameter indicates that the DSD is typical of storm with large hails while the low density is typical of hail therefore their estimation starting from such initial guesses may be problematic. In our first test, the two parameters could not converge to their true values, as shown by the gray curves in the left column of Fig. 5.5. Considering that the initial sampling error may affect the estimation of the parameters, five more tests were performed, which used the same data but different realizations of the initial parameter ensemble. Their results are shown in the right column of Fig. 5.5. In all of these five experiments, n_{0h} and ρ_h can converge to their true values. Fig. 5.5b and Fig. 5.5d show that the two-parameter estimation results, in terms of the convergence time of the estimated parameters, are very sensitive to the realization of the initial parameter ensemble. In the other four experiments shown in Fig. 5.5a and Fig. 5.5c, not only the realizations of the initial ensemble are different, the imperfect observation data used are also different, yet there is no problem with the convergence of these two parameters in these cases. Several variations on the

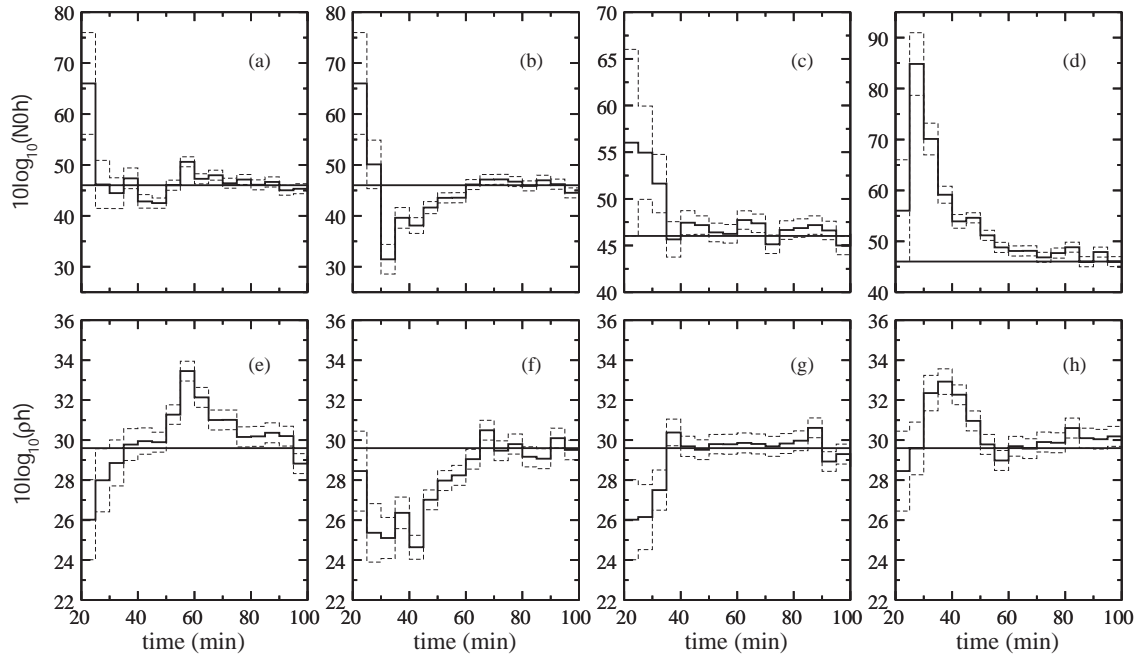


Fig. 5.4. The evolution of the parameter distribution (solid curves: ensemble mean, dashed curves: $1\sigma_{P_i}$ ensemble width) vs. true parameter values (straight lines) for experiments simultaneously estimating n_{oh} (the upper row) and ρ_h (the lower row). The four columns are the results of four experiments with different combination of the initial guesses of the two parameters.

realization of the initial ensemble have also been performed for the former four initial guesses; in all cases, the two parameters converge to their true values.

Fig. 5.6a-e and Fig. 5.6f-j show the rms errors of the estimated hydrometeor mixing ratios from the parameter estimation experiments shown in the 1st and 4th columns of Fig. 5.4, respectively. In both experiments, after the two parameters converge to their true values, the rms errors of the mixing ratios are very close to those of CNTL. Relatively larger differences between CNTL and these experiments are found in the two most sensitive species, q_s and q_h .

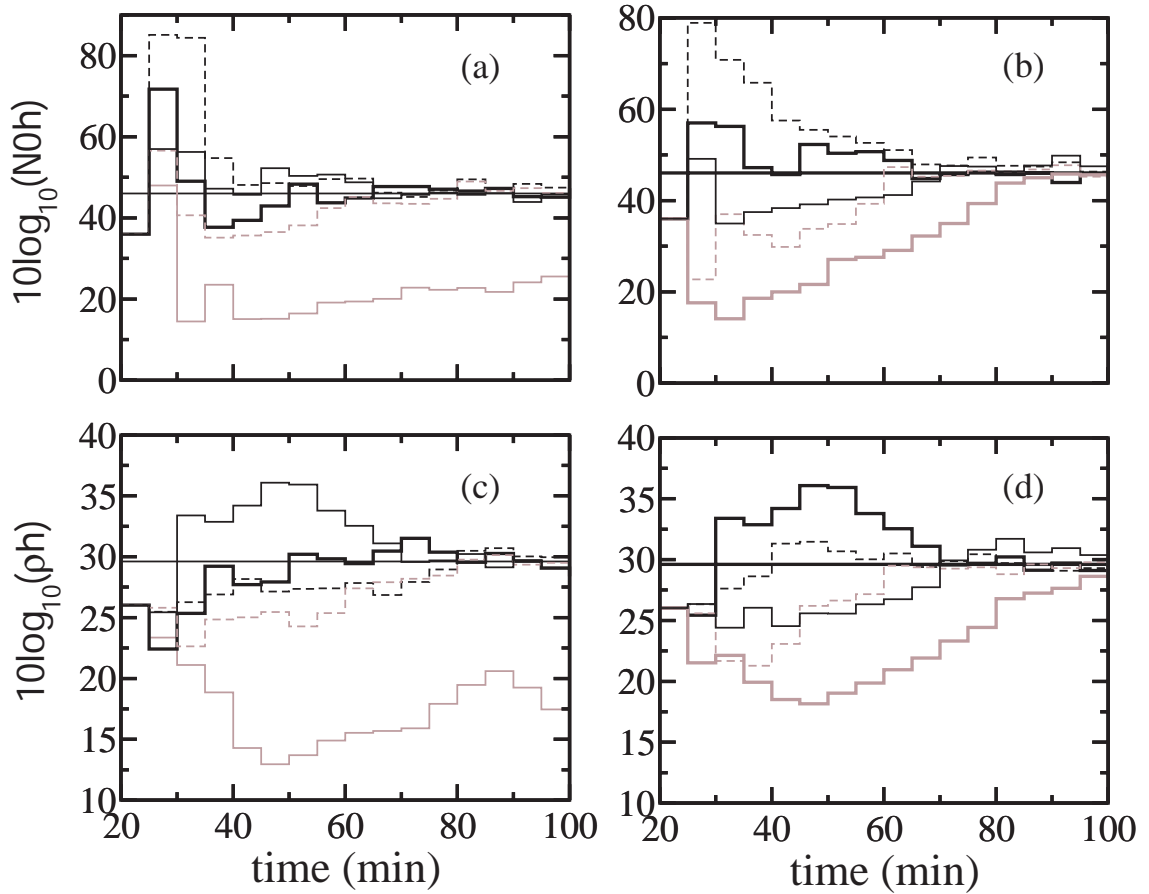


Fig. 5.5. The evolutions of the ensemble means together with the true values (straight line) of n_{oh} (a)-(b), and ρ_h (c)-(d), from experiments estimating (n_{oh}, ρ_h) starting from $(4 \times 10^5 \text{ m}^{-4}, 400 \text{ kg m}^{-3})$. The different line types in each column represent different experiments. The left column shows the results of experiments using different realizations of the initial ensemble and data with different errors. The experiments in the right column use the same data as that indicated by the gray curves in the left column but with different initial ensemble realizations.

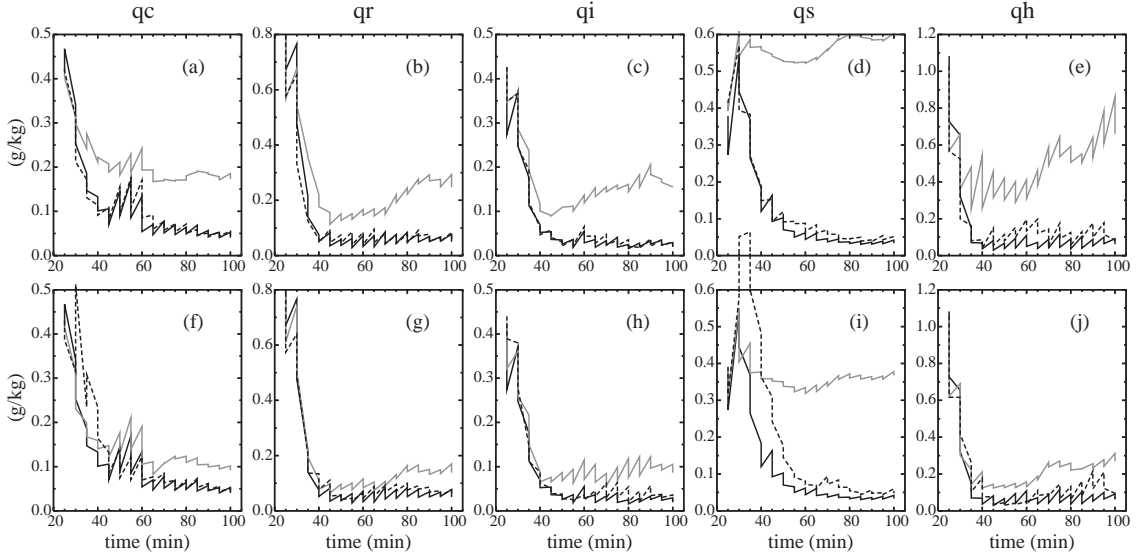


Fig. 5.6. The same as Fig. 5.3, but for the two-parameter set (n_{oh}, ρ_h) . The experiments shown have initial guess or imperfect value of $(n_{oh}, \rho_h) = (4 \times 10^6 \text{ m}^{-4}, 400 \text{ kg m}^{-3})$ (a-e), and $(n_{oh}, \rho_h) = (4 \times 10^6 \text{ m}^{-4}, 400 \text{ kg m}^{-3})$ (f-j), which correspond to the experiments in the 1st and the 4th column of Fig. 5.4, respectively.

The results of simultaneous estimation of two snow parameters, (n_{os}, ρ_s) , are shown in Fig. 5.7. The four initial guesses for the two parameters are $(3 \times 10^7 \text{ m}^{-4}, 300 \text{ kg m}^{-3})$, $(3 \times 10^7 \text{ m}^{-4}, 50 \text{ kg m}^{-3})$, $(7 \times 10^5 \text{ m}^{-4}, 300 \text{ kg m}^{-3})$ and $(7 \times 10^5 \text{ m}^{-4}, 50 \text{ kg m}^{-3})$. We first performed experiments using 40 ensemble members, which are shown by the gray curves in Fig. 5.7. It can be seen that the results are generally not very good. In the four cases, either the two parameters converge to the true values slowly (gray curves in the 1st and 3rd columns), or one or both parameters do not converge to the true values at all (gray curves in the 2nd and 4th columns). We repeated these four experiments using ‘error-free’ data and different realizations of the initial parameter ensemble, but still found the results to be generally poor. We then repeated the first four experiments using 100 ensemble members instead (black curves in Fig. 5.7). The large ensemble generally

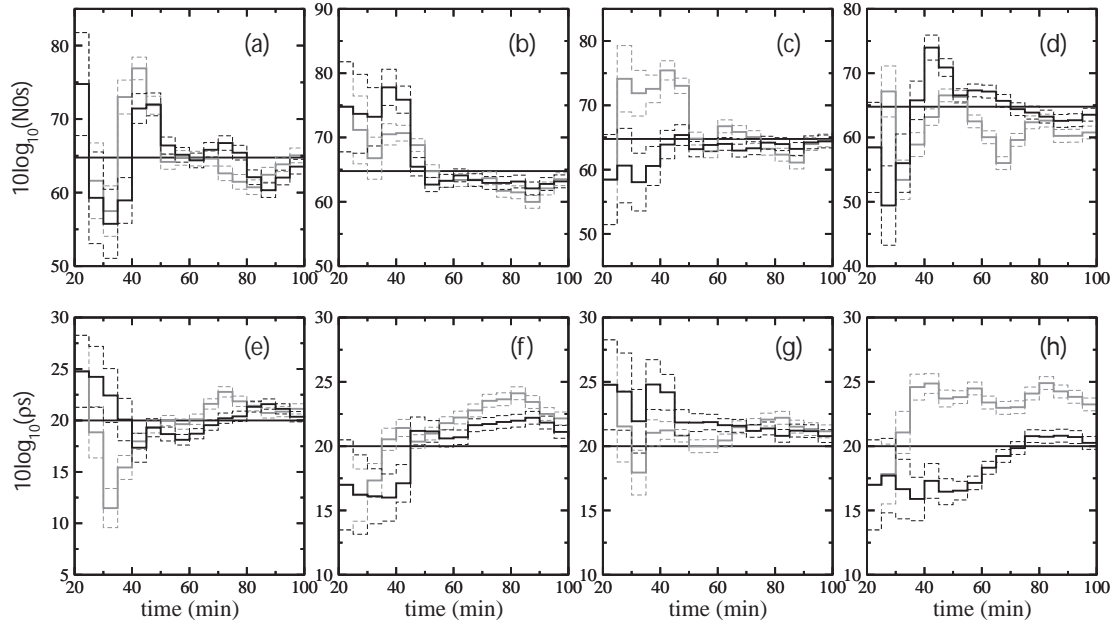


Fig. 5.7. The evolutions of the ensemble means together with the true values (straight lines) of n_{0s} (upper panel) and ρ_s (lower panel) from experiments simultaneously estimating (n_{0s}, ρ_s) starting from four different initial guesses (one column for each). The gray and black curves are from the experiments using 40 and 100 ensemble members, respectively.

improved the estimation, as seen, e.g., from the 2nd and 4th columns of Fig. 5.7. However, even with 100 members, the estimations of (n_{0s}, ρ_s) are still not as good as those of (n_{0h}, ρ_h) (c.f., Fig. 5.4), in term of the convergence rate and accuracy of the estimation. Consistently, the model state estimations are not as good as compared to Fig. 5.6, although improvement is still significant compared to the case of no parameter estimation (not shown).

5.4.2.2 Simultaneous estimation of three parameters

The results of simultaneously estimating three intercept parameters together are presented in Fig. 5.8, for which 40 ensemble members are used. Based on the two initial guesses of each intercept parameter in Table 5.3, 8 combinations of initial guesses were

used for estimating these three parameters. The experiments were first performed using ‘error-free’ radar data, and the results are shown in the first column of Fig. 5.8. The realizations of the initial ensemble were also different among these experiments. The different line types represent these 8 different experiments.

It can be seen from Fig. 5.8a, Fig. 5.8d and Fig. 5.8g, for the experiments using error-free data, different initial guesses lead to similar ending points that are all close to the true values. The estimation of n_{0h} and n_{0r} are better than that of n_{0s} , which has a larger variability among different cases. The estimated n_{0s} values also converge to the true value slower than the other two parameters. In some cases, the estimated n_{0s} has even larger error than its initial guess for a major portion of the assimilation cycles (e.g. the thin black curve in Fig. 5.8d). However, even in such a case, n_{0s} still converges to the truth in the end.

The thick black curves in the first column of Fig. 5.8 represent the best case among the 8 experiments. In this case, the curve of estimated n_{0h} almost exactly overlies the true value line after 6 assimilation cycles (Fig. 5.8g), and the estimated n_{0r} converges to the true value after 3 assimilation cycles and remains very close to the true value afterwards (Fig. 5.8a). The estimated n_{0s} converges to the true value after 6 assimilation cycles. Although some deviation from the true value occurs to n_{0s} during later cycles, the estimation becomes very accurate by the last two cycles (Fig. 5.8d).

Encouraged by the results using error-free data, we then repeated the experiments using error-containing data, with each set containing random error [vector v in Eqs. (5.6) and (5.7)] of different realizations. The results are shown in the 2nd column of Fig. 5.8. Even with these imperfect observations, the three intercept

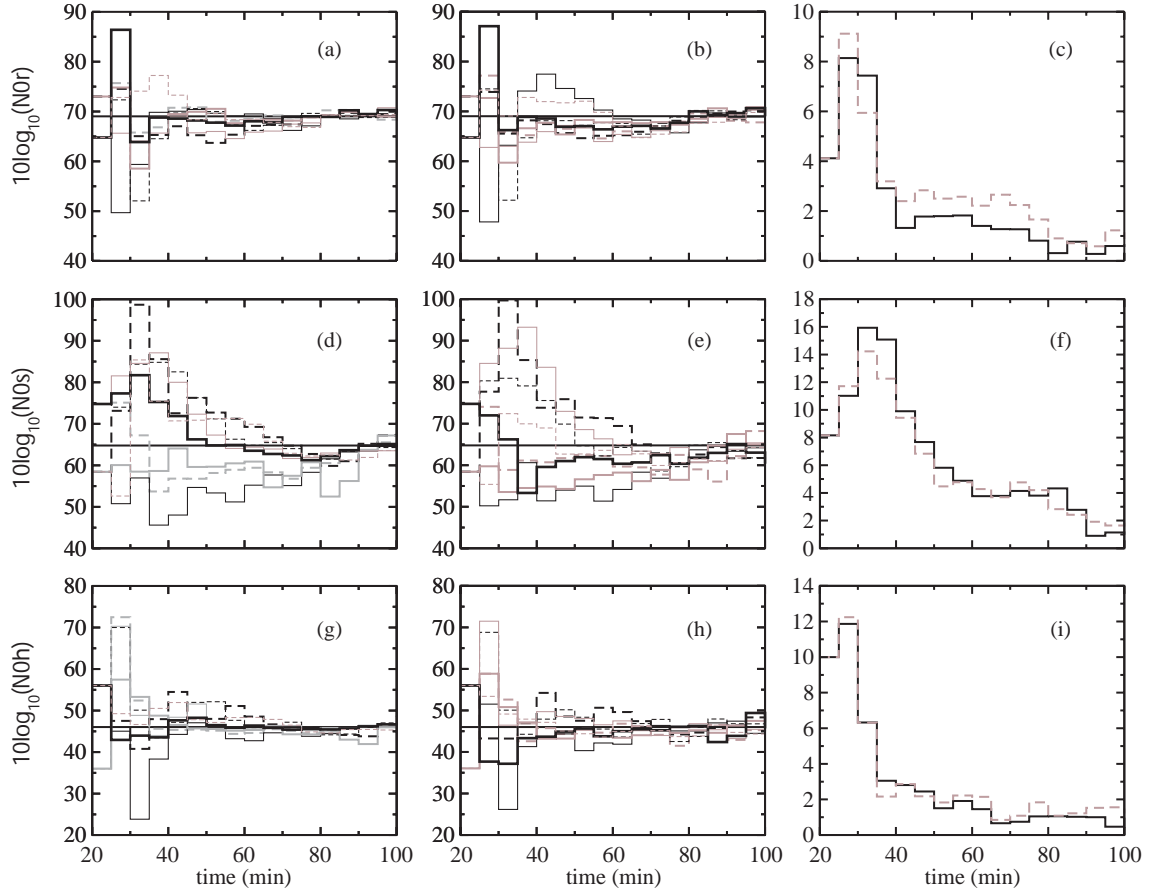


Fig. 5.8. The left and central columns show the ensemble means of n_{or} (a)-(b), n_{os} (d)-(e), and n_{oh} (g)-(h) of the experiments estimating three intercept parameters simultaneously. In the right column are the average ensemble-mean absolute errors of the experiments in the left column (black solid) and experiments in the central column (gray dash) of $10\log_{10}(n_{or})$ (c), $10\log_{10}(n_{os})$ (f), and $10\log_{10}(n_{oh})$ (i). The 8 different line types represent the experiments starting from 8 different initial guesses of the intercept parameters, which are combinations of the values listed in Table 5.3. The experiments shown in the left column assimilated ‘error-free’ data while those in the central column used ‘error-containing’ data.

parameters still converge to the points close to the true values; again, n_{oh} and n_{or} are better estimated than n_{os} .

The 3rd column of Fig. 5.8 compares the ensemble mean absolute errors of the three parameters estimated using error-free data (black solid) and error-containing data (gray dash), averaged over the 8 estimation experiments. The largest difference

between the two sets of experiments is with n_{0r} (Fig. 5.8c). The error in the estimated n_{0r} using error-containing data is most of the time notably larger than that using error-free data. The average absolute error of n_{0r} can decrease below $\underline{\sigma}_{P_i}$ in the last 7 assimilation cycles in the error-free data case; it can also decrease below $\underline{\sigma}_{P_i}$ in later assimilation cycles in the imperfect data case. The average error of n_{0s} does not become close to $\underline{\sigma}_{P_i}$ until the last two assimilation cycles if error-free data are used. The corresponding error in the imperfect data case remains above $\underline{\sigma}_{P_i}$ (close to $2\underline{\sigma}_{P_i}$) even by the end of assimilation cycles. The average error of n_{0h} decreases faster in both sets of experiments than the errors of the other two parameters and become very close to $\underline{\sigma}_{P_i}$ during the last 8 assimilation cycles in both cases.

We picked two cases, which correspond to the thin black and thick black curves in Fig. 5.8, to demonstrate the impact of the estimation of the three parameters on the model state estimation. In the first case, n_{0s} approaches to the true value very slowly (thin black curves in Fig. 5.8e). As a result, the analyses of q_i and q_s improved slowly (Fig. 5.9c and d). However, as long as the parameters converge to the true values, the model state estimation can be as good as that of CNTL in the end (Fig. 5.9a-e). In the second case, the three parameters approach the true values faster, but the estimation of n_{0h} ends up with a relatively large error in the end. As a result, the analysis error of q_s is larger than that of CNTL, but still significantly smaller than the case without parameter estimation.

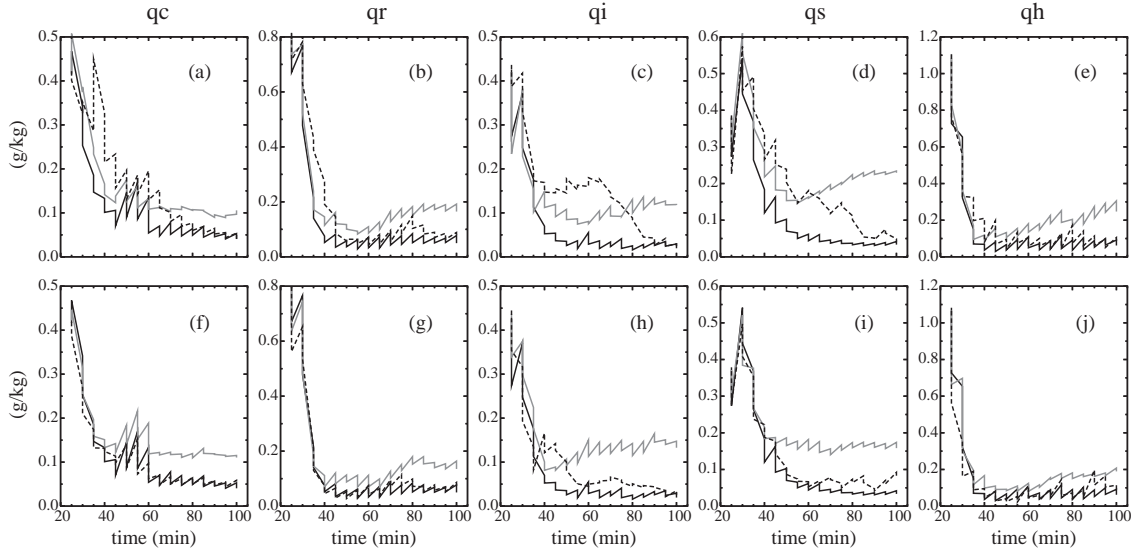


Fig. 5.9. The same as Fig. 5.3, but for the three-parameter set (n_{0r}, n_{0s}, n_{0h}) . The experiments shown have initial guesses or imperfect values of $(n_{0r}, n_{0s}, n_{0h}) = (0.03 \text{ m}^{-4}, 0.007 \text{ m}^{-4}, 0.00004 \text{ m}^{-4})$ (a-e), and $(n_{0r}, n_{0s}, n_{0h}) = (0.03 \text{ m}^{-4}, 0.007 \text{ m}^{-4}, 0.00004 \text{ m}^{-4})$ (f-j), which correspond to the thin black curves and the thick black curves in the 2nd column of Fig. 5.8, respectively.

5.4.2.3 Simultaneous estimation of four parameters

Given the encouraging results of simultaneously estimating three intercept parameters, we now move on to the estimation of four parameters, with the hail density as the additional one. A total of 16 combinations of the initial guesses of n_{0r} , n_{0s} , n_{0h} , and ρ_h were tested initially using 40 ensemble members. Among the 16 experiments, only 3 resulted in the errors that are smaller than $\underline{\sigma}_{P_i}$ for all 4 parameters at the end of the assimilation cycles. Five other experiments approached the true values but the errors of some parameters were between 1 $\underline{\sigma}_{P_i}$ and 3 $\underline{\sigma}_{P_i}$; they were generally much smaller than the initial errors though. The results from the other 8 experiments were poor. These

results indicate increased difficulties when more parameters are estimated simultaneously. The use of more ensemble members hopefully will help.

The estimation of the four-parameter set can indeed be significantly improved by using 100 ensemble members (Fig. 5.10). In the two cases shown in the 1st column of Fig. 5.10, all four parameters converge to their true values; the resultant errors of all four parameters are no larger than $\underline{\sigma}_{P_i}$. We also see that the convergence rates of the four parameters are very good. The parameter that approaches to the true value fastest (within 6 to 7 cycles or 30 to 35 minutes) is n_{0r} . Hail density has the slowest convergence rate but the convergence still occurs within one hour.

The 2nd column of Fig. 5.10 shows 2 of 6 cases, in which the 4 parameters approach to the true values but the ending errors for some of the parameters are around $2 \underline{\sigma}_{P_i}$. The 3rd column of the figure shows 2 of 4 cases, in which two or three parameters approach the true values slowly and some of them have errors larger than $3 \underline{\sigma}_{P_i}$ in the end. The relatively poor estimation usually happens to n_{0h} and ρ_h , and sometimes to n_{0s} . The intercept parameter of rain is estimated very well in all cases.

Fig. 5.11 shows the absolute ensemble mean errors of the four parameters averaged over the 16 experiments with different initial guesses. The gray dash curves represent the experiments using error-containing data, i.e., those experiments discussed above. The average absolute error of n_{0r} decreases below $2 \underline{\sigma}_{P_i}$ after 5 assimilation cycles, and the error reduced below $1 \underline{\sigma}_{P_i}$ in the last 3 assimilation cycles. The error of n_{0s} decreases faster than that of n_{0h} and ρ_h . At the end of the assimilation cycles, the errors of n_{0s} , n_{0h} and ρ_h are all between $1 \underline{\sigma}_{P_i}$ and $2 \underline{\sigma}_{P_i}$. The black curves in Fig. 5.11

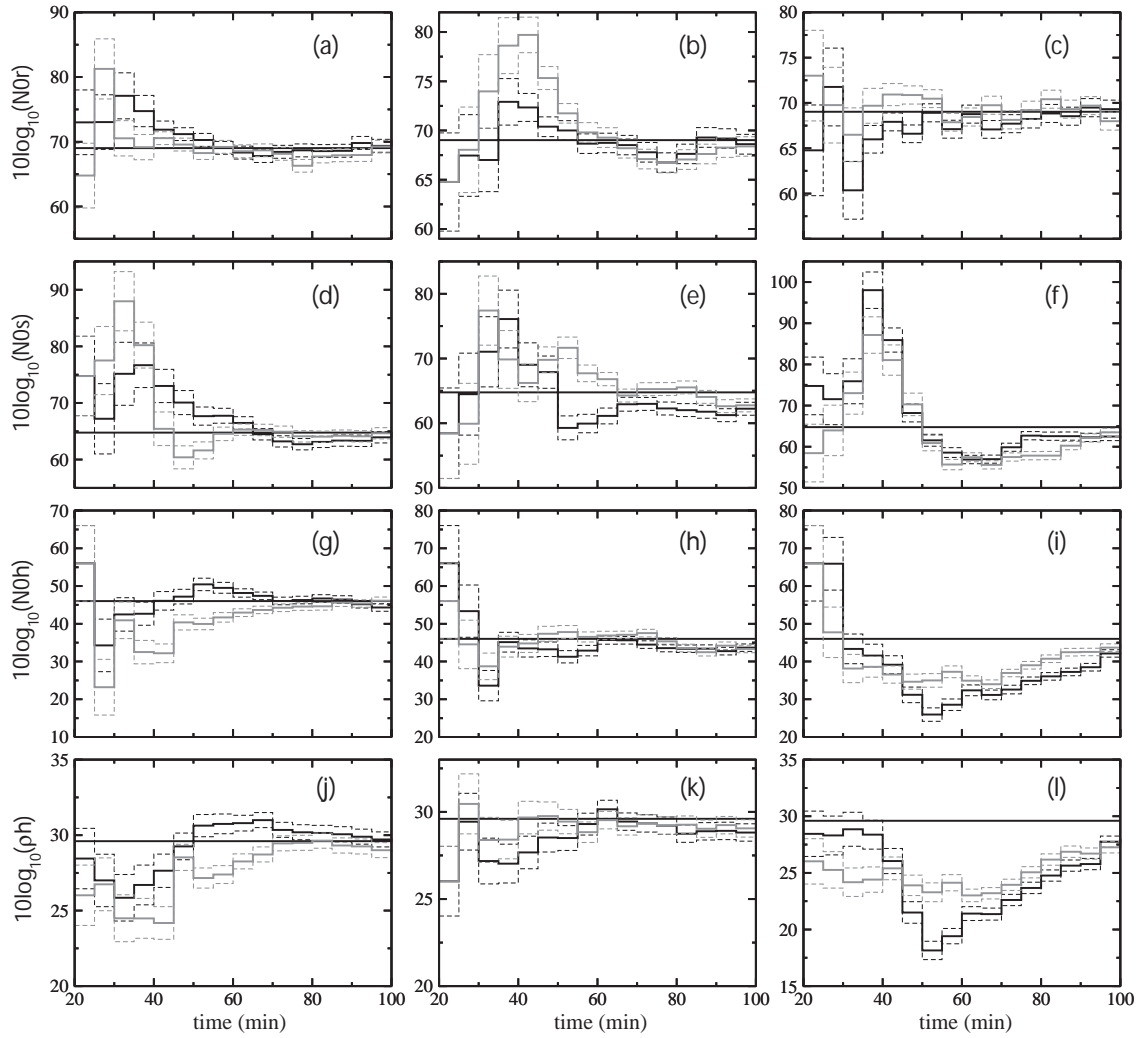


Fig. 5.10. The same as Fig. 5.4, but for experiments estimating n_{0r} (a-c), n_{0s} (d-f), n_{0h} (g-i), and ρ_h (j-l), simultaneously. The results of 6 (2 in each column) of totally 16 experiments with different initial guesses of $(n_{0r}, n_{0s}, n_{0h}, \rho_h)$ are presented, with each experiment presented by the same type of curves in each column.

are for the errors calculated from the corresponding experiments but using error-free data. Although the data are error free, the same error variances for V_r (1 m s⁻¹) and Z (3 dBZ) are used during the assimilation. Using the error-free data, the errors of the estimated parameters are significantly smaller; they are reduced below $1 \sigma_{P_i}$ for all four parameters at the end of the assimilation cycles.

The impact of the four-parameter on the state estimation is shown in Fig. 5.12, in which the *rms* ensemble mean errors of the mixing ratios from the 3 experiments represented by the black curves in each column of Fig. 5.12 are presented. The *rms* errors from the experiment with successful parameter estimation (black curves in Fig. 5.10a, d, g and j) are comparable to those of CNTL after 60 min or 8 assimilation cycles for all five hydrometeors (Fig. 5.12a-e). The larger errors in the estimated parameters in Fig. 5.10b, e, h and k result in larger errors in q_r , q_i and q_s in certain assimilation cycles (Fig. 5.12g, h and i) compared to those in Fig. 5.12b, c and d; the state estimation is also good, however, and is much better than the corresponding case without parameter estimation (the gray lines). For the experiment with relatively poor parameter estimation (black curves in Fig. 5.10c, f, i and l), the model state estimation is generally not as good as that of CNTL but is also much better than the case with no parameter estimation (Fig. 5.12k-o). For this case, we can also see that in the last two assimilation cycles, the *rms* errors of the mixing ratios are very close to those of CNTL, except for q_s . This, we believe, is because the estimations of n_{oh} and ρ_h are poor in this experiment (Fig. 5.10i and l) and q_s is very sensitive to their errors, as indicated by the gray curve in Fig. 5.12n.

Several additional experiments were performed with different realizations of the randomness in the initial ensemble and observation error for the four cases of poor parameter estimation, and we did not find any case that is worse than those shown in Fig. 5.10i and Fig. 5.10j. In most of those additional trials, the quality the estimations is similar to the two cases shown in the 2nd column of Fig. 5.10, and some cases even end up with parameter errors being no larger than $1 \sigma_{P_i}$.

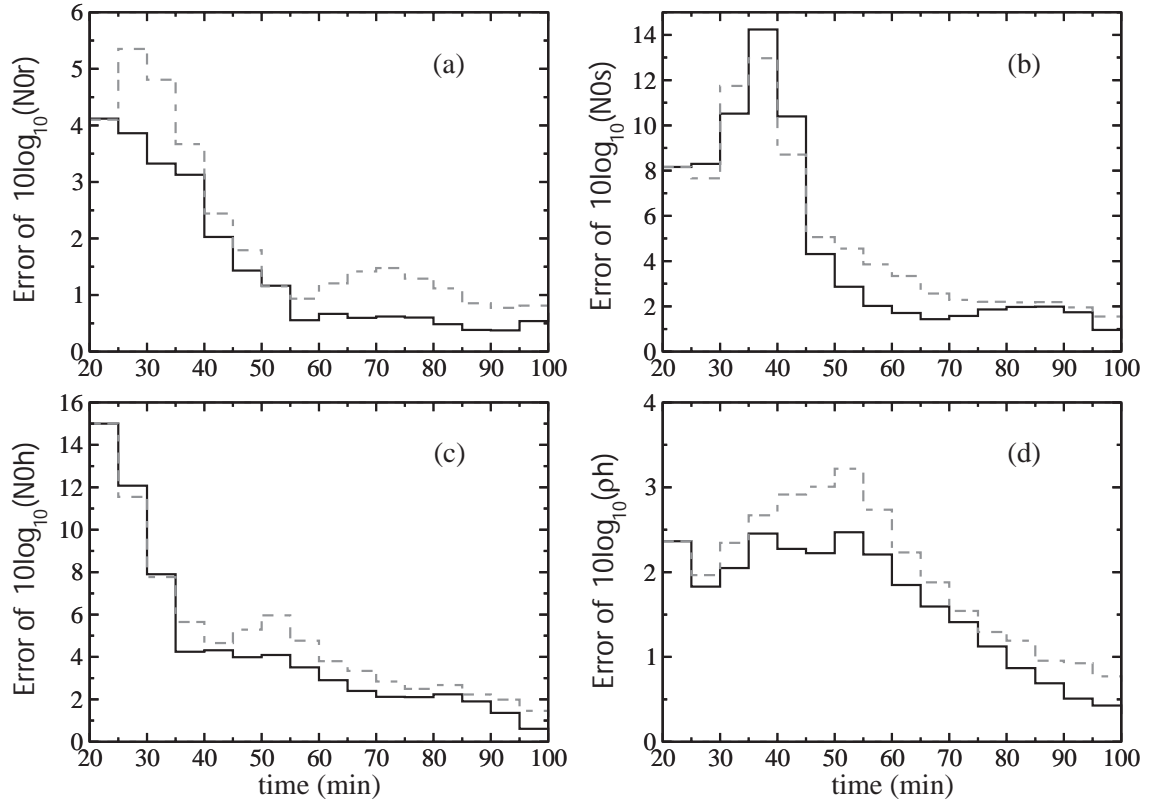


Fig. 5.11. The evolution of the average ensemble-mean absolute error of $10\log_{10}(n_{Or})$ (a), $10\log_{10}(n_{Os})$ (b), $10\log_{10}(n_{Oh})$ (c), and $10\log_{10}(\rho_h)$ (d), calculated from the 16 experiments simultaneously estimating $(n_{Or}, n_{Os}, n_{Oh}, \rho_h)$ using error-containing data (gray) and error-free data (black).

5.4.2.4 Simultaneous estimation of five parameters

We present next the results of simultaneous estimation of all five microphysical parameters. Using the two values of each parameter in Fig. 5.13 as initial guesses, 32 combinations of the initial guesses were used for estimating the five-parameter set $(n_{Or}, n_{Os}, n_{Oh}, \rho_s, \rho_h)$. In this case, there are more variations in the success of parameter estimation across the experiments. According to the quality of parameter estimation, we classify the experiments into three classes and present two experiments for each class as we did for the four-parameter experiments.

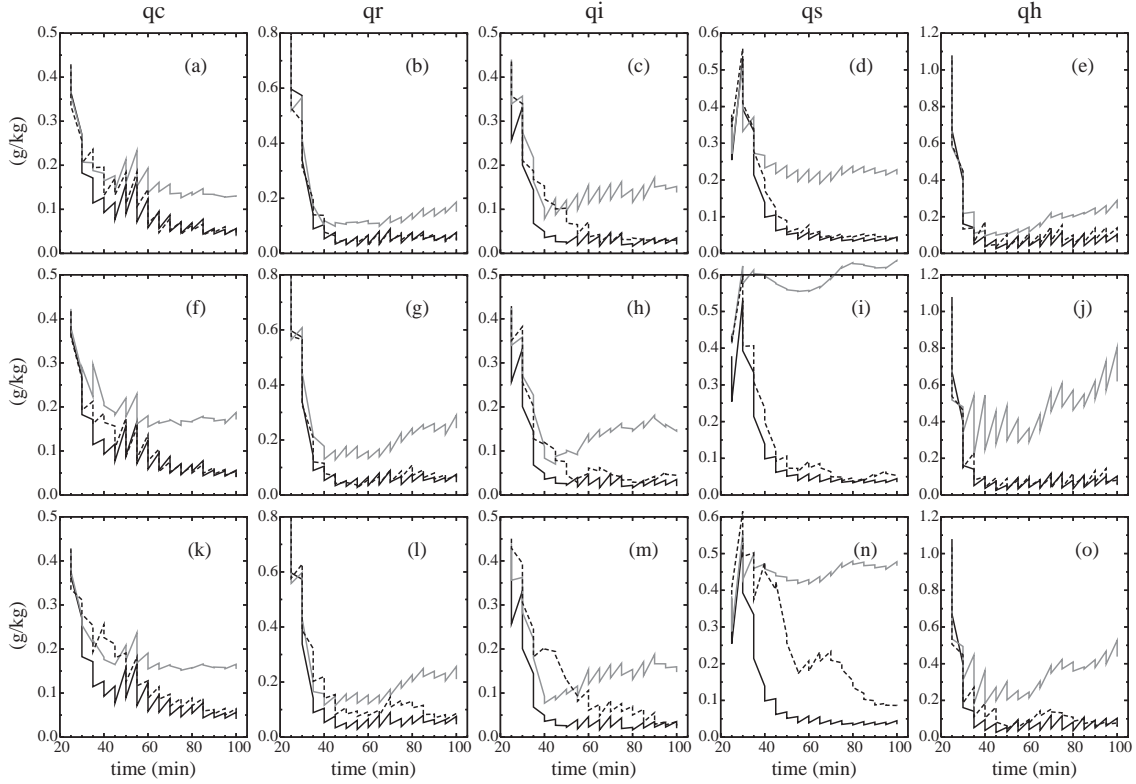


Fig. 5.12. The same as Fig. 5.3, but for the four-parameter set $(n_{0r}, n_{0s}, n_{0h}, \rho_h)$. The experiments shown have initial guesses of $(n_{0r}, n_{0s}, n_{0h}, \rho_h) = (0.2 \text{ m}^{-4}, 0.3 \text{ m}^{-4}, 0.004 \text{ m}^{-4}, 700 \text{ kg m}^{-3})$ (a-e), $(n_{0r}, n_{0s}, n_{0h}, \rho_h) = (0.03 \text{ m}^{-4}, 0.007 \text{ m}^{-4}, 0.04 \text{ m}^{-4}, 400 \text{ kg m}^{-3})$ (f-j), and $(n_{0r}, n_{0s}, n_{0h}, \rho_h) = (0.03 \text{ m}^{-4}, 0.3 \text{ m}^{-4}, 0.04 \text{ m}^{-4}, 700 \text{ kg m}^{-3})$ (k-o), which correspond to the black curves in the 1st, 2nd and 3rd column of Fig. 5.10, respectively. To be consistent, 100 ensemble members are used in the control experiment shown here.

The two cases shown in the 1st column of Fig. 5.13 represent very good estimations, in which the five parameters all converge to their true values with the final errors for all parameters being no larger than $1 \underline{\sigma}_{P_i}$. Unfortunately, only 4 of the 32 experiments result in very successful estimations. The two estimations shown in the 2nd column of Fig. 5.13 are still acceptable; one or two parameters end up with errors larger than $1 \underline{\sigma}_{P_i}$ but less than $3 \underline{\sigma}_{P_i}$. Only 4 of the 32 experiments belong to this class. In the remaining 24 experiments, at least one of the five parameters can not converge to the

true values. Two of such examples are shown in the 3rd column of Fig. 5.13. Nine more poor estimations are similar to the black curve case in this column, for which the estimated n_{0h} , n_{0s} and ρ_h have negative biases (Fig. 5.13f, i and o). The gray curve case shown also has the similar biases and the errors are larger during the earlier cycles. Similar to what was found in the four-parameter experiments, n_{0r} always converges to the true value, no matter how poorly the other parameters are estimated.

5.5 Discussions

In this section, we return to the issue of parameter identifiability and discuss some factors that might affect the parameter estimation using the EnKF method.

First, whether the uncertain parameters are identifiable is ultimately determined by whether the inverse problem has a unique solution. According to the definition of the least square identifiability of Chavent (Chavent 1979), a parameter is said to be least square identifiable if the least square performance function for identifying the parameter has a unique minimization in a given region and if the minimization is continuously dependent on the measurement errors. The EnKF algorithm does not explicitly minimize the performance function, which usually measures the difference between the model solution and the observations, but the adjustment made to the prior in the EnKF is proportional to that difference. If different values of a single parameter or different combinations of multiple parameters result in the same model solution or system response, then the correct parameter estimation can not be guaranteed because multiple possible solutions exist.

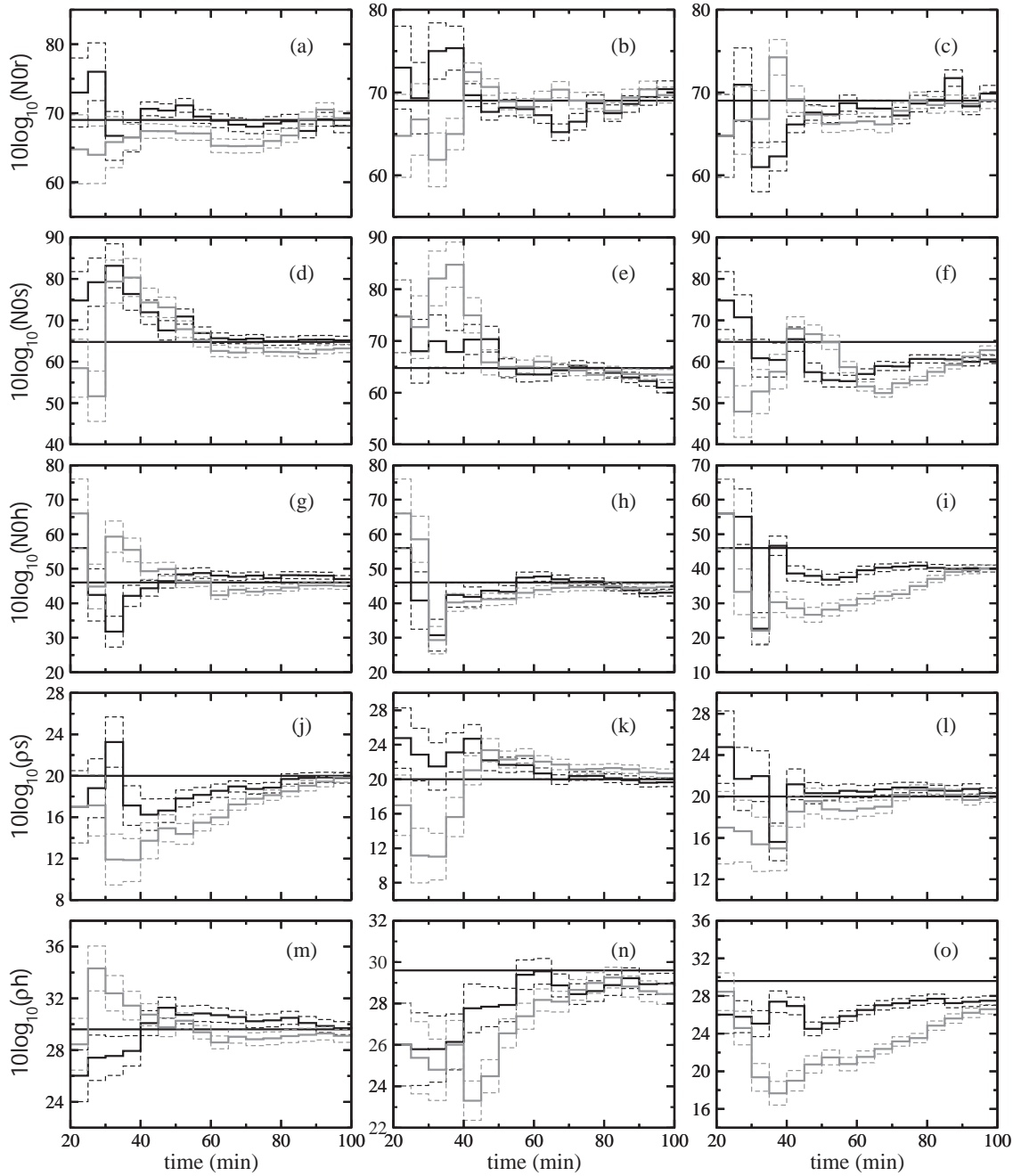


Fig. 5.13. Same as Fig. 5.4, but for n_{or} (a)-(c), n_{os} (d)-(f), n_{oh} (g)-(i), ρ_s (j)-(l), and ρ_h (m)-(o) from experiments simultaneously estimating the four parameters. The results of 6 of a total of 16 experiments with different initial guesses of $(n_{or}, n_{os}, n_{oh}, \rho_h)$ are presented, with each experiment represented by the same type of curves in each column.

Since we have shown that single parameters can always be estimated with good enough accuracy, because of the unique global minima of the response functions, we further discuss the identifiability of multiple-parameter sets only. The results of four- and five-parameter sets suggest that multiple local minima do exist, which is not surprising because of the high nonlinearity of the microphysical processes and their interaction with the model dynamics. The multiple minima could significantly impact the estimation of multiple parameters. What is interesting to us is that in the four experiments with poor estimations in the four-parameter case, n_{0h} and ρ_h always converge to values that smaller than their true values in tandem. In two of the four experiments, n_{0s} also converges to a value smaller than the true value. As mentioned earlier, in 11 of the 24 poor-estimation experiments for the five-parameter case, the estimated n_{0h} and ρ_h are significantly smaller (absolute error $< 3\sigma_p$) than their true values, and in 10 of the 11 experiments, the estimated n_{0s} is also smaller than its true values. Further, the evolutions of the estimated n_{0h} , ρ_h and n_{0s} are similar in those experiments, as can be seen from Fig. 5.13f, i and o.

Fig. 5.14 shows the correlations between radar reflectivity and the five parameters, which are calculated from the prior (forecast) ensemble at 70 min. The results shown are from single-parameter estimation experiments. The correlation patterns in Fig. 5.14 are similar to those obtained from ensemble forecast in Chapter 4 and the physical meanings of those correlations have already been discussed there. Here, we try to use the correlation information to estimate the possible model response in terms of reflectivity to the combination of the errors in the five parameters. Comparing Fig. 5.14a, f with Fig. 5.14d, i, we can see that the correlations are similar in pattern, but the

signs are reversed. This means if smaller n_{0h} results in smaller reflectivity in the southern anvil region (positive correlations in Fig. 5.14f), smaller ρ_h can compensate for the reduction of reflectivity in that region (negative correlations in Fig. 5.14i). The correlation of n_{0s} also shows a reversed pattern with that of n_{0h} in the anvil region. Therefore, the increase/decrease in Z in the anvil due to the increase/decrease in n_{0h} can be compensated by the increase/decrease in n_{0s} . Similarly, the increase in Z at low-level convective region due to smaller ρ_h (Fig. 5.14d) can be compensated for by smaller n_{0h} (Fig. 5.14a). The increase in Z at the southern part of the anvil region due to smaller ρ_h can be compensated for by smaller n_{0s} (negative correlations in Fig. 5.14b). Therefore, the errors of n_{0h} , ρ_h and n_{0s} can be combined in such a way (e.g., with all of them being smaller than their true values) that the difference between the model solution and the observations is small in terms of Z . In another word, such a combination could result in a minimum of the response function for the five-parameter set. Even though the correlations are still meaningful and significant, and the filter can adjust the parameters in the right directions, the ending values of parameter estimation may not be correct because the response function is already at a minimum.

In other five-parameter experiments with poor estimation, if neither n_{0h} nor ρ_h converges to the true values, they must have the same bias. If neither n_{0s} nor ρ_s converges to the true values, their biases should be reversed in sign. Based on the correlation information, similar explanations can be applied to these situations and to the estimation of other multiple-parameter experiments. The three intercept parameters can usually be retrieved accurately, especially in the absence of density error. The model responses to the errors in these parameters are apparently more independent of

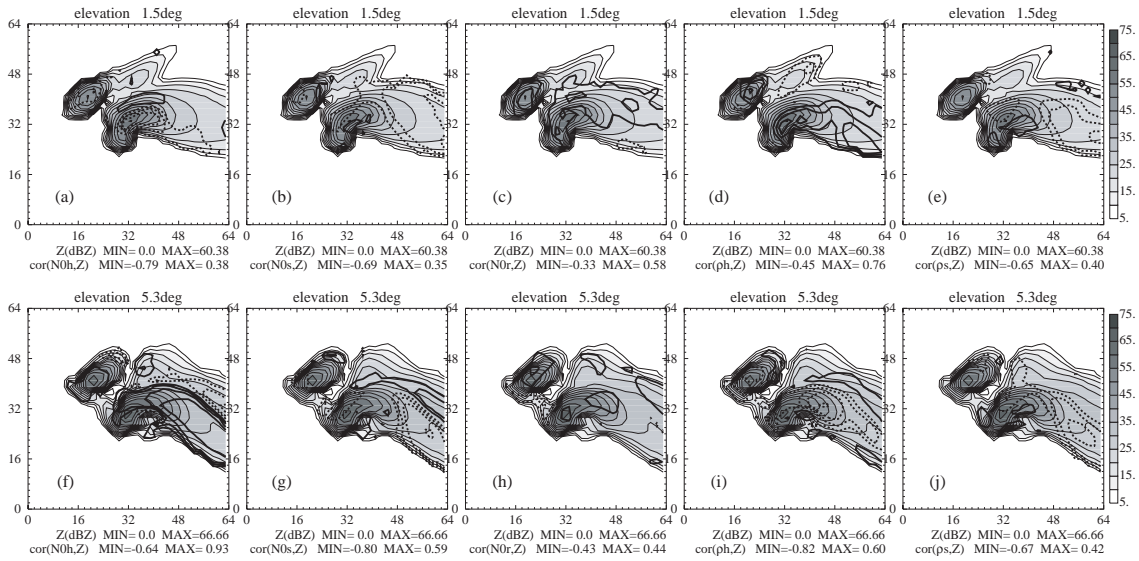


Fig. 5.14. Correlation coefficients calculated from the forecast ensemble at $t = 70$ min from single-parameter estimation experiments. The correlation coefficients [thick solid (dashed) contours represent positive (negative) values at intervals of 0.2] between Z at 1.5° elevation and n_{0h} (a), n_{0s} (b), n_{0r} (c), ρ_h (d), and ρ_s (e); and the correlation coefficients between Z at 5.3° elevation and n_{0h} (f), n_{0s} (g), n_{0r} (h), ρ_h (i), and ρ_s (j). The shading and thin solid contours represent Z from the truth simulation.

each other. However, the qualities of estimation are not necessarily the same for these intercept parameters. The estimation of n_{0s} is generally not as good at those of n_{0h} and n_{0r} , although the average correlation for n_{0s} is higher than that of n_{0r} (not shown). This is probably because the model responds less independently to the changes in n_{0h} and n_{0s} , as can be seen from Fig. 5.14f and g.

The identifiability of the parameters depends not only on the uniqueness of the inverse solution but also on the quality of observational data. This dependence can be clearly seen in Fig. 5.9 and Fig. 5.11. The estimated parameters are closer to their true values when the observation error is reduced. It can be seen that the impact of reducing observation error is larger when the number of uncertain parameters increases. When

using error-free observational data, the number of successful estimations for the four-parameter set increases to 8 and the number of poor estimation decreases to 1 (not shown). We did not perform the five-parameter experiments with error-free data for all 32 cases, but did so for 6 cases that had poor estimations. Using error-free data, the parameters converge to the true values perfectly in 5 of the 6 cases. This indicates that the instability of the inverse problem increases as the number of parameters to estimate increases.

Parameter estimation using the EnKF method is found in this study to be very sensitive to the random realization of the initial ensemble. For single-parameter estimations, different realizations lead to different convergence rates (Fig. 5.2). For multiple-parameter estimations, it even affects the success of the estimation (Fig. 5.5). Because the random numbers sampled for the parameters do not change during the forecast step, they can directly affect the model response and the reliability of the error covariances estimated from the ensemble. For example, Fig. 5.15 compares the correlations calculated from a successful estimation experiment (Fig. 5.15a-d) and a poor estimation experiment (Fig. 5.15c-h), for the case of estimating (n_{oh}, ρ_h) . The only difference between the two experiments is the realization of the initial parameter ensemble. It can be seen that significant correlations are missing in the poor estimation experiment (Fig. 5.15e, f, g).

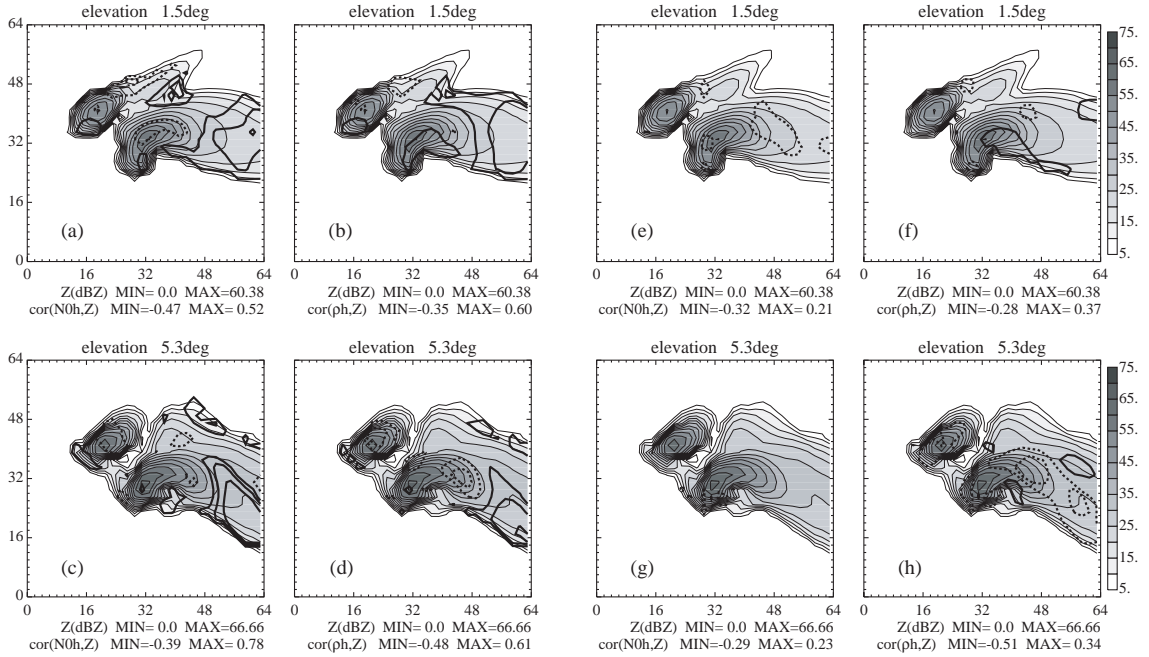


Fig. 5.15. As in Fig. 5.14, but for correlation coefficients between n_{0h} and ρ_h from two experiments estimating (n_{0h}, ρ_h) . (a)-(d) are for the experiment corresponding to the thick black curves in Fig. 5.5b, d that yields a good estimation, and (e)-(h) are for the experiment corresponding to the thick gray curves in Fig. 5.5a, c that has a poor estimation.

5.6 Summary and conclusions

In this study, we investigated the possibility of correcting model errors associated with uncertain microphysical parameters used in a popular single-moment ice microphysics scheme through parameter estimation using the EnKF method and radar data. The parameters we estimate include the intercept parameters of the assumed exponential drop size distributions (DSDs) for rain, snow and hail, and the densities of hail and snow. Sensitivity analyses were performed for individual parameters in Chapter 4 to provide guidance to the parameter estimation experiments. Parameter identifiability was also discussed. In this chapter, we use the EnKF method to estimate these

microphysical parameters individually or in different combinations. The identifiability of multiple parameters is further investigated.

For parameter estimation purpose, only radar reflectivity data are used, because the model state is more sensitive to reflectivity than to radial velocity. A data selection procedure based on covariance information and an ensemble inflation procedure with a pre-specified spread limit were applied, which effectively avoided the problem of filter divergence and ensured that the data used could provide useful information.

To explore the identifiability of different parameters or different combinations of the parameters, the parameter estimation experiments started from different initial guesses. The experiments showed that when the microphysical parameters are estimated individually (with other parameters being perfect), they all can closely converge to their true values. The resultant model state estimations are generally as good as that of the corresponding control that had no parameter error. This is not surprising because the sensitivity analyses in Chapter 4 show that the inverse problems for single-parameter estimation have unique solutions. The results of single-parameter estimations also indicate that the EnKF can be effectively used in simultaneous state and parameter estimation as long as the problem is well posed.

The results of multiple-parameter estimations are not as good as those of single-parameter estimations, but the results estimating parameter sets (n_{0h}, ρ_h) , (n_{0r}, n_{0s}, n_{0h}) and $(n_{0r}, n_{0s}, n_{0h}, \rho_h)$ are very encouraging. The estimations of (n_{0h}, ρ_h) and $(n_{0r}, n_{0s}, n_{0h}, \rho_h, \rho_s)$ are relatively poor. In a major portion of the five-parameter experiments, some of the parameters can not converge to the true values by the end of the assimilation window. The problem with such as case is that the model responses to the errors in

different parameters can cancel each other. Certain combinations of the multiple parameters can result in a good fit of the model solution to the observations. In another word, the solution of the inverse problem for multiple parameters can be not unique. Further, the results of estimation are also sensitive to the quality of the observational data in such a case.

The quality of parameter estimation, as well as the parameter convergence rate, is strongly influenced by the realization of the initial ensemble. This is mainly due to the sampling error associated with relatively small ensemble. It was shown that using a larger ensemble (100 instead of 40) improves the estimation of especially multiple parameters.

The sensitivities of the analysis and forecast to the microphysical parameters and the identifiability of these parameters can be case dependent and may differ for different types of convective systems. In this study, we applied the parameter estimation to a supercell storm only. Some parameters or combinations of the parameters may be more identifiable with other convective systems, such as the squall lines that contain both vigorous convection and the stratiform precipitation regions. Other data sources, such as those of dual-polarization radar, may be very helpful for microphysical parameter estimation because of their information content on DSDs and hydrometeor types. At least, the dual-polarization data can provide additional constraints on the inverse problem, which hopefully can alleviate the problem of multiple minima. Work in assimilating polarimetric Doppler radar data using the EnKF is in progress (Jung et al. 2005). The estimation of microphysical parameters, such as the fall speed coefficients

and collection efficiencies, are worthy of investigations, because they tend to have a large impact on the simulation and prediction of convective systems.

We should point out again that in our current problem we considered only the uncertainties in the microphysical parameters in the prediction model. The microphysical parameters are actually also involved in the observation operators of reflectivity. In this study, this additional complication is not considered; true values of these parameters are used in the observational operators. Preliminary tests showed that the analysis is very sensitive to parameter errors in the observation operators because they directly affect what the model thinks the observational data are. It is necessary to investigate how to correct the errors in both prediction model and the observation operators, if parameter estimation is to be applied in real world problems. In fact, this part of work is in process.

Chapter 6

Assimilation of Real Radar Data for the May 29, 2004 Central Oklahoma Tornadic Thunderstorm Case

6.1 Introduction

In the OSSE (Observing System Simulation Experiments) studies of Chapter 3 and Xue et al. (2006, XTD06 hereafter), the state variables that involve a multi-class ice microphysics scheme are analyzed accurately, by directly assimilating both radial velocity and reflectivity data, when the forecast model is assumed to be perfect. Encouraged by those OSSE results, we move toward applying the EnKF algorithm to real radar data in this chapter.

Compared to studies using simulated data, the number of real data studies with EnKF is much more limited. The biggest issue with real data is the presence of and the lack of good knowledge about model errors, where the model includes both prediction model and the forward observation operator. Uncertainties with data errors contribute to additional difficulties. Moreover, the lack of a truth also makes the verification less certain.

Existing studies using real data include that of Keppenne and Rienecker (2002), who applied a massively parallel implementation of EnKF to an ocean circulation model. For the atmosphere, Whitaker et al. (2004) experimented with the analysis of

sub-sampled surface pressure data at a density similar to that at the early nineteenth century, and obtained analysis whose 500 hPa analysis errors are comparable to today's 2.5-day forecast errors. More recently, Houtekamer et al. (2005) applied their double-ensemble Kalman filter with perturbed observations to a global primitive equation model, and analyzed most of the data used by an operational 3DVAR system. It is found that by adding model errors to the forecast background whose covariances is proportional to the background error covariances of an operational 3DVAR system, innovation statistics that agree with the ensemble-based estimation of innovation magnitudes can be obtained. The added model errors are found to dominate the error growth but even with the inclusion of model errors, the quality of the 6-hour ensemble mean background forecasts is only similar to that obtained using 3DVAR analyses. The rather simplistic treatment of model errors is believed to be one of the causes of the similarity. The results also suggest that much work is still needed in applying EnKF methods to real data.

At the convective scale, Dowell et al. (2004) is the only currently published paper that analyzes Doppler radar data using EnKF method. By assimilating radial velocity and reflectivity data from one radar over a 47 minute period, wind fields that are of similar quality as dual-Doppler wind analyses were obtained for a supercell thunderstorm. The analysis system used is based on the EnSRF algorithm and an anelastic cloud model with warm rain microphysics, and was used earlier by Snyder and Zhang (2003) and Zhang et al. (2004) for OSSEs. The study also found a relatively large sensitivity to the ensemble initialization procedure. The analyzed low-level cold pool was too strong and the analysis was ineffective in correcting the cold pool errors.

The study focused on the retrieval of wind and temperature fields, with no attempt made to produce forecast starting from the analysis.

In this chapter, the radar data assimilation system (XTD06 and Chapter 4, 5) based on the ensemble square-root filter (Whitaker and Hamill 2002) is applied to the central Oklahoma tornadic thunderstorm case of 29-30 May 2004. The main storm of this case was covered by the Oklahoma City WSR-88D radar (KTLX) and another WSR-88D radar to its north (KVNK at Enid, Oklahoma). We performed a set of experiments assimilating data from either one or two radars. In section 6.2, we will introduce the case and data. In section 6.3, the assimilation experiments using homogeneous environment conditions provided by a single sounding are described and the results of both analysis and forecast are presented. In Sections 6.4, the results of using time evolving environment conditions obtained by a 3DVAR analysis is presented. Summary and discussions are given in section 6.5.

6.2 The 29-30 May 2004 case, data and observation operators

6.2.1 Case description

In the late afternoon through evening of May 29, 2004 CST (Central Standard Time), a long-lasting tornadic thunderstorm swept through central Oklahoma and produced 16 tornadoes along a long path from Custer County, west-central Oklahoma, to Mayes County, northeastern Oklahoma (Fig. 6.1). The first tornado touched down near Thomas in Custer County at 1729 CST (2329 UTC) May 29 while the last tornado from the

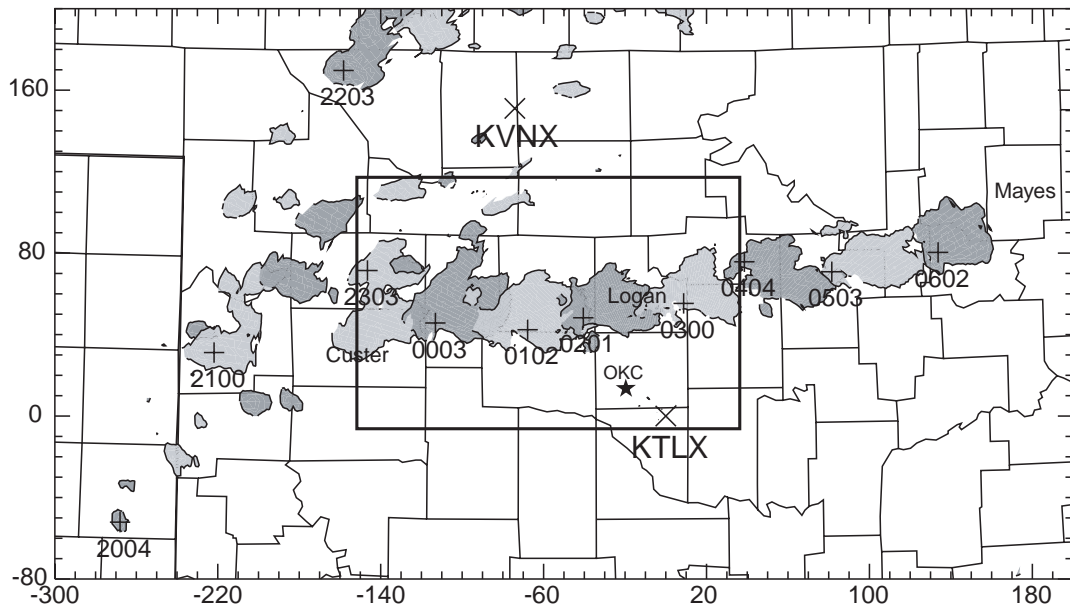


Fig. 6.1. Storm positions indicated by the area greater than 40 dBZ at the first elevation of the KTLX radar with a time interval of 1 hour. The locations of the KTLX and KVNx radar are marked by ×. The x and y distances are relative to the KTLX radar. The location of the maximum reflectivity is marked by +. The bold rectangular box indicates the analysis and prediction domain. The star indicates Oklahoma City. Several counties are also labeled.

same tornadic thunderstorm occurred near Murphy in Mayes County at 0051 CST (0651 UTC) May 30. In UTC, the thunderstorm spans across 29th and 30th of May 2004, with most of the tornadic activities occurring in May 30.

The most prominent feature at the surface in the storm environment is a dryline which formed in the morning hours in the Texas (TX) panhandle area and intensified by local noon (1800 UTC, Fig. 6.2a) and propagated into western Oklahoma (OK) by late afternoon (0000 UTC, Fig. 6.2b). Associated with this dryline is a deep trough with a low center moving from the Kansas (KS) and Colorado (CO) border at 1800 UTC (Fig. 6.2a) to western KS by 0000 (Fig. 6.2b). The western and central OK was located within strong southerly low-level flows that developed an easterly component

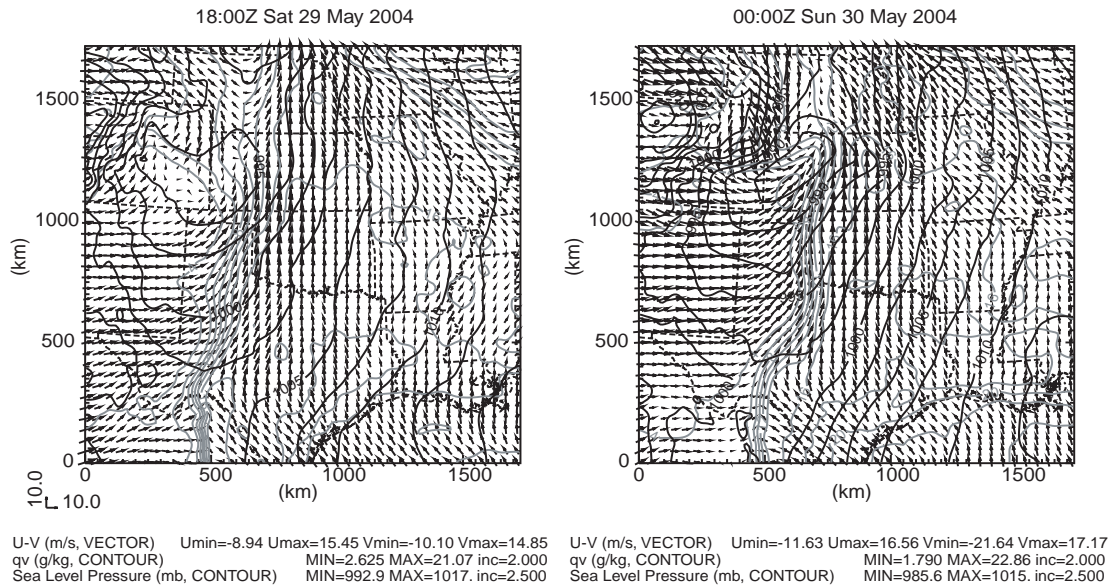


Fig. 6.2. Surface wind (vectors), mean sea level pressure (black contours, at intervals of 2.5 hPa) and surface specific humidity (gray contours at intervals of 2 g kg⁻¹) from NCEP Eta model analyses at (a) 1800 May 29, and (b) 0000 May 30, 2004.

by late afternoon (Fig. 6.2). At the 500 hPa level is a trough extending from Oregon to New Mexico (not shown). In the afternoon of 29 May, CDT, Oklahoma was located underneath a broad area of mid-level west-southwesterlies ahead of the trough, and this flow strengthened significantly throughout the day.

At around 1930, 29 May, several small convective cells were triggered along the dryline and by 2000 they were lined up near the western border of OK (not shown). This line of cells quickly moved north-northeastwards and entered western OK by 2100 UTC (Fig. 6.1). The cells at the central portion of the line grew the fastest initially but it was the smaller cells located at the southern portion of the line that evolved into the central OK tornadic thunderstorm later. Between 2230 and 2300, three smaller southern cells merged together and became a single strong supercell that continued moving northeastwards. The supercell grew very fast from 2300 to 2330 and spawned the first

tornado at 2329 in Custer County. During the period, the northern cell dissipated. So, central OK tornadic thunderstorm had its origin at the dryline and it took at least two hours for it to grow into its tornadic phase. The storm also produced hails, with the largest ones produced at around 2325 UTC measuring 120.65 mm in diameter. This storm continued its eastward propagation for the next a few hours, passing by Oklahoma City on its north side. The storm finally decayed at the east boarder of OK at 0730 UTC on May 30.

Fig. 6.3a shows the Norman, OK (OUN) sounding taken 0000 UTC, May 30. The sounding carries a moderate CAPE of 2261 J kg^{-1} and a CIN of 62 J kg^{-1} . Temperature and dew point profiles show that the boundary layer was warm and moist. The vertical wind veered with height from a southerly of 19 m s^{-1} at the surface to more than 50 m s^{-1} of westerly at round the tropopause and the vertical shear over the lowest 6 km was about 25 m s^{-1} . Both instability and shear suggest the potential of tornadic supercells.

6.2.2 Radar data and forward observation operators

The WSR-88D radars, KTLX and KVNXX, collected PPI volume scans in precipitation mode on the tornadic thunderstorm when it passed through central Oklahoma. In this study, we choose an assimilation window between 2355 of 29 May and 0100 of 30 May, which is during the mature and tornadic stage of the storm. During the data assimilation period, the KTLX and KVNXX radars provide some dual-Doppler wind coverage, although at relatively long ranges. Scanning in the standard Volume

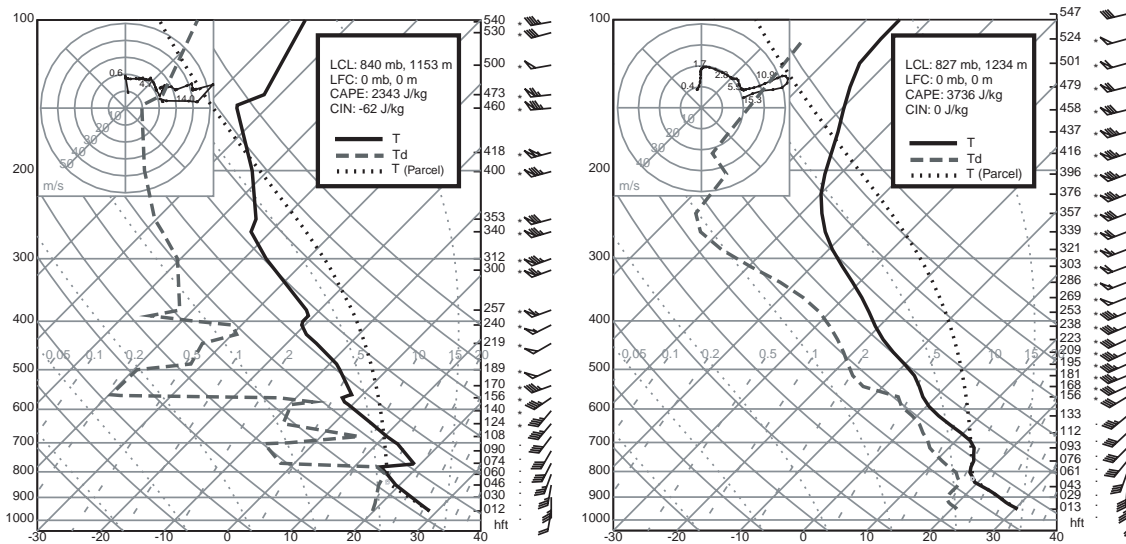


Fig. 6.3. (a) The observed Norman, OK (OUN) sounding at 0000 UTC, May 30, and (b) the modified sounding used in data assimilation experiments.

Coverage Pattern 11 (VCP 11), these radars complete a full volume scan with 14 elevations in about 5 minutes, with the elevations ranging between 0.5° and 19.9° . The range resolution is 250 m for radial velocity (V_r) and about 1 km for reflectivity and the azimuthal resolution is about 1° .

Quality control and interpolation of the data are performed before they are assimilated into our model. In the quality control process, undesired radar signatures, such as ground clutter are removed and aliased radial velocities are unfolded. Within each elevation level, quality-controlled data are interpolated to the locations of model grid columns from the nearest four polar-grid observations. Since the data remain within the PPI surfaces, no vertical interpolation is performed. In another word, the data that are assimilated are located on constant elevation levels but at the locations of model vertical columns. The horizontal interpolation helps keep the horizontal resolution of the data more uniform while potentially large errors associated with vertical

interpolation, especially at longer ranges, is avoided. Similar data processing is done in earlier studies (e.g., Sun and Crook 2001; Dowell et al. 2004), and is also assumed by the simulated data in XTD05. To simplify the assimilation of radar data, we preprocess the data, through temporal interpolations of the data at the same elevation levels, for them to be valid at the whole 5 minutes. Assimilation cycles of 5 minute intervals are therefore performed.

The observation operators used to obtain the radial velocity and reflectivity on the elevation angle levels from forecasted model state variables are the same as those in Chapter 5.

6.3 Assimilation experiments using homogeneous environmental conditions provided by single sounding

6.3.1 The EnSRF assimilation system and experiments

6.3.1.1 Model configurations

Our EnSRF data assimilation system is based on the ARPS (Advanced Regional Prediction System) model (Xue et al. 2000; 2001; 2003). The ARPS is compressible and nonhydrostatic. It contains 12 prognostics variables, including velocity components u , v , w , potential temperature θ , pressure p , the mixing ratios for water vapor q_v , cloud water q_c , rainwater q_r , cloud ice q_i , snow q_s and hail q_h , plus the turbulent kinetic energy used by the 1.5-order subgrid-scale turbulent closure scheme. The modified three-category ice scheme of Lin *et al.* (1983) is used for our assimilation experiments.

As our first attempt to assimilation real radar data, we use the APPS model in a simple cloud model mode. The analysis and forecast domain covers an area of $180 \times 120 \text{ km}^2$ (The rectangular box in Fig. 6.1), at a 1 km horizontal resolution. The vertical grid is stretched with the grid spacing increasing from 100 m near the surface to 700 m at the top of the domain. The domain is 16 km deep with 40 physical layers. Open boundary condition is applied at lateral boundaries. The top boundary is a rigid lid with a 4-km deep Rayleigh relaxation layer; the lower boundary is free slip. Surface physics and radiation processes are not included in current experiments.

6.3.1.2 The EnSRF assimilation experiments

Data from either KTLX radar alone (single-radar analysis) or from both KTLX and KVNX radars (dual-radar analysis) are assimilated. We start our initial ensemble forecast at 2355 UTC of 29 May and perform the first analysis at 0000 UTC of 30 May. Over the 65 minutes assimilation period from 2355 of 29 May to 0100 of 30 May, the storm was located at distance ranging from 125 to 83 km to the KTLX radar, and from 115 to 105 km to the KVNX radar (Fig. 6.1). At 0000 UTC, the radar beams that cover the main storm were close to 90° angles from the two radars whereas by the 0100 UTC, the angles were about 135° ; therefore there was a good dual-Doppler coverage on the main storm during this period (Fig. 6.1). All experiments use 40 ensemble members.

As an initial study with real data, we assimilate observational data from Doppler radar only, while defining the environmental conditions of the storm using a single sounding. This is the same as in the study of Dowell et al. (2004). To start off the assimilation cycles, the first guess of the initial condition is horizontally homogeneous

and is defined by a modified Norman sounding valid at 0000, 30 May. In fact, this sounding is extracted from a 3DVAR analysis valid at this time, at a location north of the tornadic storm. The modifications include weakening the stable layer between 800 mb and 700 mb and increasing the humidity in the dry layer between 800 mb and 600 mb. The 3DVAR analysis follows the procedure of Hu et al. (2006a) and includes both rawinsondes and surface observations, including those from the Oklahoma Mesonet. The sounding actually used is plotted in Fig. 6.3b. This sounding has a higher CAPE (3750 J kg^{-1}) than the Norman 0000 UTC sounding (Fig. 6.3a) and has zero CIN. Despite the lack of CIN, a layer with strong stability is evident between 830 and 700 hPa. The presence of this stable layer imposes a less favorable condition for promoting convection within a cloud model, compared to the soundings used in most existing radar data assimilation studies [e.g. Dowell et al. (2004) and Sun (2005)]. In the absence of any mesoscale forcing, convection may be difficult to develop with a cloud model when a low-level stable layer exists. This is also the reason that modifications to observed soundings are often necessary for cloud-model simulations.

An ensemble of 40 initial model states was generated by adding random perturbations to the first-guess state. An initial attempt to add random noise to the environment state as what was done in Chapter 3 resulted in a poor analysis. The problem of populating the initial ensemble with random noise is that the random noise has no spatial correlations and can be easily damped by numerical diffusion in the model during the first few forecast steps. Therefore, the spatial correlations and correlations between different model variables that could be built up through the ensemble forecast are very weak and the initial ensemble spread is very small. The large

discrepancy between the background error and the ensemble spread makes the correction to the model state by the observations insufficient. The underweighting of observations can feed back on itself and become more serious in subsequent assimilation cycles, whereby leading to filter divergence.

The analysis is improved when spatially smoothed perturbations are used to generate the initial ensemble members. The spatially smoothed random perturbations are generated in the same way as in Chapter 5 (see Section 5.2.1), which contain larger spatial scales and correlations. The standard deviations of the perturbations are, respectively, 3 m s^{-1} for u , v and w , 3 K for perturbation potential temperature, 1.0 g kg^{-1} for q_v , q_c , q_r , q_i , q_s and q_h . For the five hydrometeors, the perturbations are added only at the points within a distance from where precipitation is observed, and this distance is equal to the cutoff radius used in the covariance localization function. Their perturbations are further limited to the levels where the corresponding hydrometeors can be expected. For q_c , the perturbations are confined to 1 to 9 km level, for q_r , from surface to 5 km, for q_i , between 5 and 14 km, for q_s , between 4 to 13 km, and for q_h from surface to 12 km. Negative perturbations for the hydrometeor mixing ratios are set to zero. The perturbations for velocity components, potential temperature and specific humidity are added in the entire domain, because there are uncertainties associated with these fields even outside the observed precipitation region. Spurious cells that may develop in the non-precipitation regions can be suppressed by assimilating reflectivity everywhere.

Covariance localization is applied to reduce the influence of the poorly estimated distant error covariances due to the limited ensemble size. The same

covariance localization procedure used here is the same as that used in Chapters 3, 4 and 5. The cutoff radius for the covariance localization is 6 km in all three directions, in the experiments that are presented in section 5.4.

Radar scan volumes are assimilated at five minute intervals. At the beginning, the ensemble members are integrated for 5 minutes before the first scan volume is assimilated. Both radial velocity and reflectivity are assimilated in all experiments. To save computational time, reflectivity data at every other model column is assimilated in the clear air regions. The observation errors are assumed to be uncorrelated and observations are assimilated serially one at a time. All model variables are updated when assimilating both radial velocity and reflectivity. It was found in Chapter 3 that when assimilating reflectivity, updating variables that are not directly related to reflectivity via the observation operators, i.e., updating u , v , w , θ' , p' , q_v , q_c and q_i hurts the analysis in the first few cycles. Random initial perturbations were used in Chapter 3. By applying the smoothed initial perturbations introduced in Chapter 5, updating these indirectly related variables during the first few cycles no longer hurts the analysis. For this reason, we update all analysis variables when assimilating reflectivity starting from the first cycle. However, this does not exclude the possibility that model errors and errors in the observation operator in the real data experiment cause a similar adverse effect. Some sensitivity studies will be performed to test the effect of assimilating reflectivity in this context.

In ensemble-based data assimilation methods, the forecast and analysis uncertainties are often systematically underestimated due to small ensemble size as well as model error. Too small an ensemble spread could lead to filter divergence, which has

already been found in our initial tests. Increasing the ensemble size significantly is an impractical solution here because the computational cost is already rather high. It will not necessarily overcome the model error problem either. Covariance inflation is one way to counteract the tendency of filter divergence. We experimented with inflation amounts between 10% and 50% and found that 20%-30% inflation give better analysis. Further increase the inflation amount to 50% causes some prediction members to fail, however.

A limitation of the covariance inflation approach is that it can not change the subspace spanned by the ensemble, although it increases the variance. Hence, if model error projects into a substantially different subspace, the covariance inflation may not be effective. One example is when all members fail to predict a convective disturbance where it is observed, the inflation will not create any spread that is initially zero.

Too small an ensemble spread can also be, and is often, caused by ignoring the model deficiency, or ignoring the model error covariance term when estimating the background error covariances from the forecast ensemble. This problem can become rather serious when we deal with real data. For example, Houtekamer et al. (2005) found that the model error they add to their system dominates the error growth while neglecting model error results in too smaller an ensemble spread.

We actually experimented with adding assumed model errors to each ensemble member before or after the analysis, and the same spatially smoothed random perturbations used when generating the initial ensemble are used here, except that the magnitudes are different. Filter divergence can be alleviated by doing so, but we haven't found any advances of this way to deal with filter divergence over covariance

inflation in this case. More researches are needed on how to parameterize the additive model errors. In Section 6.3.2, we only show the results using covariance inflation.

6.3.1.3 Verification of EnSRF analysis

Unlike OSSEs, the real truth is unknown for real cases. Even the observations can not be completely trusted because they also contained errors. The verification of the assimilation results requires careful considerations.

For both single-radar and dual-radar cases, we calculate the fit of the analysis to the observations, from KTLX and KVNK radars. This is measured in terms of the root-mean square differences (RMSD) between the observations and the analysis projected to the observation points using the forward observation operators:

$$\text{RMSD} = \sqrt{\frac{1}{M} \sum_{m=1}^M \left[\overline{[H(\bar{\mathbf{x}}^a)]_m} - y_m \right]^2}, \quad (6.1)$$

where the overbar represents the ensemble mean and M is the total number of observations used in the verification at a particular time. For reflectivity, M is the number of observations that are greater than 0 dBZ. The above equation is applied to the reflectivity and radial velocity observations separately.

In the case of single-radar assimilation experiment, the observations from the radar that are not assimilated form an independent data set for verification. For the wind field, the radial velocity data from the other radar often represent a significant portion of the cross-beam component of wind that is not measured by the assimilated radar. In the case of dual-radar assimilation, the above calculations measure the fit of analysis to the observations.

We further verify the analyzed wind fields against the analysis that use radial velocity (V_r) and reflectivity (Z) data from both KTLX and KVNK radars. To reduce the computational cost assimilating both radars, the data on every other model column are assimilated.

In addition, innovation statistics are used to check the behavior of the EnSRF. The innovation is the difference between the observation and the background forecast:

$$\mathbf{v} = \mathbf{y} - H(\bar{\mathbf{x}}^f), \quad (6.2)$$

where \mathbf{y} is the observation vector, and \mathbf{x}^f is the state vector on the model grid, and H is the observation operator that projects \mathbf{x}^f to the observation space. The overbar denotes ensemble mean. \mathbf{v} is the innovation vector that can also be expressed as

$$\mathbf{v} = \boldsymbol{\varepsilon}^o - \boldsymbol{\varepsilon}^f, \quad (6.3)$$

where $\boldsymbol{\varepsilon}^o$ is the observation error vector defined by $\boldsymbol{\varepsilon}^o = \mathbf{y} - H(\mathbf{x}^t)$ and $\boldsymbol{\varepsilon}^f$ is the forecast error vector defined by $\boldsymbol{\varepsilon}^f = H(\bar{\mathbf{x}}^f) - H(\mathbf{x}^t)$, with \mathbf{x}^t being the true state vector. The rms (root-mean square) of the innovation is calculated with respect to each of the two radars, and the quantity measures the fit of the prior (forecast) model state to the observations. The following relationship can be derived from (6.3) according to Dee (1995),

$$E(\mathbf{v}\mathbf{v}^T) = \mathbf{H}\mathbf{P}^f\mathbf{H}^T + \mathbf{R}, \quad (6.4)$$

where \mathbf{H} , \mathbf{P} and \mathbf{R} are, respectively, the Jacobian of the observation operator H , the forecast and observation error covariance matrices; E is the expectation operator.

Considering only the diagonal of (6.4), then

$$\sigma_v^2 = \sigma_f^2 + \sigma_o^2, \quad (6.5)$$

where σ_v^2 , σ_f^2 and σ_o^2 are the variances of the innovation vector, the observation error and the forecast error, respectively. This relationship is often used to check the consistency between the background error covariance and the ensemble spread [e.g., Dowell et al. (2004) and Houtekamer et al. (2005)]. From Eq. (6.5), the forecast error variance is calculated from the observations according to

$$\sigma_f^2 = \sigma_v^2 - \sigma_o^2, \quad (6.6)$$

while the forecast error variance estimated from the forecast ensemble is

$$\hat{\sigma}_f^2 = \left\langle \frac{1}{N-1} \sum_{n=1}^N [H(\mathbf{x}^f) - \overline{H(\mathbf{x}^f)}] [H(\mathbf{x}^f) - \overline{H(\mathbf{x}^f)}]^T \right\rangle, \quad (6.7)$$

When the ensemble spread properly reflects the forecast error, σ_f^2 calculated from (6.6) and $\hat{\sigma}_f^2$ from (6.7) should be equal. Here, the expectation operator $\langle \rangle$ represents the average over all, or M number of observation points. Since we assumed global observation errors for V_r and Z , the variance of the observation errors are simply the square of the standard deviations of the assumed errors. We calculate the variance of the innovation according to,

$$\sigma_v^2 = \left\langle (\mathbf{v} - \langle \mathbf{v} \rangle)(\mathbf{v} - \langle \mathbf{v} \rangle)^T \right\rangle. \quad (6.8)$$

6.3.2 Results

6.3.2.1 Dual-radar analysis

Although the typical spacing between the WSR-88D radars generally precludes dual-Doppler analysis, in this case, as pointed out earlier, the KTLX and KVNK radars

provide good dual-Doppler coverage of the main storm of interest during our data assimilation period. At the early assimilation period, the two radars observe the main storm at almost right angle. Hence, we expect a good wind analysis when data from both radars are used, at least in the regions where coverage is available from both radars.

For the dual-radar analysis the assumed observation error is 1 m s^{-1} for radial velocity and 3 dBZ for reflectivity. Covariance inflation is 30%. Fig. 6.4 compares the analyzed radial velocity and reflectivity against the radial velocity observations from both radars and the reflectivity observations from KTLX radar. We can see that both the analyzed radial velocity and reflectivity match the observations very well within regions with observation coverage. It can be seen from Fig. 6.4b and Fig. 6.4d that two inbound-outbound couplets of radial velocity exist, and are located on the northwest and east side of the hook echo, respectively. Interestingly, two couplets can also be evident in the analyzed radial velocity fields (Fig. 6.4a and Fig. 6.4c). The intensities of the analyzed and observed storms are comparable, in terms of the maximum reflectivity; regions with reflectivity greater than 60 dBZ exist in both analysis and observations and the reflectivity patterns also match rather well (Fig. 6.4e and Fig. 6.4f)

The solid black curves in Fig. 6.5a–d indicate the fit of the dual-radar analysis to the observations of KTLX or KVNK radar. It can be seen that the difference between the analyzed and observed radial velocity fields with respect to either radar is about 2.5 m s^{-1} and about 5 dBZ for reflectivity, through the assimilation cycles. The rms differences between the ensemble forecasts (dashed black lines in Fig. 6.5a–d) and the observations are much larger, however, but generally decrease with time. The

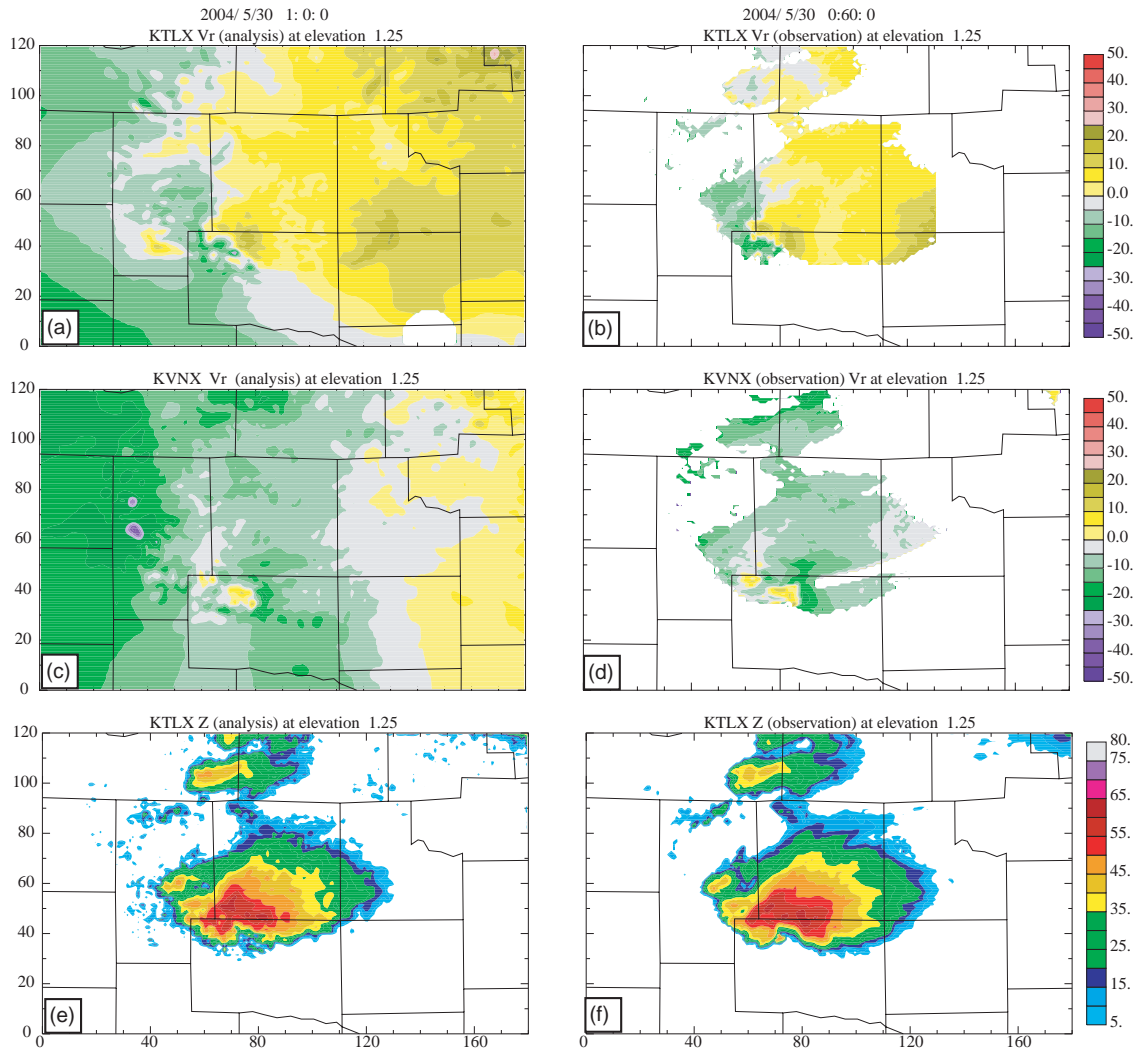


Fig. 6.4. (a) Dual-radar analyzed radial velocity as viewed from KTLX radar at the 1.25° elevation and (b) the corresponding observation; (c) analyzed radial velocity as viewed from KVNx radar and (d) the corresponding; (e) ensemble mean analysis of reflectivity in the 1.25° elevation plane of KTLX radar and (f) the corresponding observation, valid at 0100 UTC, May 30. The analysis shown is the ensemble mean.

differences with respect to KTLX radar are generally smaller than those with respect to KVNx radar. After 25 minutes, or 5 analysis cycles, the forecast rms differences in reflectivity remain at or below 8 dBZ, close to the 5 dBZ or so of the analyses, while the forecast differences in radial velocity remain above 5 m s⁻¹ with respect to KTLX radar,

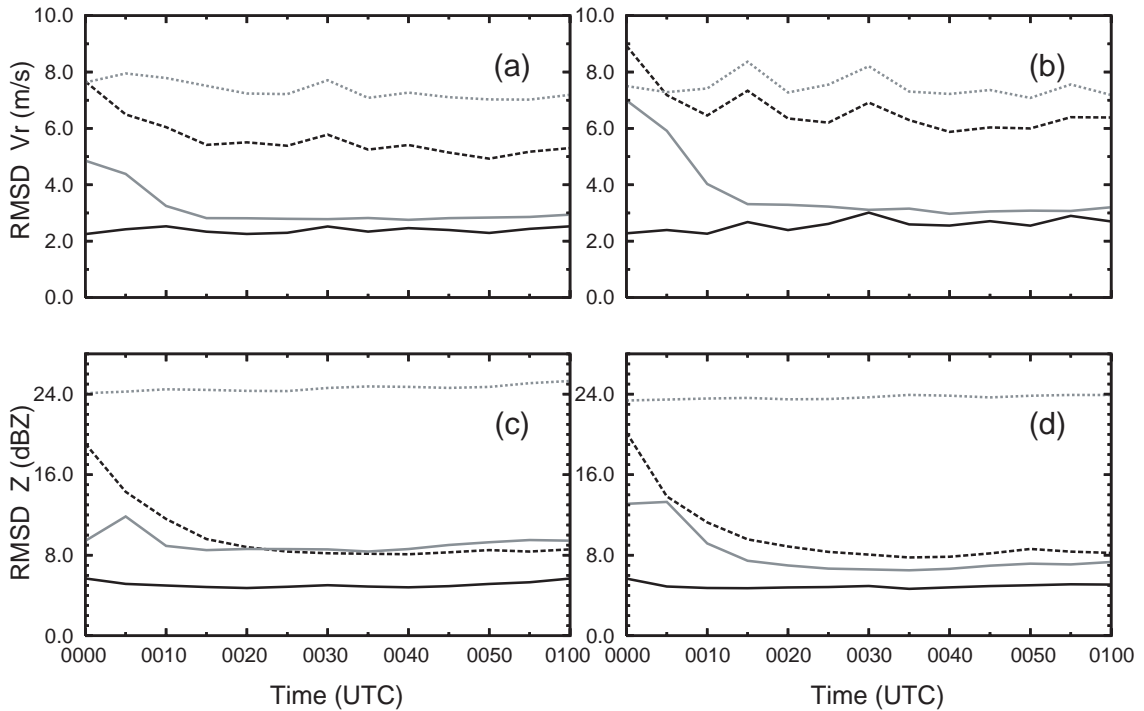


Fig. 6.5. Diagnostics and scores for the dual-radar analysis. (a) radial velocity rms differences with respect to the KTLX observations for ensemble mean analysis (solid black), ensemble mean forecast (dashed black), horizontally uniform wind from the sounding (dotted gray) and the ensemble spread (standard deviation) of the prior (forecast) radial velocity (solid gray). (b) The same as (a) but with respect to the KVNx radial velocity. (c) The same as (a) but with respect to the KTLX reflectivity. (d) The same as (c), but with respect to the KVNx reflectivity.

and above 6 m s^{-1} with respect to KVNx. These are much higher than the $2\text{--}3 \text{ m s}^{-1}$ in the analyses (Fig. 6.5a–b).

The fact that the radial velocity rms differences for the prior forecast states are much larger than those of analyses while reflectivity rms differences are much close for the forecasts and analyses suggest that the errors in the velocity fields grow much faster in the forecast than those in the microphysical fields. This may be because the velocity fields contain more small scale features that have larger growth rates than the

microphysical variables, or because the velocity responds to errors in other state variables, such as pressure and temperature (which directly affects buoyancy). Since we do not have any direct observations of pressure or temperature, we do not have any means to quantitatively access their quality; the analysis of these variables depend very much on the cross-covariance derived from the forecast ensemble and on the dynamic adjustment during the forecast. Of course, errors in the model and in the storm environment specified using the initial sounding can also cause forecast error growth.

As a reference, the rms differences calculated against the horizontally homogenous base state defined by the initial sounding are also calculated and plotted in dotted gray. It can be seen that the model forecast state does become better than the homogeneous environment after the first volume of radar data is assimilated (Fig. 6.5a–d), and even more so for the reflectivity.

The curves in Fig. 6.6a and Fig. 6.6b represent ratio $(\sigma_o^2 + \hat{\sigma}_f^2)\sigma_v^{-2}$ from dual-radar analysis, which should be close to 1 if ensemble variance $\hat{\sigma}_f^2$ properly presents forecast error variance σ_f^2 . The calculated ratio for the radial velocity data of KTLX is around 0.4 and that for the KVNx radar decreases from the initial value of 0.6 to 0.3 in the end. The ratio for the reflectivity data of KTLX increases from the initial value of 0.5 to values greater than 1 and that of KVNx is smaller than but close to 1. The ratios of the prior state estimate are generally better for reflectivity data than for the radial velocity. The smallness in the ratios for radial velocity implies that either the ensemble spread or the assumed radial velocity observation error variance is too small or both.

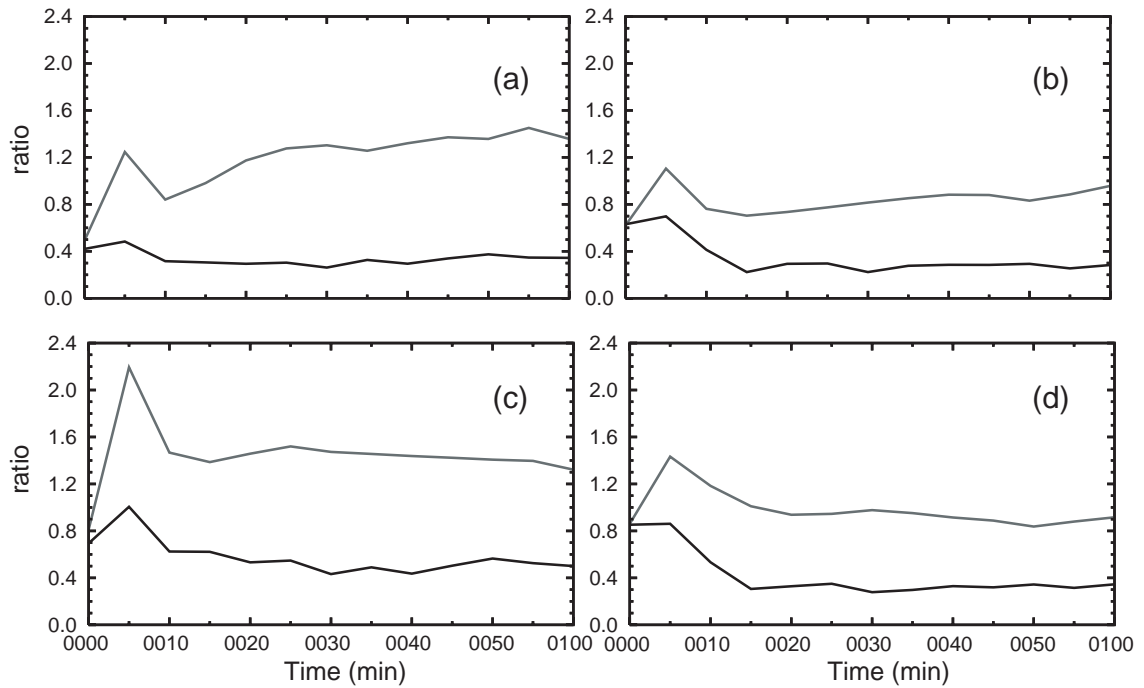


Fig. 6.6. Ratio $(\sigma_o^2 + \sigma_f^2) / \sigma_v^2$ from dual-radar analysis corresponding to (a) KTLX radar and (b) KVN radar; and from single-radar analysis corresponding to (c) KTLX radar and (d) KVN radar for radial velocity (black) and reflectivity data (gray).

More discussions on the consistency between the actual innovation variance and the ensemble estimated innovation variance will be given in later sections.

Overall, the very good fit of the analyzed winds to the observed radial velocities from both radars indicate the analyzed wind fields are rather accurate. The fits of both analyzed and forecast reflectivity to the observations of both radars are good. In the next section, we will compare the single-radar wind analysis against the dual-radar wind analysis obtained in this section.

6.3.2.2 Single-radar analyses

In this section, we examine the results assimilating data from a single Doppler radar. The analyzed fields, especially the winds, are compared with those of the dual-radar analysis obtained in the previous section. In the single-radar experiment presented here, the assumed rms error of radial velocity observations is 3 m s^{-1} and that of the reflectivity is 5 dBZ. The covariance inflation factor used is 20%. This experiment is one of several single-radar experiments that we performed, which gives a better forecast result.

While we have performed experiments that assimilating either KTLX or KVNK radar, we report only results assimilating KTLX radar in this prospectus. Fig. 6.7 shows the ensemble statistics for the single-radar control experiment that assimilates KTLX radar data only. It can be seen from Fig. 6.7a and Fig. 6.7c that the analyses of both winds and reflectivity fit the KTLX observations very well, which can also be seen in Fig. 6.8. The analysis rms differences for radial velocity range from 2 m s^{-1} to 3 m s^{-1} . The analysis rms difference for reflectivity is decreased to about 4 dBZ and remains at that level after two volumes of data are assimilated (Fig. 6.7c). The analyzed reflectivity field in Fig. 6.8e also looks very close to the KTLX observation, except that the region with reflectivity greater than 50 dBZ is smaller than in the observation. The fit of the analyzed reflectivity to the independent KVNK observations is also good, even though the rms difference of reflectivity with respect to KVNK is about 2 dB larger than that with respect to the KTLX data (Fig. 6.7d). However, the retrieved velocity fields do not match the observation of KVNK well. Fig. 6.7b shows that the match of the retrieved wind fields to the KVNK observations (solid black curve) is barely as good as the fit to

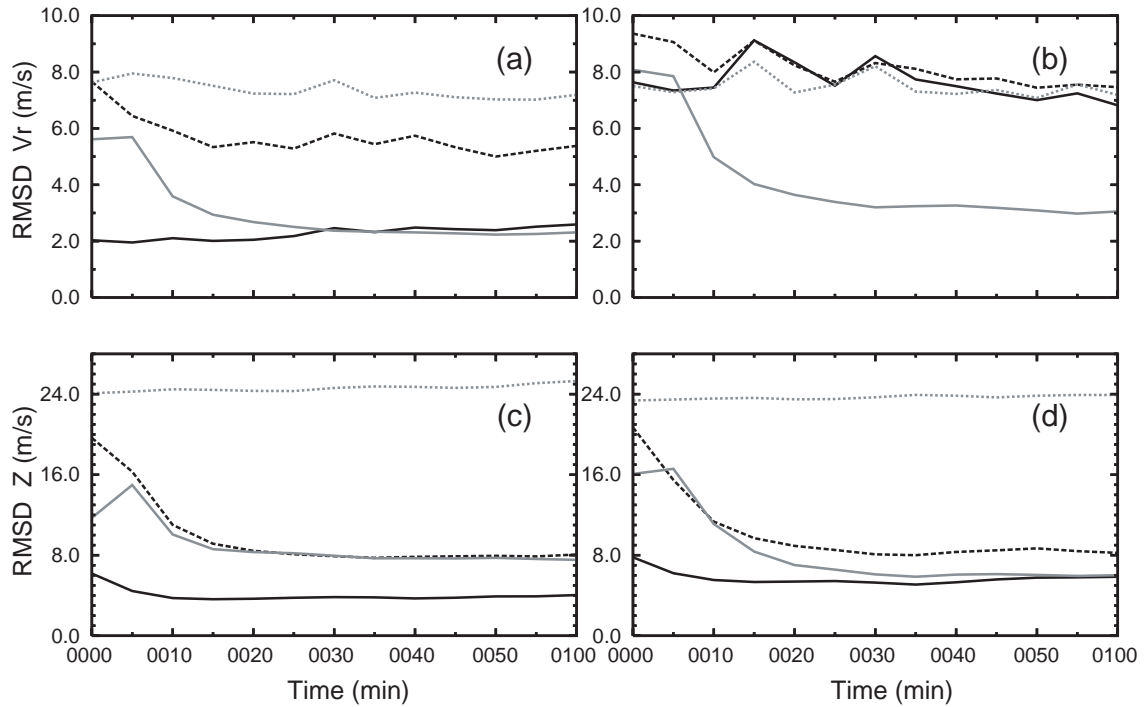


Fig. 6.7. The same as Fig. 6.5, but for the single-radar analysis that assimilates KTLX radar data only.

the horizontally homogeneous wind field defined by the sounding (dotted gray curve), at some times the fit is even poorer. Compared with the prior state (dashed black curve), the analyzed radial velocity as viewed from KVNIX radar shows little improvement between 0015 UTC and 0030 UTC and some, though still small, improvement from 0035 UTC onward. In the analyzed field, the two radial velocity couplets are invisible from KVNIX radar (Fig. 6.8c). These results suggested that the cross-beam component of winds is not well analyzed, at least those associated with small-scale structures. The reason of this failure is under investigation. For the reflectivity field, the fit to the homogeneous background, which is zero, is of course very poor (dotted gray curves in Fig. 6.7c and Fig. 6.7d).

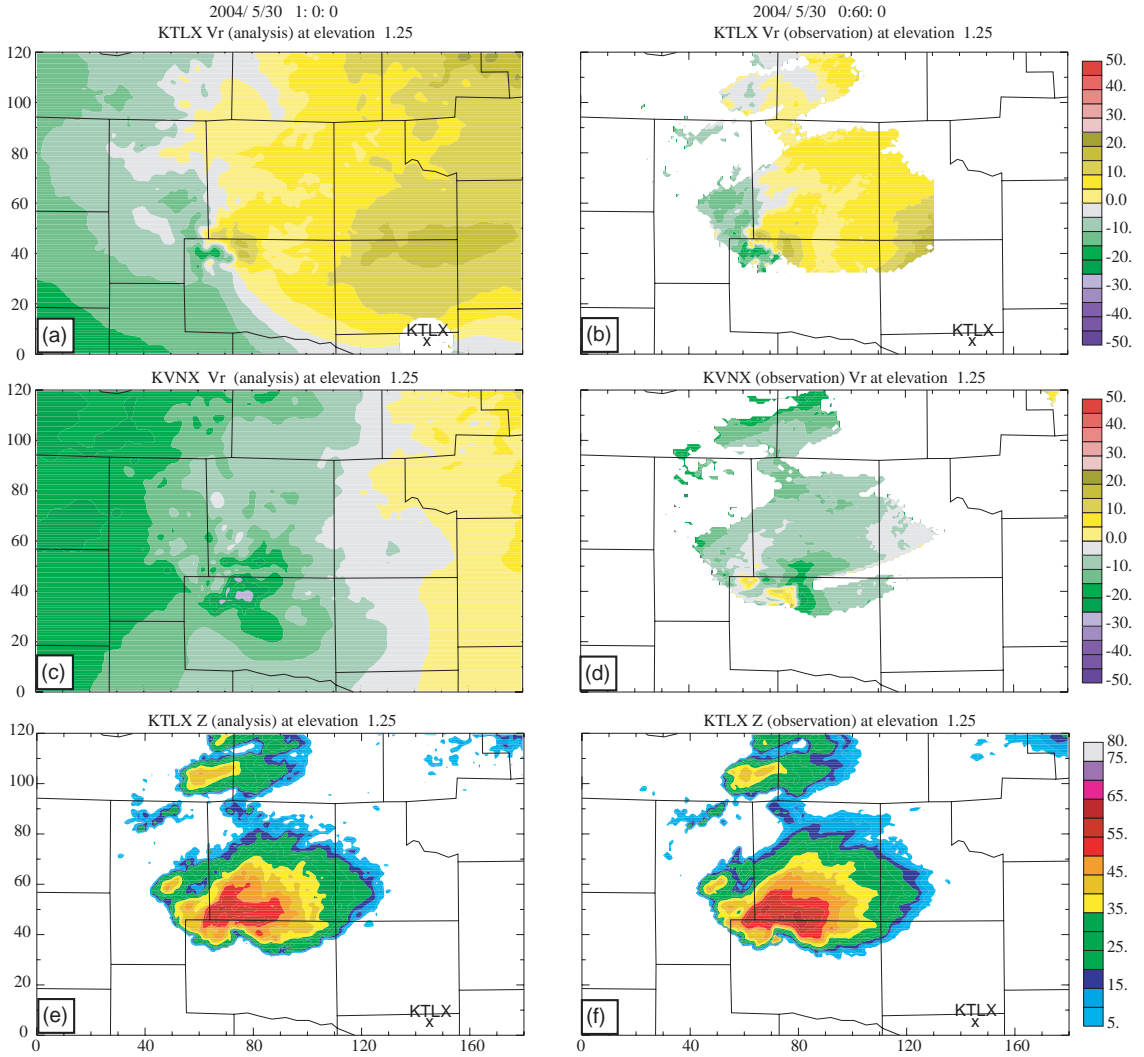


Fig. 6.8. The same as Fig. 6.4, but for the single-radar control experiment that assimilates KTLX radar data only.

The ensemble-based variance ($\sigma_o^2 + \hat{\sigma}_f^2$) with respect to the reflectivity of KTLX is overestimated compared to the innovation variance, σ_v^2 . The ensemble-based variances for radial velocity of both radars are still significantly lower than the actual innovation variances, as was the case with dual-radar radar analysis, even though the assumed standard deviation of radial velocity observation errors has been increased from 1 to 3 ms^{-1} . The ratio for the radial velocity generally decreases with time (black

curves in Fig. 6.6c, d), while the actual observation innovation variance (the dominator of the ratio) also decreases with time (not shown); this implies that the ensemble spread (the second term of the numerator of the ratio) decreases with time faster than the innovation variance because the observation error variance does not change. Fig. 6.6c and Fig. 6.6d suggest that the ensemble spread of the KVN_X-viewed radial velocity decreases more than the spread of KTL_X-viewed radial velocity. Too small ensemble spread in the unobserved wind component may be one of the reasons for the failure in analyzing the component. However, simply increasing the inflation factor did not improve the result. The limitation of covariance inflation is that it only increases the error variance and has little effect on the cross-covariances, which play a critical role in retrieving unobserved model state variables.

The analyzed 1.5 km and 4 km height-level horizontal velocity and reflectivity fields from the dual-radar and single-radar analysis experiments are shown in Fig. 6.9, at the middle (0030 UTC) and the end (0100 UTC) of the assimilation window. Note that the storm is in its tornadic stage during the assimilation period. An F2 tornado was observed at Blaine County from 0017 UTC to 0038 UTC and this F2 tornado crossed into Canadian County at 0038 UTC and remained on the group until 0111 UTC (c.f., Fig. 6.1).

The hook echo structure at the 1.5 km level can be seen from both the dual-radar and single-radar analyses (Fig. 6.9a, c, e and g). At 0030 UTC, the strong southeasterly flows into the storm can be seen clearly at the region of weak reflectivity in both cases. The flow along the south flank of the storm is mainly southerly in the single-radar

analysis, while there exist westerlies at the south side of the hook in the dual-radar analysis (Fig. 6.9a and c).

At 0100 UTC, a cyclonic circulation can be seen within the hook at the 1.5 km level in both analyses (marked by 'c' in Fig. 6.9e and g) while that of dual-radar analysis is clearly better defined. In the dual-radar analysis, on the east side of the circulation is a strong southeasterly inflow while the south edge of the hook is dominated by a surge of outflow. The appendage of the hook-shaped reflectivity is clearly associated with this inflow-outflow pattern and the cyclonic circulation. In the single-radar analysis, the flow west of the circulation center is mainly southwesterly, while in the dual-radar analysis, the flow is northwesterly and there exists a weaker anticyclonic circulation (marked by 'A' in Fig. 6.9e) west of the cyclonic circulation.

At the mid-level ($z=4\text{km}$), two cyclonic circulation centers can be seen in the dual-radar analysis (Fig. 6.9b and f) at both 0030 and 0100 UTC. The two circulations are consistent with the two observed radial velocity couplets revealed by Fig. 6.4b and Fig. 6.4d. The circulations can be seen more clearly in the perturbation (from the sounding-defined base state) horizontal wind fields (Fig. 6.10). However, only one cyclonic circulation center, rather than two, is found in the single-radar analysis at the 4 km level (Fig. 6.10c).

With the winds between the two circulation centers being mostly in the southwest-northeast directions, it is difficult for them to be analyzed accurately, using data from KTLX, because these winds are mostly in the cross-beam direction. The smallness of these flow structures and the distance of the radar from these features (about 83 km) probably have also contributed to the inaccuracy of single-radar analysis.

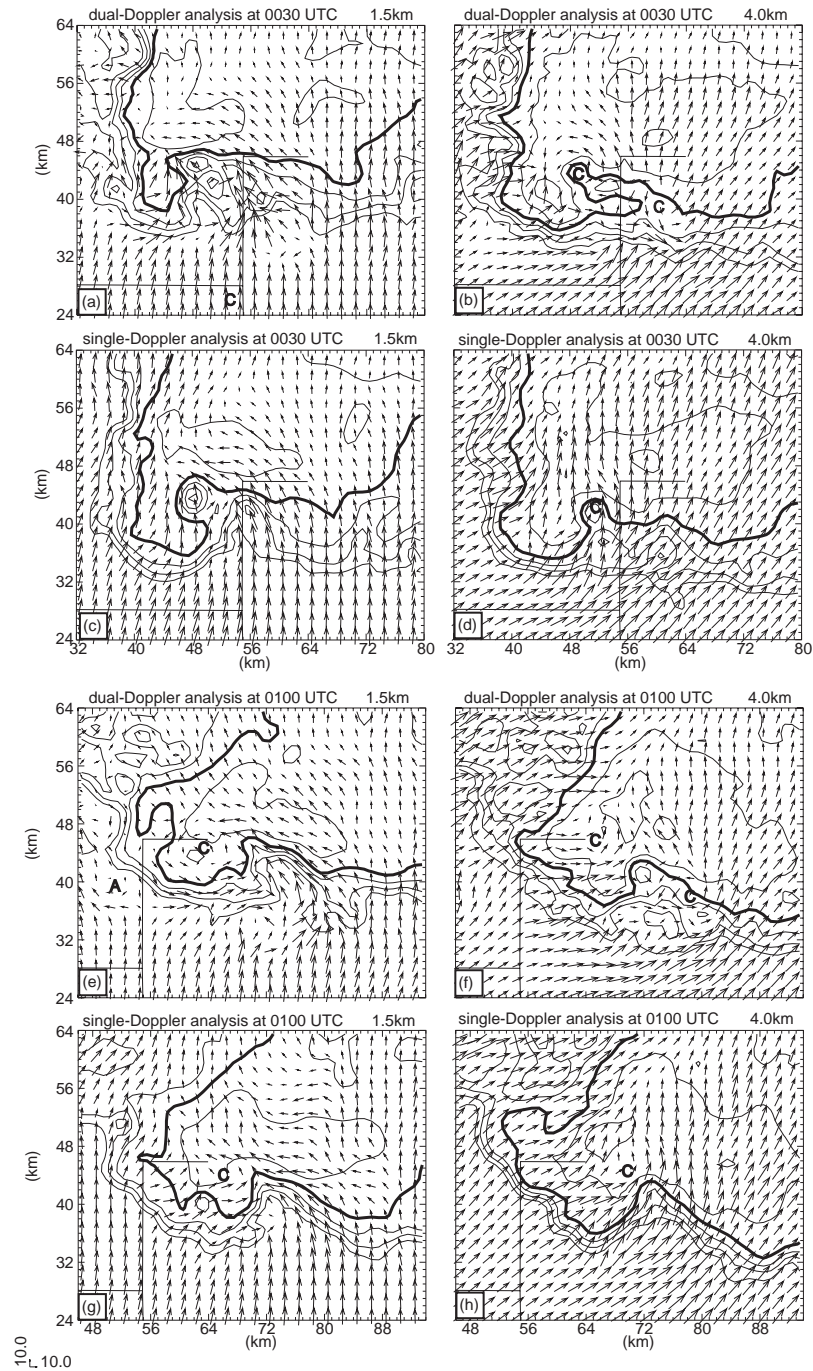


Fig. 6.9. Horizontal velocity vectors (m s^{-1}) and reflectivity contours (at intervals of 10 dBZ starting from 10dBZ, with the 40 dBZ contours highlighted) of ensemble mean analyses at 0030 UTC (a - d) and 0100 UTC (e - h) from dual-radar analysis experiment (a, b, e and f) and the single-radar analysis experiment (c, d, g and h). The left and right columns are for the 1.5 km and 4 km height levels, respectively. 'C' in the figure marks the circulation centers and 'A' marks the anticyclonic circulation center.

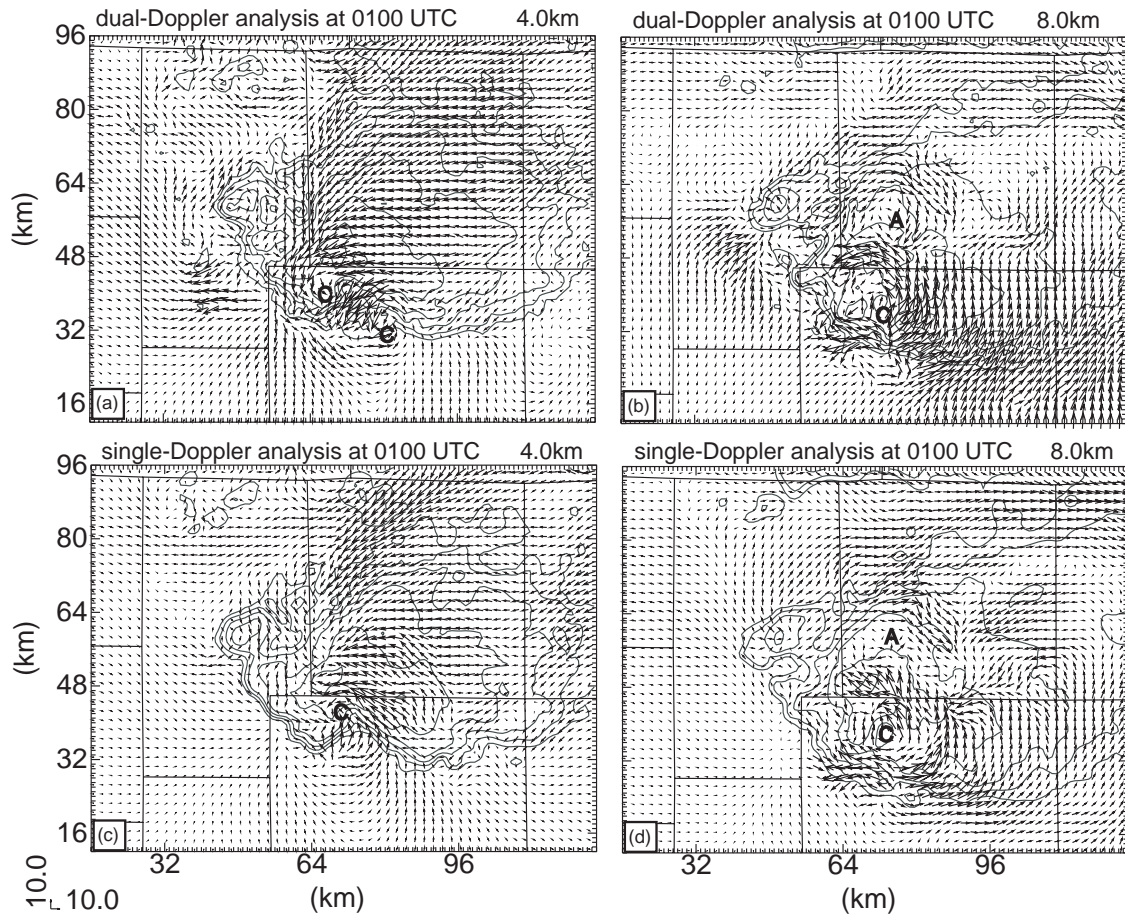


Fig. 6.10. Storm-relative horizontal wind vectors and reflectivity contours (at 10 dBZ intervals starting from 10 dBZ) for dual-radar (upper panel) and single-radar (lower panel) analyses at $z = 4\text{km}$ (left panel) and $z=8\text{km}$ (right panel), at 0100 UTC, 30 May 2004.

At the higher 8 km level, a cyclonic-anticyclone vortex couplet can be seen in both dual-radar and single-radar analyses (Fig. 6.10b and Fig. 6.10d), which can be explained by the tilting of environmental horizontal vorticity by the storm updraft.

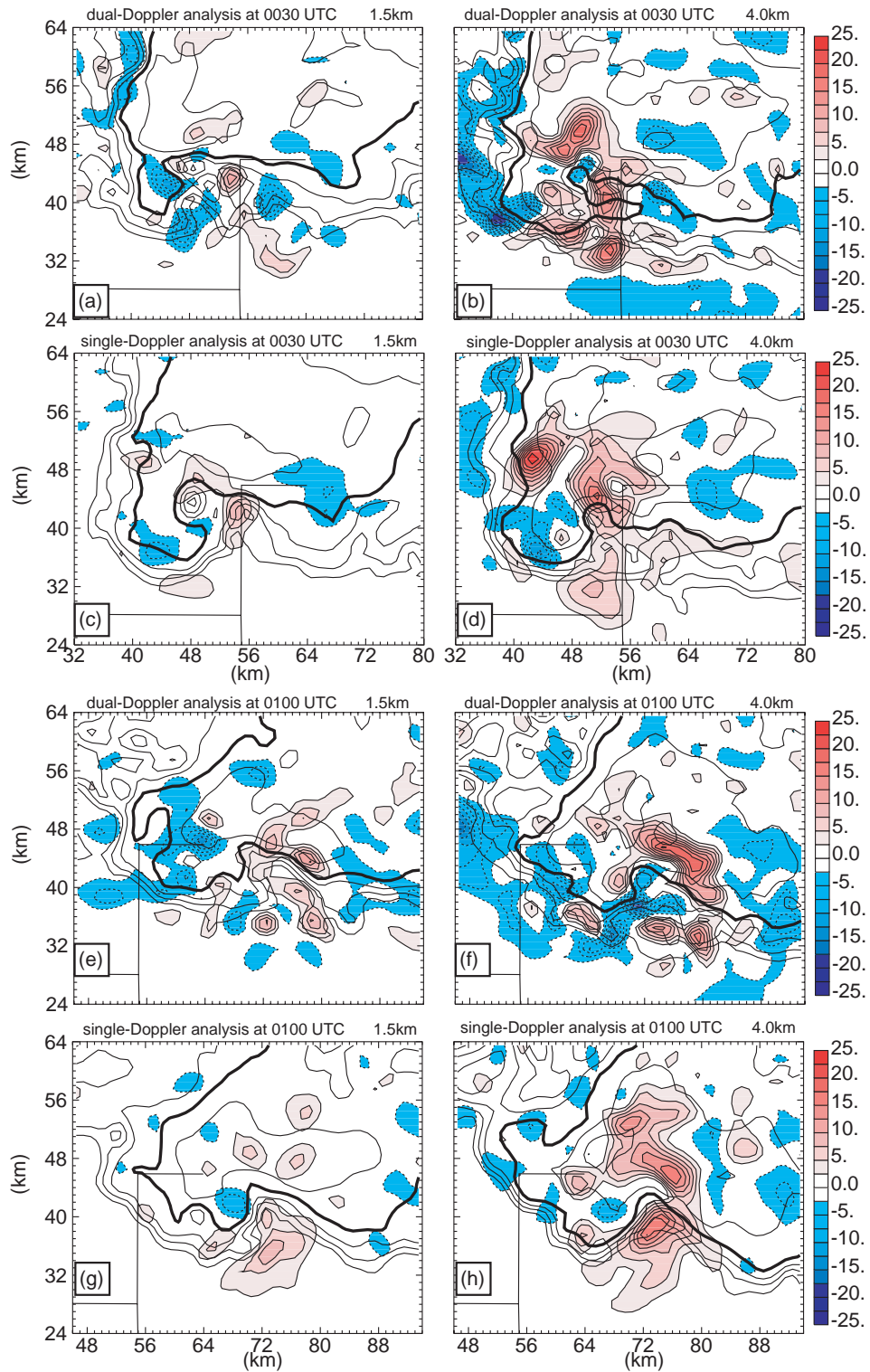


Fig. 6.11. Same as Fig. 6.9, but for vertical velocity (color shading at intervals of 2.5 m s⁻¹) and reflectivity (contours at intervals of 10 dBZ starting from 10dBZ).

The analyzed w fields at the 1.5 and 4 km levels are somewhat noisier. At the 1.5 km level, the updrafts are generally found in the inflow region, towards the kink of the hook echo while downdrafts are mostly found at and around the southeastward extruding appendage of the hook echo. At the leading edge of this extruding appendage lies the low-level rear-flank gust front. Signs of weak forced upward motion is found along this gust front (Fig. 6.11a and c). The dual-radar analysis of w contains more small-scale structures than the single-radar analysis, presumably associated with the stronger small-scale horizontal convergence/divergence analyzed with radial velocity data from both radars.

At the 4 km level, the broader structures of the w fields exhibit a spiral pattern, with a band of negative and a band of positive vertical velocities converging towards the center of mesocyclone. At the finer scales, the small circulation centers identified earlier at this level are generally located inbetween the upward and downdraft couplets, indicating the important role played by tilting and the associated stretching in creating the vertical vorticity.

The analyzed vertical vorticity fields at the surface and at the 1.5 km level are plotted in Fig. 6.12. At the 1.5 km level, the vorticity and vertical velocity fields are positively correlated. The vorticity is generally stronger in the dual-radar analysis than that in the single-radar analysis. In the single-radar analysis, the vorticity become stronger at 0100 UTC, with a positive maximum greater than $1 \times 10^{-2} \text{ s}^{-1}$ at the weak echo region and extends from 1.5 km down to the surface, which may be a signature of tornado. The surface vertical vorticity in the dual-radar analysis also increases between 0030 and 0100 UTC (Fig. 6.12a and Fig. 6.12e).

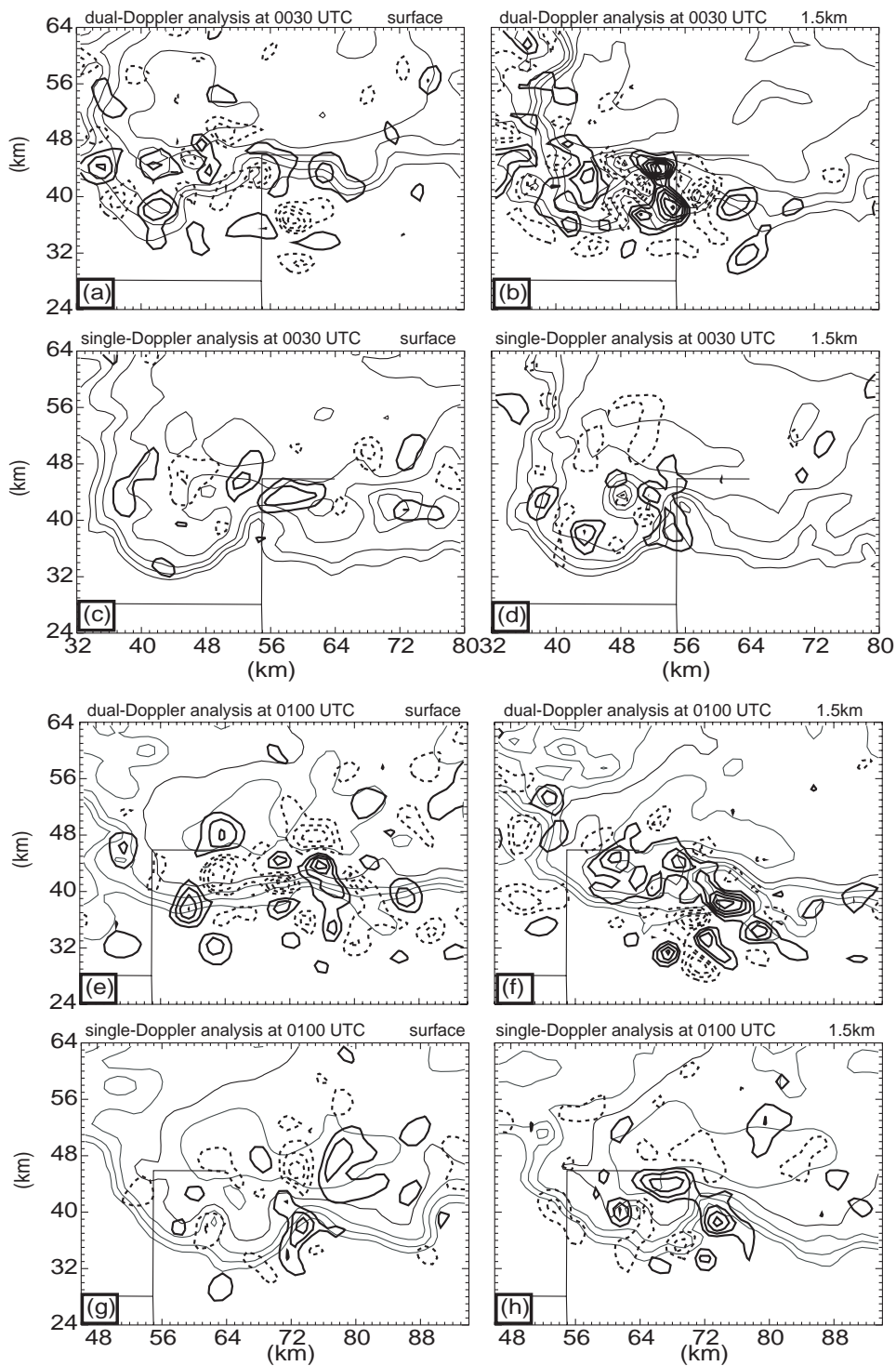


Fig. 6.12. The same as Fig. 6.9, but for vertical vorticity (thick contours at intervals of 0.003 s^{-1}) and reflectivity (thin contours at intervals of 10 dBZ starting from 10dBZ) at the surface (left column) and at the 1.5 km height level (right column).

The fields close to the surface are more difficult to retrieve because of the lack of radar coverage there due to the effects of radar beam elevation and the earth curvature. The difficulty in retrieving low-level cold pool was found also in Weygandt et al. (2002b) and Dowell et al. (2004). Dowell et al. (2004) found that the characteristics of the retrieved cool pool are mainly associated with the integrated effect of evaporative cooling in the model rather than the result of assimilating velocity observations. In their study, warm rain microphysics scheme is used and only the radial velocity observations are assimilated. In this study, we use an ice microphysics scheme and attempt to analyze the state variables, especially the unobserved variables, from both radial velocity and reflectivity observations. While the ice microphysics and extra data should in principle improve the results, they also introduce additional uncertainties that are associated with the microphysical processes; both the forward operator for reflectivity data and the microphysics parameterization depend on the assumed drop size distribution. It is known, through sensitivity experiments, that the simulated cold pool is sensitive to the intercept parameters used in the assumed drop size distributions for the hydrometeors.

Fig. 6.13a-b shows the analyzed wind, perturbation potential temperature and reflectivity fields at the surface for the single-radar analysis experiment. The hook-shaped reflectivity appendages are not as pronounced as those at 1.5 km level. In our early test, when only 10% covariance inflation was used, the echo at the surface was much weaker and narrower than that in Fig. 6.13, which was found to be due to the loss of ensemble spread in microphysical fields. At 0030 UTC, a convergent cyclonic circulation can be clearly seen northwest of the southeasterly inflow. The coldest air is

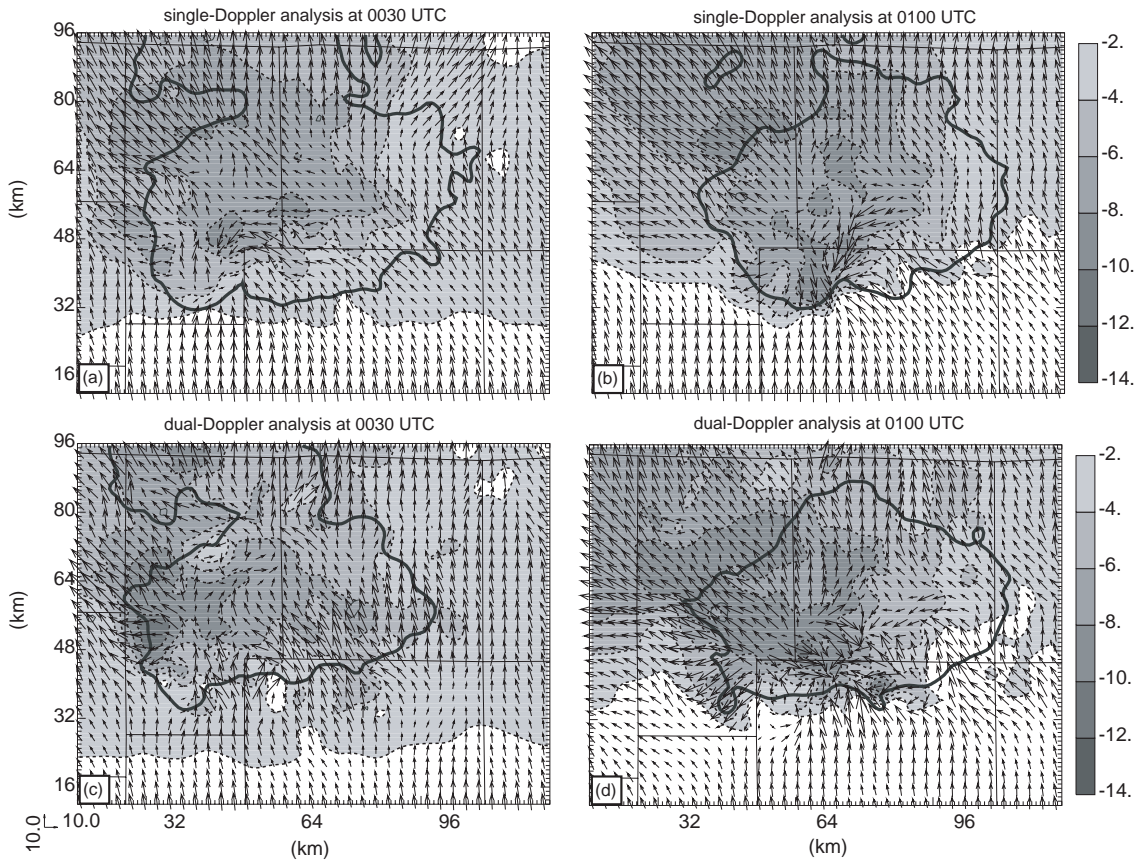


Fig. 6.13. Surface horizontal velocity vectors (m s^{-1}), perturbation (from sounding-defined base state) potential temperature (shaded dashed contours at 2 K intervals) and reflectivity (only 10dBZ contour is plotted and highlighted) from ensemble mean analysis of single-radar analysis experiment at (a) 0030 UTC and (b) 0100 UTC; of dual-radar analysis experiment at (c) 0030 UTC and (d) 0100 UTC.

found to the northwest of the cyclonic circulation and at the forward flank of the storm. The minimum perturbation potential temperature is less than -8 K. At 0100 UTC, the cold air outflow behind the rear flank gust front becomes stronger and spreads towards the southeast, south and southwest directions, leading to a stronger gust front. The coldest air is now shifted towards the rear flank of the storm behind the gust and stronger convergence can be seen along the gust front and near the occlusion region. Although it is hard to say whether the cold pool and the gust front are retrieved

accurately, they are dynamically consistent with the development of a typical supercell thunderstorm. The retrieved surface wind fields are noisier in the dual-radar analysis. The analyzed reflectivity echo is even smaller than that of single-radar analysis at 0300 UTC and hook echo are also not well defined.

6.3.2.3 Forecast starting from single-radar analysis

We performed a two-hour forecast, starting from the ensemble mean analysis of the single-radar assimilation experiment at 0100 UTC. During this period, seven actual tornadoes were observed.

Comparing Fig. 6.14 and Fig. 6.15, we can see that the forecasted storm propagates eastwards as the observed storm did, but at a higher speed than the observed one. After one hour of forecast, at 0200 UTC, the center of the predicted storm has reached to the center of Logan County (c.f., Fig. 6.1), while the observed storm was still at the west border of this county. After two hours of forecast, at 0300 UTC, the main body of the predicted storm has moved out of our model domain, while the observed one reaches the east border of Logan County. The position error at one and half hours of the forecast is about 20 km.

The low-level features of the forecast storm, during the first 40 minutes, are very typical of a supercell at its tornadic stage (Fig. 6.16). The hook echo shape remains pronounced but the high reflectivity region becomes more concentrated and does not extend to the forward flank of the storm as in the observed one. The low-level updraft becomes more organized in the forecast, with a continuous band of updraft forming along the rear flank gust front. A stronger cyclonic circulation develops and can be seen

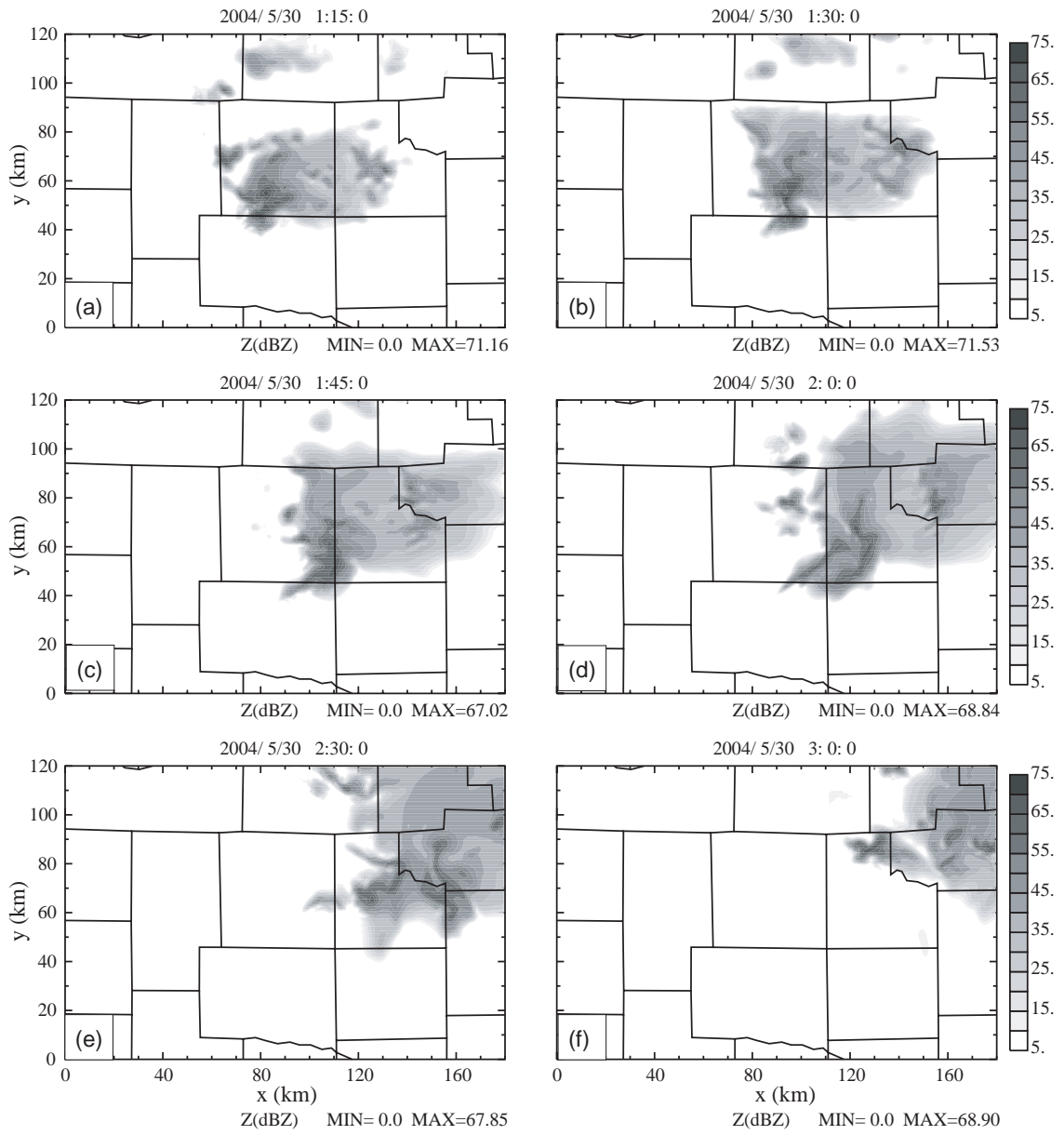


Fig. 6.14. Reflectivity as viewed from KTLX radar at the 1.25° elevation of the predicted storm initialized from single-radar ensemble mean analysis at 0100 UTC at (a) 0115 UTC, (b) 0130 UTC, (c) 0145 UTC, (d) 0200 UTC, (e) 0230 UTC and (f) 0300 UTC of 30 May 2004.

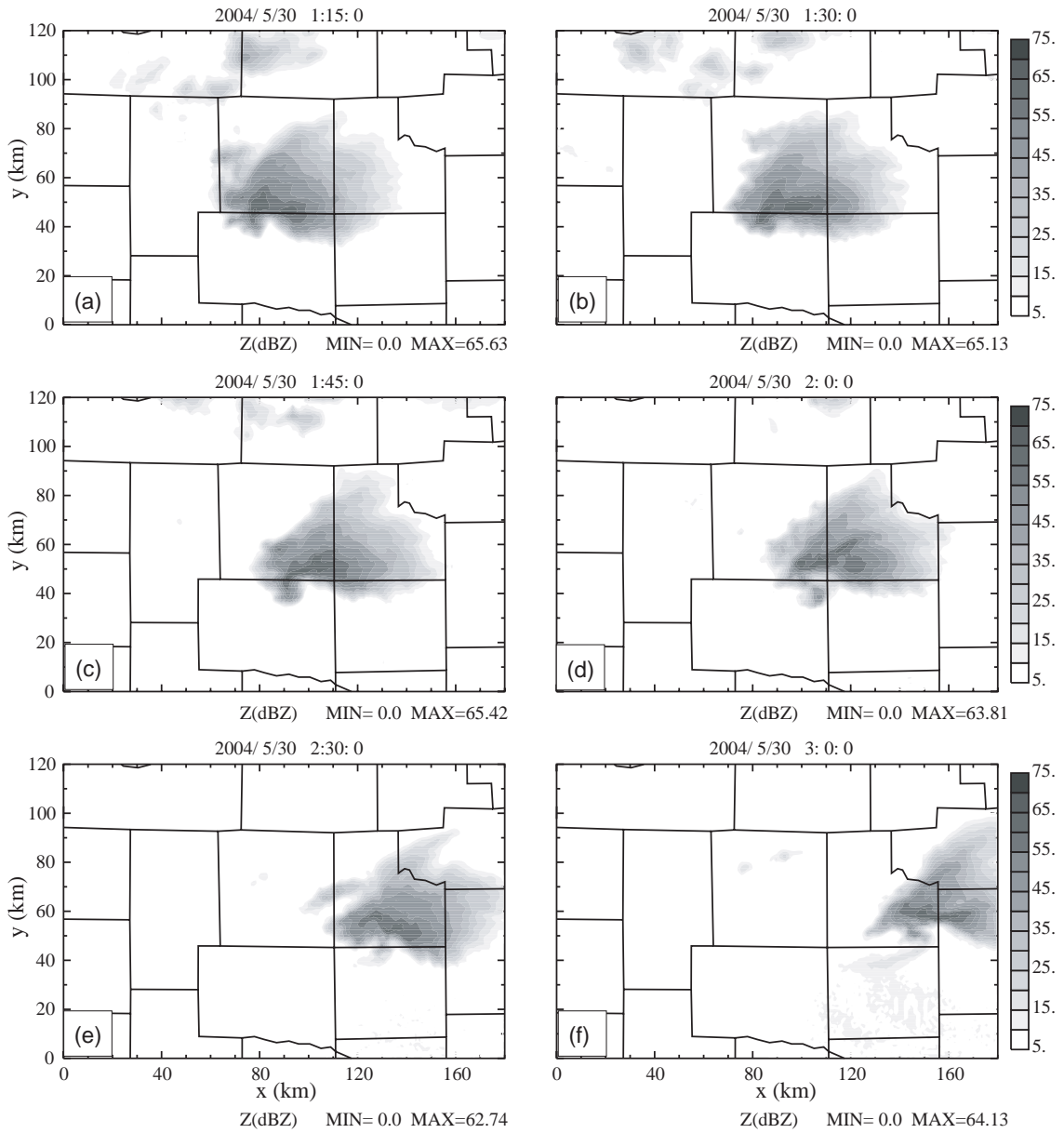


Fig. 6.15 The radar reflectivity observed by KTLX radar on the 1.25° elevation level at (a) 0115 UTC, (b) 0130 UTC, (c) 0145 UTC, (d) 0200 UTC, (e) 0230 UTC and (f) 0300 UTC of 30 May 2004.

clearly at 0120, 0130 and 0140 UTC, and the strengthening of the circulation is partly due to the intensification of eastward pushing cold outflow behind the gust front. At the mid-level, the mesocyclone circulation continues (not shown). At later times, the

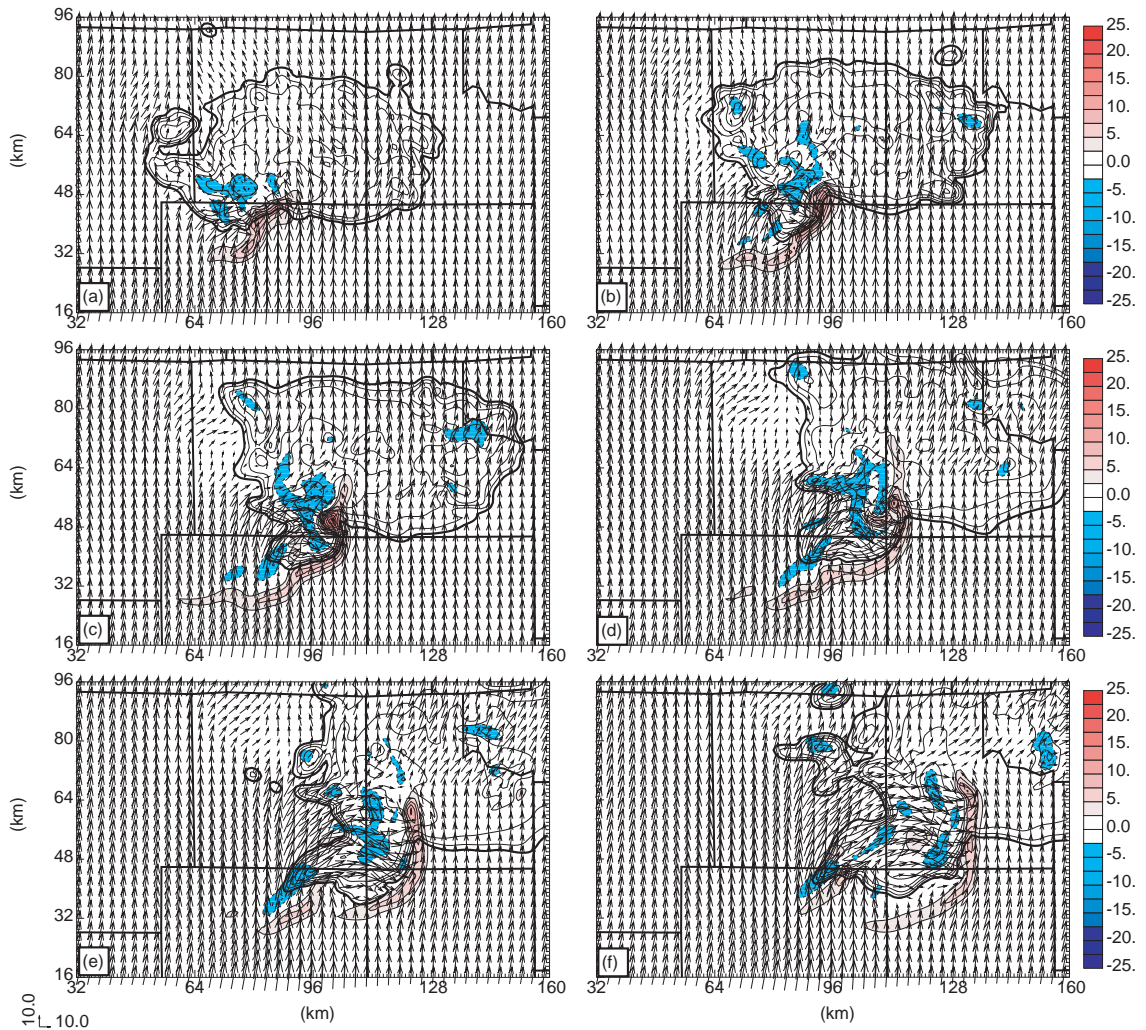


Fig. 6.16. Horizontal velocity vectors (m s^{-1}), vertical velocity (color shading) and reflective (contours at intervals of 10 dBZ starting from 10dBZ) at $z=1.5$ km from ensemble mean forecast initialized from single-radar ensemble mean analysis using KTLX data at 0100 UTC at (a) 0110 UTC, (b) 0120 UTC, (c) 0130 UTC, (d) 0140 UTC, (e) 0150 UTC and (f) 0200 UTC of 30 May 2004.

northwesterly and westerly outflow behind the gust front become even stronger, pushes the gust front and the associated updraft region into a mostly north-south orientation. The reflectivity appendage expands and the hook echo feature is gradually lost. The minimum perturbation potential temperature at the surface is less than -10 K after 0110 UTC. The too fast eastward propagation of the forecast storm suggests that model cold

pool is probably too strong, and possible errors in the microphysics may have been responsible for this too strong a cold pool.

6.4 Assimilation experiments using inhomogeneous environmental conditions provided by 3DVAR analysis

The results in Section 6.3.2 with a homogeneous storm environment defined by a single sounding suggest that the EnSRF analysis and the subsequent forecast are substantially affected by possible errors in the forecast model and/or in the storm environment. There are different sources of error that are usually hard to identify for real cases, where exact truth is unknown. In this section, we try to improve the analysis and prediction results by reducing/removing some of the uncertainties.

First, the assumption of a horizontally homogeneous storm environment with the vertical profiles defined by a sounding is problematic because of the inherent uncertainties. Several experiments we performed with somewhat different soundings show that both the analysis and forecast are sensitive to the prespecified environmental conditions. An example is that the forecast storm initialized from an analysis, in which the vertical profiles contain a dry layer found in the observed 0000 UTC OUN (Norman Oklahoma) sounding between the 800 hPa and 600 hPa levels, decays faster than the true storm and propagates northeastward rather than eastward as the true storm did. Errors in the environment condition can have a similar effect on model storms as systematic model error, in that they affect the evolution of each ensemble member during the forecast step and result in a biased analysis. One way to reduce the

uncertainty in the environmental condition is to let it be sufficiently constrained by observations. Skamarock and Snyder (presentation at the 2004 NCAR EnKF workshop) tried to tackle this problem by treating the mean profiles of the model state as uncertain parameters and retrieve them simultaneously with the model state, in a similar way as our microphysical parameter estimation in Chapter 5. However, the limitation is that the large-scale environment is still assumed to be horizontal homogeneous. Our way to reduce the uncertainty with the storm environment is to use 3-D dimensional environmental conditions provided by a 3DVAR analysis using all conventional observations and try to predict the temporal changes in the environmental condition.

Except for the microphysical processes, no other physical processes were included in the experiments presented in Section 6.3. In the experiments of this subsection, full model physics are used, including the land-surface processes that include surface heating, moisture and momentum fluxes, and the radiation processes. By doing so, the environmental condition of the storms will evolve in time, in response to the physics. It is therefore expected to be more accurate during the later times of assimilation and prediction.

6.4.1 Experimental design

The model configurations are the same as those in Section 6.3.1.1, except that full model physics are included and external boundary condition is applied at lateral boundaries. The external boundary conditions are obtained from the ARPS forecast initialized from a 3DVAR analysis using soundings, wind profiles, surface

observations, and Oklahoma Mesonet data at 0000 UTC and this forecast used a 3 km horizontal resolution.

Forty ensemble members are initialized the same way as in Section 6.3.1.2, except that spatially smoothed perturbations are added to the horizontally inhomogeneous initial guess provided by the 3DVAR analysis at 0000 UTC of 30 May. The first analysis is performed at 0005 UTC. The data assimilation window spans 0000 through 0100 UTC. The radar scan volumes are assimilated at five minute intervals. Data from either KTLX radar alone (single-radar analysis) or from both KTLX and KVNK radars (dual-radar analysis) are assimilated. Radial velocity data from single or both radars, and reflectivity data from KTLX, are assimilated.

In the experiments that will be shown in the following section, the estimated rms observation error is 2 m s^{-1} for V_r and 3 dBZ for Z . The cutoff radius for the covariance localization is 4 km. We still apply covariance inflation to prevent filter divergence. The inflation amount applied is 35% in the single-radar analysis and 50% in the dual-radar analysis.

6.4.2 Results of analysis

The rms differences as indicated by the black solid/dash curves in Fig. 6.17 measure how well the ensemble mean background forecasts and analyses match the observations of the two radars whose data are assimilated. Similar to what was found in Section 6.3, the analyses match the observations very well, with the rms differences of V_r remaining at around 2 m s^{-1} and those of Z below 5 dBZ compared to KTLX radar and below 6 dBZ for KVNK radar. The EnSRF is very effective in constraining the

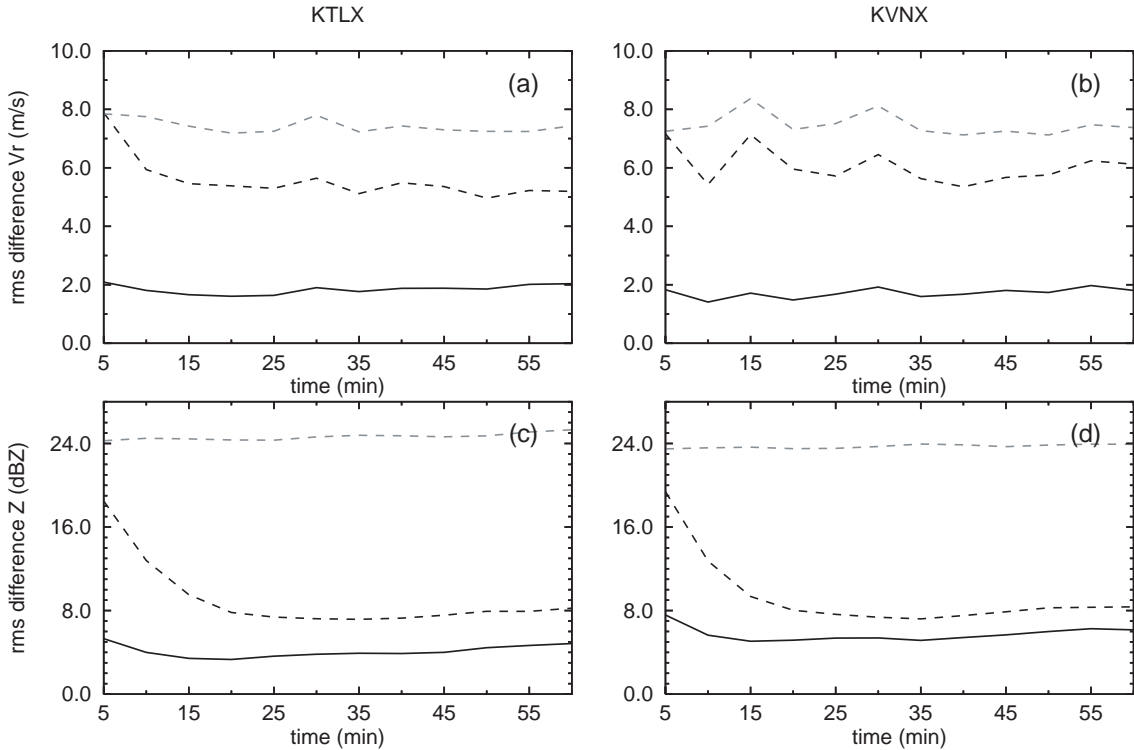


Fig. 6.17. Diagnostics and scores for the dual-radar analysis. (a) radial velocity rms differences with respect to the KTLX observations for ensemble mean analysis (solid black), ensemble mean forecast (dashed black), Environmental state obtained from the forecast initialized from 3DVAR analysis (dashed gray). (b) The same as (a) but with respect to the KVNIX radial velocity. (c) The same as (a) but with respect to the KTLX reflectivity. (d) The same as (c), but with respect to the KVNIX reflectivity.

model state toward the observations. However, the analyzed velocity fields quickly deviate from the observations within just 5 minutes of forecast of each cycle as indicated by the large gap between the rms differences for the forecasts and the analyses (Fig. 6.17a and b). Again, the gap is smaller for reflectivity (relative to the initial gap) than for radial velocity. For single-radar analyses, the analyzed reflectivity fields fit the observations of both radars very well (solid black curve in Fig. 6.18c, d) even though reflectivity data from KTLX only were assimilated. As was found earlier with the single sounding case, the radial wind component as seen by KVNIX radar is not well

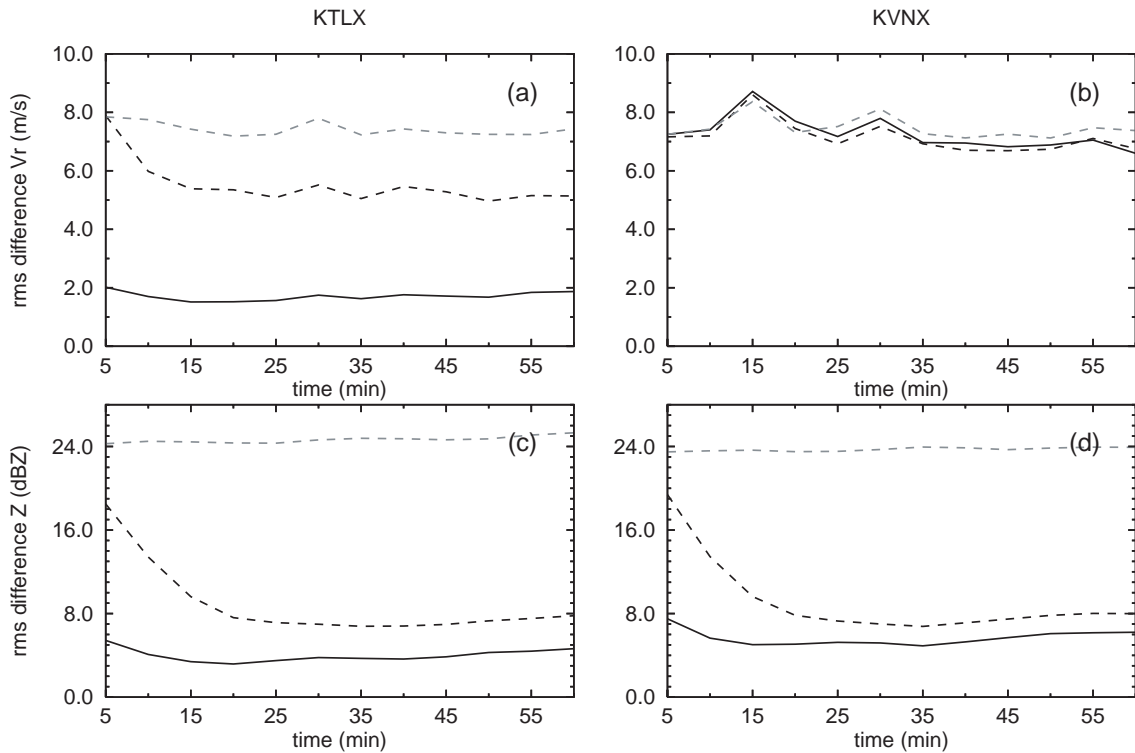


Fig. 6.18. The same as Fig. 6.17, but for single-radar case.

retrieved (Fig. 6.18b). The forecast background radial velocity fields of KVNIX are barely improved by the analysis.

To more quantitatively evaluate the performance of the EnSRF, innovation statistics are calculated for both dual-radar and single-radar analyses. It can be seen that there are general discrepancies between the standard deviation of the innovations and the corresponding ensemble estimate in both cases (compare thick solid black and thin solid black lines in Fig. 6.19 and Fig. 6.20). The ensemble spread is generally too small (the dashed curves in Fig. 6.19 and Fig. 6.20), especially for radial velocity. The large discrepancy for the radial velocity of KVNIX in single-radar analysis is believed to contribute to the poor estimation of the wind component seen by KVNIX radar (Fig. 6.20b).

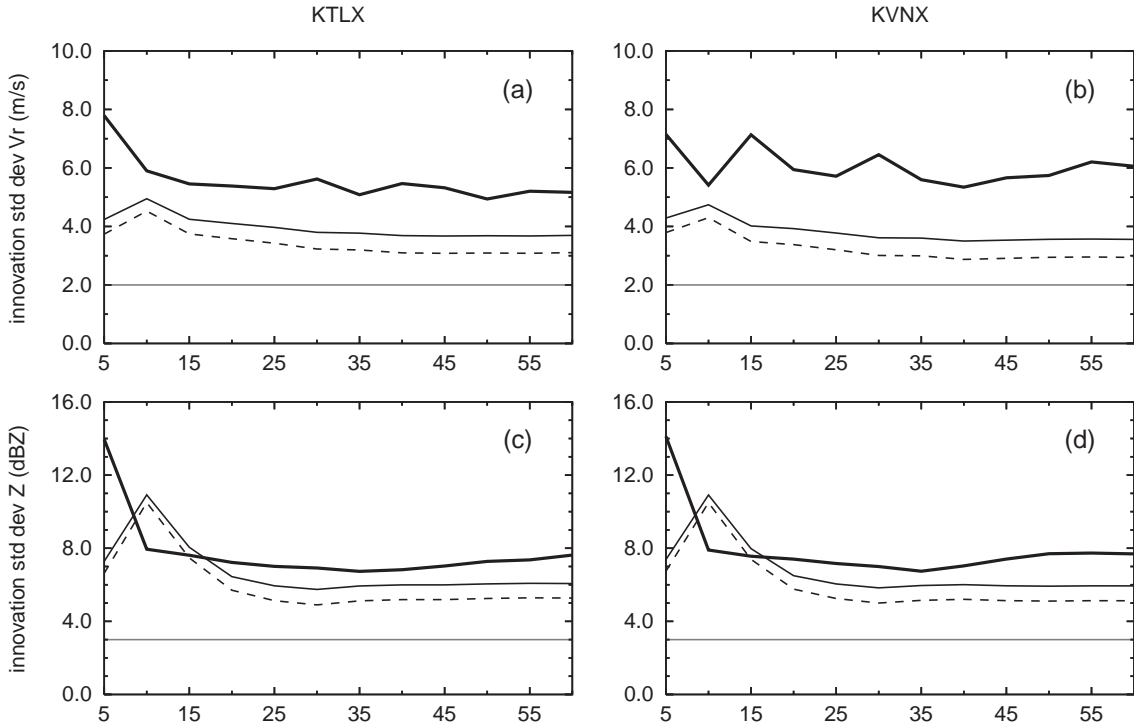


Fig. 6.19. Innovation statistics for the dual-radar analysis. (a) Observed innovation std dev σ_v (thick solid black), rms observation error σ_o (solid gray), rms ensemble spread σ_f (dashed black), and predicted innovation std dev $\sqrt{\sigma_o^2 + \sigma_f^2}$ (thin solid black) corresponding to KTLX radar for radial velocity. (b) The same as (a) but corresponding to KVNIX radar for radial velocity. (c) The same as (a) but for reflectivity. (d) the same as (b) but for reflectivity.

Fig. 6.21a and Fig. 6.21c show the retrieved wind fields and analyzed reflectivity at 4 km height level at 0055 UTC and 0100 UTC, respectively. The mid-level updraft is located within the broad mid-level cyclonic circulation with some downdrafts found to its west and southwest. Some finer structure can also be seen, including the two smaller cyclonic circulations indicated by ‘c’ in Fig. 6.21c, which corresponds to the two outflow-inflow couplets in Fig. 6.8b, d. In the single-radar analysis, such finer structures are hard to identify, however (Fig. 6.23b). At the 1.5 km height level, a very strong updraft ($> 20 \text{ m s}^{-1}$) is found at the weak reflectivity region

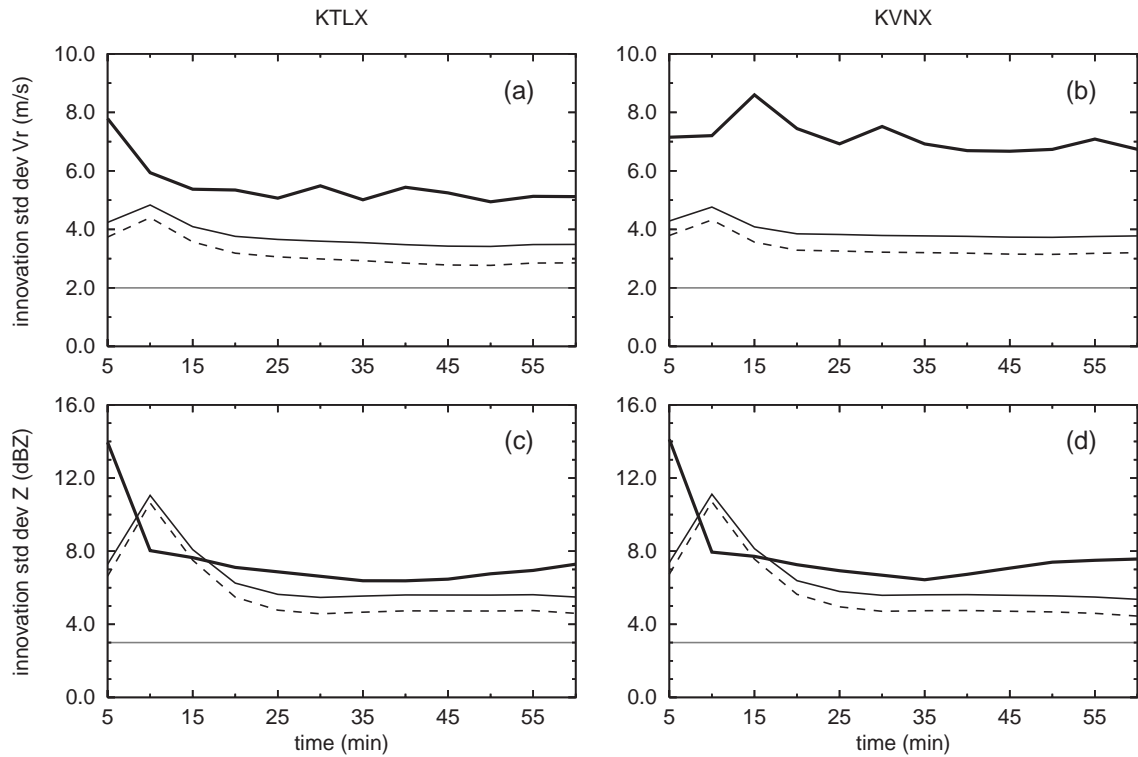


Fig. 6.20. The same as Fig. 6.19, but for single-radar analysis.

next to the reflectivity appendage in the dual-radar analysis (Fig. 6.22a, c). The updraft at the same level is much weaker ($< 10 \text{ m s}^{-1}$) in the single-radar analysis (Fig. 6.23a). At the surface, the retrieved cold pool is very strong and the hook echo feature is less pronounced in both cases than at the 1.5 km, suggesting an underestimation of rotation features near the surface, presumably due to the lack of radar data coverage at the low levels. The lowest elevation is about 0.5° for both radars. At 0100 UTC, when the storm is closest to both radars during the data assimilation period, the center of the storm is at a distance of 80 km from the KTLX radar and of 105 km from the KVN radar (Fig. 6.1). According to radar geometry (c.f., Fig. 2 in XTD06), data at the distance of 80 to 105 km from the radar on the first elevation level are distributed between 1 to 1.5 km. The atmosphere below 500 m is not observed by the two radars.

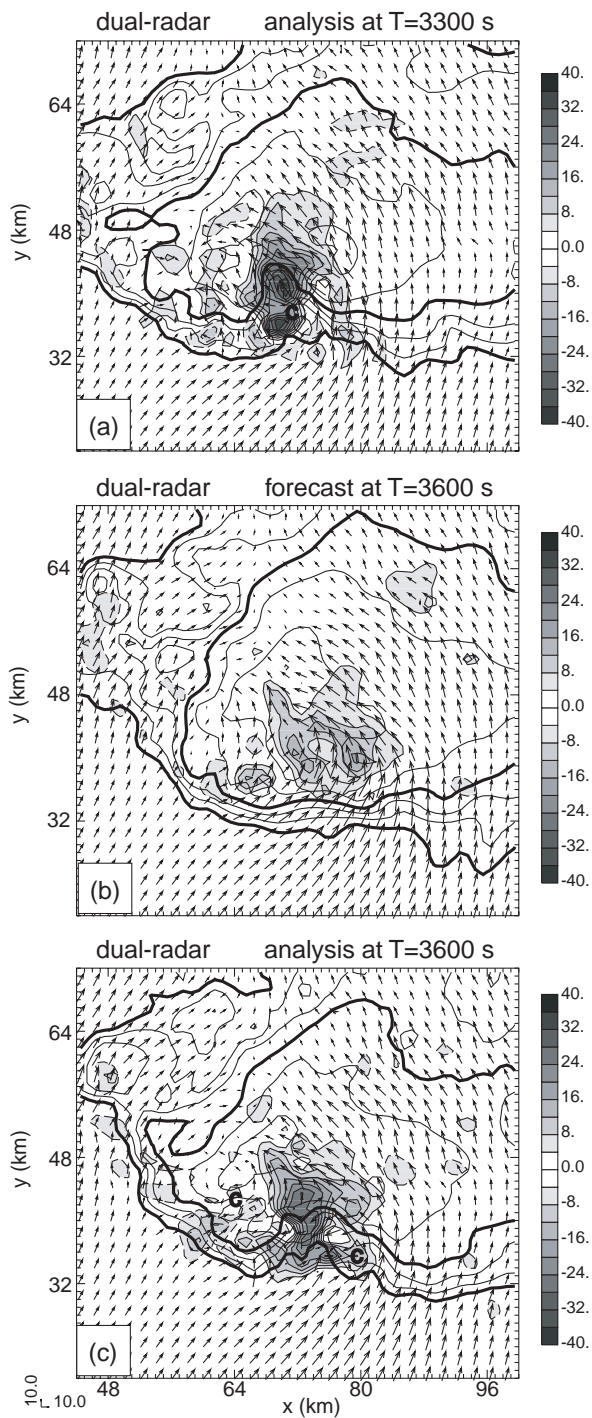


Fig. 6.21. Vertical velocity [contours and shading, solid (dash) contours represent positive (negative) w] and horizontal storm-relative winds (vectors, plotted every other grid point) and reflectivity (contours at intervals of 10 dBZ starting from 10dBZ, with the 40 dBZ contours highlighted) at 4 km MSL from dual-radar analysis experiment. (a) ensemble mean analysis at 0055 UTC (b) ensemble mean forecast of dual-radar analysis at 0010 UTC (c) ensemble mean analysis at 0100 UTC

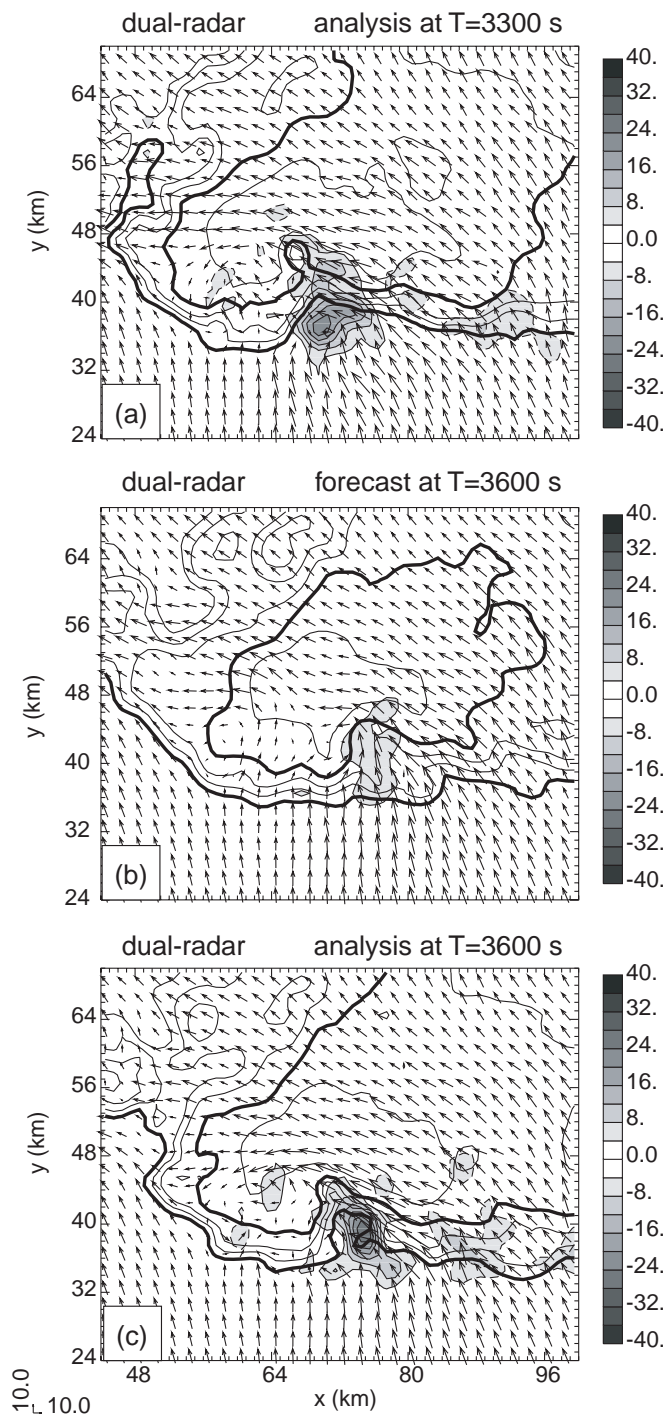


Fig. 6.22. The same as Fig. 6.21, but for the ensemble mean analyses and forecast at 1.5 km MSL.

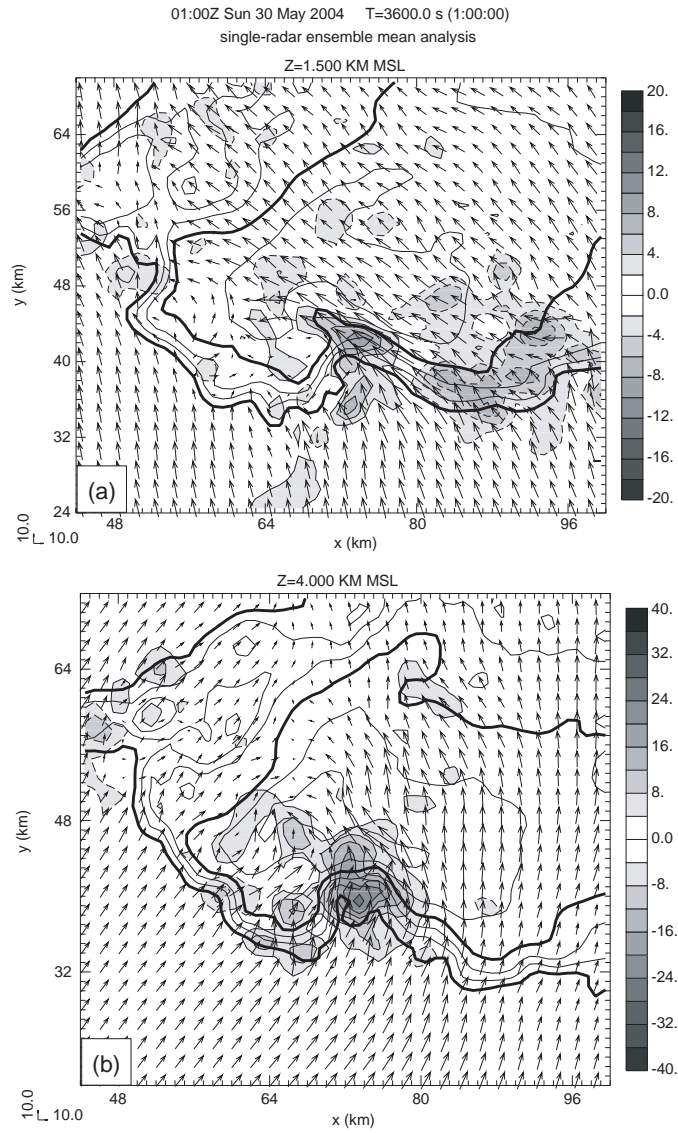
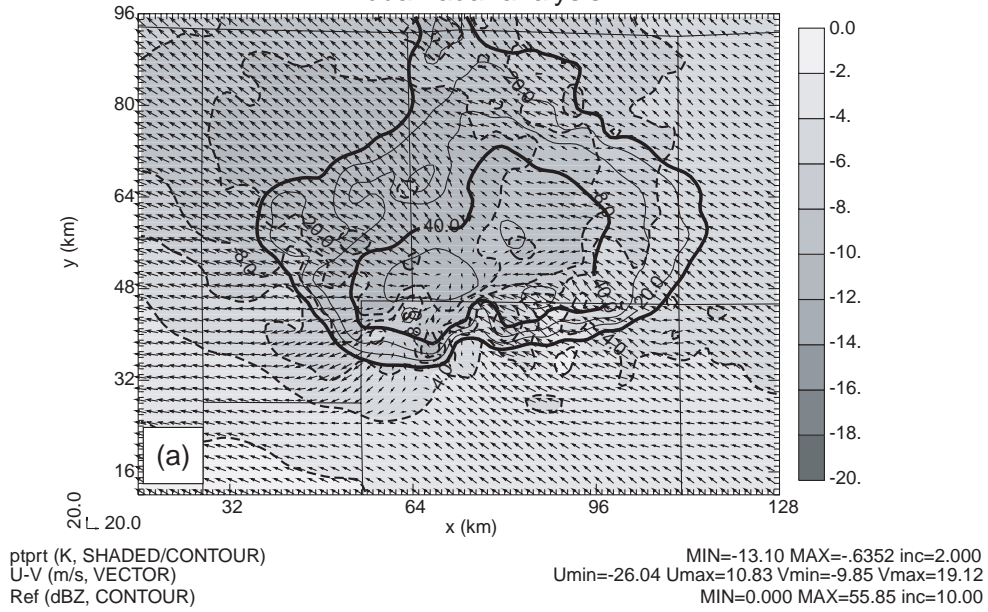


Fig. 6.23. The same as Fig. 6.21, but for single-radar ensemble mean analysis at (a) 4km and (b) 1.5 km.

01:00Z Sun 30 May 2004 T=3600.0 s (1:00:00)
 FIRST LEVEL ABOVE GROUND (SURFACE)
 dual-radar analysis



single-radar analysis

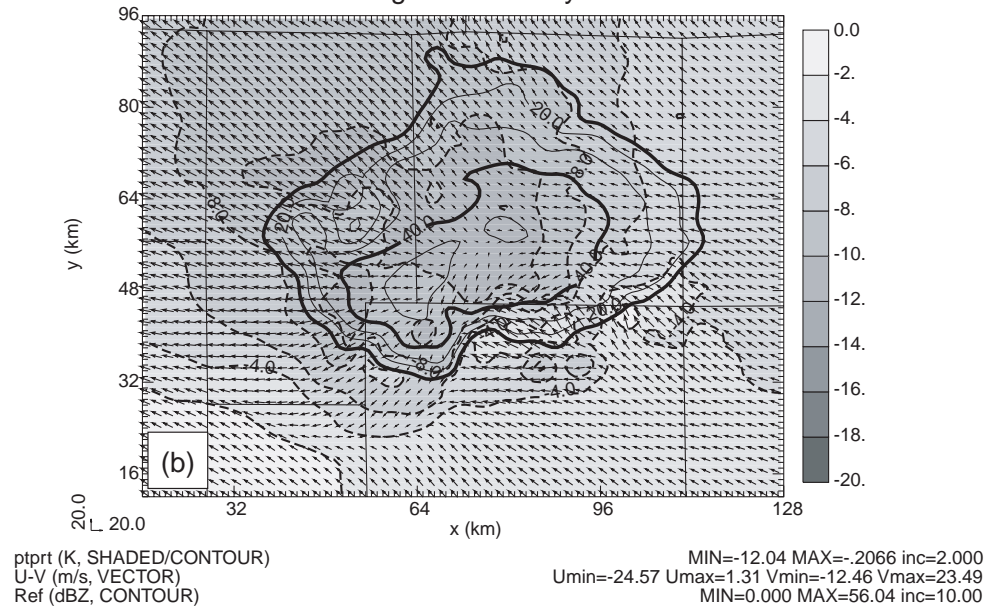


Fig. 6.24. Surface horizontal storm-relative velocity vectors (m s^{-1}), perturbation potential temperature (shaded dashed contours at 2 K intervals) and reflectivity (only 10dBZ contour is plotted and highlighted) from (a) dual-radar ensemble mean analysis and (b) single-radar ensemble mean analysis at 0100 UTC.

Although dynamically consistent patterns typical of supercell storms, including strong mid-level rotation, updraft and low-level hook echo, can be retrieved from the radar data, such structures are not maintained well during the forecast step (Fig. 6.21b and Fig. 6.22b). As we can see that after 5 minutes of forecast, the low-level updraft becomes much weaker and the hook echo is becomes less well defined (Fig. 6.22b). The reason why the model fails to maintain seemingly dynamically consistent features during the short-time 5-minute forecasts needs to be investigated, by, for example, examining the low-level convergence and time series of pressure perturbation to see if mass continuity appears to be satisfied and if significant flow adjustment occurs in the forecast, which will help us identify the source of error. The fact that fine-scale structures, such as the cyclonic circulation within the reflectivity appendage at the low levels and the small circulations at the middle level, disappear quickly during the model integration suggests that the current 1 km resolution may still be insufficient, leading to poor fit of the forecast to observations.

6.4.3 Results of forecast

Two-hour forecasts starting from the ensemble mean analyses at 0100 UTC are performed for both dual-radar and single-radar assimilation experiments. The predicted reflectivity fields mapped to the 1.25° elevation of KTLX radar are shown in Fig. 6.25 and Fig. 6.26 for the two cases, respectively.

The predicted storms in both cases propagate in the right direction, but at a much higher speed (15.5 versus 11.1 m s^{-1}) than the observed storm (Fig. 6.15), similar to the single sounding case discussed in Section 6.3.2.3. The strong low-level cold pool

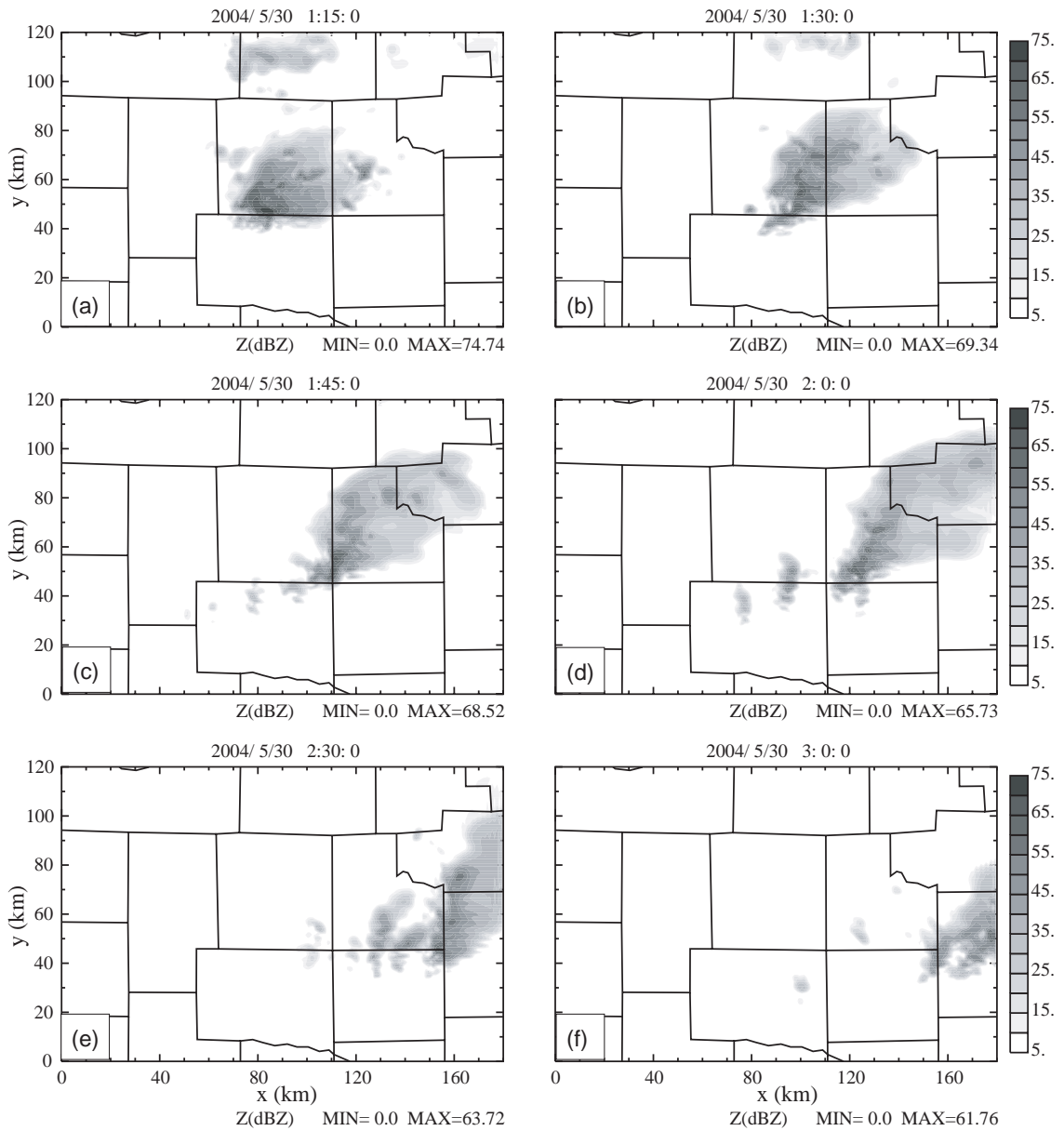


Fig. 6.25. Reflectivity as viewed from KTLX radar at the 1.25° elevation of the predicted storm initialized from the dual-radar ensemble mean analysis at 0100 UTC at (a) 0115 UTC, (b) 0130 UTC, (c) 0145 UTC, (d) 0200 UTC, (e) 0230 UTC and (f) 0300 UTC.

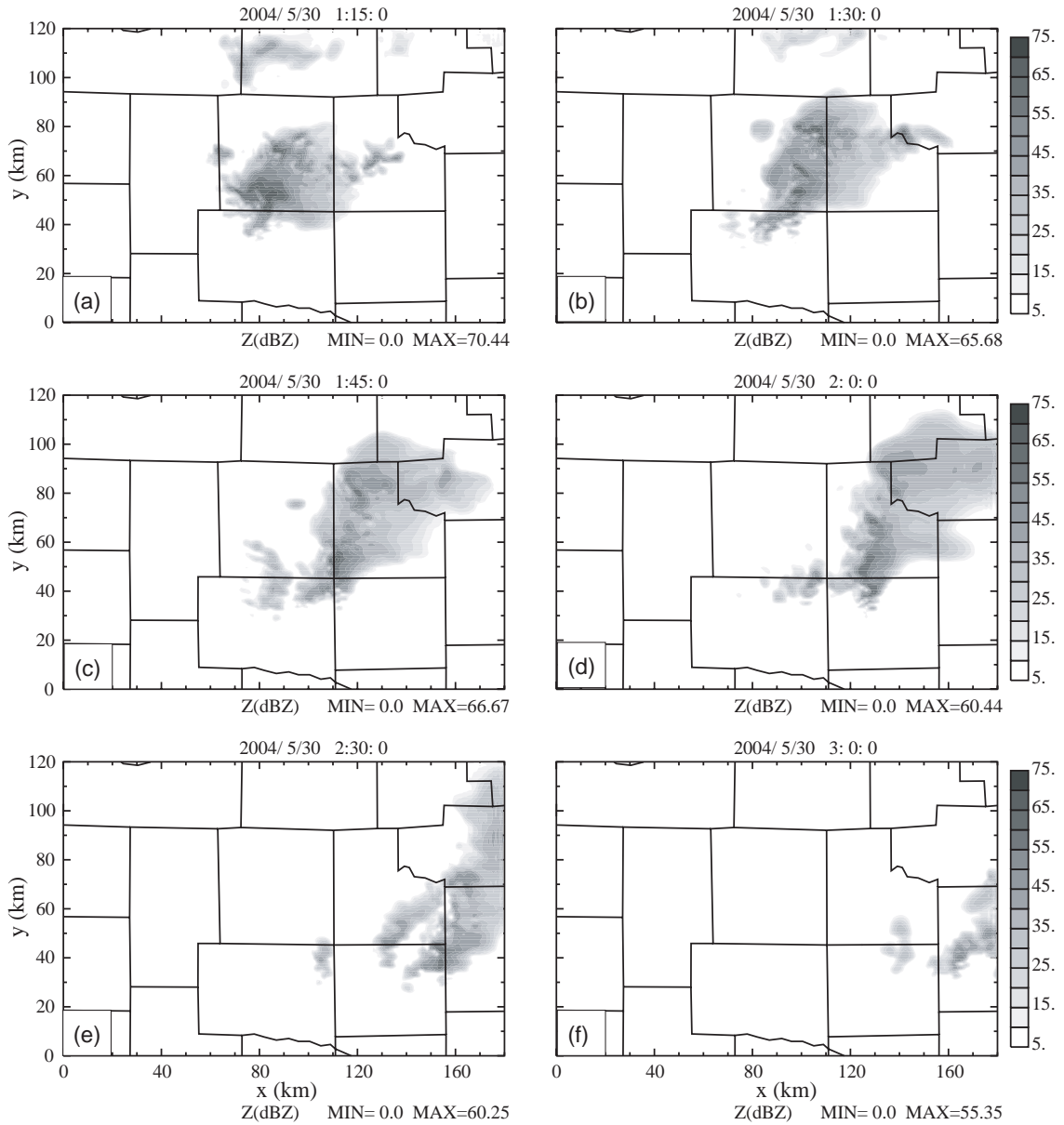


Fig. 6.26. The same as Fig. 6.25, but the forecast is initialized for single-radar analysis.

at the initial time is believed to be at least partially responsible for the fast propagation speed. Including surface friction in current cases does not seem to help reducing the propagation speed of the predicted storm.

During the forecast period, the shape of the storm changes significantly and becomes more south-north oriented. Spurious cells start to pop up to the west of the

predicted storm from 0130 UTC. The hook echo feature is barely seen in both cases. Although the retrieval of the wind fields is significantly improved when radial velocity data from both radars are used, this improvement does not, unfortunately, lead to better forecast in this case. A summary and discussions on these and earlier results will be offered next.

6.5 Summary and discussions

In this chapter we applied the EnSRF to the assimilation of real radar data for a tornadic supercell thunderstorm that produced 16 tornadoes along its way through central Oklahoma on May 29-30, 2004. The storm at its mature stage was observed by two WSR-88D radars (KTLX from Oklahoma City and KVNK from the Vance Air Force Base, Kansas) at distances ranging from 126 to 80 km. We performed EnSRF analyses using either single (KTLX) and both (KTLX and KVNK) radars.

In our first attempt to assimilate these data, the storm environment is assumed to be horizontally homogeneous as defined by a modified observational sounding. The ARPS model is used in a simple cloud model mode. The analyzed radial velocity and reflectivity from both single- and dual-radar experiments match very well the observations from the radar(s) that are directly assimilated. For the single-radar analysis, the analyzed radial velocity does not fit the independent radial velocity observations from the KVNK radar very well, however. In the analyzed velocity fields, two cyclonic circulations are found at the mid-level in the dual-radar analysis, which correspond well with the two inbound-outbound radial velocity couplets found in the observations from both radars, while only one cyclonic circulation is found in the

single-radar analysis. The velocity component of KVXN radar at the location of the storm is almost perpendicular to that of KTLX in the early period of the assimilation window. The EnSRF depends on the estimated error covariances between observed radial wind component and the unobserved wind components in retrieving the latter. The relatively poor quality of analysis of the latter suggests that the background error covariances were not estimated accurately.

Although several aspects of the analysis need to be improved, especially of the cross-beam wind components, the results of current single-radar analysis are still encouraging. Key features of supercell thunderstorm are captured by the analysis, including a mid-level mesocyclone accompanied by rotating updrafts and a pronounced hook echo. The retrieved low-level features are typical of a supercell at its tornadic stage. The predicted storm maintains the characteristics of a supercell for more than one hour and propagates in the right direction, though at too fast a speed. The analyzed gust front and cold pool appear to be too strong and become even stronger during the prediction period, which appears to be responsible for the position error of the predicted storm. Both model error and errors in the initial condition may be responsible for this propagation speed error.

We then tried to improve the EnSRF analysis by using a hopefully better 3D environmental condition provided by a 3DVAR analysis of all conventional observations. Full model physics are also included so that the environment can properly evolve with time. However, the general results of the analysis and forecast are no better than those of the single-sounding case. A number of additional experiments were conducted by adjusting the cutoff radius of covariance localization, the amount of

covariance inflation and the magnitude of the estimated observational error. Still no significant improvement was found in either analysis or forecast. The results suggest that model errors, most probably those related to microphysics and resolution, dominate the inaccuracy of the analysis and forecast.

Experiments were also conducted by tuning the microphysical parameters according to the sensitivity study in Chapter 4. For example, we tried decreasing the rain water intercept parameter by an order of magnitude; the minimum perturbation potential temperature at surface was only decreased by less than 2 K, however, and this change did not help reduce the propagation speed error during the forecast. We also tested another single-moment microphysics scheme from the WRF (Weather Research and Forecasting) model. In this case, the forecast results were even worse; the model storm quickly disintegrated during the forecast. It appears that neither scheme, with their currently parameter setting at least, are suitable for the current case, contributing to significant model errors.

Inadequate accounting for model error also leads to too small an ensemble spread, which is indicated by the innovation statistics. It was found that this problem can not be solved by simply increasing covariance inflation, suggesting the presence of model bias.

The lack of low-level radar data coverage due to the relatively large distances of the storm from the two radars might have also contributed to the inaccuracy of analysis. The impact of data coverage on the analysis can be further investigated by returning to OSS experiments and examining the dependency of the error covariance estimation on the data.

In the future, more research should be performed on the best ways for dealing with model error. More careful analysis and understanding of our current results are also necessary in helping us identify the main sources of error.

Finally, we note that for this particular case, observations from two mobile Doppler radars located much closer to the storm were collected, which, if available to us, can help answer some of the questions that we raised above.

Chapter 7

Summary and Future work

7.1 Summary

The original ensemble Kalman filter (EnKF) method was introduced as a data assimilation method about a decade ago and several variations of EnKF have been developed in recent years. A number of attractive properties of EnKF made it very popular in recent years. First of all, the method provides a flexible as well as practical way for explicitly calculating and evolving the forecast error statistics. With flow-dependent error covariances calculated from the forecast ensemble, observational information can be properly spread in space and used to update unobserved state variables. Compared with the four-dimensional variational (4DVAR) data assimilation method, the current method of choice by operational NWP centers, EnKF is easier to implement, because the analysis code is independent of the forecast model and the algorithm does not require the adjoint code of either the forward observational operators or the prediction model. The development of such adjoint codes, especially for numerical weather prediction (NWP) models that contain complex physical processes, is a very labor intensive task. Moreover, an ensemble based assimilation system can provide, in addition, probabilistic information on the analysis, and a set of initial conditions that can be used to create ensemble forecast.

Initializing short-range NWP models at the convective scale using Doppler radar data is a challenging task, because the state variables are not directly observed by the radar. The advantages of the EnKF method make it an attractive candidate for this task. In this dissertation, we investigated the ability of the ensemble Kalman filter (EnKF) and its variant, the ensemble square-root Kalman filter (EnSRF), in assimilating Doppler radar data for thunderstorm initialization and prediction.

As our first implementation of the EnKF method, the simulated observations of radial velocity and reflectivity for a supercell thunderstorm are directly assimilated (Chapter 3), using the original EnKF algorithm that involves perturbed observations. The EnKF method is found to be able to retrieve accurately the wind and thermodynamic fields, as well as multiple microphysical species associated with a multi-class ice microphysics scheme, an area that 4DVAR techniques and all other data assimilation methods have had difficulties. The assimilation of reflectivity data, not explored by earlier EnKF work, is shown to also have a positive impact on the analysis and subsequent forecast. The relative roles of the radial velocity and reflectivity data and the best way of utilizing them are also carefully evaluated and quantified. The cross-covariances are found to play an important role in retrieving variables indirectly related to the observations. The prediction of the storm initialized from the best analysis, in which radial velocity and full coverage reflectivity data are used, remains very good for at least 2 hours. This represents the first time that multiple microphysical species associated with a complex ice microphysics scheme are accurately retrieved. It is also the first time that the EnKF algorithm is coupled with a compressible NWP

model, the Advanced Regional Prediction System (ARPS). The main results of this study have been published in Tong and Xue (2005a).

The ensemble square root Kalman filter (EnSRF) is then implemented in our EnKF framework. We first applied this algorithm to test the potential impact of the Oklahoma testbed radars of CASA (Center for Collaborative Adaptive Sensing of the Atmosphere, an NSF Engineering Research Center). The results have been published in a journal article and are not detailed in this dissertation.

We then explored the ability of the EnSRF algorithm in correcting model errors associated with uncertain model parameters through simultaneous state and parameter estimation. Five fundamental microphysical parameters are selected for this purpose, which include the intercept parameters of rain, snow and hail drop/particle size distributions and the densities of snow and hail. The possibility of estimating such parameters from radar observations is first investigated for a model-simulated supercell storm by examining parameter sensitivity and identifiability (Chapter 4). Both forecast and assimilation sensitivity experiments show that radar reflectivity observations are preferred over radial velocity data for microphysical parameter estimation because of their larger sensitivity to the microphysical parameters. The time scales of forecast response to errors in individual parameters are also investigated. The results suggest that a successful estimation of the parameters can be expected within the typical lengths of assimilation window that are needed to obtain a good state estimation. The response functions calculated for the forecast as well as assimilation sensitivity experiments for all five individual parameters show concave shapes and unique minima equaling or being very close to those of truth simulation; therefore true values of these parameters

can be retrieved at least in those cases where only one parameter contains error at a time. The identifiability of multiple parameters together is evaluated from their correlations with the model forecast. Significant levels of correlations are found that can be interpreted physically. As the number of uncertain parameters increases, both the level and the area coverage of significant correlations decrease, which implies that the degree of difficulties will be higher with multiple-parameter than single-parameter estimation.

The results of parameter estimation experiments using the EnSRF method and simulated radar data are reported in Chapter 5. In these experiments, individual parameters are estimated separately or in combinations. A data selection procedure based on correlation information is introduced, which, combined with variance inflation, effectively avoids the collapse of the parameter ensemble hence filter divergence. Our parameter estimation results demonstrate, for the first time, that the EnSRF method can be used to correct model errors resulting from uncertain microphysical parameters through simultaneous state and parameter estimation, using radar observations. When error exists in only one of the microphysical parameters, the parameter can be successfully estimated without exception. The results of multiple parameter estimation are generally less consistent than the results of single parameter estimation, mainly because the identifiability of the parameters become weaker and the problem might have no unique solution. The parameter estimation results are found to be very sensitive to the realization of the initial parameter ensemble, which is mainly due to the use of relatively small ensemble sizes (typically less than 100). Increasing

ensemble size generally improves the analysis. The quality of parameter estimation also depends on the quality of observation data.

The ultimate application of the ensemble Kalman filter is the initialization of realistic NWP models using real data. In Chapter 6, we apply the EnSRF method to a tornadic thunderstorm case that occurred on May 29 - 30, 2004 near Oklahoma City. A long lasting supercell produced sixteen tornadoes over a period of several hours. Radial velocity and reflectivity data from one or two WSR-88D Doppler radars are assimilated, in which the storm environment is, at first, defined by single sounding and the prediction model, the ARPS, is used in a simplified cloud model mode. The analyzed radial velocity and reflectivity fields match assimilated observations well. The flow fields show dynamically consistent patterns typical of supercell storms, including strong mid-level rotation and low-level hook echo. Predicted storm maintained supercell characteristics for more than 1 hour, but was generally weaker and propagated too fast. The cross-beam component of wind is, however, not analyzed well when using data from single radar.

To improve the results, better an environmental condition is then used, which is provided by a 3DVAR analysis of all conventional observations. Also a full suite of model physics is used so that the storm environment evolves with time. The surface friction effect is also properly included which might affect the storm propagation. However, no significant improvement is found with the analysis and forecast, compared to the corresponding single sounding cases using either single and two WSR-88D radars. Various tuning of the EnSRF including adjusting the cut-off radius of covariance localization, the amount of covariance inflation, or the estimated observational error did

not significantly improve the forecast results. This suggests that model errors, most probably those related to microphysics and resolution, dominate the inaccuracy in analysis and forecast. The lack of low-level radar data coverage due to the large distances between the storm and the radars might have contributed to a poor estimation of the low-level atmospheric state including cold pool and gust front, which affects subsequent forecast.

7.2 Future work

Our current results demonstrate that the ensemble-based Kalman filter algorithms are very promising for radar data assimilation, but much research is needed to improve the application of these algorithms to real case using real data.

First of all, model errors should be sufficiently taken into account in the analysis. This is, however, a very challenging task, which includes both identifying the sources of the errors and correcting them. As suggested by the results of Chapter 4, microphysical parameterization can significantly affect the structure and evolution of storms and leads to biased estimate. A possible way to deal with this type of model error is through parameter estimation, which is investigated in Chapter 5 through OSSEs. The possibility of incorporating parameter estimation in real cases, where many unknown sources of errors may exist, needs much further investigation. Another possible way of accounting for model errors or uncertainties is to apply multiple microphysics schemes to different ensemble members. The purpose is to increase the space spanned by the ensemble members in phase space. The results in Chapter 6 suggest that resolution is also a potential source of model error while recent studies by

e.g., Bryan et al (2003), suggest that resolutions as high as 100 meters may be needed by explicit thunderstorm forecast. The resolution error can be partially alleviated by using higher resolutions, but the available computing resources will always be a limiting factor. The dual-resolution approach proposed by Gao and Xue (2006) might be a good way of minimizing the resolution-related error at a reasonably computational cost. It can be tested with real cases in the future.

Without properly accounting for the model error in the prognostic equations, the estimated error covariance will be missing the model error covariance term in the Kalman filter equations, leading to a major discrepancy between the spread of the background forecast ensemble and the true background error. The background error covariance estimated from the ensemble can therefore be unreliable. Including parameterized model errors into the model equations is another approach to dealing with the filter divergence problem and to improve the filter performance. This is important area of research.

Previous studies on limited-area modeling have shown that errors in lateral boundary conditions can result in large forecast errors. Nutter et al. (2004a; 2004b) show that ensemble boundary conditions must be properly perturbed to prevent the ensemble forecast from losing its variance for increasing leading time. Like early ensemble Kalman filter studies with limited-area models, our current experiments included no boundary condition perturbations. This does not seem to be a significant problem for our experiments with relatively short forecast ranges and relatively large domains. Still, a proper treatment of lateral boundary perturbations for the forecast

ensembles is needed and several methods proposed recently by Torn et al. (2006) can be evaluated for small-scale nonhydrostatic systems.

For the microphysical parameter estimation, it is expected that additional parameters obtained by polarimetric radars, including the differential reflectivity and specific differential phase that contain DSD information, are helpful in reducing and/or avoiding the non-uniqueness of the solution, and improve the results of parameter estimation. In fact, initial results obtained so far by our research group are encouraging. The additional information provided by polarimetric measurements can hopefully also improve the state estimation of microphysical species.

References

- Aksoy, A., F. Zhang, and J. W. Nielsen-Gammon, 2006: Treatment of model error in thermally driven circulations through ensemble-based simultaneous state and parameter estimation. *Mon. Wea. Rev.*, accepted.
- Allen, M., J. Kettleborough, and D. Stainforth, 2003: Model error in weather and climate forecasting. *ECMWF 2002 seminar on predictability of weather and climate*, ECMWF, Shinfield Park, Reading, RG2 9AX UK, ECMWF, 275-294.
- Anderson, J. L., 2001: An ensemble adjustment Kalman filter for data assimilation. *Mon. Wea. Rev.*, **129**, 2884-2903.
- Annan, J. D. and J. C. Hargreaves, 2004: Efficient parameter estimation for a highly chaotic system. *Tellus*, **56A**, 520-526.
- Annan, J. D., J. C. Hargreaves, N. R. Edwards, and R. Marsh, 2005a: Parameter estimation in an intermediate complexity Earth System Model using an ensemble Kalman filter. *Ocean Modelling*, **8**, 135-154.
- Annan, J. D., D. J. Lunt, J. C. Hargreaves, and P. J. Valdes, 2005b: Parameter estimation in an atmospheric GCM using the Ensemble Kalman Filter. *Nonlinear Processes in Geophysics*, **12**, 363-371.
- Bishop, C. H., B. J. Etherton, and S. J. Majumdar, 2001: Adaptive sampling with the ensemble transform Kalman filter. Part I: Theoretical aspects. *Mon. Wea. Rev.*, **129**, 420.
- Braham, R. R. J., 1990: Snow Particle Size Spectra in Lake Effect Snows. *J. Appl. Meteor.*, **29**, 200-207.
- Bryan, G. H., J. C. Wyngaard, and J. M. Fritsch, 2003: Resolution Requirements for the Simulation of Deep Moist Convection. *Mon. Wea. Rev.*, **131**, 2394-2416.
- Burgers, G., P. J. v. Leeuwen, and G. Evensen, 1998: Analysis scheme in the ensemble Kalman filter. *Mon. Wea. Rev.*, **126**, 1719-1724.
- Caya, A., J. Sun, and C. Snyder, 2005: A Comparison between the 4DVAR and the Ensemble Kalman Filter Techniques for Radar Data Assimilation. *Mon. Wea. Rev.*, **133**, 3081-3094.
- Chavent, G., 1974: Identification of functional parameter in partial differential equations. In *Identification of Parameter in Distributed Systems*, R. E. Goodson and M. P. Polis, Eds., American Society of Mechanical Engineers, 31-48.
- Chavent, G., 1979: Identification of Distributed Parameter System: About the Output Least Squares Method, Its Implementation and Identifiability. *The fifth IFAC symposium*, Pergamon, New York, 85-97.

- Cifelli, R., C. R. Williams, D. K. Rajopadhyaya, S. K. Avery, K. S. Gage, and P. T. May, 2000: Drop-Size Distribution Characteristics in Tropical Mesoscale Convective Systems. *J. Appl. Meteor.*, **39**, 760-777.
- Cohard, J.-M. and J.-P. Printy, 2000: A comprehensive two-moment warm microphysical bulk scheme. I: Description and tests. *Q. J. Roy. Meteor. Soc.*, **126**, 1815-1842.
- Courtier, P. and O. Talagrand, 1987: Variational assimilation of Meteorological observations with the adjoint equation. Part II: Numerical results. *Quart. J. Roy. Meteor. Soc.*, **113**, 1329-1347.
- Crook, N. A., 1996: Sensitivity of moist convection forced by boundary layer processes to low-level thermodynamic fields. *Mon. Wea. Rev.*, **124**, 1767-1785.
- Crook, N. A., D. Dowell, J. Sun, and Y. Zhang, 2004: Assimilation of radar observations of a supercell storm using 4DVar: Parameter retrieval experiments. *22nd Conference on Severe Local Storms*, Hyannis, Massachusetts, Amer. Meteor. Soc., CDROM 8A.2.
- Dee, D. P., 1995: On-line estimation of error covariance parameters for atmospheric data assimilation. *Mon. Wea. Rev.*, **123**, 112-81145.
- Doviak, R. and D. Zrnic, 1993: *Doppler Radar and Weather Observations*. 2nd ed. Academic Press, 562 pp.
- Dowell, D., F. Zhang, L. J. Wicker, C. Snyder, and N. A. Crook, 2004: Wind and temperature retrievals in the 17 May 1981 Arcadia, Oklahoma supercell: Ensemble Kalman filter experiments. *Mon. Wea. Rev.*, 1982-2005.
- Droegemeier, K. K., 1990: Toward a science of storm-scale prediction. *Preprint, 16th conf. on Severe Local Storms*, Kananaskis Park, Alberta, Canada, Amer. Meteor. Soc., 256-262.
- Droegemeier, K. K., 1997: The numerical prediction of thunderstorms: Challenges, potential benefits, and results from real time operational tests. *WMO Bulletin*, **46**, 324-336.
- Epstein, E. S., 1969: Stochastic dynamic prediction. *Tellus, Ser. A*, **21**, 739-759.
- Evensen, G., 1992: Using the extended Kalman filter with a multi-layer quasi-geostrophic ocean model. *J. Geophys. Res.*, **97(C11)**, 17 905-17 924.
- Evensen, G., 1993: Open boundary conditions for the extended Kalman filter with a quasi-geostrophic model. *J. Geophys. Res.*, **98(C9)**, 16 529-16 546.
- Evensen, G., 1994: Sequential data assimilation with a nonlinear quasi-geostrophic model using Monte Carlo methods to forecast error statistics. *J. Geophys. Res.*, **99(C5)**, 10 143-10 162.
- Evensen, G. and P. J. van Leeuwen, 1996: Assimilation of Geosat Altimeter Data for the Agulhas Current Using the Ensemble Kalman Filter with a Quasigeostrophic Model. *Mon. Wea. Rev.*, **124**, 85-96.

- Evensen, G., 2003: The ensemble Kalman filter: Theoretical formulation and practical implementation. *Ocean Dynamics*, **53**, 343-367.
- Ferrier, B. S., 1994: A double-moment multiple-phase four-class bulk ice scheme. Part I: Description. *J. Atmos. Sci.*, **51**, 249-280.
- Ferrier, B. S., W.-K. Tao, and J. Simpson, 1995: A Double-Moment Multiple-Phase Four-Class Bulk Ice Scheme. Part II: Simulations of Convective Storms in Different Large-Scale Environments and Comparisons with other Bulk Parameterizations. *J. Atmos. Sci.*, **52**, 1001-1033.
- Gal-Chen, T., 1978: A method for the initialization of the anelastic equations: Implications for matching models with observations. *Mon. Wea. Rev.*, **106**, 587-606.
- Gao, J., M. Xue, Z. Wang, and K. K. Droegemeier, 1998: The initial condition and explicit prediction of convection using ARPS adjoint and other retrievals methods with WSR-88D data. *12th Conf. Num. Wea. Pred.*, Phoenix AZ, Amer. Meteor. Soc., 176-178.
- Gao, J.-D., M. Xue, A. Shapiro, and K. K. Droegemeier, 1999: A variational method for the analysis of three-dimensional wind fields from two Doppler radars. *Mon. Wea. Rev.*, **127**, 2128-2142.
- Gao, J.-D. and M. Xue, 2006: An Efficient Dual-Resolution Ensemble Data Assimilation Approach and Tests with the Assimilation of Doppler Radar Data. *Extended abstract, 10th Symposium on Integrated Observing and Assimilation Systems for the Atmosphere, Oceans and Land Surface (IOAS-AOLS)*, Atlanta, GA, Amer. Meteor. Soc.,.
- Gaspari, G. and S. E. Cohn, 1999: Construction of correlation functions in two and three dimensions. *Quart. J. Roy. Meteor. Soc.*, **125**, 723-757.
- Gilmore, M. S., J. M. Straka, and E. N. Rasmussen, 2004: Precipitation uncertainty due to variations in precipitation particle parameters within a simple microphysics scheme. *Mon. Wea. Rev.*, **132**, 2610-2627.
- Gunn, K. L. S. and J. S. Marshall, 1958: The distribution with size of aggregate snow flakes. *J. Meteor.*, **15**, 452-461.
- Hacker, J. P. and C. Snyder, 2005: Ensemble Kalman Filter Assimilation of Fixed Screen-Height Observations in a Parameterized PBL. *Mon. Wea. Rev.*, **133**, 3260-3275.
- Hamill, T. M., J. S. Whitaker, and C. Snyder, 2001: Distance-dependent filtering of background error covariance estimates in an ensemble Kalman filter. *Mon. Wea. Rev.*, **129**, 2776-2790.
- Hamill, T. M., 2004: Ensemble-based atmospheric data assimilation. http://www.cdc.noaa.gov/people/tom.hamill/efda_review5.pdf.
- Hansen, J. A., 2002: Accounting for Model Error in Ensemble-Based State Estimation and Forecasting. *Mon. Wea. Rev.*, **130**, 2373-2391.

- Hao, Z. and M. Ghil, 1995: Sequential parameter estimation for a coupled ocean-atmosphere model. *Proceeding, WMO 2nd International Symposium on Assimilation of Observations in Meteorology and Oceanography*, Tokyo, Japan, 181-186.
- Houtekamer, P. L. and H. L. Mitchell, 1998: Data assimilation using an ensemble Kalman filter technique. *Mon. Wea. Rev.*, **126**, 796-811.
- Houtekamer, P. L. and H. L. Mitchell, 2001: A sequential ensemble Kalman filter for atmospheric data assimilation. *Mon. Wea. Rev.*, **129**, 123-137.
- Houtekamer, P. L., H. L. Mitchell, G. Pellerin, M. Buehner, M. Charron, L. Spacek, and B. Hansen, 2005: Atmospheric data assimilation with an ensemble Kalman filter: Results with real observations. *Mon. Wea. Rev.*, **133**, 604-620.
- Houze, R. A. J., P. V. Hobbs, P. H. Herzegh, and D. B. Parsons, 1979: Size distributions of precipitation particles in frontal clouds. *J. Atmos. Sci.*, **36**, 156-162.
- Hu, M., M. Xue, and K. Brewster, 2006a: 3DVAR and Cloud Analysis with WSR-88D Level-II Data for the Prediction of the Fort Worth, Texas, Tornadoic Thunderstorms. Part I: Cloud Analysis and Its Impact. *Mon. Wea. Rev.*, **134**, 675-698.
- Hu, M., M. Xue, J. Gao, and K. Brewster, 2006b: 3DVAR and Cloud Analysis with WSR-88D Level-II Data for the Prediction of the Fort Worth, Texas, Tornadoic Thunderstorms. Part II: Impact of Radial Velocity Analysis via 3DVAR. *Mon. Wea. Rev.*, **134**, 699-721.
- Ide, K., P. Courtier, M. Ghil, and A. Lorenc, 1997: Unified notation for data assimilation: Operational, sequential and variational. *J. Meteor. Soc. Japan*, **75**, 181-189.
- Jazwinski, A. H., 1970: *Stochastic Processes and Filtering Theory*. Academic Press, 376 pp.
- Joss, J. and A. Waldvogel, 1969: Raindrop size distribution and sampling size errors. *J. Atmos. Sci.*, **26**, 566-569.
- Judson, A. and N. Doesken, 2000: Density of Freshly Fallen Snow in the Central Rocky Mountains. *Bull. Amer. Meteor. Soc.*, **81**, 1577-1587.
- Jung, Y., M. Xue, and J. M. Straka, 2005: Assimilation of polarimetric radar data using ensemble Kalman filter: Experiments with simulated data. *Extended abstract, 17th Conf. Num. Wea. Pred.*, Washington DC, Amer. Meteor. Soc., 13A.3.
- Keppenne, C. L. and M. M. Rienecker, 2002: Initial testing of a massively parallel ensemble Kalman filter with the Poseidon isopycnal ocean general circulation model. *Mon. Wea. Rev.*, **130**, 2951-2965.
- Kitamura, S. and S. Nakagiri, 1977: Identifiability of Spatially-Varying and Constant Parameters in Distributed Systems of Parabolic Type. *SIAM Journal of Control and Optimization*, **15**, 785-802.

- Kivman, G. A., 2003: Sequential parameter estimation for stochastic systems. *Nonlinear Processes in Geophysics*, **10**, 253-259.
- Le Dimet, F. X. and O. Talagrand, 1986: Variational algorithms for analysis and assimilation of meteorological observations: Theoretical aspects. *Tellus*, **38A**, 97-110.
- Lilly, D. K., 1990: Numerical prediction of thunderstorms - Has its time come? *Quart. J. Roy. Meteor. Soc.*, **116**, 779-798.
- Lin, Y.-L., R. D. Farley, and H. D. Orville, 1983: Bulk parameterization of the snow field in a cloud model. *J. Climate Appl. Meteor.*, **22**, 1065-1092.
- Liou, Y. C., T. Cal-Chen, and D. K. Lilly, 1991: Retrievals of wind, temperature and pressure from single-Doppler radar and a numerical model. *Preprint, 25th Int. Conf. on Radar Meteor.*, Paris, France, Amer. Meteor. Soc., 151-154.
- Lo, K. K. and R. E. P. Jr., 1982: The growth of snow in winter storms: An airborne observational study. *J. Atmos. Sci.*, **39**, 697-706.
- Lord, S. J., E. Kalnay, R. Daley, G. D. Emmitt, and R. Atlas, 1997: Using OSSEs in the design of the future generation of integrated observing systems. *Preprint volume, 1st Symposium on Integrated Observation Systems*, Long Beach, CA, Amer. Meteor. Soc., 45-47.
- Lord, S. J., M. Masutani, J. S. Woollen, J. C. Derber, R. Atlas, J. Terry, G. D. Emmitt, S. A. Wood, S. Greco, and T. J. Kleespies, 2001: Observing System Simulation Experiments for NPOESS. *Preprint, 5th Symposium on Integrated Observing Systems*, Albuquerque, NM, Amer. Meteor. Soc., 168-173.
- Lorenc, A., 1995: Atmospheric Data Assimilation. *the Second WMO Symposium on Assimilation of Observations in Meteorology and Oceanography*, Tokyo, Japan.
- Lorenc, A., 2003: The potential of the ensemble Kalman filter for NWP - a comparison with 4D-Var. *Quart. J. Roy. Meteor. Soc.*, **129**, 3183-3204.
- McCumber, M., W.-K. Tao, and J. Simpson, 1991: Comparison of ice-phase microphysical parameterization schemes using numerical simulations of tropical convection. *J. Appl. Meteor.*, **30**, 985-1004.
- Meyers, M. P., R. L. Walko, J. R. Harrington, and W. R. Cotton, 1997: New RAMS cloud microphysics parameterization. Part II: The two-moment scheme. *Atmos. Res.*, **45**, 3-39.
- Milbrandt, J. A. and M. K. Yau, 2005a: A Multimoment Bulk Microphysics Parameterization. Part I: Analysis of the Role of the Spectral Shape Parameter. *J. Atmos. Sci.*, **62**, 3051-3064.
- Milbrandt, J. A. and M. K. Yau, 2005b: A Multimoment Bulk Microphysics Parameterization. Part II: A Proposed Three-Moment Closure and Scheme Description. *J. Atmos. Sci.*, **62**, 3065-3081.

- Mitchell, D. L., 1988: Evolution of snow-size spectra in cyclonic storms. Part I: Snow growth by vapor deposition and aggregation. *J. Atmos. Sci.*, **45**, 3431-3451.
- Mitchell, H. L. and P. L. Houtekamer, 2000: An adaptive ensemble Kalman filter. *Mon. Wea. Rev.*, **128**, 416-433.
- Murakami, M., 1990: Numerical modeling of dynamic and microphysical evolution of an isolated convective cloud-The 19 July 1981 CCOPE cloud. *J. Meteor. Soc. Japan.*, **68**, 107-127.
- Murphy, J. M., 1988: The impact of ensemble forecasts on predictability. *Quart. J. Roy. Meteor. Soc.*, **114**, 463-493.
- Navon, I. M., 1997: Practical and theoretical aspects of adjoint parameter estimation and identifiability in meteorology and oceanography. *Dynamics of Atmospheres and Oceans*, **27**, 55-79.
- Nutter, P., D. Stensrud, and M. Xue, 2004a: Effects of coarsely-resolved and temporally-interpolated lateral boundary conditions on the dispersion of limited-area ensemble forecasts. *Mon. Wea. Rev.*, **132**, 2358-2377.
- Nutter, P., M. Xue, and D. Stensrud, 2004b: Application of lateral boundary condition perturbations to help restore dispersion in limited area ensemble forecasts. *Mon. Wea. Rev.*, **132**, 2378-2390.
- Passarelli, R. E. J., 1978: Theoretical and Observational Study of Snow-Size Spectra and Snowflake Aggregation Efficiencies. *J. Atmos. Sci.*, **35**, 882-889.
- Pruppacher, H. R. and J. D. Klett, 1978: *Microphysics of Clouds and Precipitation*. D. Reidel Publishers, 714 pp.
- Qiu, C.-J. and Q. Xu, 1992: A simple adjoint method of wind analysis for single-Doppler data. *J. Atmos. Oceanic Tech.*, **9**, 588-598.
- Ray, P. S., B. Johnson, K. W. Johnson, J. S. Bradberry, J. J. Stephens, K. K. Wagner, R. B. Wilhelmson, and J. B. Klemp, 1981: The morphology of severe tornadic storms on 20 May 1977. *J. Atmos. Sci.*, **38**, 1643-1663.
- Rutledge, S. A. and P. V. Hobbs, 1984: The mesoscale and microscale structure and organization of clouds and precipitation in midlatitude cyclones. Part XII: A diagnostic modeling study of precipitation development in narrow cold-frontal rainbands. *J. Atmos. Sci.*, **41**, 2949-2972.
- Shapiro, A., S. Ellis, and J. Shaw, 1995: Single-Doppler radar retrievals with Phoenix II data: Clear air and microburst wind retrievals in the planetary boundary layer. *J. Atmos. Sci.*, **52**, 1265-1287.
- Smith, P. L., Jr., C. G. Myers, and H. D. Orville, 1975: Radar reflectivity factor calculations in numerical cloud models using bulk parameterization of precipitation processes. *J. Appl. Meteor.*, **14**, 1156-1165.
- Snyder, C. and F. Zhang, 2003: Assimilation of simulated Doppler radar observations with an ensemble Kalman filter. *Mon. Wea. Rev.*, **131**, 1663-1677.

- Straka, J. M. and E. R. Mansell, 2005: A Bulk Microphysics Parameterization with Multiple Ice Precipitation Categories. *J. Appl. Meteor.*, **44**, 445-466.
- Sun, J., D. W. Flicker, and D. K. Lilly, 1991: Recovery of three-dimensional wind and temperature fields from simulated single-Doppler radar data. *J. Atmos. Sci.*, **48**, 876-890.
- Sun, J. and N. A. Crook, 1997: Dynamical and microphysical retrieval from Doppler radar observations using a cloud model and its adjoint. Part I: Model development and simulated data experiments. *J. Atmos. Sci.*, **54**, 1642-1661.
- Sun, J. and N. A. Crook, 2001: Real-time low-level wind and temperature analysis using single WSR-88D data. *Wea. Forecasting*, **16**, 117-132.
- Sun, J., 2005: Initialization and Numerical Forecasting of a Supercell Storm Observed during STEPS. *Monthly Weather Review*, **133**, 793-813.
- Sun, N., N.-Z. Sun, M. Elimelech, and J. N. Ryan, 2001: Sensitivity analysis and parameter identifiability for colloid transport in geochemically heterogeneous porous media. *Water Resour. Res.*, **37**, 209-222.
- Sun, N.-Z. and W. W.-G. Yeh, 1990: Coupled Inverse Problems in Groundwater Modeling, 2. Identifiability and Experimental Design. *Water Resour. Res.*, **26**, 2527-2540.
- Tao, W.-K. and J. Simpson, 1993: Goddard cumulus ensemble model. Part I: Model description. *Terres. Atmos. Ocean Sci.*, **4**, 35-72.
- Tippett, M. K., J. L. Anderson, C. H. Bishop, T. M. Hamill, and J. S. Whitaker, 2003: Ensemble square root filters. *Monthly Weather Review*, **131**, 1485-1490.
- Tokay, A., D. A. Short, and O. W. Thiele, 1995: Convective vs. stratiform rain over Kapingamarangi atoll during TOGA COARE: Evidence from raindrop spectra. *Preprints, Conf. on.*
- Tokay, A. and D. A. Short, 1996: Evidence from Tropical Raindrop Spectra of the Origin of Rain from Stratiform versus Convective Clouds. *J. Appl. Meteor.*, **35**, 355-371.
- Tong, M. and M. Xue, 2004: Ensemble Kalman filter assimilation of Doppler radar data with a compressible nonhydrostatic model. *Extended Abstract, 20th Conf. Wea. Analy. Forecasting/16th Conf. Num. Wea. Pred.*, Seattle, WA, Amer. Meteor. Soc.
- Tong, M. and M. Xue, 2005a: Ensemble Kalman filter assimilation of Doppler radar data with a compressible nonhydrostatic model: OSS Experiments. *Mon. Wea. Rev.*, 1789-1807.
- Tong, M. and M. Xue, 2005b: Simultaneous retrieval of microphysical parameters and atmospheric state variables with radar data and ensemble Kalman filter method. *Extended abstract, 17th Conf. Num. Wea. Pred.*, Washington DC, Amer. Meteor. Soc., P1.30.

- Toth, Z. and E. Kalnay, 1997: Ensemble forecasting at NCEP and the breeding method. *Mon. Wea. Rev.*, **125**, 3297-3319.
- van den Heever, S. C. and W. R. Cotton, 2004: The Impact of Hail Size on Simulated Supercell Storms. *J. Atmos. Sci.*, **61**, 1596-1609.
- van Leeuwen, P. J., 1999: Comment on "Data Assimilation Using an Ensemble Kalman Filter Technique". *Mon. Wea. Rev.*, **127**, 1374-1377.
- Waldvogel, A., 1974: The N0-jump of raindrop spectra. *J. Atmos. Sci.*, **31**, 1067-1078.
- Weygandt, S. S., A. Shapiro, and K. K. Droegemeier, 2002a: Retrieval of Model Initial Fields from Single-Doppler Observations of a Supercell Thunderstorm. Part I: Single-Doppler Velocity Retrieval. *Mon. Wea. Rev.*, **130**, 433-453.
- Weygandt, S. S., A. Shapiro, and K. K. Droegemeier, 2002b: Retrieval of Model Initial Fields from Single-Doppler Observations of a Supercell Thunderstorm. Part II: Thermodynamic Retrieval and Numerical Prediction. *Mon. Wea. Rev.*, **130**, 454-476.
- Whitaker, J. S. and T. M. Hamill, 2002: Ensemble data assimilation without perturbed observations. *Mon. Wea. Rev.*, **130**, 1913-1924.
- Whitaker, J. S., G. P. Compo, X. Wei, and T. M. Hamill, 2004: Reanalysis without radiosondes using ensemble data assimilation. *Mon. Wea. Rev.*, **132**.
- Wood, V. T. and R. A. Brown, 1997: Effects of radar sampling on single-Doppler velocity signatures of mesocyclones and tornadoes. *Wea. Forecasting*, **12**, 928-938.
- Wu, B., J. Verlinde, and J. Sun, 2000: Dynamical and microphysical retrievals from Doppler radar observations of a deep convective cloud. *J. Atmos. Sci.*, **57**, 262-283.
- Xue, M., K. Brewster, K. K. Droegemeier, F. Carr, V. Wong, Y. Liu, A. Sathye, G. Bassett, P. Janish, J. Levit, and P. Bothwell, 1996: Real-time numerical prediction of storm-scale weather during VORTEX-95. Part II: Operation summary and example cases. *Preprint: 18th Conf. on Severe Local Storms*, San Francisco, CA., Amer. Meteor. Soc., 178-182.
- Xue, M., K. K. Droegemeier, and V. Wong, 2000: The Advanced Regional Prediction System (ARPS) - A multiscale nonhydrostatic atmospheric simulation and prediction tool. Part I: Model dynamics and verification. *Meteor. Atmos. Physics*, **75**, 161-193.
- Xue, M., K. K. Droegemeier, V. Wong, A. Shapiro, K. Brewster, F. Carr, D. Weber, Y. Liu, and D.-H. Wang, 2001: The Advanced Regional Prediction System (ARPS) - A multiscale nonhydrostatic atmospheric simulation and prediction tool. Part II: Model physics and applications. *Meteor. Atmos. Phy.*, **76**, 143-165.
- Xue, M. and J. Min, 2003: Precipitation verification on CAPS Real-time forecasts during IHOP 2002. *Presentation, IHOP Spring Science Meeting*, Boulder CO.

- Xue, M., D.-H. Wang, J.-D. Gao, K. Brewster, and K. K. Droegemeier, 2003: The Advanced Regional Prediction System (ARPS), storm-scale numerical weather prediction and data assimilation. *Meteor. Atmos. Physics*, **82**, 139-170.
- Xue, M., M. Tong, and K. K. Droegemeier, 2006: An OSSE Framework Based on the Ensemble Square Root Kalman Filter for Evaluating the Impact of Data from Radar Networks on Thunderstorm Analysis and Forecasting. *J. Atmos. Oceanic Tech.*, **23**, 46-66.
- Yakowitz, S. and L. Duckstein, 1980: Instability in Aquifer Identification: Theory and Case Studies. *Water Resour. Res.*, **16**, 1045-1064.
- Yeh, W. W.-G., 1986: Review of Parameter Identification Procedures in Groundwater Hydrology: The Inverse Problem. *Water Resour. Res.*, **22**, 95-108.
- Yu, L. and J. J. O'Brien, 1991: Variational estimation of the wind stress drag coefficient and the oceanic eddy viscosity profile. *J. Phys. Oceanogr.*, **21**, 709-719.
- Zhang, F., C. , Snyder, and J. Sun, 2004: Impacts of initial estimate and observations on the convective-scale data assimilation with an ensemble Kalman filter. *Mon. Wea. Rev.*, **132**, 1238-1253.
- Ziegler, C. L., 1985: Retrieval of thermal and microphysical variables in observed convective storms. Part I: Model development and preliminary testing. *J. Atmos. Sci.*, **42**, 1487-1509.
- Zou, X., I. M. Navon, and F. X. Le Dimet, 1992: An optimal nudging data assimilation scheme using parameter estimation. *Quart. J. Roy. Meteor. Soc.*, **118**, 1163-1186.

Nomenclature

Roman Symbols

A	Correlation matrix
$A_{i,j}$	Element of matrix A
B	Covariance matrix
C	Schur product of correlation matrix A with covariance matrix B
D_x	Particle diameter
D_e	Forecast-observation error covariance matrix
e₀	Initial state error vector
E	Expectation operator
E	Scaling factor for smoothed initial state perturbations (Chapter 5)
G	Model error forcing (Chapter 2)
G	Two-way Gaussian power weighting function (Chapter 5)
H	Observation operator
H	Jacobian matrix of observation operator H
I	Identity matrix
J	Response function
K_i	Dielectric factor for ice
K_r	Dielectric factor for water
K	Kalman gain
$\tilde{\mathbf{K}}$	Modified Kalman gain used in the EnSRF

L	Loss function operator (Chapter 2)
M	Forecast model
\mathbf{M}	Jacobian matrix of forecast model M
n_{0h}	Intercept parameter of hail/graupel size distribution
n_{0r}	Intercept parameter of rain size distribution
n_{0s}	Intercept parameter of snow size distribution
n_{0x}	Intercept parameter of drop size distribution
N	Ensemble size (number of ensemble members)
p	probability density function (Chapter 2)
p	Pressure (Chapter 3, 4 and 6)
p'	Pressure perturbation
p_i	Model parameter (Chapter 4, 5)
p_i^t	True (control) value of parameter p_i (Chapter 4, 5)
\bar{p}_i	Upper bound of parameter p_i
\underline{p}_i	Lower bound of parameter p_i
p_{i0}^m	The m th initial guess of parameter p_i
\mathbf{p}	Model parameter vector
\mathbf{p}^t	True model parameter vector
$\hat{\mathbf{p}}$	Estimate of parameter vector \mathbf{p}
P_{ad}	Admissible set of parameter vector \mathbf{p}
P_i	Logarithmically transformed microphysical parameter

P_{i0}^m	The m th initial guess of logarithmically transformed parameter P_i
P_i^t	True value of logarithmically transformed parameter P_i
\underline{P}_i	Lower bound of logarithmically transformed parameter P_i
\overline{P}_i	Upper bound of logarithmically transformed parameter P_i
\mathbf{P}	Logarithmically transformed parameter vector
\mathbf{P}_0	Initial guess of logarithmically transformed parameter vector \mathbf{P}
\mathbf{P}_t	Covariance matrix at time t
\mathbf{P}_t^a	Analysis error covariance matrix at time t
\mathbf{P}_t^f	Forecast (background) error covariance matrix at time t
\mathbf{P}_e^a	Analysis error covariance matrix estimated from ensemble
\mathbf{P}_e^f	Forecast error covariance matrix estimated from ensemble
q_c	Mixing ration for cloud water
q_h	Mixing ration for hail
q_i	Mixing ration for cloud ice
q_r	Mixing ration for rainwater
q_s	Mixing ration for snow
q_v	Water vapor specific humidity
\mathbf{q}_t	White Gaussian model error vector
\mathbf{Q}	Model error covariance matrix
r	Correlation inflation factor (Chapter 2)

r	Gaussian random number (Chapter 5)
r	Correlation coefficient (Chapter 5)
R	Observation error covariance matrix
S	$n \times n$ positive semi-definite matrix (Chapter 2)
t	Time
$T_{n_{0x}}$	Time scale of model response to intercept parameter n_{0x}
T_{ρ_x}	Time scale of model response to particle density ρ_x
u	Horizontal velocity in the x direction
v	Horizontal velocity in the y direction
v	Innovation vector
V_r	Radial velocity
w	Vertical velocity
w_t	Bulk terminal velocity
w_{th}	Mass-weighted mean terminal velocity for hail
w_{tr}	Mass-weighted mean terminal velocity for rain
w_{ts}	Mass-weighted mean terminal velocity for snow
w	White noise vector (Chapter 2)
W	Distant-dependent weighting function (Chapter 5)
x, y	Horizontal coordinates
\mathbf{x}_t	State vector at time t
$\hat{\mathbf{x}}_t$	Estimate of \mathbf{x}_t

\mathbf{x}_t^a	Analysis state vector at time t
\mathbf{x}_t^f	Forecast state vector at time t
$\mathbf{x}_{t,i}^a$	Analysis state of ensemble member at time t
$\mathbf{x}_{t,i}^f$	Forecast state of ensemble member at time t
$\bar{\mathbf{x}}^a$	Ensemble mean of analysis state
$\bar{\mathbf{x}}^f$	Ensemble mean of forecast state
$\tilde{\mathbf{x}}_t$	Error in estimate $\hat{\mathbf{x}}_t$
\mathbf{x}^t	True model state vector (Chapter 4)
\mathbf{y}_t	Observation vector at time t
\mathbf{y}_i	The i th perturbed observation vector
\mathbf{Y}_t	Observation matrix before time t
\mathbf{Y}_τ	Observation matrix before time τ
z	Vertical coordinate
Z	Reflectivity (factor)
Z_e	Equivalent reflectivity factor
Z_{eh}	Equivalent reflectivity factor for hail
Z_{er}	Equivalent reflectivity factor for rain
Z_{es}	Equivalent reflectivity factor for snow

Greek Symbols

α	Coefficient of modified Kalman gain in EnSRF
β	Time decorrelation coefficient for stochastic forcing
ε	Smoothed random perturbation (Chapter 5)
ε_t	Observation error vector at time t (Chapter 2)
ε_i	Perturbed observation error vector (Chapter 2)
ε^o	Observation error vector (Chapter 6)
ε^f	Forecast error vector (Chapter 6)
ϕ	Radar elevation angle
ϕ_g	Radar elevation at model grid point
ϕ_0	Radar elevation at beam center
ϕ_w	One degree radar beam width
η	Radar observed quantity V_r or Z
η_e	Elevation level value of radar observed quantity
η_e	Grid point value of radar observed quantity
η^*	Error-containing radar observation (Chapter 4)
φ	Azimuth angle of radar beam
λ_x	Slope parameter of drop size distribution
θ	Potential temperature
θ'	Perturbation potential temperature
ρ°	Schur product

ρ	Density of air
ρ_x	Bulk particle density
ρ_h	Density of hail/grauel
ρ_i	Density of ice
ρ_r	Density of rainwater
ρ_s	Density of snow
σ_{V_r}	Standard deviation of observation error for radial velocity
σ_Z	Standard deviation of observation error for reflectivity
σ_{P_i}	Standard deviation of initial parameter perturbations
$\underline{\sigma}_{P_i}$	Minimum ensemble spread of parameter for ensemble inflation
σ_f^2	Variance of forecast error vector
$\hat{\sigma}_f^2$	Variance of forecast error vector estimated from ensemble
σ_o^2	Variance of observation error vector
σ_v^2	Variance of innovation vector
τ	Time
\mathbf{v}	Gaussian random error vector
ξ	n -vector
\mathfrak{R}^n	Euclidean n -space
\wp	Phase space

Acronyms

ARPS	Advanced Regional Prediction System
CASA	Center for Adaptive Sensing of the Atmosphere
CAPE	Convective available potential energy
CDT	Central Daylight Time
CIN	Convective inhibition
CST	Central Standard Time
DEnKF	Double ensemble Kalman filter
DSD	Drop size distribution
EAKF	Ensemble adjustment Kalman filter
EKF	Extended Kalman filter
EnKF	Ensemble Kalman filter
EnSRF	Ensemble square root filter
ETKF	Ensemble transform Kalman filter
GCM	General Circulation Model
NCAR	National Center for Atmospheric Research
NWP	Numerical Weather Prediction
OSSE	Observing System Simulation Experiment
PBL	Planetary boundary layer
pdf	probability density function
PPI	Plan position indicator
rms	Root-mean-square
RMSD	Root-mean-square difference

UTC	Coordinated Universal Time
VCP	Volume Coverage Pattern
WSR-88D	Weather Surveillance Radar 88 Doppler
3DVAR	Three-dimensional variational method
4DVAR	Four-dimensional variational method